**The Dissertation Committee for Joshua Allen Hubbard Certifies that this is the approved version of the following dissertation:**

# Enhanced Real-Time Bioaerosol Detection: Atmospheric Dispersion Modeling and Characterization of a Family of Wetted-Wall Bioaerosol Sampling Cyclones

**Committee:**

Ofodike Ezekoye, Supervisor

John Haglund, Supervisor

Matt Hall

Atila Novoselac

Carlos Hidrovo

# Enhanced Real-Time Bioaerosol Detection: Atmospheric Dispersion Modeling and Characterization of a Family of Wetted-Wall Bioaerosol Sampling Cyclones

by

**Joshua Allen Hubbard, M.S.; B.S.M.E.**

**Dissertation**

Presented to the Faculty of the Graduate School of
The University of Texas at Austin
in Partial Fulfillment
of the Requirements
for the Degree of

**Doctor of Philosophy**

**The University of Texas at Austin**
**August 2009**

# Dedication

This work is dedicated to Marilee, my mother, whose faith, perseverance, and unselfish love prove anything is possible.

# Acknowledgements

I am grateful for the mentorship of Doctor John Haglund and Professor Ofodike Ezekoye during my tenure at the University of Texas.  Dr. Haglund’s shared knowledge of experimental methods and aerosol systems integration has been invaluable to my development as an independent researcher.  Dr. Ezekoye’s distinguished comprehension of physics, mathematics, and engineering has given me a greater appreciation for learning and a deep desire to educate others.  I have been humbled by their dedication and patience.

I also express appreciation to the research staff at the Applied Research Labs in Austin, Texas.  Don Tucker, John Copeland, Eric Burton, Sarah Chandler, and Brian Humphrey made important contributions to my work and I am thankful for their individual expertise.  The staff at the Aerosol Technology Laboratory, Texas A&M University, College Station, Texas, is also acknowledged.  I am thankful to have collaborated with accomplished researchers like Dr. Maria King and Dr. Andrew McFarland.

Lastly, this work would not have been possible without the financial sponsorship of The Texas Engineering Experiment Station (Contract W911SR-07-C-0056, Subrecipient Agreement A1601-1, and Contract DAAD13-03-C-0050, Subrecipient Agreement A0181).

# Enhanced Real-Time Bioaerosol Detection:
# Atmospheric Dispersion Modeling and Characterization of a Family of Wetted-Wall Bioaerosol Sampling Cyclones

Publication No._____________

Joshua Allen Hubbard, Ph.D.
The University of Texas at Austin, 2009

Supervisor: Ofodike A. Ezekoye
Supervisor: John S. Haglund

This work is a multi-scale effort to confront the rapidly evolving threat of biological weapons attacks through improved bioaerosol surveillance, detection, and response capabilities.

The effects of bioaerosol release characteristics, transport in the atmospheric surface layer, and implications for bioaerosol sampler design and real-time detection were studied to develop risk assessment and modeling tools to enhance our ability to respond to biological weapons attacks. A simple convection-diffusion-sedimentation model was formulated and used to simulate atmospheric bioaerosol dispersion. Model predictions suggest particles smaller than 60 micrometers in aerodynamic diameter (AD) are likely to be transported several kilometers from the source. A five fold increase in effective mass collection rate, a significant bioaerosol detection advantage, is projected for samplers designed to collect particles larger than the traditional limit of 10 micrometers AD when such particles are present in the source distribution.

A family of dynamically scaled wetted-wall bioaerosol sampling cyclones (WWC) was studied to provide bioaerosol sampling capability under various threat scenarios. The effects of sampling environment, i.e. air conditions, and air flow rate on liquid recovery rate and response time were systematically studied. The discovery of a critical liquid input rate parameter enabled the description of all data with self-similar relationships. Empirical correlations were then integrated into system control algorithms to maintain microfluidic liquid output rates ideally suited for advanced biological detection technologies. Autonomous ambient air sampling with an output rate of 25±5 μL/min was achieved with open-loop control. These liquid output rates correspond to concentration rates on the order of 2,000,000, a substantial increase with respect to other commercially available bioaerosol samplers.

Modeling of the WWC was performed to investigate the underlying physics of liquid recovery. The set of conservative equations governing multiphase heat and mass transfer within the WWC were formulated and solved numerically. Approximate solutions were derived for the special cases of adiabatic and isothermal conditions. The heat and mass transfer models were then used to supplement empirical correlations. The resulting semi-empirical models offer enhanced control over liquid concentration factor and further enable the WWC to be deployed as an autonomous bioaerosol sampler.

# Table of Contents

# List of Tables

# List of Figures

# Introduction

The destructive power of biological weapons and the malevolence of terrorist groups have awakened us to the growing threats faced from the dissemination of airborne pathogens. A report by the Commission on the Prevention of WMD Proliferation and Terrorism details the rapidly evolving nature of these threats and urges the world community to act urgently and decisively to address them (Graham et al., 2008).

The United States has implemented a multi-faceted strategy to confront the threat of biological weapons (BW). Biodefense for the 21st century, a directive initiated by former President George W. Bush, outlines four pillars of our biodefense program: threat awareness, prevention and protection, surveillance and detection, and response and recovery (USDHS, 2004). This dissertation is a multi-scale effort to strengthen our biodefense infrastructure through improved bioaerosol surveillance, detection, and response capabilities.

A relatively isolated release of BW agents in the atmosphere could result in widespread loss of life, economic damage, and social disruption. Forecasting the spread of bioaerosols is of great importance to implementing a swift and highly focused response as well as designing effective sensor networks. Furthermore, in the case of an attack, dispersion modeling could provide forensic tools to investigate the source. Atmospheric aerosol dispersion modeling is therefore an essential component of our biodefense program.

Chapter 1 is devoted to increasing our ability to predict the dispersion of bioaerosols in the atmosphere. A simple convection-diffusion-sedimentation model was developed to predict the evolution of particle size distributions in the atmospheric surface layer. Results of this study advance the wider body of knowledge on atmospheric coarse particulate transport and modeling. Contemporary bioaerosol sampling strategies and detector designs are also evaluated with respect to model simulations and recommendations are made to enhance real-time detection and response.

Surveillance and detection systems are the second component of our biodefense program studied here. Programs like BioWatch, a national network of biosensors in major U.S. cities, have been established to facilitate rapid and efficacious response to BW attacks. Biosensor systems are increasingly complex devices due to the requirements of high efficiency collection and sample concentration, and high specificity and sensitivity during the analysis and identification process (USDHS, 2007). Additionally, sampling systems must function consistently in a wide variety of geographical locations and environmental conditions.

Chapters 2 through 4 focus on the development of one particular bioaerosol sampling system, the wetted-wall bioaerosol sampling cyclone (WWC). Performance characteristics like response time and liquid recovery rate were measured experimentally to develop accurate controls over the concentration factor. Physical processes occurring within the WWC were also studied with numerical heat and mass transfer models. These works enable integration of WWC and advanced detection technologies to form the next generation of real-time biosensor systems.

# 1. ATMOSPHERIC BIOAEROSOL DISPERSION MODELING AND IMPLICATIONS FOR REAL-TIME BIOAEROSOL DETECTION AND SAMPLER DESIGN

## 1.1. Background

The Centers for Disease Control (CDC) and World Health Organization (WHO) have tremendous interest in the spread of airborne pathogens like foot and mouth disease (FMD) and Severe Acute Respiratory Syndrome (SARS). An outbreak of FMD in the United Kingdom in 2001 had a total estimated economic cost of $7-10 billion (Thompson et al. 2002). The Hong Kong SARS outbreak of 2003 resulted in nearly 300 deaths and highlighted the alarming risk of disease spreading through the atmosphere (Yu et al. 2004). Both instances of naturally occurring disease engendered widespread anxiety. People feared these relatively isolated events would grow to a global scale with unimaginable consequences.

The deliberate dissemination of pathogenic organisms as agents of biological warfare is a rapidly evolving threat. High morbidity, ease of transmission and dissemination, fear and anxiety, and sparsely developed medical treatments make agents like Hemorrhagic Fever viruses, Smallpox virus, and Tularemia bacteria ideal candidates for use by terrorist organizations. The Commission on the Prevention of WMD Proliferation and Terrorism recently predicted the United States will face this threat within the next five years (Graham et al., 2008). The Department of Homeland Security (DHS) and other agencies have therefore been developing multi-layered responses, like emergency protocols and sensor networks, to address these risks.

Whether natural or deliberate, understanding atmospheric dispersion of pathogenic aerosols is paramount to protecting the health and prosperity of peoples and societies throughout the world. The identification of threats and modeling how they spread enables the design and placement of effective sensor systems. This study was completed to analyze the effects of atmospheric dispersion on real-time bioaerosol detection with emphases on improved dispersion modeling and bioaerosol collector design.

## 1.2. State of Atmospheric Dispersion Modeling

There exist a large number of atmospheric dispersion models to simulate and predict the spread of pollutants and particulate in the atmosphere. These models are largely supported by the United States Environmental Protection Agency (EPA) and help determine compliance with the National Ambient Air Quality Standards (NAAQS). However, very few of these models provide proper accounting for gravitational settling and particle inertia that make coarse particulate (>10 micrometers AD) transport distinctly different from that of the gas phase. The development of particulate dispersion models is further complicated by the scarcity of experimental data needed for validation. Out-of-date particulate models are often applied within the context of current research, and current models fail to show consistent results between measured values of total suspended particulate and model predictions. Particulate dispersion models need to be developed, on a fundamental and programmatic basis, to better suit the needs of the modeling community.

AERMOD is considered the EPA's state-of-the-art dispersion model. A joint effort between the American Meteorological Society (AMS) and EPA began in 1991 to incorporate the most sophisticated developments in atmospheric sciences into a regulatory dispersion model (Cimorelli, 2005). This platform replaced the Industrial Source Complex (ISC3) model and became the EPA recommended model in 2005 (EPA, 2005). ISC3 remains an EPA alternative model although its use must be justified and approved on a case-by-case basis. The Fugitive Dust Model (FDM) was the precursor to ISC3 and AERMOD but is no longer endorsed or supported by the EPA. However, FDM remains a widely utilized tool in research, indicating a lack of consistent application across disciplines.

AERMOD is a three-dimensional, steady-state, short range (~50 km), modified Gaussian plume model that accounts for the complex physics of the planetary boundary layer. Topographical and meteorological preprocessors allow the model to be applied over complex terrains with real-time meteorological conditions. Algorithms for the effects of building wakes are also employed to extend the application to urban environments. AERMOD allows the user to specify the aerosol source in terms of geometry, magnitude, and particle size distribution. Wet and dry deposition algorithms are included to account for the effects of plume depletion.

Validation of AERMOD, during development, was only performed with data for the dispersion of tracer gases (Perry, 2005; Holmes, 2006). Tracer gas comparisons focused on modeling complex physics of urban dispersion and the newest advances in planetary boundary layer science. However, AERMOD validation for coarse particulate dispersion was neglected. Large scale studies on coarse particulate have been performed sparsely in the past. The logistics and scope associated with conducting such studies are daunting. For these reasons AERMOD predictions are almost universally compared to ISC3 or FDM predictions for validation purposes. Furthermore, the comparison of all three models to measurements of total suspended particulate (TSP) demonstrate an inconsistent ability to model particulate dispersion with past and present regulatory models.

Kim and Larson studied FDM predictions for coarse particulate (1-100 micrometers) dispersion in stable atmospheric stratification against their own Monte Carlo Plume Model (2001). They recognized the errors inherent to the ISC and FDM models arising from neglecting vertical variations of wind speed and turbulent intensity in the atmospheric surface layer. They also point out that these two models exclude the vertical advection component, i.e. gravitational settling velocity, which manifests itself as plume sedimentation, although a plume depletion ‘sink’ term is included through the ground deposition algorithm. Experimental data from the Hanford studies showed FDM over-predicted downwind concentration and under-predicted deposition. Predicted values of the normalized cross-wind integrated concentration were 1.5-2.0 times higher than measured values. The authors attributed this to an inaccurate deposition velocity model and corrected it according to work done by Kim et al. (2000). They do not compare the results to the ISC model citing past studies demonstrating the superiority of FDM to ISC3.

Vesovic et al. examined coarse particulate (~100 micrometers) dispersion and deposition from elevated releases in neutral atmospheres (2001). They compared their two-dimensional Lagrangian model to FDM and experimental data. They found FDM to over-predict (ca. 60%) peak concentrations while under-predicting, or not-predicting, long-range particulate concentrations. The authors recognized the need for additional work in coarse particulate dispersion due to the complex interactions between particles and turbulent eddies, and the lack of accounting of gravitational settling, or vertical advection, in many gas phase models.

Etyemezian et al. found reasonable agreement between the ISC3 and FDM models for road dust emissions less than 10 micrometers (2004). Tsai et al. employed FDM to model spray drift from agricultural operations (2005). They were able to match measurements to model predictions by varying the source particle size distribution in the model. Although effective, this ad hoc method fails to produce much utility to the broader modeling community. Abdul-Wahab found FDM under-predicted measured concentrations of cement dust (50-150 micrometers) by approximately 20% at distances less than 1 kilometer from source (2006) and concluded the FDM model was adequate for estimating short range transport of cement dusts. Scott and Proctor evaluated AERMOD, ISC3, and FDM by modeling the dispersion of soil due to wind erosion and vehicle traffic over unpaved roads (2008). They found FDM and ISC to overestimate TSP and Chromium levels by factors ranging from 2-8. AERMOD predicted particulate levels approximately 5-14 times greater than measured. This study illustrates significant prediction errors that are potentially associated with source modeling and other confounding issues.

This brief review of current atmospheric dispersion studies illustrates the deficiencies present in current coarse particulate dispersion models: the neglect of vertical variations in wind speed and turbulence in the atmospheric surface layer in FDM and ISC, and the absence of vertical advection velocities due to gravitational settling in all EPA models although indirectly accounted for with deposition algorithms. Furthermore, consistent application of the EPA recommended model (AERMOD) is hampered by a lack of developmental validation, and inconsistent, sometimes substantial, errors when compared to measurements.

## 1.3. Convection-Diffusion-Sedimentation Dispersion Model

A new physical model for coarse particulate transport in the atmospheric surface layer is proposed to remedy the errors associated with existing models. This model accounts for vertical variations in wind speed and turbulent diffusivity as well as the vertical advection component associated with gravitational settling. The proposed model is illustrated in Figure 1.1. An instantaneous aerosol puff is mixed by atmospheric turbulence, convected downstream of the source by horizontal wind, and settles and deposits on the ground due to the gravitational settling velocity. Both atmospheric turbulence and horizontal wind speed, $u(z)$, are assumed to be functions of height from the ground and the gravitational settling velocity, $v_g$, is constant for a given particle size.

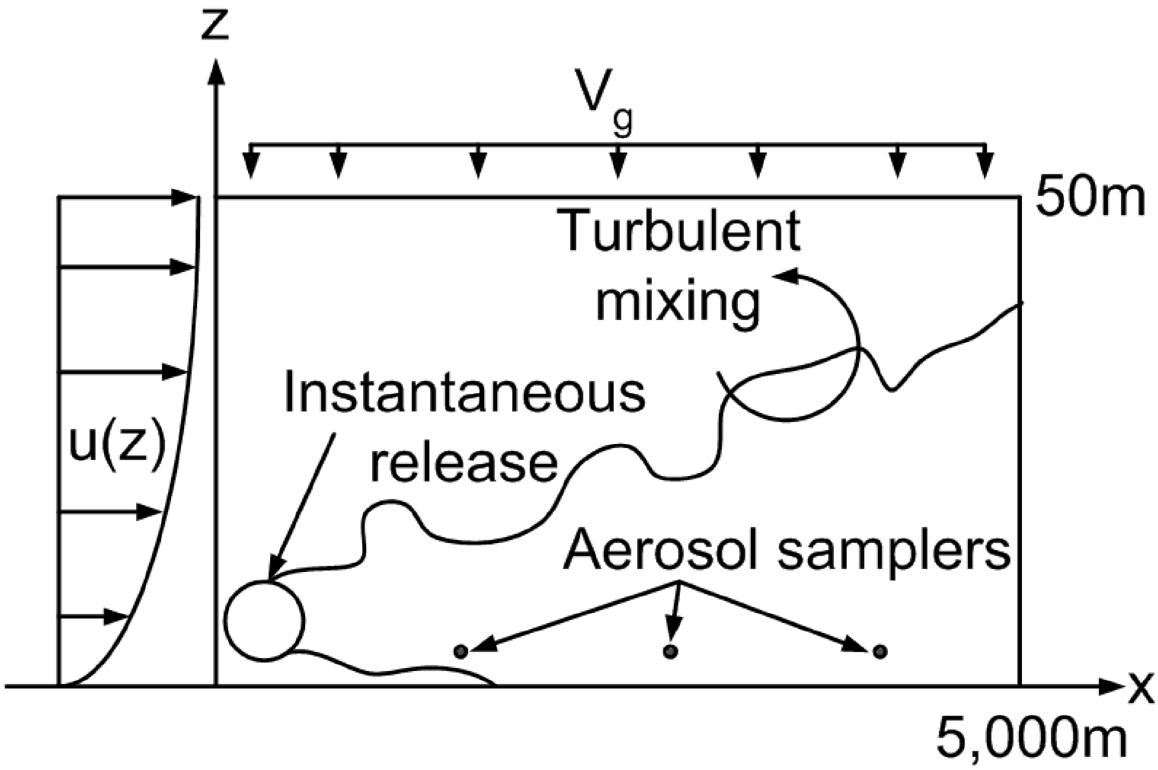

Figure 1.1: Simulation domain including turbulent mixing, gravitational settling, and longitudinal convection in the lowest 50 meters of the atmospheric surface layer

### 1.3.1. TRANSPORT EQUATION

The two-dimensional transient convection-diffusion equation,

$$\frac{\partial C_i}{\partial t}+\frac{\partial (uC_i)}{\partial x}+\frac{\partial (v_g C_i)}{\partial z}=\frac{\partial}{\partial x}\left(K_x\frac{\partial C_i}{\partial x}\right)+\frac{\partial}{\partial z}\left(K_z\frac{\partial C_i}{\partial z}\right) \tag{1.1}$$

governs particulate transport in the atmospheric surface layer, where $C_i$ is the particulate concentration of particle size $i$, $u$ represents the horizontal wind velocity component, $v_g$ represents the gravitational settling velocity, and $K_x$ and $K_z$ represent particulate diffusivities due to turbulent mixing in the longitudinal, $x$, and vertical, $z$, directions. The longitudinal extent of coarse particulate transport and relative importance of gravitational settling to vertical mixing are the main focuses of this study. Therefore, the model is simplified to two-dimensions. The omission of lateral wind velocity in the governing transport equation is justified since Coriolis forces are negligible in this lower region of the atmosphere.

### 1.3.2. MONIN-OKHUBOV SURFACE LAYER SIMILARITY THEORY

The horizontal wind speed and turbulent diffusivities are characterized by Monin-Okhubov (M-O) similarity theory. A cursory review of M-O theory will be presented here, but the reader is referred to Wyngaard (1973) for an in-depth description of atmospheric surface layer scaling. Monin and Okhubov theorized the turbulent fluxes of heat and momentum in the atmospheric surface layer could be described by the surface stress, $\tau_0$, heat flux to the surface, $H_0$, buoyancy variable, $g/T_0$, and the height above the surface, $z$. Ultimately, the surface layer wind speed and turbulent diffusivities can be expressed in terms of velocity and length scales, the friction velocity, $u_* = (\tau_0 / \rho)^{1/2}$, and Monin-Okhubov length, $L = (\tau_0 / \rho)^{3/2} / [\kappa (g / T_0)(H_0 / \rho c_p)]$, respectively, where $\kappa$ is the Von-Karman constant.

Arya (1999) gives a physical description of the M-O length as the height to which shear effects are comparable to those of buoyancy in turbulence production. A ratio of the actual height to M-O length is the stability parameter, $\zeta = z / L$, and can be examined with the governing surface layer parameters to gain qualitative understanding of the relation of the similarity variables to atmospheric stability. Large, positive, values of $\zeta$ coincide with very stable conditions. Thus, the M-O length is approaching zero and positive. During unstable conditions, the heat flux to the surface is negative because the ground is losing heat to the air adjacent to the surface. This makes $H_0$ negative, resulting in a negative M-O length. The stability parameter for unstable conditions is large and negative, corresponding to an M-O length which is approaching zero and negative. The M-O length approaches infinity in the limit of zero heat flux to the ground (i.e. neutral stability) and applies to small positive and negative values of the heat flux. Thus, the stability parameter is zero for neutral conditions with large positive or negative values of the M-O length.

By applying the M-O hypothesis, one can show that dimensionless wind shear and temperature gradients in the constant flux layer depend only on a stability parameter, $\zeta = z / L$. The dimensionless wind shear and temperature gradients are given by Equations (1.2) and (1.3), respectively.

$$\phi_m(\zeta) = \frac{\kappa z}{u_*}\left(\frac{\partial \overline{u}}{\partial z}\right) \tag{1.2}$$

$$\phi_h(\zeta) = \frac{\kappa z}{\theta_*}\left(\frac{\partial \overline{\theta}}{\partial z}\right) \tag{1.3}$$

Finally, the eddy diffusivities of momentum and heat can be related to the dimensionless wind and temperature gradients (Arya, 1999) by Equations (1.4) and (1.5).

$$\frac{K_m}{\kappa z u_*} = \frac{1}{\varphi_m(\zeta)} \tag{1.4}$$

$$\frac{K_h}{\kappa z u_*} = \frac{1}{\varphi_h(\zeta)} \tag{1.5}$$

Businger et al. (1971) experimentally quantified the dimensionless shear and temperature gradients for a variety of atmospheric conditions and found good agreement with M-O theory. By substituting the empirical relations of Businger et al. for $\phi_m(\zeta)$ and $\phi_h(\zeta)$ into Equations (1.4) and (1.5), and integrating along the vertical coordinate, the mean wind speed and turbulent diffusivities can be determined as functions of height in the atmospheric surface layer. For stable atmospheric conditions, $\zeta > 0$, the mean wind speed and turbulent eddy diffusivity are given by Equations (1.6) and (1.7), respectively.

$$\bar{u} = \frac{u_*}{0.35}\left[\ln\left(\frac{z}{z_0}\right) + 4.7\zeta\right] \tag{1.6}$$

$$K_z = \frac{0.35 u_* z}{0.74\left[1 + 6.3\zeta\right]} \tag{1.7}$$

The wind speed and turbulent diffusivity for unstable atmospheric conditions, $\zeta < 0$, are given by

$$\bar{u} = \frac{u_*}{0.35}\left[\ln\left(\frac{z}{z_0}\right) - 2\ln\left(\frac{1+x}{2}\right) - \ln\left(\frac{1+x^2}{2}\right) + 2\tan^{-1}(x) - \frac{\pi}{2}\right] \tag{1.8}$$

and

$$K_z = \frac{0.35 u_* z}{0.74\left[1 - 9\zeta\right]^{-1/2}} \tag{1.9}$$

where $x = \left(1 - 15\zeta\right)^{1/4}$. The horizontal turbulent diffusivity is assumed equal to the vertical turbulent diffusivity. Although approximate, the assumption of equal horizontal and vertical diffusivity will be shown to have a negligible effect on the results because of the relative dominance of convection in the longitudinal direction.

The turbulent eddy diffusivities were derived from the dimensionless temperature gradient rather than the dimensionless wind shear. The ratio of dimensionless wind shear and temperature gradients is approximately 1.35 in neutral conditions, and increases with increasing instability (Businger et al., 1971). Thus the assumption of proportionality between vertical diffusion of species concentration and the transfer of heat can be applied with greater confidence for stable and neutral conditions, but may be less accurate in the limit of very unstable conditions (Nieuwstadt and van Ulden, 1978). However, several dispersion studies have employed this assumption and it will be applied over all stability classes for uniformity (van Ulden, 1978 and Ragland and Dennis, 1975). Since wind speed and diffusivity profiles are equal in the limit of $\zeta \to 0$, Equations (1.6) and (1.7) were used to specify wind speed and turbulent diffusivity profiles for both stable and neutral atmospheric conditions.

### 1.3.3. EFFECTS OF PARTICLE INERTIA

Particulate motion may deviate from that of turbulent eddies when particle inertia becomes significant. The seminal work of Yudine (1959) lists three effects of particle inertia and was the first to show particle diffusion is inversely proportional to the particle settling velocity. The first effect of particle inertia is a net vertical displacement caused by particle settling. The vertical advection term in (1.1) directly accounts for this effect. Secondly, when the particle relaxation time becomes large with respect to the turbulent time scale, relative motion will occur as some finite time is required for the particle to attain the velocity of its surroundings. This effect becomes negligible for particles smaller than approximately 300 micrometers in diameter due to the large length and time scales associated with atmospheric turbulence (Csanady, 1963; Hashem and Parkin, 1991; Wang 1995). Although these two effects are insignificant to the present study, the effect of crossing trajectories has been shown to significantly reduce the diffusion of particulate with respect to that of the gas phase.

Large gravitational settling velocities will cause particles to fall through turbulent eddies more rapidly than they decay. The particle velocity autocorrelation function is altered by this effect and results in a reduction in the ratio of particle to gas diffusion. This is called the crossing trajectories effect and has been studied extensively on a fundamental level (Snyder and Lumley, 1971; Wells and Stock, 1983; Stock, 1996).

Lagrangian stochastic dispersion models often account for the crossing trajectories effect through the modification of model parameters, e.g. Langevin equation parameters (Boehm, 2005; Wilson, 2000; Wang, 1995; Sawford, 1991).

Csanady derived a relation for the reduction in vertical particulate diffusivity due to the crossing trajectories effect

$$\frac{K_{z,p}}{K_{z,g}} = \left(1 + \frac{\beta^2 v_g{}^2}{\overline{w'^2}}\right)^{-0.5} \tag{1.10}$$

where $K_{z,p}$, $K_{z,g}$, $\beta$, and $\overline{w'^2}$ are the particulate phase vertical diffusivity, gas phase particulate diffusivity, ratio of Lagrangian to Eulerian time scales, and vertical root-mean-square (rms) turbulent velocity fluctuation, respectively. This derivation affirms Yudine's prediction that the particulate diffusivity is inversely proportional to the particle settling velocity. The particulate diffusivity ratio (1.10) can be estimated for various particle sizes and atmospheric conditions under certain simplifying assumptions. The ratio of the vertical rms velocity fluctuation, $\sigma_w = \overline{w'^2}$, to friction velocity has been shown constant, $\sigma_w / u_* = 1.3$, in the neutral atmospheric surface layer. This relation is also approximately valid in the stable boundary layer (Arya, 1999). The magnitude of the rms vertical velocity fluctuation will increase with increasing atmospheric instability. Therefore, $\overline{w'^2} \sim 1.3 \cdot u_*$ should provide an estimate of the smallest turbulent velocity scale and largest expected reduction in particulate diffusivity.

Specification of $\beta$ is more difficult due to experimental difficulties associated with measuring the Lagrangian time constant. Csanady made estimates of his derived parameter under the assumption $\beta \approx 1$ (1963). Hanna performed measurements in the convective boundary layer and found $\beta \approx 1.6$ (1981). More recent works in the field of Lagrangian stochastic dispersion simulation have adopted values of 2.0 and 1.5 (Wilson, 2000; Wang, 1995). Yet others suggest $\beta \approx 4$ is more general and appropriate near the ground (Koeltzsch, 1999).

Figure 1.2 shows the particle diffusivity ratio in the neutral surface layer, assuming $\beta \approx 2$, as a function of increasing particle diameter due to the crossing trajectories effect. Particulate diffusion is analogous to gas diffusion as the settling velocity goes to zero and the crossing trajectories effect becomes insignificant. The particle velocity autocorrelation function decreases with increasing particle diameter causing the particulate diffusivity to decrease relative to the gas phase. Friction velocities of 0.1, 0.2, 0.3, 0.4, and 0.5 meters per second were chosen to specify the rms vertical velocity fluctuation.

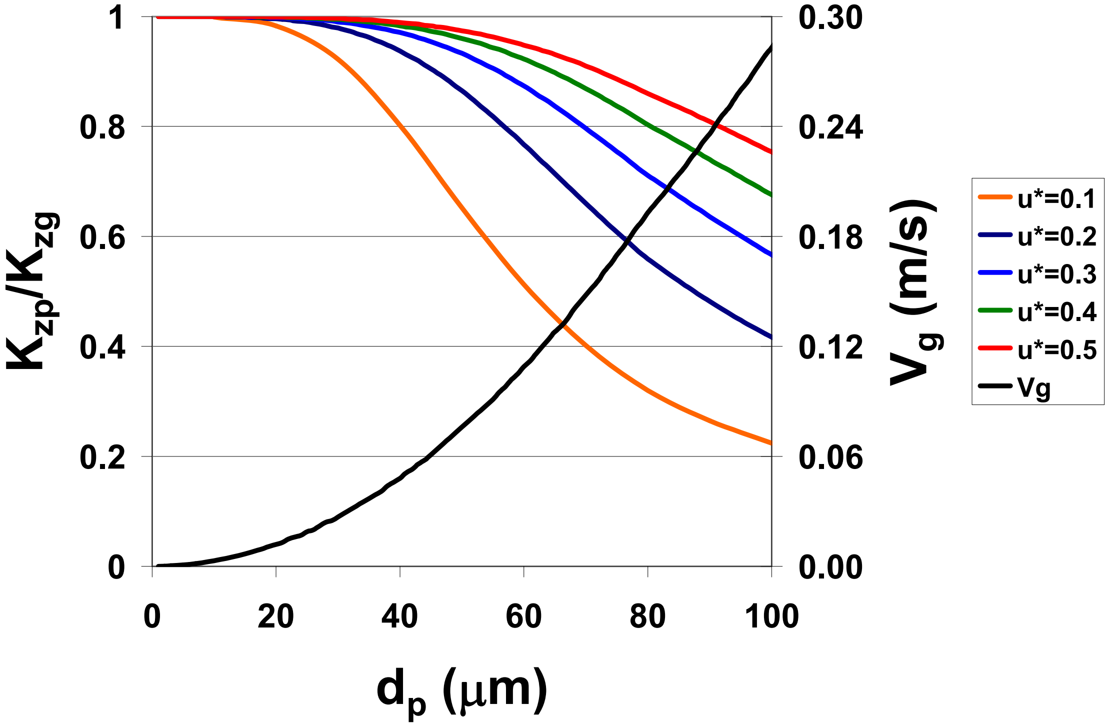

Figure 1.2: Ratio of particle to gas phase diffusivity as a function of particle diameter (inertia) due to crossing trajectories effect

Increased friction velocity signifies increased shear driven turbulence, hence increasing $\overline{w'^2}$ . A value of $u_* = 0.1$ represents very stable atmospheric stratification and suggests the particle diffusivity will be 50% and 20% of the gas phase diffusivity for particle aerodynamic diameters of 60 and 100 micrometers, respectively. Reductions in particulate diffusivity of approximately 23, 13, 8, and 5% occur for particles of 60 micrometers AD, at more typical daytime friction velocities of 0.2, 0.3, 0.4, and 0.5 meters per second, respectively. Significant reductions in particulate diffusivity occur for particles larger than 60 micrometers AD. The simplifying assumption of equal particle and gas phase diffusivity becomes questionable for these particles. Model simulations of near ground releases will show particulate above approximately 60 micrometers AD is lost rapidly due to sedimentation. Therefore, the effect of crossing trajectories does not have a significant impact on the results to be presented here.

### 1.3.4. BOUNDARY CONDITIONS

The airflow across the inflow, or upstream, vertical boundary is devoid of particulate and therefore written as a zero concentration condition. No formal boundary condition is prescribed at the downwind vertical boundary. This is often referred to as an outflow boundary because it allows the convection of particulate out of the domain without specializing the discretization equations along the outflow boundary (Patankar, 1980). The ground was prescribed as a particle sink, i.e. no particle rebound or resuspension was considered here. The lower boundary has the partial character of an outflow boundary due to the gravitational settling velocity. Physically this means the ground flux includes both gravitational settling of particles as well as the turbulent diffusion flux due to the ground level concentration gradient,

$$J_i\Big|_{z=0} = \left[ K_z \frac{\partial C_i}{\partial z} + v_g C_i \right]_{z=0} \tag{1.11}$$

where $J_i\big|_{z=0}$ is the ground deposition flux of particle size $i$. Intuitively, one should expect that ground deposition would be influenced by both processes. This form of the ground flux is utilized in the FDM transport model. Recent work on coarse particulate deposition in the quasi-laminar sub-layer shows the deposition flux may be more accurately modeled proportional to the sum of an inertial velocity, $v_i$, and gravitational settling velocity,

$$J_i\big|_{z=0} = \left[v_i C_i + v_g C_i\right]_{z=0} \tag{1.12}$$

rather than proportional to the concentration gradient (Kim et al., 2000). Kim et al. formulate an inertial deposition velocity which accounts for particle properties as well as those of the surrounding turbulence in the quasi-laminar sub-layer. Furthermore, they report a significant under-prediction (ca. seven times) of the deposition velocity of particles in the 10-100 micrometer size range when modeling the deposition flux in the form of (1.11). Comparison of deposition velocities from the present model and that of Kim et al. are discussed in following sections.

The upper boundary is modeled as a no flux boundary. The effects of this boundary condition can be examined for two limiting cases: particles whose transport in the vertical direction is dominated by diffusion, and particles for which gravitational settling is dominant. Particles may reach the upper boundary and remain in the domain in the former case. Here the no-flux upper boundary has the effect of maintaining particulate concentration inside the domain, for small particles, and may result in an increase in the ground level concentration. In the case of particles whose settling velocities are much larger than vertical diffusion, the height of the upper boundary has little effect as a negligible quantity of particles of this size reach the upper boundary. The focus of the present study is on the latter category of particles.

## 1.4. Numerical Methods

The finite-volume technique, and power law scheme, described by Patankar (1980) were used to discretize the two-dimensional transient convection-diffusion equation. The set of discretized algebraic equations were then solved using Gauss-Seidel point by point iteration. The numerical implementation of the model was verified for species conservation, convergence, and spatial and temporal discretization error according to NPARC Alliance recommendations (Slater, 2007). The discretization error was determined to scale with both the square of the spatial and temporal step size. The code was also verified by comparison to transient convection-diffusion benchmark solutions for which analytical solutions were derived.

### 1.4.1. TRANSPORT EQUATION DISCRETIZATION

The finite volume discretization method and power law scheme reduce the two-dimensional transient convection diffusion equation into a set of algebraic equations that can be solved numerically. The solution domain is broken into an array of control volumes for which the internal concentration is considered uniform. A single algebraic equation is written for each control volume and the set is solved simultaneously for the time and spatially evolving concentration field.

Figure 1.3 shows a control volume of interest. The internal cell concentration is specified at point "$P$" and is expressed as a function of its neighboring node concentrations denoted west "$W$", east "$E$", south "$S$", and north "$N$". Subscripts of capital letters signify nodal quantities whereas lowercase letters define interfacial quantities. The control volume has length $\Delta x$ and height $\Delta z$. Distances between adjacent nodes are written $\delta x$ and $\delta z$ with the appropriate directional interfacial subscript. A mass balance on the control volume results in an algebraic function having the simplified form

$$a_P C_P = a_E C_E + a_W C_W + a_S C_S + a_N C_N + b \tag{1.13}$$

where node coefficients, e.g. $a_E$, are functions of the interface velocities and diffusivities and the constant $b$ accounts for transient effects and source or destruction terms when required.

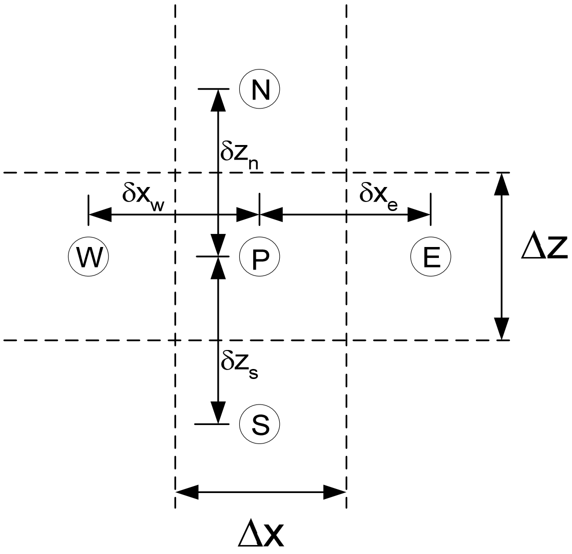

Figure 1.3: Schematic of discretized control volume with nodal concentration at “P” with neighboring nodes, control volume dimensions, and distances between nodes

The magnitudes of the diffusive and convective fluxes at the eastern interface are

$$D_e = \frac{K_{xe}\Delta z}{\delta x_e} \tag{1.14}$$

and

$$F_e = U_e \Delta z \tag{1.15}$$

respectively, where $\Delta z$ is the interfacial area over which the flux is active. Patankar uses the Peclet number as a relative measure of these fluxes

$$Pe_e = \frac{F_e}{D_e} \tag{1.16}$$

where a large Peclet number signifies convection dominated transport. Expressions for the western interface are written by substituting $w$ for $e$ in (1.14) through (1.16). The interfacial area is different for transport in the $z$ direction; $\Delta z$ is replaced by $\Delta x$ in the expressions for the north and south nodes, e.g. $F_s = V_s \Delta x$.

The power law scheme is used to specify the node coefficients as functions of the interfacial Peclet numbers. The diffusive flux is completely neglected when the convective flux is an order of magnitude larger than the diffusive flux. Node coefficients for the power law discretization scheme are given in Equation set (1.17).

$$\begin{aligned} a_E &= \max[D_e(1-0.1Pe_e)^5, 0] \\ a_W &= \max[D_w(1-0.1Pe_w)^5] + F_w \\ a_S &= \max[D_s(1-0.1Pe_s)^5] \\ a_N &= \max[D_n(1-0.1Pe_n)^5] + F_n \end{aligned} \tag{1.17}$$

No convection fluxes are included in the coefficients for the east and south nodes since the flow direction is explicitly specified as from the west and from the north. The coefficient for node $P$ is written

$$a_P = a_W + a_E + a_N + a_S + a_{P0} \tag{1.18}$$

where

$$a_{P0} = \frac{\Delta x \Delta z}{\Delta t} \tag{1.19}$$

and

$$b = C_P{}^o \frac{\Delta x \Delta z}{\Delta t} \tag{1.20}$$

where the previous value of the node concentration, $C_P{}^o$, appears in the constant term $b$.

### 1.4.2. SPATIAL AND TEMPORAL DOMAIN DISCRETIZATION

Figure 1.4 shows a simulation domain discretized into a grid of N x N nodes. Each node corresponds to a specific location $(i, j)$ in the solution matrix (concentration) in the numerical code. This figure is useful for illustrating schemes utilized in the code such as locating the nodes and interfaces, and specifying interfacial transport properties. Ghost nodes line the periphery of the domain and are used to specify boundary conditions. This technique eliminates the need to write unique half-cell coefficients for the boundary cells (Patankar, 1980). Nodes are located in the geometric centers of each cell. Variable grid spacing is used to achieve finer spatial resolution in areas with large concentration gradients, e.g. near the release. The concentration $C(0,1)$ corresponds to the $(i = 0, j = 1)$ location in the solution matrix. Similarly, the interfacial distances and cell dimensions are written in vector form with subscripts signifying their location.

The time step, $\Delta t$, used in the transient calculation was selected to ensure proper representation of transport phenomena. Four time scales based on the spatial discretization, convection velocities, and turbulent diffusivities were considered: $\Delta x^2 / K_x$, $\Delta z^2 / K_z$, $\Delta x / u$, and $\Delta z / v_g$. All four time scales were calculated for each cell over the entire domain and the smallest value was selected. Simulation speed could be increased in future works by adopting an adaptive time discretization scheme to determine the smallest time scale in regions of importance rather than the entire domain.

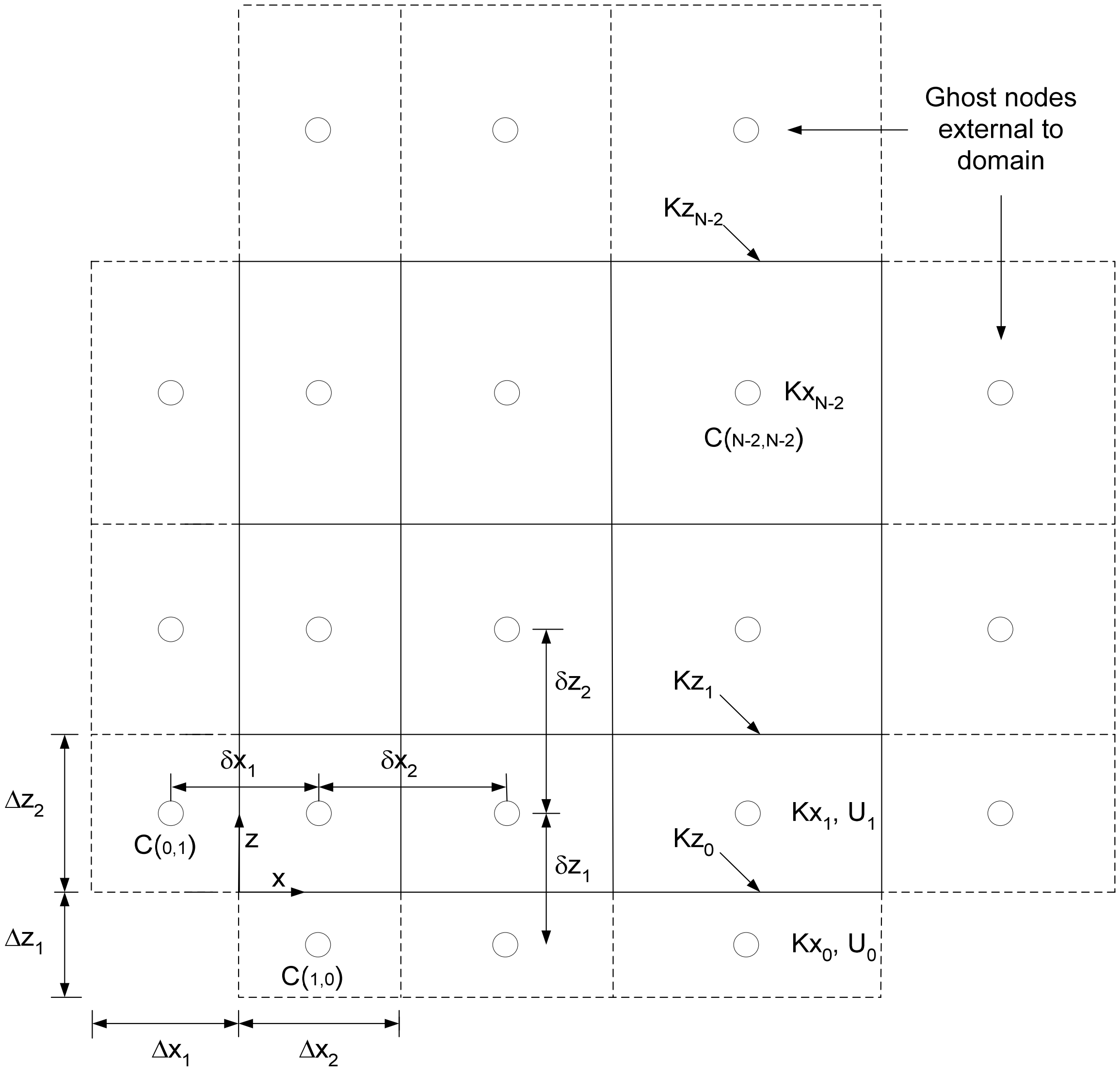

Figure 1.4: Discretized domain showing spatial discretization techniques, interface positions and values, and numerical coding number scheme

### 1.4.3. BOUNDARY CONDITION SPECIFICATION

All boundary nodes were defined with zero concentration. Defining zero concentration on the upstream vertical boundary models an inflow of air without particulate. All particulate is contained within the instantaneous puff source defined by the initial conditions. Node concentrations on the upstream vertical boundary could be defined as non-zero to simulate the dispersion from a constant line source, at various heights, under steady-state conditions.  Interestingly, an “outflow” boundary condition exists at the downstream boundary regardless of any specified boundary conditions.  This means convection fluxes exist at downstream boundaries even if a hypothetically specified zero velocity boundary condition is written at the downstream boundary.  This peculiar behavior is a consequence of specifying the flow field, $u(z)$ and $v_g$, rather than solving for it.  Specifying the downstream boundary interface velocity to be zero violates conservation of mass principals used in the derivation of Patankar’s Power Law Scheme, thereby resulting in a violation of the conservation principle.

The upper horizontal boundary is an “inflow” boundary due to the convection velocity $v_g$.  Zero concentration must be specified here or it would act as a source term. But a zero concentration boundary establishes a concentration gradient which results in a diffusive flux out of the upper boundary.  The interfacial diffusivity, $K_z(i, j = N-2)$, was therefore set equal to zero to establish a no flux upper boundary condition.  The outflux of particulate at the ground, $z = 0$, obeys (1.11).  The zero concentration boundary sets up a concentration gradient and diffusive flux at the ground surface.  A convective flux, $v_g C(i, j = 1)\Delta x$, also exists due to the settling velocity.  In future studies the ground deposition flux could be modified to give a flux similar to (1.12) by manipulating the ground level diffusivity.  The finite-volume formulation is conservative regardless of the boundary conditions.  Thus, all particulate entering or initially present in the domain must sediment or leave at the downstream outflow boundary.

### 1.4.4. SOLUTION METHOD

An equation of the form (1.13) is written for each node of unknown concentration.  The set of equations is then solved with the Gauss-Seidel Point by Point method.  The Tri-diagonal Matrix Algorithm was determined to converge much faster for systems in which nodal coefficients were non-zero over the entire computational domain. However, the Power Law Scheme can result in zero coefficients for the east and south nodes when interfacial Peclet numbers are greater than 10. For this case the solution must be determined with a method that does not require the existence of a tri-diagonal matrix.

## 1.5. Code Verification

The numerical methods described above were written in the C++ programming language. The code was verified for convergence, conservativeness, and discretization error to ensure no coding errors were present. All code verification was performed for a flow field corresponding to the following atmospheric stability parameters: $L_{mo} = 542\,m$, $z_0 = 0.1\,m$, and $u_f = 0.352\,m$. Boundary conditions were as follows: no flux across the upper boundary, zero concentration at the bottom and downstream boundaries, constant concentration at the left boundary with value depending on the particular verification study.

### 1.5.1. CONSERVATIVENESS

The finite volume method is a conservative discretization scheme. For example, if the initial concentration field contains a total of 10,000 particles, at any point in the simulation all of those particles should be accounted for in the sum of the time integrated boundary fluxes or particles remaining in the domain. This property is called conservativeness and is used to ensure coding errors do not cause creation or destruction of mass. The two-dimensional transient convection-diffusion code was checked for conservativeness by creating a puff release and letting time move forward until the sum of the particles within the domain was zero, i.e. all particles had exited at the boundaries. A 100 x 50 node domain with grid spacing of $\Delta x = \Delta z = 0.25\,m$ was constructed, the particle settling velocity was specified as $v_g = 0.05 m/s$, and the left boundary had zero concentration. Figure 1.5 shows the sum of particles inside the computational domain normalized to the initial number of particles as a function of simulation time. The residual number of particles decays to zero as all particles convect and diffuse out of the domain. The sum of the time integrated boundary fluxes and number of particles in the computational domain, normalized to the initial number of particles, is also plotted as a function of simulation time. This sum is constant, 1, and indicates proper coding of the conservative numerical formulation.

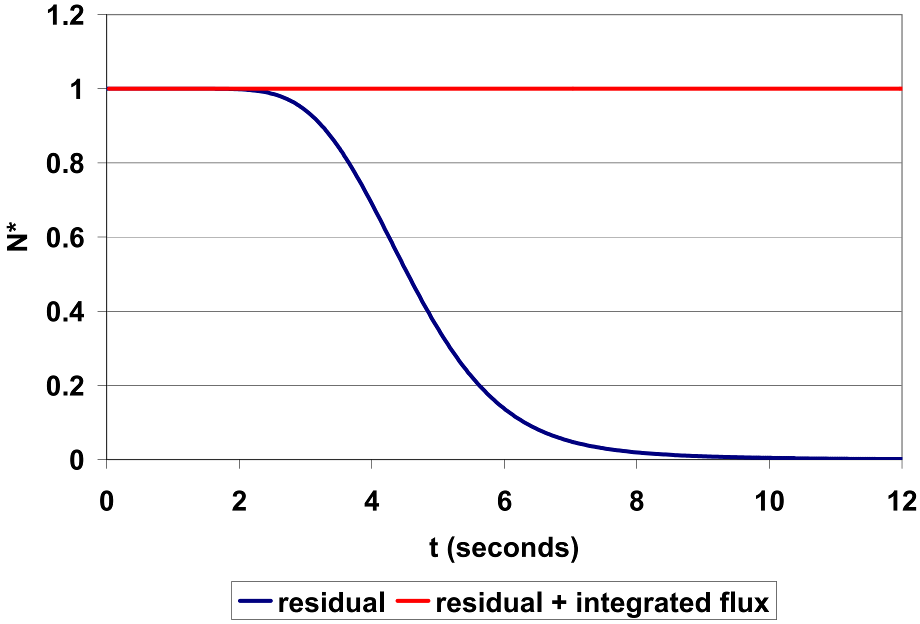

Figure 1.5: Normalized sum of residual particles in simulation domain, and normalized sum of residual particles and time integrated particle boundary fluxes for an arbitrary puff release

### 1.5.2. CONVERGENCE

A check of convergence was performed to observe how the temporally and spatially dependent solution changed per iteration of the Guass-Seidel point by point solution method. The residual is defined as an average measure of the difference in concentration field solutions between two successive iterations

$$R = \sum \left| \frac{C_{i,j} - C^{o}{}_{i,j}}{C_{i,j}} \right| \tag{1.21}$$

where the superscript "o" denotes the previous value of the nodal concentration, and the sum is performed over all nodes in the computational domain. The solution is considered to be converged to the next time step once the residual becomes sufficiently small. Figure 1.6 shows the calculated residual at every iteration for the tenth time step of the simulation analyzed for conservativeness. The convergence criterion was $R \leq 0.001$. The solver function moved on to the next time step once the residual criterion was satisfied.

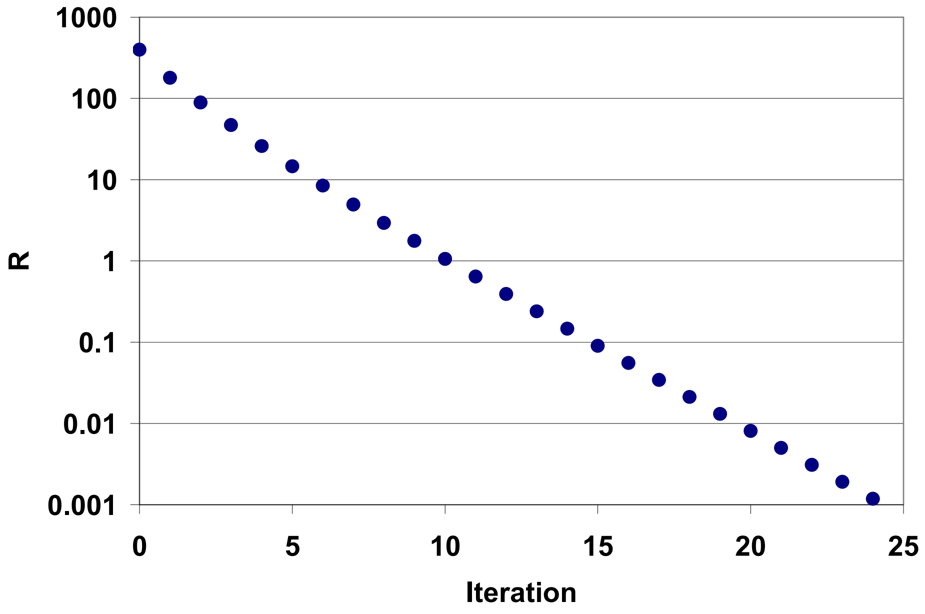

Figure 1.6: Convergence of the solution residual with increasing solver iteration for a single time step for an arbitrary puff release

### 1.5.3. DISCRETIZATION ERROR

Spatial and temporal discretization results in a set of algebraic equations that approximate the actual solution to the transient convection-diffusion equation. The numerical solution is therefore an approximation to the actual solution. The magnitude of the discretization error scales with the spatial step size depending on which discretization scheme is employed. Finer grid resolution results in less error and a numerical solution closer to the actual solution. The form used here is similar to that of the central difference scheme which has a spatial discretization error of order two.

The simulation domain for the grid independence study was 100 meters by 50 meters. The concentration at the left boundary was constant and non-zero and the settling velocity set to 0.25 m/s. Uniform grids of $\Delta x = \Delta z = 0.1$, 0.15, 0.2, 0.25, 0.3, 0.4, and 0.5 meters were used with the smallest being defined as the exact solution of the discrete equations. The time step used for all spatial grid resolutions was determined from the finest grid, $\Delta t = 0.001\,s$. Each grid was simulated to an elapsed time of 10 seconds and the spatial concentration profile was recorded.

The total spatial discretization error for a single grid may be expressed as the difference in actual and grid specific solutions to the concentration field

$$E = \sum_{(x,z)} e^n(x,z) = \sum_{i,j} \left| \bar{C}^n(x,z) - C^n(x,z) \right| \tag{1.22}$$

where the overbar denotes the exact solution at location $(x,z)$ at specific time $n$. All of the grids were interpolated onto one standard grid so that concentrations at specific locations, rather than nodes, were compared. The standard grid had resolution equal to the finest grid. The plotting software Tecplot Focus was used to interpolate the data. An inverse weighting technique was used that incorporated the values at the nearest 4 nodes. Figure 1.7 shows the logarithm of the total discretization error plotted as a function of the logarithm of grid size. Least squares regression was used to find the slope of the data and gives the order of the spatial discretization error, $O(\Delta x^2)$, as expected. The discretization error would scale with the maximum grid size if variable grid spacing were employed.

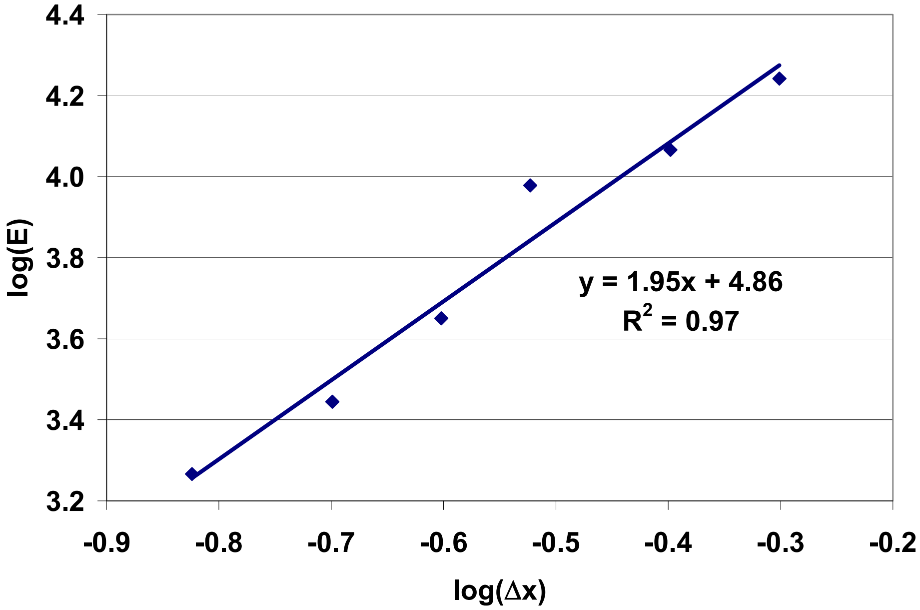

Figure 1.7: Spatial discretization error as a function of grid size for an arbitrary constant inflow boundary concentration

The power law scheme is fully implicit. The fluxes at the cell boundaries are calculated from “current” concentrations rather than those from a previous time step. The final formulation is temporally discretized with a forward differencing scheme. This implies the temporal discretization error should be of order one. A constant grid size of $\Delta x = \Delta z = 0.4m$ was used to isolate temporal errors from spatial discretization errors. Domain size, boundary conditions, wind speed, diffusion, and settling velocity were identical to the simulation run for the spatial discretization error. Total simulation durations of 5.0 seconds were comprised of times steps of $\Delta t = 0.001$, 0.005, 0.015, 0.025, 0.035, 0.045, and 0.055 seconds. The total temporal discretization error was calculated according to (1.22) with the summation performed over time and space. No interpolation was necessary because the same grid size was used for each simulation. The total error was divided by the total number of time steps as proportionality exists between the two. Figure 1.8 shows the logarithm of total error per time step as a function of the logarithm of the time step. Least squares regression shows a temporal discretization error of order two.

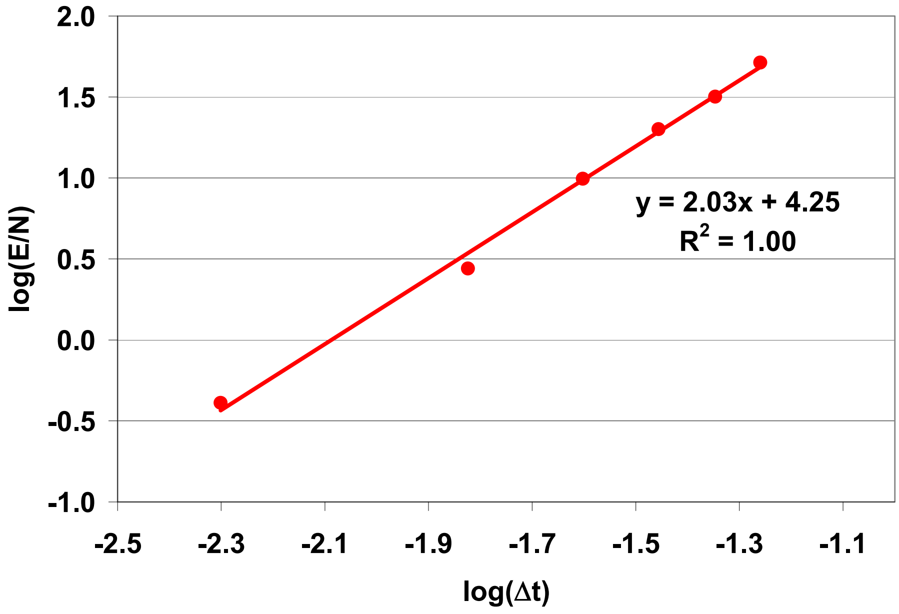

Figure 1.8: Temporal discretization error as a function of time step for an arbitrary

### 1.5.4. BENCHMARK SOLUTIONS

Checking the two-dimensional transient convection-diffusion code against benchmark solutions is another critical step in code verification. Analytical solutions can be found under certain simplifying assumptions and checked against numerical solutions. Simplified cases of transient, one-dimensional, diffusion and convection-diffusion were simulated.

The first benchmark solution corresponds to pure diffusion: zero wind speed, zero settling velocity, constant diffusivity, constant concentration vertical boundaries, and zero flux horizontal boundaries, as shown in Figure 1.9.

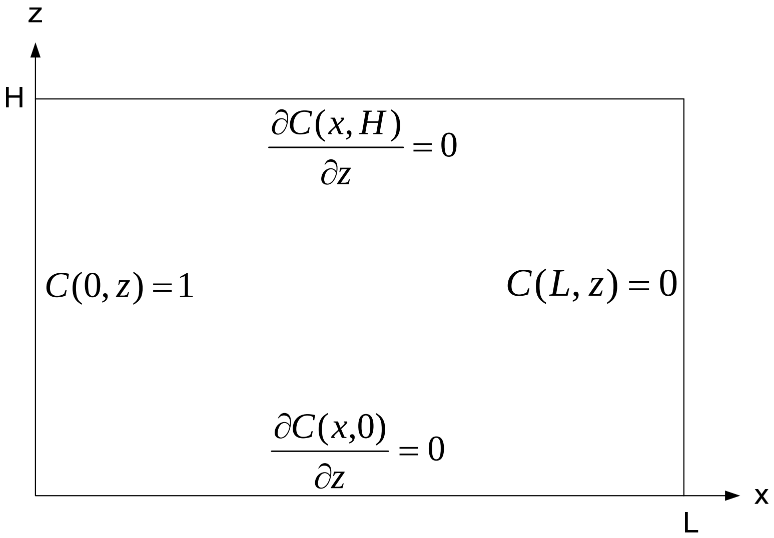

Figure 1.9: Illustration of solution domain and boundary conditions for the transient, one-dimensional, pure diffusion benchmark solution

The solution is expected to be one-dimensional in $x$ since both horizontal boundaries have zero flux and the vertical boundaries are not functions of $z$. The problem simplifies to a transient, one-dimensional, constant coefficient partial differential equation

$$\frac{\partial C}{\partial t}=K\frac{\partial^2 C}{\partial x^2} \tag{1.23}$$

with constant boundary conditions

$$C(0,t)=1 \tag{1.24}$$

$$C(L,t)=0 \tag{1.25}$$

and initial condition

$$C(x,0)=0 \tag{1.26}$$

where $K$ is the diffusivity. The concentration profile, at sufficiently large times, can be determined with the separation of variables method

$$C(x,t)=\left[\sum_{n=1}^{\infty} B_n e^{-\left(\frac{n\pi}{L}\right)^2 K\cdot t}\sin\left(\frac{n\pi x}{L}\right)\right]+\left(1-\frac{x}{L}\right) \tag{1.27}$$

with coefficients

$$B_n=\frac{2}{L}\int_0^L\left(\frac{x}{L}-1\right)\sin\left(\frac{n\pi x}{L}\right)dx \tag{1.28}$$

where $1-x/L$ is the steady-state solution. The transient numerical solution for $u=v_g=0$, $K=1$, $L=1$, $\Delta x=\Delta z=0.05$, $\Delta t=\Delta x^2/K=0.0025$ is plotted in Figure 1.10. Analytical solutions (solid lines), approximated by the first $n=50$ series terms, are shown alongside numerical solutions (points). Good agreement is observed with a standard error, $\sigma=\sqrt{\sum\left(e_i^2/n-2\right)}$, of 0.001.

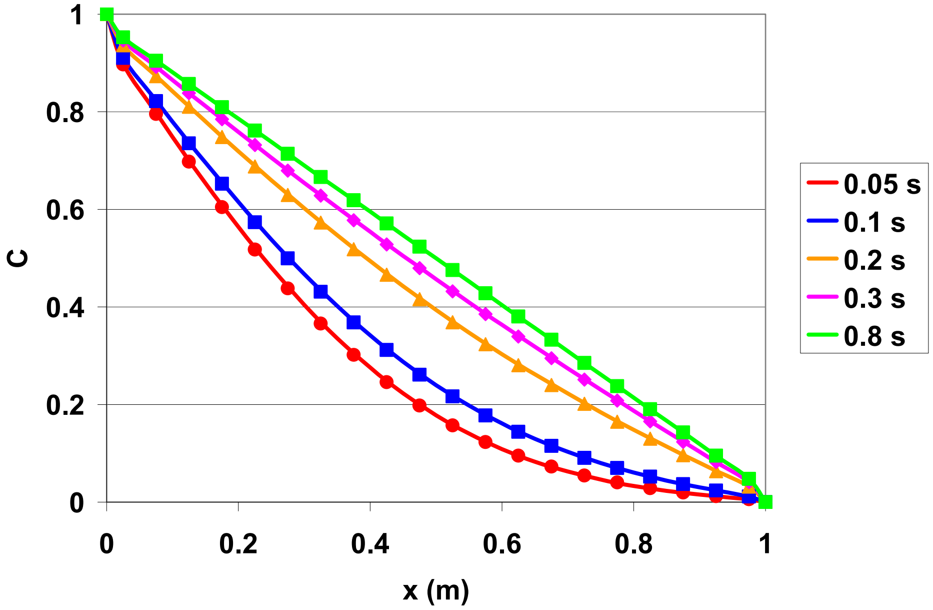

Figure 1.10: Numerical and analytical solutions to transient, one-dimensional, pure diffusion benchmark solution

The second benchmark check of the transient convection-diffusion code was an extension of the pure diffusion case to include horizontal convection. Constant wind speed was added to the problem formulation, shown in Figure 1.11. The problem simplifies to the following transient, one-dimensional, constant coefficient, partial differential equation

$$\frac{\partial C}{\partial t} + u\frac{\partial C}{\partial x} = K\frac{\partial^2 C}{\partial x^2} \tag{1.29}$$

with constant boundary conditions

$$C(0,t) = 1 \tag{1.30}$$

$$C(L,t) = 0 \tag{1.31}$$

and initial concentration profile

$$C(x,0)=0 \tag{1.32}$$

where $u$ and $K$ are constant.

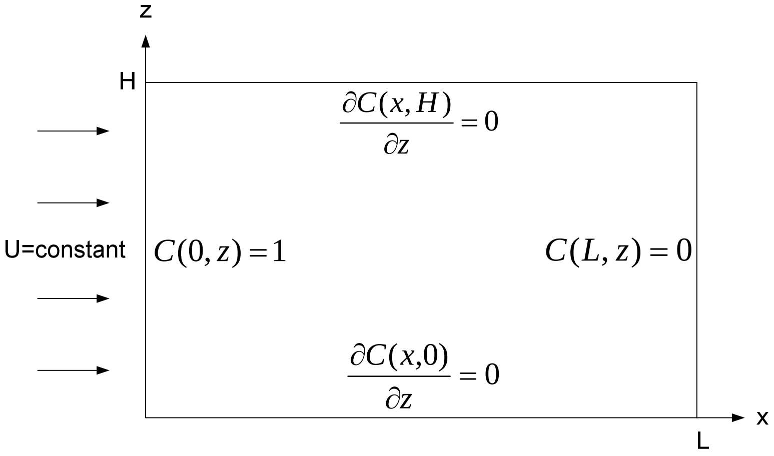

Figure 1.11: Illustration of solution domain and boundary conditions for the transient, one-dimensional, convection- diffusion benchmark solution

The separation of variables method is again applied to give the series solution for the concentration profile

$$C(x,t)=\left[\sum_{n=1}^{\infty} B_n e^{-\left(\frac{n\pi}{L}\right)^2 K\cdot t} \sin\left(\frac{n\pi x}{L}\right) e^{\left(\frac{ux}{2K}\right)}\right]+C_s(x) \tag{1.33}$$

with coefficients

$$B_n=-\frac{2}{L}\int_0^L C_s(x)\sin\left(\frac{n\pi x}{L}\right)dx \tag{1.34}$$

and

$$C_s(x)=\frac{e^{\frac{ux}{K}}-e^{\frac{uL}{K}}}{1-e^{\frac{uL}{K}}} \tag{1.35}$$

where $C_s(x)$ is the steady state solution determined from the solution of the ordinary differential equation associated with (1.29). The transient numerical solution was calculated for $V_g = 0$, $u = 0.5$, $K = 1$, $L = 1$, $\Delta x = \Delta z = 0.05$, and $\Delta t = \Delta x^2 / K = 0.0025$. Approximate analytical solutions for the concentration profiles (lines), given by the first $n = 50$ terms of the series solution, are compared to numerical results (points) in Figure 1.12. Good agreement is observed with a standard error of 0.007.

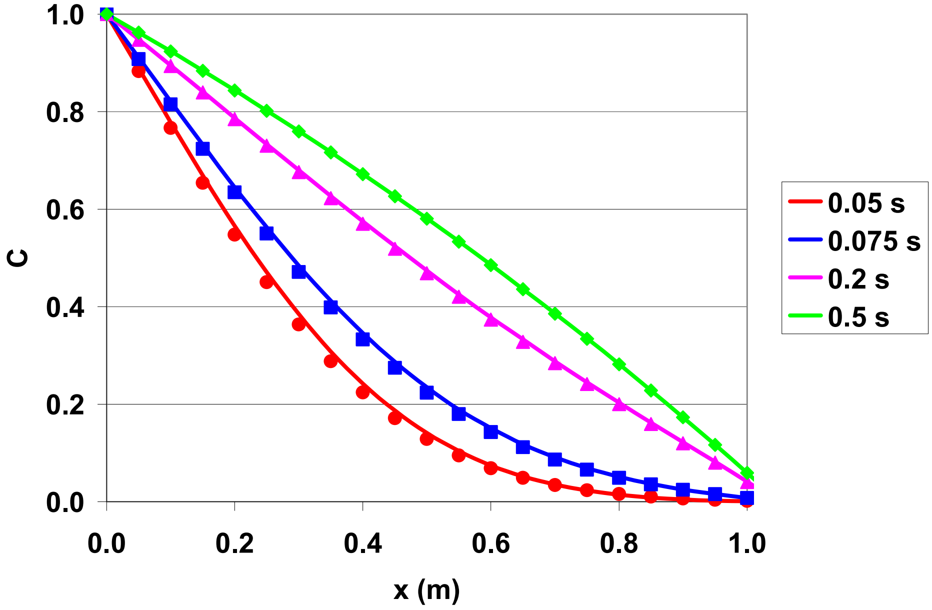

Figure 1.12: Numerical and analytical solutions to transient, one-dimensional, convection- diffusion benchmark solution

## 1.6. Model Validation

### 1.6.1. SUFFIELD DEPOSITION EXPERIMENTS

The model was validated by comparing predictions of coarse particulate deposition to available experimental data. Experiments were conducted at Suffield

Experiment Station, Ralston, Alberta, Canada, to measure the downwind particulate ground deposits from a continuous elevated source of solid glass spherical particles (Walker, 1965). Trials were conducted under various atmospheric conditions with trials G, H, I, and L being the focus of comparison with the present model. Trials G, H, and I represent experiments conducted for neutral to stably stratified atmospheric conditions. Trial L represents unstable atmospheric conditions and greater turbulent mixing with respect to trials G, H, and I. Particles were emitted continuously from a height of 7.42 meters over periods ranging from 30 to 60 minutes. The particle deposits were collected on adhesive papers spaced evenly along arcs up to 800 meters from the source. The cumulative mass distribution and density of the test particles were given. The mass mean diameter was 56 micrometers, with $\rho_g = 2200$ kg/m$^3$, resulting in a settling velocity of 0.19 m/s. The corresponding aerodynamic diameter was approximately 80 micrometers. Walker counted the deposited particles under ultraviolet light and provided the total number collected, the particulate standard deviation (radians), total number of sampling papers along each arc, and crosswind integrated ground deposits (mg/g/m). Measurements of wind speed and temperature in the lowest five to ten meters of the surface layer were also made.

### 1.6.2. CONVECTION-DIFFUSION-SEDIMENTATION MODEL SIMULATIONS

Wilson determined M-O similarity parameters corresponding to the atmospheric temperature and wind speed measurements provided by Walker (2001). The resulting M-O parameters are provided in Table 1.1 and were used to specify the wind speed and turbulent diffusivity profiles. A simulation domain 1,100 meters in length and 50 meters in height was discretized with variable grid spacing in the longitudinal direction, $0.4 < \Delta x < 1.0$ meters, and constant grid spacing in the vertical direction, $\Delta z = 0.4$ meters.

**Experimental Study M-O Parameters**

| Suffield Trial | L (m) | u* (m/s) | $z_0$ (m) |
|---|---|---|---|
| G | 52 | 0.21 | 0.043 |
| H | 35 | 0.28 | 0.004 |
| I | 16 | 0.18 | 0.016 |
| L | -50 | 0.57 | 0.012 |

Table 1.1: M-O Parameters for Suffield Deposition Experiments (G,H,I,L) taken from Wilson (2000)

The particulate source was modeled by the specification of boundary node concentrations for three nodes at the experimental source height. The concentration magnitude of the source nodes was estimated from the total amount of particulate emitted in the experiments to provide a similar particle influx. A particle size distribution for the source particles was also derived from data given by Walker assuming it was lognormal. The mass median diameter was 56 micrometers with a geometric standard deviation of 1.1, corresponding to a count median diameter of approximately 54 micrometers. The particle size distribution was discretized into three particle size bins with midpoints of 50, 54, and 58 micrometers although nominally monodisperse. Three simulations, one for each particle size bin, were performed to model each experimental trial. The source strength, i.e. boundary concentration, for each particle size (e.g. Trial G, 50 micrometers) was weighted by the count based probability density function. The settling velocity was also adjusted according to particle size and density. The steady-state solution for downwind ground deposits was calculated for each experimental trial. The steady-state assumption is valid since the duration of experiments was at least an order of magnitude larger than the characteristic convection time, e.g. $\tau_c \approx X / U \approx 800m / 4ms^{-1} \approx 200s$.

### 1.6.3. MODEL COMPARISON

Figure 1.13 illustrates the differences between three-dimensional actual dispersion and two-dimensional simulated dispersion. Model validation requires that these differences be resolved in order to compare simulated ground deposits to experimental data. Dispersion in the longitudinal ($x$) and vertical ($z$) directions is properly modeled with advection and diffusion terms in the transport equation (1.1). However, transport in the lateral direction ($y$) is neglected in the two-dimensional model. Two-dimensional model results thus have two physical interpretations: downwind deposits from an infinite line source, or downwind deposits from a source of unit depth where transport in the lateral direction is constrained by impermeable boundaries also separated by a unit depth. The latter will be adopted here when reconciling two-dimensional model predictions to experimental data from a three-dimensional world.

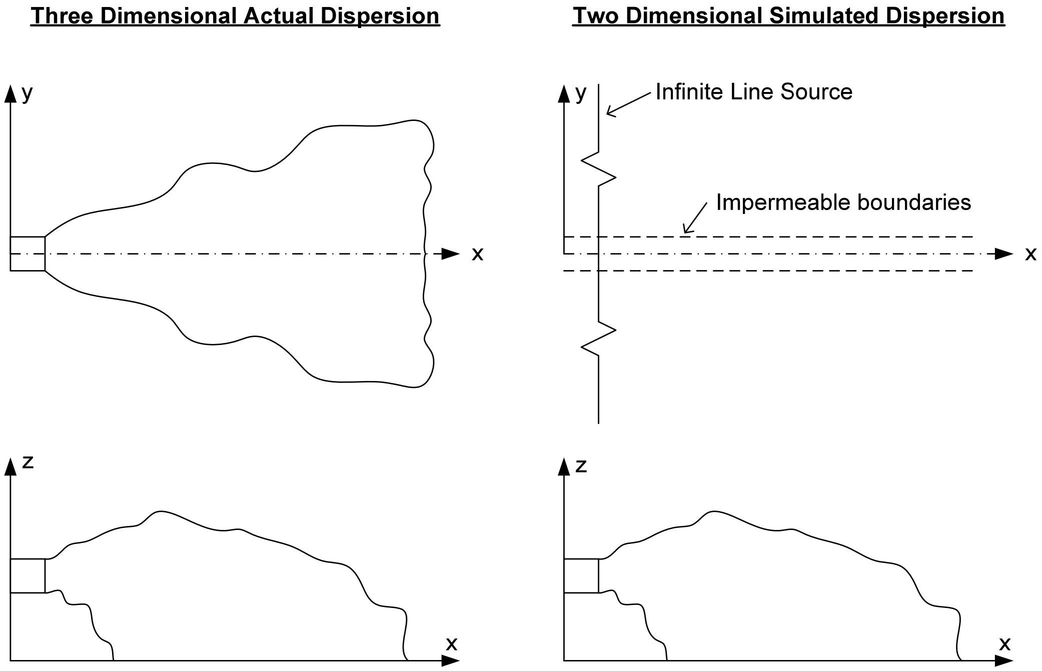

Figure 1.13: Illustrated differences in actual dispersion in three dimensions (left) and simulated dispersion in two dimensions (right)

Crosswind integration is a method used to collapse lateral dispersion data to a vertical plane parallel to the direction of prevailing winds ($x$). This can be performed on any arbitrary measurement

$$\beta(x) = \int_{-\infty}^{\infty} \beta(x, y) \cdot dy \tag{1.36}$$

and effectively maps three-dimensional dispersion data to a two-dimensional coordinate system.

Figure 1.14 shows the sampling coordinate system used by Walker to measure downwind deposits. Walker placed sampling papers along arcs of constant radius from the source and measured lateral and longitudinal dispersion as the number of particles deposited per area of sampling paper, $N''(x, \theta)$. Crosswind integration was performed by piecewise integration along the sampling arcs,

$$D_o(x) = \sum_j N''(x, \theta_j) \cdot \left( x \cdot \Delta\theta \right) \tag{1.37}$$

where $x \cdot \Delta\theta$ is the arc length between sampling papers. The resulting crosswind integrated deposit has units of $m^{-1}$ when normalized by the number of particles emitted. This denotes the number of particles deposited per unit length in the x-direction. In theory, all particulate should be accounted for if the crosswind integrated deposits were integrated in the longitudinal direction, $\int D_o(x) \cdot dx = 1$. The crosswind integrated deposits essentially transforms the data set into one which can be modeled in two-dimensions with the transport equation (1.1).

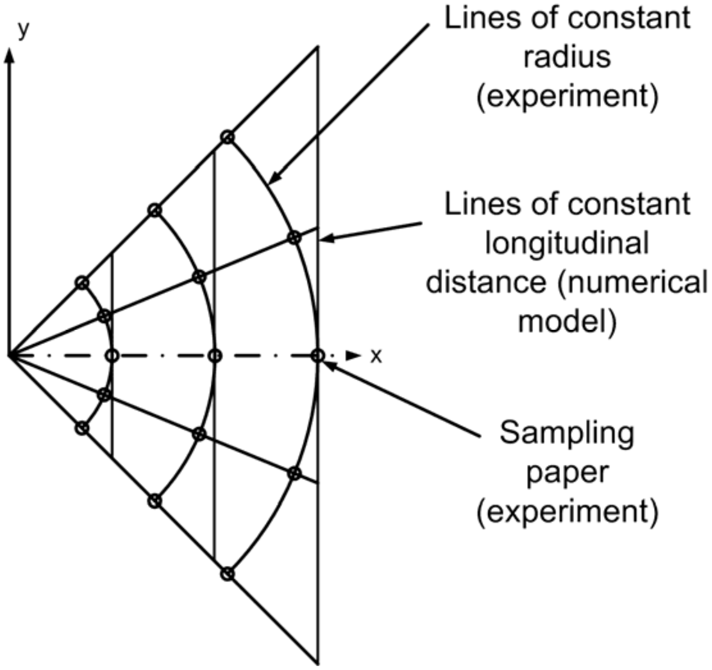

Figure 1.14: Sampling grid utilized by Walker et al. for the measurement of coarse particulate ground deposits used in comparing to simulated data

Simulated normalized crosswind integrated ground deposits ($D_o$) were calculated according to

$$D_o(x) = \frac{\sum \dot{d}_i''(x)}{\sum \dot{S}_i'} \tag{1.38}$$

where $\dot{d}_i''$ represents the ground particle flux ($m^{-2}s^{-1}$) for particle size $i$. As previously mentioned, the lateral length scale is assumed to be one meter. The ground particle flux was non-dimensionalized by the source particle influx per unit simulation domain depth, $\dot{S}_i'$ ($m^{-1}s^{-1}$). Lastly, a single simulation was performed for each of the three particle diameters in the discretized particle size distribution and then summed to give the net crosswind integrated deposits.

Figure 1.14 shows a schematic of the experimental sampling grid on the polar coordinate system. It should be noted that Walker integrated his data along lines of constant radius rather than constant $x$. This is not true crosswind integration as the wind is parallel to the $x$ axis. Two-dimensional model data represent true crosswind integration and should therefore be compared to experimental data integrated along the $y$ direction for greatest accuracy. The discrepancy in integrated values, along $y$ instead of $\theta$, is greatest near the source. However, predicting near source deposition is always complicated due to source modeling and is not the focus of the present study. The error associated with crosswind integration decreases with increasing experimental sampling arc radius and will be considered insignificant with respect to overall modeling error discussed below.

Figure 1.15 shows the comparison between experimental and simulated normalized, crosswind integrated deposits, $D_0$ ($m^{-1}$), for Trial G. Qualitative agreement between simulation and experimental data is observed for the case of a neutral to stably stratified atmosphere. The predicted location of maximum deposition was within 20 meters of the measured location. The experimental rate of decay in deposition with distance from the source was also well predicted after the location of maximum deposits. The model predicts approximately 20-30% less deposition close to the position of maximum deposits and 100-200% greater deposits from 200-600 meters downwind. Good agreement, 15% error, is observed at 800 meters. Relative error of 20% is often considered excellent in atmospheric dispersion modeling due to the difficulties in source and atmospheric modeling. It is also important to consider the large range for crosswind integrated deposits, $10^{-6} < D_o < 10^{-2}\, m^{-1}$, when considering the relative error between experiment and simulation. It should be noted that Wilson modeled the same Suffield experimental data with a Lagrangian stochastic (LS) model in which the crossing trajectory effect was included (2000). Wilson's LS model predictions of peak deposits had a relative error of 100% in the worst case, very stable conditions, and 20% more generally.

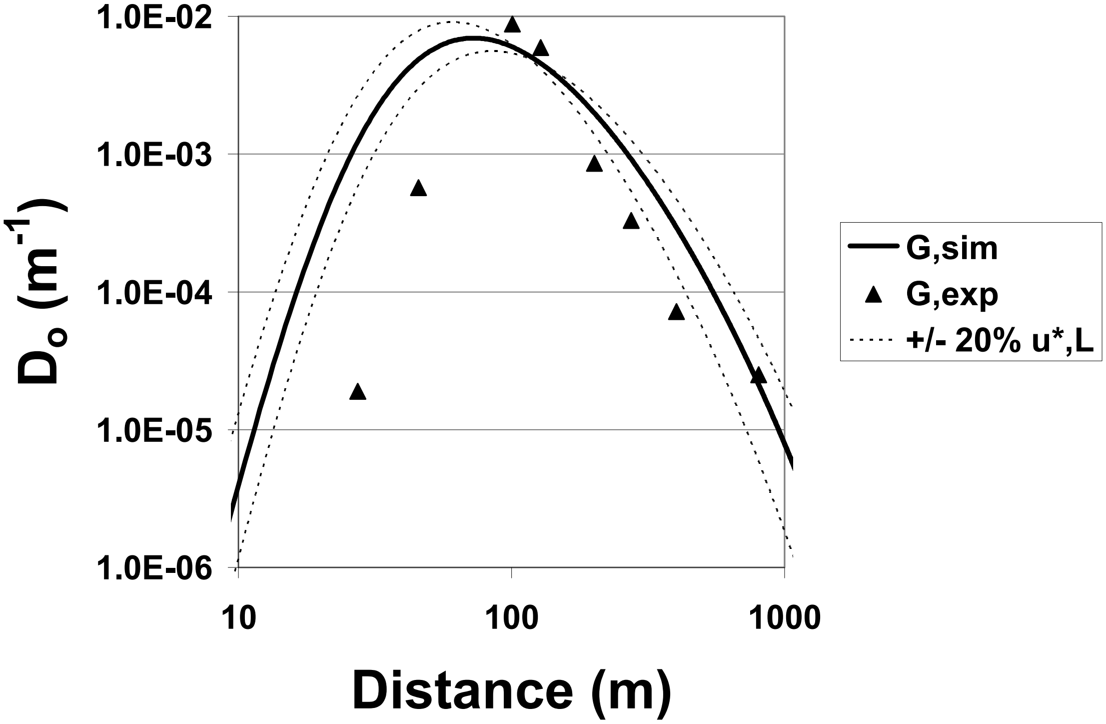

Figure 1.15: Comparison of experimental and simulated, normalized crosswind integrated ground deposits ($m^{-1}$) for Suffield Trial G

Experimental wind speed and temperature measurements were used by Wilson to estimate the M-O parameters used to specify wind speed and diffusivity profiles (2000). Additional simulations were performed to determine the sensitivity of $D_o$ to M-O parameters. The M-O length and friction velocity were both increased and decreased by 20% to form a window of values that could arise from modest estimation error. The sensitivity study M-O parameters are given in Table 1.2.

**Sensitivity Study M-O Parameters**

| Suffield Trial | +20% | | -20% | |
|---|---|---|---|---|
| | L (m) | u* (m/s) | L (m) | u* (m/s) |
| G | 62 | 0.25 | 42 | 0.17 |
| H | 42 | 0.34 | 28 | 0.22 |
| I | 19 | 0.22 | 13 | 0.14 |
| L | -60 | 0.68 | -40 | 0.46 |

Table 1.2: M-O Parameters for Suffield Deposition Sensitivity Analysis for Experiments (G,H,I,L)

The combination of minimum values for $L$ and $u_*$ gives the smallest wind speed and diffusivity profiles. Higher simulated deposits near the source would be expected since vertical and longitudinal transport terms are reduced. Conversely, the combination of maximum M-O parameters gives the largest wind speed and diffusivity profiles which would result in increased downwind transport. Simulated $D_o$ for the modified M-O parameters are shown in Figure 1.15 as dashed lines. The error associated with M-O parameter estimation appears less significant near the location of maximum deposits and increases to approximately ±50-100% with increasing upwind and downwind distance. Sensitivity to the specification of source CMAD (±10%) was negligible from similar analysis.

Figure 1.16 and Figure 1.17 show the simulated and experimental crosswind integrated deposits for trials H and I, respectively. Good agreement is observed for the location of maximum deposits (±20 meters) and deposition magnitude (±25%) for each of the trials with increasingly stable stratification. Sensitivity analyses to M-O parameters were performed for trials H and I and the range of predicted ground deposits is bounded by dashed lines in the figures. Particularly good agreement is observed between model and experiment when M-O parameter estimation is error is considered.

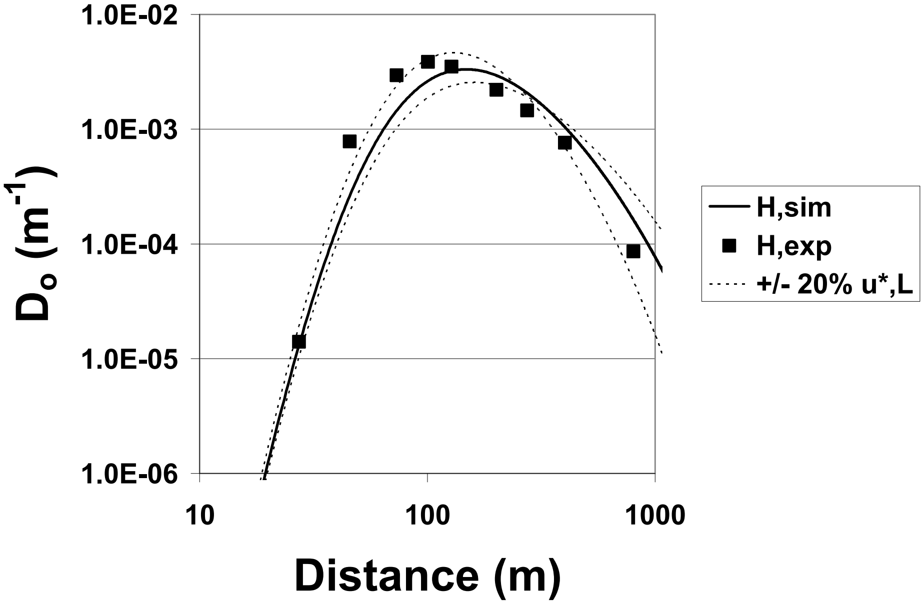

Figure 1.16: Comparison of experimental and simulated, normalized crosswind integrated ground deposits ($m^{-1}$) for Suffield Trial H

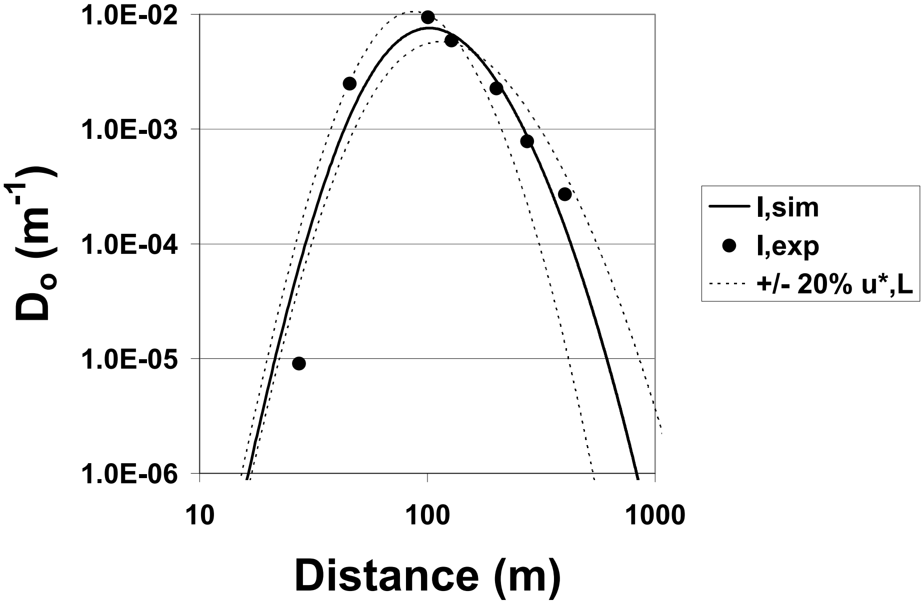

Figure 1.17: Comparison of experimental and simulated, normalized crosswind integrated ground deposits ($m^{-1}$) for Suffield Trial I

Model validation and experimental deposition data for an unstably stratified atmosphere, Trial L, are shown in Figure 1.18. The location of the deposition maxima are in good agreement. Downwind deposits appear to be underestimated to a greater degree, with a relative error of approximately 50%, for unstable stratification. The error in $D_o$ decreases to approximately ±10% at distances of 300 to 800 meters. Sensitivity to M-O parameters is decreased in unstable atmospheric conditions. This is most likely the result of the relative dominance of turbulent mixing to particle settling that will be explored in later sections.

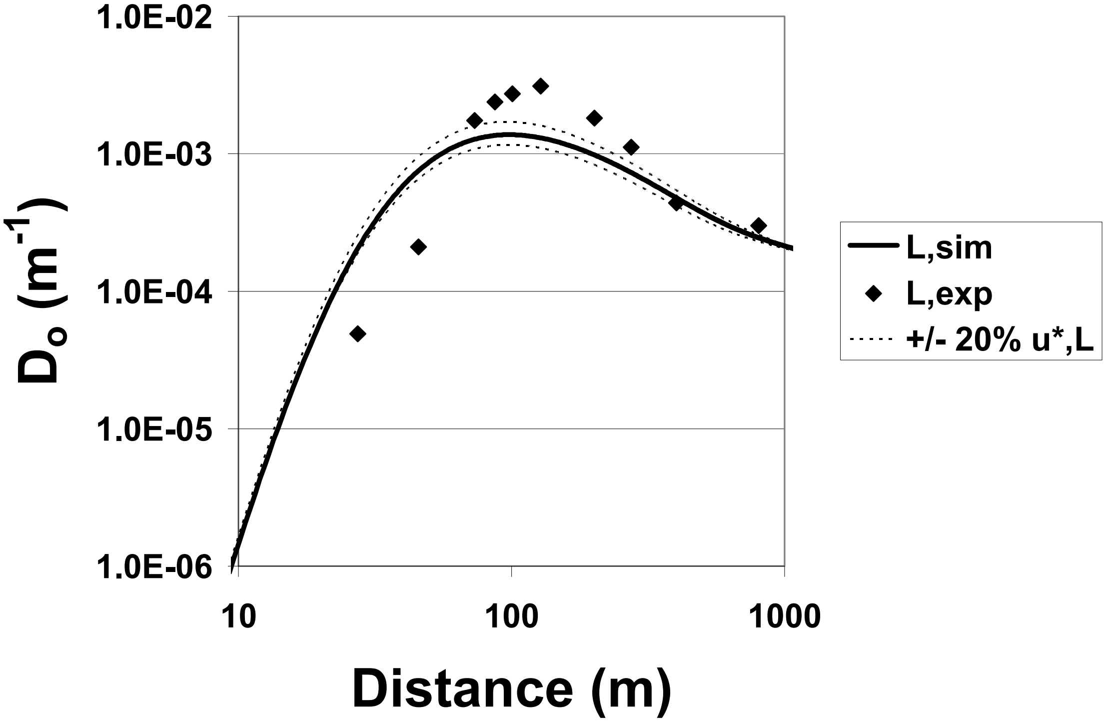

Figure 1.18: Comparison of experimental and simulated, normalized crosswind integrated ground deposits ($m^{-1}$) for Suffield Trial L

### 1.6.4. GAUSSIAN CORRECTION FACTOR

It is also possible to compare model predictions to experimental data based on centerline deposit densities rather than crosswind integrated deposits. The simulated, two-dimensional data can be corrected to account for lateral spreading that would occur in a three-dimensional domain. Figure 1.19 illustrates this concept. This method assumes the lateral variance in plume concentration can be characterized by a Gaussian distribution. Two-dimensional model results can be multiplied by a simple scaling factor to predict centerline plume concentrations if transport in the third dimension were included.

Lateral plume standard deviations proposed by Briggs were adopted in this study (Gifford, 1976). The Gaussian dispersion parameter, $\sigma_y$, increases with distance from the source and is a function of atmospheric stability class. Different Briggs formulas are given for the atmospheric stability classes developed by Pasquill and can be correlated to the M-O parameters used here. A correction factor, $R_G$, can be computed to estimate the three-dimensional centerline plume concentration and deposits from the two-dimensional model. The correction factor has the form

$$R_G = \frac{1}{\sqrt{2\pi}\sigma_y(x)} \tag{1.39}$$

where the standard deviation, $\sigma_y$, is provided by Briggs' relations.

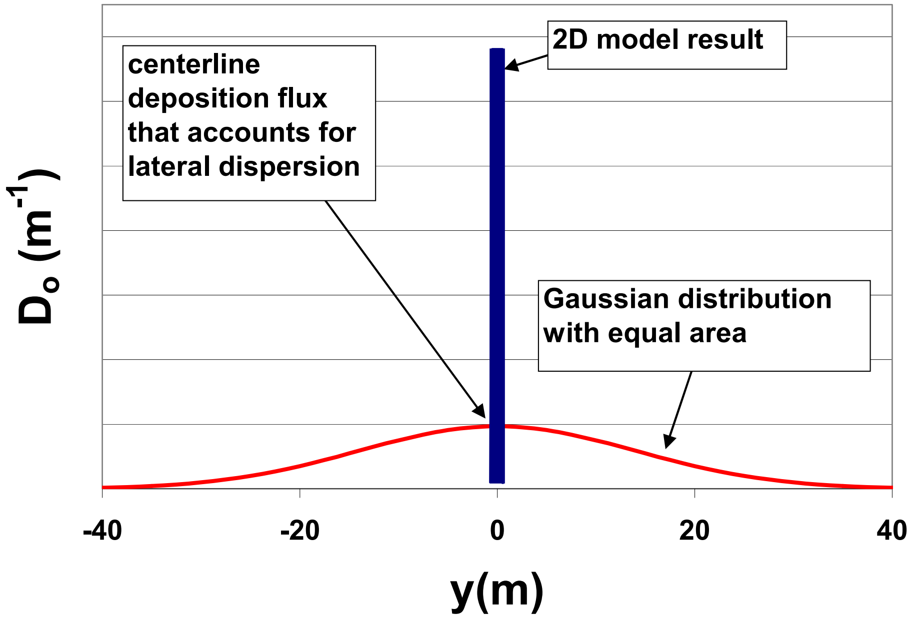

Figure 1.19: Application of Gaussian correction factor to transform two-dimensional model result into predicted centerline value for three-dimensional dispersion

Trends similar to those in Figure 1.15 through Figure 1.18 were observed when simulated data were multiplied by the correction factor and compared to experimentally measured centerline deposition densities. Henceforth, the Gaussian correction factor is applied to all simulated data as a simple method to account for dispersion in the lateral direction.

## 1.7. Simulations of Evolving Particle Size Distribution

Simulations were conducted to explore the effects of gravitational sedimentation and turbulent mixing on the collection of coarse particulate downwind from a near-ground release of aerosol particles. Virtual samplers were simulated at various distances downwind from the point of release to determine the time-integrated aerosol mass collected (dosage). Nine log-normal particle size distributions were modeled in the simulation, each for four classes of atmospheric stability. The time-integrated aerosol mass collected was determined at each of the virtual sampling points for each simulated release.

### 1.7.1. ATMOSPHERIC CONDITIONS

Four sets of atmospheric conditions were simulated to explore the differences in downwind dosage with varying degrees of vertical mixing. The M-O parameters for each set of atmospheric conditions are given in Table 1.3. The roughness length, $z_0$, was constant for all simulations and represented a ground cover height of approximately 5 centimeters. The M-O lengths were selected to represent varying degrees of atmospheric stability. The friction velocity, $u_*$, was calculated to give the same average horizontal wind speed, 5.6 m/s, so that the degrees of downwind dispersion due to convection were comparable.

| | **Atmospheric Stability Class** | | | |
|---|---|---|---|---|
| Parameter | Unstable | Neutral | Stable | Extremely Stable |
| $L_{mo}$ (m) | -200 | 200 | 25 | 1 |
| $u_*$ (m/s) | 0.304 | 0.352 | 0.186 | 0.016 |
| $z_0$ (m) | 0.05 | 0.05 | 0.05 | 0.05 |

Table 1.3: Monin-Okhubov similarity parameters for simulated extremely stable, stable, neutral, and unstable atmospheric conditions

Figure 1.20 and Figure 1.21 show simulated surface layer wind speeds and turbulent diffusivities as functions of height above the surface for the specified atmospheric conditions. The degree of mixing was approximately zero throughout the surface layer in the limit of extreme stability. Although non-physical, this scenario provided a baseline measurement of the downwind transport when only longitudinal convection and gravitational settling were present. The degree of mixing increased dramatically as the atmosphere became increasingly unstable. During typical daytime conditions, radiation from the sun heats the ground, which then heats the adjacent air. This gives rise to buoyancy driven turbulence and is commonly referred to as an unstable atmosphere. During nighttime conditions, the temperature gradient becomes inverted with respect to the unstable atmosphere. This acts to suppress turbulence and is commonly referred to as a stable atmosphere. Neutral atmospheres have a negligible heat transfer rate from the ground to the adjacent air; turbulence is neither produced nor suppressed. Although the scenarios given in Table 1.3 are specific, the diffusivity and wind speed profiles are representative of any conditions which produce similar transport behavior, for instance, dispersion in an urban atmosphere with increased shear driven turbulence due to surface roughness.

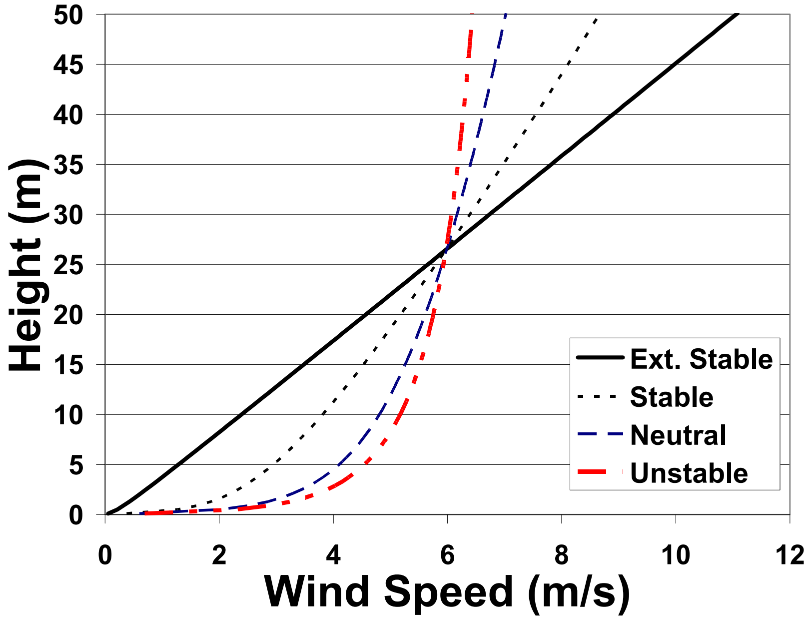

Figure 1.20: Simulated wind speed profiles for extremely stable, stable, neutral, and unstable atmospheric conditions

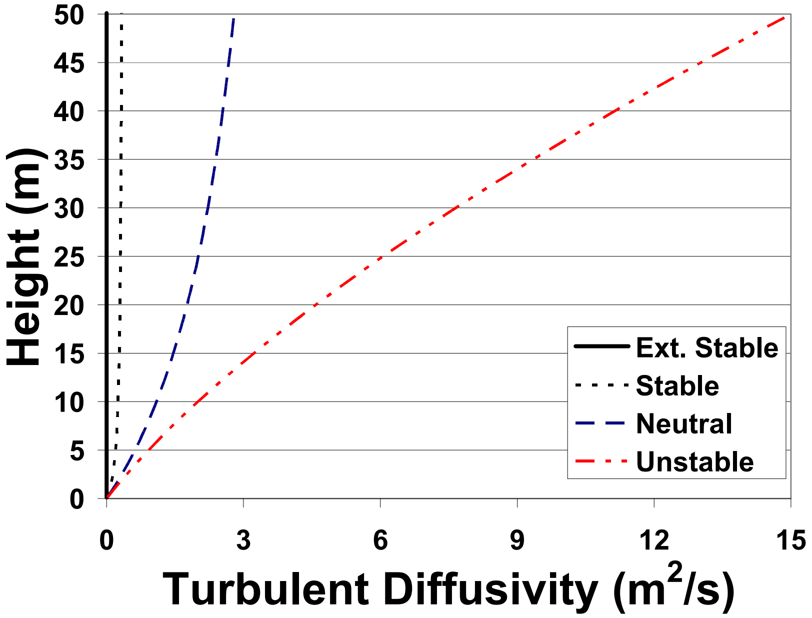

Figure 1.21: Simulated turbulent diffusivity profiles for extremely stable, stable, neutral, and unstable atmospheric conditions

### 1.7.2. BIOAEROSOL PUFF RELEASE

Nine lognormal particle size distributions (PSD) were simulated for each set of atmospheric conditions. Size distributions having count median aerodynamic diameters (CMAD) of 2.5, 10, and 40 micrometers were selected to represent a range of possible coarse particulate size distributions. Three geometric standard deviations (GSD) of 1.2, 1.6, and 2.0 were simulated for each CMAD. The count median aerodynamic diameters, geometric standard deviations, and corresponding mass median diameters (MMAD) for all nine size distributions are given in Table 1.4. The mass median aerodynamic diameters were calculated from the Hatch-Chaote equations (Hinds, 1999). The cumulative number fractions for all simulated distributions are shown in Figure 1.22.

| CMAD ($\mu$m) | GSD | MMAD ($\mu$m) |
|---|---|---|
| 2.5 | 1.2 | 2.76 |
| 10.0 | 1.2 | 11.05 |
| 40.0 | 1.2 | 44.19 |
| 2.5 | 1.6 | 4.85 |
| 10.0 | 1.6 | 19.40 |
| 40.0 | 1.6 | 77.60 |
| 2.5 | 2.0 | 10.57 |
| 10.0 | 2.0 | 42.26 |
| 40.0 | 2.0 | 169.06 |

Table 1.4: Count median diameters (CMAD), geometric standard deviations, and corresponding mass median diameters (MMAD) for nine simulated releases

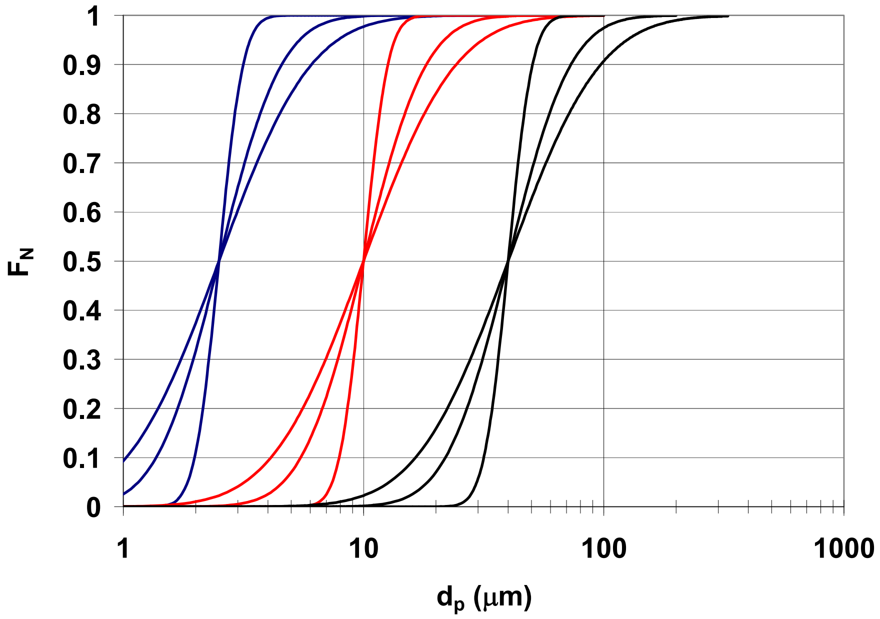

Figure 1.22: Cumulative number fraction for nine simulated releases

The simulated instantaneous puff aerosol release was centered at coordinates $(x,z)=(2.5m,2.5m)$, with a radius of two meters, and concentration profile given by

$$C(d_p,r)=Q(d_p)\cdot\exp(-r) \tag{1.40}$$

where $Q(d_p)$ was the source strength for a particular particle size in the initial particle size distribution. The decay in source concentration with puff radius was chosen to smooth concentration gradients at the instant of release but arbitrary otherwise.

### 1.7.3. SIMULATION METHODOLOGY

The simulated particle size distribution was discretized into approximately 20 size bins, spanning 99.5% of the particle size distribution by number. An arithmetic sequence was used to select the particle size associated with each bin. The dispersion of each particle size was simulated independently, implying no interaction between particles of different sizes. The initial concentration field was assigned according to (1.40). Transport of the coarse particulate puff throughout the simulation domain was simulated according to the methodology described above. Downwind dosages were also calculated for virtual sampling units located at a height of 1.25 meters. The simulated dosage calculated by each virtual sampling unit was determined from the time integrated product of concentration and sampling flow rate for particle size $i$,

$$N_i(x, z = 1.25m) = \int_0^t Q_s \cdot C_i(x, z = 1.25m) \cdot dt \tag{1.41}$$

where $Q_s$ was the sampling flow rate equal to 1250 Lpm. The virtual samplers were assumed to be perfectly efficient for all particle sizes and wind speeds in contrast to actual systems. The dosages were determined by integration over the total time in which the concentration field was non-zero, and were corrected for lateral dispersion according to the Gaussian correction factor.

### 1.7.4. DATA PROCESSING

Particle size distributions were reconstructed according to the set of dosage data at each virtual sampling point. The analysis is similar to the procedure utilized with cascade impactors to construct a particle size distribution from the relative fraction of particles collected on each stage. The total number of particles collected at a given distance from the source was determined by summation of the dosages from all the particle size simulations.

$$N(x) = \sum_i N_i(x) \tag{1.42}$$

The probability density function of particle size, based on number, was then calculated for each sampling location by

$$f_n(x, d_p) = \frac{1}{\Delta d_p} \frac{N_i(x)}{N(x)} \tag{1.43}$$

where $\Delta d_p$ is the particle size bin width from simulation. The mass based frequency function, $f_m(x, d_p)$ was calculated in the same manner with mass dosage replacing number dosage. Finally, the cumulative number and mass fractions, $F_n(x, d_p)$ and $F_m(x, d_p)$, respectively, were calculated by discrete integration of the probability density functions

$$F(x, d_A) = \int_0^{d_A} f(x, d_p) dd_p \tag{1.44}$$

where $d_A$ is the size at which the cumulative number or mass fraction is desired.

### 1.7.5. RESULTS

The effects of sedimentation and dispersion on particle size distributions can be observed by the change in the mass median aerodynamic diameter (MMAD) with increasing distance from the point of release. Consider the change in the cumulative mass fraction for the particle size distribution with initial CMAD of 2.5 micrometers and GSD of 2.0 as shown in Figure 1.23. Half of all aerosol mass in the initial aerosol puff is in particle sizes below 10.5 micrometers. However, the relatively greater deposition of larger particles changes the size distribution as the plume moves further from the source.

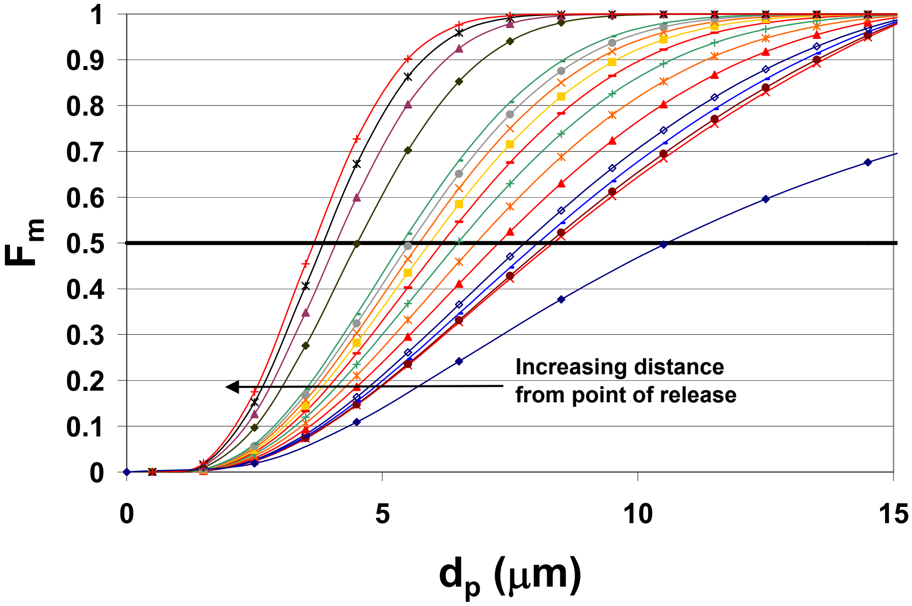

Figure 1.23: Cumulative mass fraction vs. particle aerodynamic diameter (micrometers) multiple distances from the initial release with CMAD = 2.5 micrometers and GSD = 1.2 in an extremely stable atmosphere

The MMAD values from each simulation were divided by the MMAD of the initial distribution to form the normalized MMAD (MMAD$^*$). This was done in order to collapse data for the various simulated particle size distributions and atmospheric stability classes. Figure 1.24 through Figure 1.27 show the decay of the normalized MMAD with distance from the source for extremely stable, stable, neutral, and unstable atmospheric conditions, respectively. As can be seen in the figures, deposition in the first 50 meters from the source can have a significant impact on the MMAD of the aerosol when the initial particle size distribution contains a significant fraction of coarse particulate. The release characteristics such as release height, release size, puff concentration magnitude, have significant impact on deposition within the first 100 meters from the source.

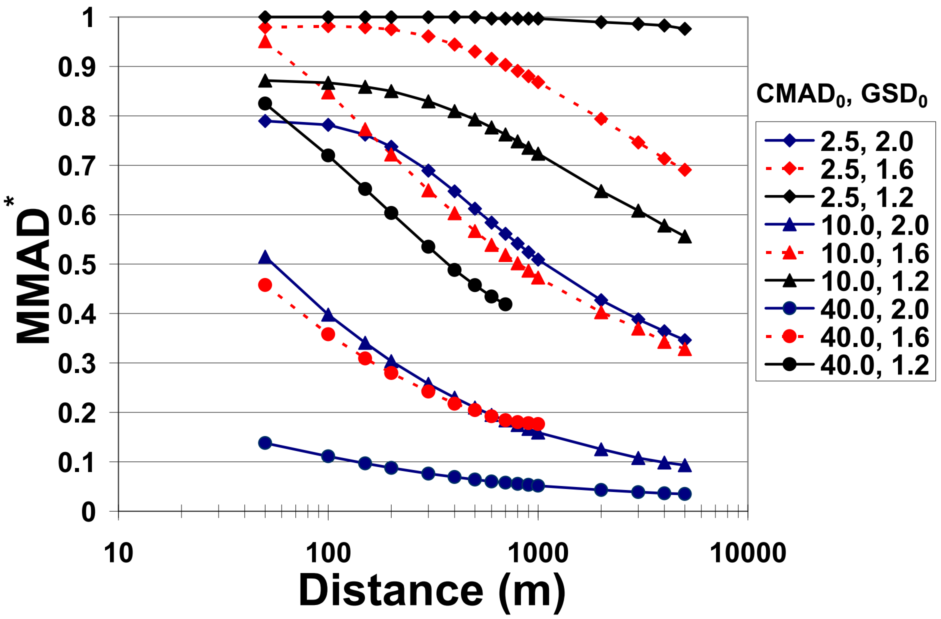

Figure 1.24: Normalized mass median aerodynamic diameter vs. distance downwind for extremely stable atmospheric conditions

Figure 1.24 shows the decay of $MMAD^*$ with distance from the source in the limit of zero vertical diffusion (extremely stable atmosphere). This case is non-physical, but does represent the theoretical maximum rate of change in MMAD* in the absence of dispersion. A simple comparison of the settling and horizontal convection velocities yields the maximum distance traveled for a given particle size in the absence of turbulent dispersion; no particles larger than 57 micrometers would be expected beyond a distance of 50 meters from the point of release. The MMAD at 5,000 meters was less than 7 micrometers for all size distributions studied in the limit of zero diffusion.

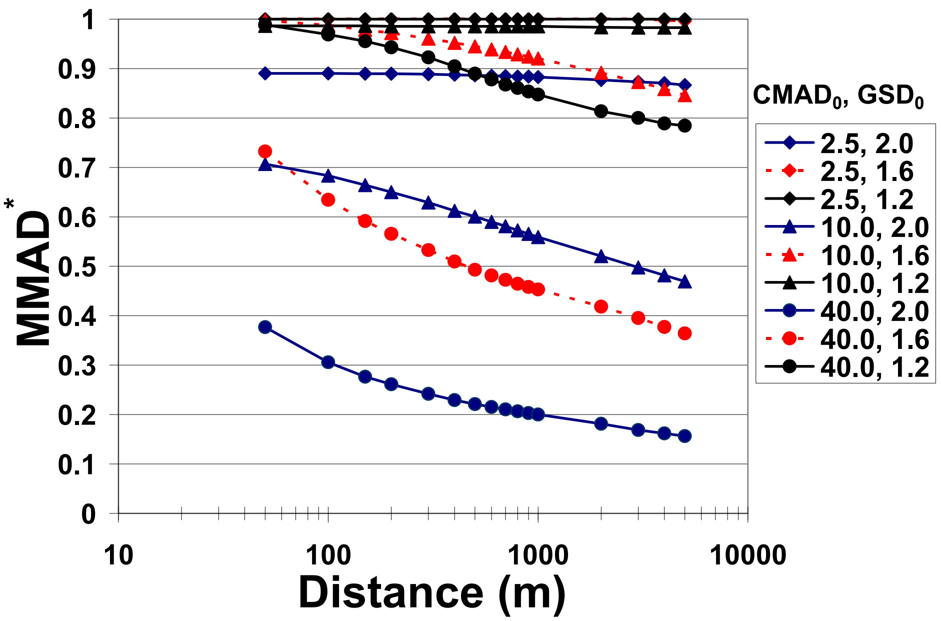

Figure 1.25: Normalized mass median aerodynamic diameter vs. distance downwind for stable atmospheric conditions

Figure 1.25 shows the evolution of MMAD$^*$ for the stably stratified atmosphere. The MMAD$^*$ decay rates are less than those in the case of zero turbulent mixing due to dispersion in the vertical direction. Coarse particulate stays aloft to greater longitudinal distances for this case. Figure 1.26 and Figure 1.27 show the simulated results for MMAD$^*$ decay for neutral and unstable atmospheric conditions, respectively. Greater vertical diffusivities yield less decay in MMAD* than extremely stable and stable simulations. However, the observed decay rates for neutral and unstable atmospheres do not appear significantly different. Vertical diffusion dominates gravitational settling for these two cases and an increase in diffusivity yields little change in the decay of MMAD$^*$. This condition corresponds to a perfectly mixed domain in which the concentration field is constant in the vertical direction after the first 50 meters. The MMAD$^*$ curves for the three size distributions having initial CMAD of 2.5 micrometers were not shown in Figure 1.26 and Figure 1.27 since no changes in MMAD* were observed.

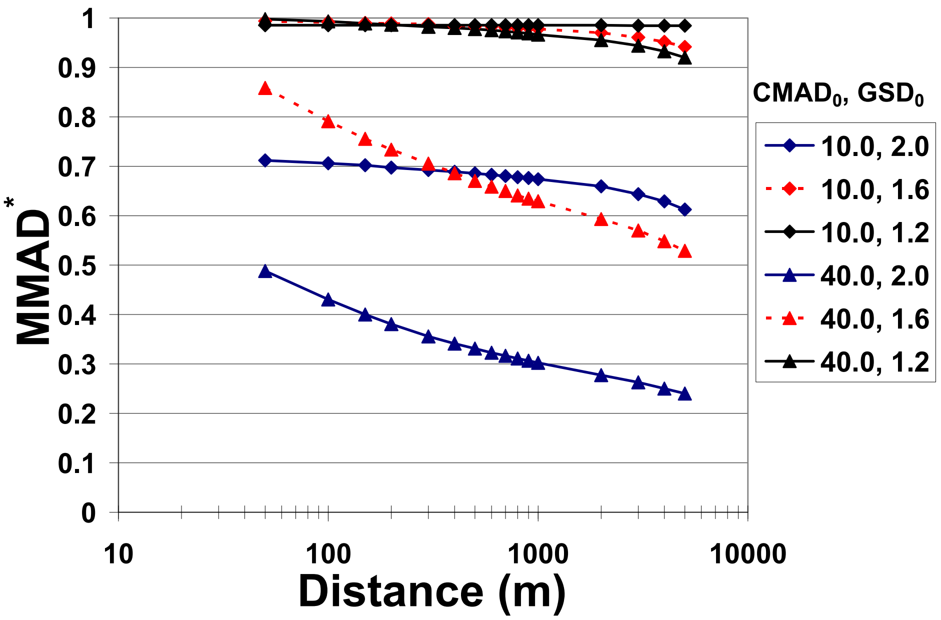

Figure 1.26: Normalized mass median aerodynamic diameter vs. distance downwind for neutral atmospheric conditions

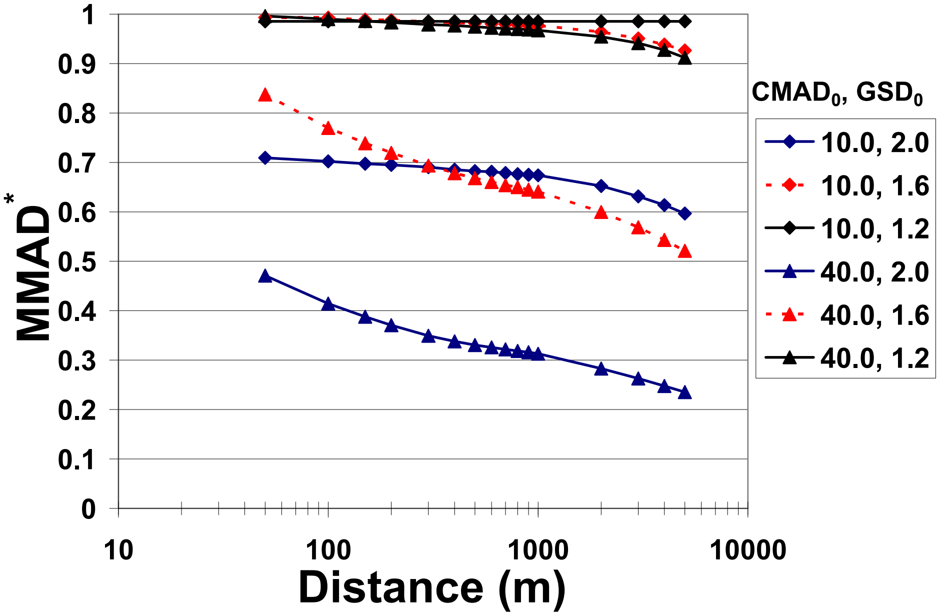

Figure 1.27: Normalized mass median aerodynamic diameter vs. distance downwind for unstable atmospheric conditions

The actual MMAD (micrometers) at 5,000 meters for all releases are given in Table 1.5. There was very little difference between neutral and unstable atmospheric stability classes because the degree of mixing for both cases was sufficient to produce a perfectly mixed atmospheric surface layer. It can also be observed that original distributions with CMAD of 2.5 and 10.0 micrometers, and having GSD of 1.2 and 1.6, change very little for all cases but the extremely stable atmosphere. Significant reduction (>15%) in MMAD occurs for the original distribution with CMAD of 10.0 micrometers and GSD of 2.0, and for all cases of CMAD of 40.0 micrometers. An interesting result was that for all cases of CMAD of 40.0 micrometers, the MMAD mapped to approximately 40 micrometers at 5,000 meters for both the neutral and unstable atmospheric stability conditions.

| CMAD$_0$ (μm) | GSD$_0$ | MMAD$_0$ (μm) | Ext. Stable MMAD$_{5000}$ (μm) | Stable MMAD$_{5000}$ (μm) | Neutral MMAD$_{5000}$ (μm) | Unstable MMAD$_{5000}$ (μm) |
|---|---|---|---|---|---|---|
| 2.5 | 1.2 | 2.8 | 2.8 | 2.8 | 2.8 | 2.8 |
| 2.5 | 1.6 | 4.9 | 3.4 | 4.8 | 4.9 | 4.9 |
| 2.5 | 2.0 | 10.6 | 3.7 | 9.2 | 10.6 | 10.6 |
| 10.0 | 1.2 | 11.0 | 3.9 | 10.9 | 10.9 | 10.9 |
| 10.0 | 1.6 | 19.4 | 6.4 | 16.4 | 18.3 | 18.3 |
| 10.0 | 2.0 | 42.3 | 6.7 | 19.8 | 25.9 | 25.9 |
| 40.0 | 1.2 | 44.2 | - | 26.5 | 40.7 | 40.7 |
| 40.0 | 1.6 | 77.6 | - | 28.3 | 41.0 | 41.0 |
| 40.0 | 2.0 | 169.1 | 5.9 | 34.7 | 40.6 | 40.6 |

Table 1.5: MMAD (micrometers) at 5,000 meters for extremely stable, stable, neutral, and unstable atmospheric conditions

### 1.7.6. DISCUSSION

The decay of MMAD with longitudinal distance from the source is influenced by gravitational settling and turbulent diffusion. The relative strengths of these two transport mechanisms govern particle motion in the vertical direction and can be examined by defining a dimensionless ratio of gravitational settling and turbulent diffusion. Such a ratio is analogous to the Peclet number which compares the relative strengths of convection and diffusion. We approximate the Particle Peclet number as

$$Pe = \frac{v_g \cdot H_0}{K_z} \tag{1.45}$$

where the height used to non-dimensionalize the settling velocity and diffusivity is the initial release height, $H_0 = 2.5m$.

Particle Peclet numbers much greater than unity imply vertical particle motion is dominated by gravitational settling while particle Peclet numbers much less than unity imply that diffusion dominates. The particle Peclet number for a particle of fixed size increases with elevation from the surface since turbulent diffusivity increases with vertical distance in the atmospheric surface layer. Thus, it is possible that the same size particle could have vertical motion that is diffusion-dominated away from the ground, and sedimentation-dominated near the ground. Figure 1.28 shows the particle Peclet number for the stably stratified atmospheric conditions simulated. Each curve in the graph represents a different particle aerodynamic diameter and gravitational settling velocity.

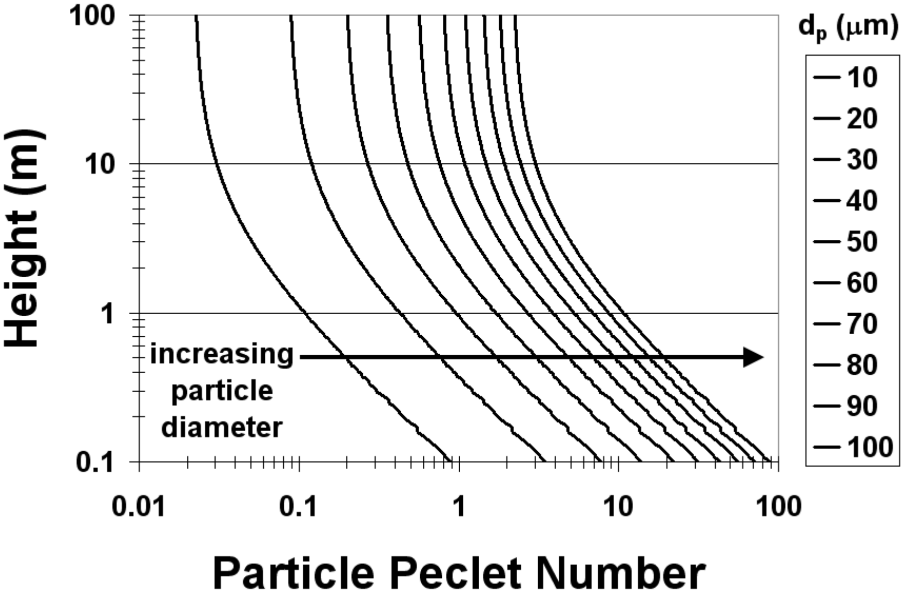

Figure 1.28: Particle Peclet number for stable atmosphere as a function of height and particle size

With respect to Figure 1.28, gravitational settling is not expected to play a significant role in vertical transport for the stable atmosphere until particle size becomes greater than 50 micrometers in aerodynamic diameter. The region in which gravitational settling is important appears limited to the first 5 meters above the ground for particles as large as 100 micrometers. The particle Peclet number becomes smaller, for particles of fixed size, as the atmosphere becomes more unstable and turbulent diffusion increases. Gravitational effects become negligible and vertical motion approximates that of the gas phase as particle Peclet number approaches zero. This limiting process explains the similarity in normalized MMAD decay curves for the neutral and unstable atmospheres.

A limiting process according to particle Peclet Number also helps explain the observed similarity in the MMAD at 5,000 meters for different initial size distributions (neutral and unstable atmospheric classes). For these simulations, particles larger than about 60 micrometers AD were rapidly lost due to sedimentation and proximity to the ground at the release point. The remaining particles were perfectly mixed in the domain. Although the initial size distributions were quite different, the differences were largely confined to the size range larger than about 60 micrometers AD. Once the large particles were removed, the resulting truncated distributions were nearly the same.

Kim and Larson determined the quasi-laminar boundary layer deposition velocity, $(V_d)_b$, to be the sum of the gravitational settling velocity and an inertial velocity dependent upon particle properties and the surrounding turbulence. The deposition velocity proposed by Kim and Larson is different from the diffusive surface flux velocity of the current model. The quasi-laminar boundary layer deposition velocity can be calculated for the simulations by

$$(V_d)_b = u^*(10^{-2.8/Stke}) + v_g \tag{1.46}$$

where the eddy Stokes number is $Stke = v_g u^{*2} / g\nu$, $g$ is the gravitational constant, and $\nu$ is the kinematic viscosity of air. An effective simulated deposition velocity, $V_d$, derived from (1.11), was calculated and compared to that of (1.46). A dimensionless ratio is formed from the two velocities and shown in Figure 1.29 for the four sets of atmospheric conditions simulated in this study. The effective deposition velocity used here is approximately three times smaller, at 30 micrometers AD in unstable conditions, than the Kim et al. model. However, this is an improvement with respect to FDM because FDM underpredicts the model of Kim et al. by an approximate factor of seven (Kim et al. 2000).

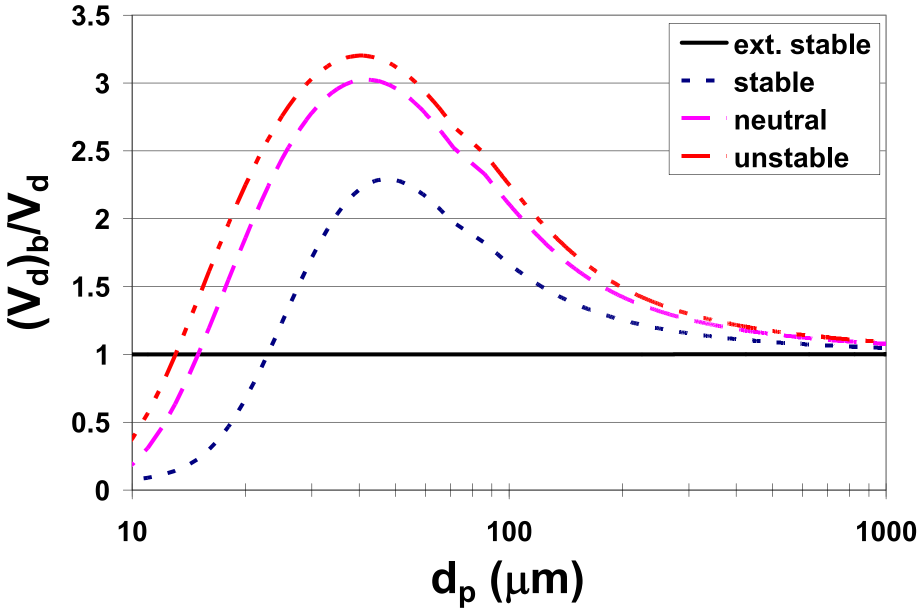

Figure 1.29: Ratio of deposition velocity from Kim et al. model to deposition velocity of transient two-dimensional convection-diffusion model

Comparison of the deposition velocity of the current model with that of Kim and Larson suggests a discrepancy in predicted deposition rates depending on particle size. The current model effective deposition velocity is approximately 2-10 times larger than that proposed by Kim and Larson for 10 micrometer particles, depending upon atmospheric stability class. Maximum differences of 225% and 320% are observed as particle diameter increases for the stable and unstable atmospheres, respectively. The maximum deviation between the two models occurs in the 40-50 micrometer size range.

The models converge to approximately the same deposition velocity as the particles become large and the inertial velocity goes to zero.

## 1.8. Implications for Bioaerosol Sampling and Detection

### 1.8.1. BACKGROUND

Atmospheric aerosol dispersion has important implications for real-time bioaerosol detection and aerosol collector design. State of the art biological identification methods consist of real-time polymerase chain reaction (RTPCR), ligand-receptor interaction, and mass spectrometry. Specific DNA sequences are targeted, isolated, and amplified in RTPCR so that a miniscule amount of biological material can be detected. Ligand-receptor methods, e.g. antibody-antigen, incorporate transducers coated with films of specific antibodies to detect the presence of their complimentary antigens. The transducer surface is physically altered upon the interaction of the antibody-antigen pair and sensed by means of phenomena such as optical or electrical properties. Lastly, mass spectrometry (MS) is based on the creation of ions from the analyte and correlating those specific ions to known biological organisms. MS is seen as one of the most promising detection technologies although marker ions have yet to be identified for many biological warfare agents (DHS, 2007). The unifying thread amongst these technologies is the proportionality between biological mass and detector response.

Increasing bioaerosol mass collected yields stronger and more robust detector signals, thus increasing the likelihood of detection and reducing the probability of false negative responses. The latter is crucial for applications that affect civilian populations since alerting the public or implementing emergency response protocols can create widespread anxiety. The particle size distribution of the collected aerosol has significant impact on the amount of biological mass collected because particle mass scales with the third power of particle size. For example, a particle with a diameter of ten micrometers contains one thousand times more mass than a particle one micrometer in diameter. Single spore bacteria have diameters of approximately one micrometer. However, spore forming bacteria often appear as agglomerates when aerosolized. Agglomerated particles tend to survive in the atmosphere longer and present a detection mass advantage with respect to single spore particles.

Typical bioaerosol collector systems are designed with a dynamic range of 1-10 micrometers AD and do not collect particles outside this range efficiently. It has been suggested that this range be extended to 1-30 micrometers AD to benefit from the detection mass advantage which arises from collecting larger particles (NRC, 2004). Justifications for a dynamic range of 1-10 micrometers AD were analyzed in light of the suggested extension to 1-30 micrometers.

The human respiratory system functions as an inertial separator. Particles larger than 10 micrometers AD rarely penetrate into the mouth and thoracic regions of the respiratory system. Thus, the health threat posed by biological particles larger than 10 micrometers AD is minimal with respect to smaller particles due to the improbability of inhalation. However, detection of bioaerosols is the emphasis here. Although particles of 10 micrometers AD may not represent a serious health risk, the detection mass advantage for such particles is substantial and should be considered when bioaerosol sampling for the explicit purpose of detection.

Another justification for limiting the dynamic range to 1-10 micrometers AD is that sampled aerosols are generally not considered to contain larger particles. The speculated absence of larger particles is often attributed to a lack of these particles in the initial release or rapid sedimentation which occurs during atmospheric dispersion.

Information regarding initial size distributions of bioaerosol releases is not available in the open literature. Sophisticated dispersion techniques like electrosprays could generate monodisperse, "weaponized", aerosols of single organisms. However, methods like agricultural spraying should be considered due to high availability and simplicity. Sprayers produce droplets several hundred micrometers in diameter. Evaporation is then likely to result in a large number of particles within the 20-30 micrometer AD size range. Conventional wisdom suggests that large particles sediment within a few hundred meters from the source. The modeling studies performed above show otherwise. Particulate above 10 micrometers AD is transported significant distances (kilometers) from the source due to the relative dominance of turbulent mixing to gravitational settling in typical daytime atmospheric conditions.

### 1.8.2. EFFECTIVE MASS COLLECTION RATE

The detection mass advantage of a system with extended dynamic range (1-30 micrometers AD) is calculated based on atmospheric dispersion model results. Two realistic, inertial based, biological aerosol collector efficiency curves are shown in Figure 1.30. The first hypothetical collector, $\eta_0$, represents an original collector designed with a 1-10 micrometer AD dynamic range. Collection efficiency is low for particles smaller than one micrometer AD as inertial forces are not sufficient to cause collection on impaction surfaces. The efficiency reaches its maximum near 2 micrometers and decreases significantly as particles become greater than 10 micrometers. This decrease is attributed to increased particle losses in system components like the collector inlet. The second hypothetical collector, $\eta$, represents the same collector with design upgrades to extend the dynamic range to 1-30 micrometers AD. Reduction of large particulate losses could be the result of optimized inlet contours, for instance. The overall efficiency is increased for particles larger than 1 micrometer and moves the upper bound of particle collection to approximately 30 micrometers.

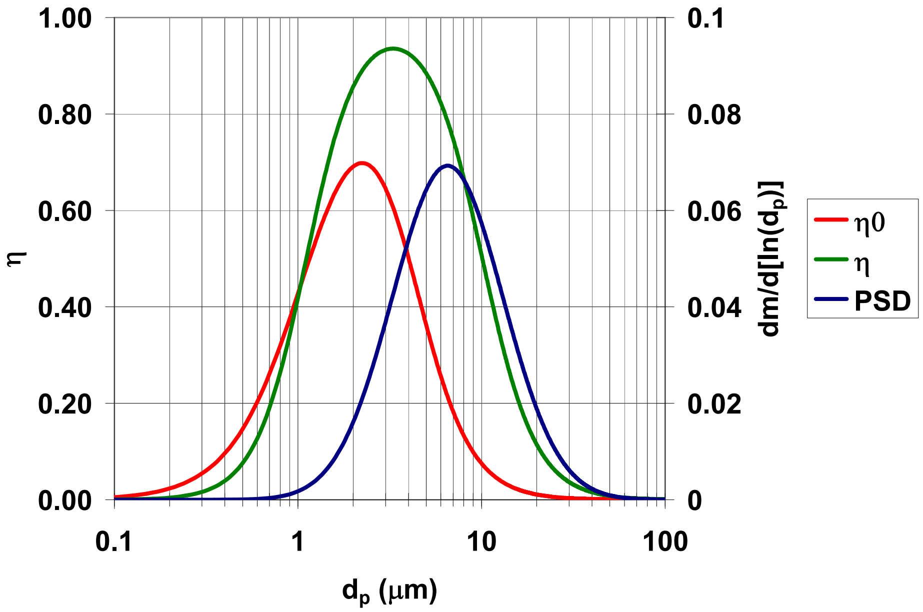

Figure 1.30: Mass based particle size distribution for CMAD 2.5 micrometers and GSD 2.0, and hypothetical collector efficiencies for original collector "0" and upgraded collector

Figure 1.30 also shows a particle size distribution with CMAD of 2.5 micrometers (MMAD 10.6 micrometers) and GSD of 2.0. Half the particles in this aerosol, by number, are smaller than 2.5 micrometers AD. However, half the mass in the aerosol is contained in particles above 10.6 micrometers AD due to the large spread and disproportionate mass contained in larger particles. Failing to collect particles above 10.6 micrometers AD consequently cuts the probability of detection in half assuming detection is proportional to mass collected. As emphasized previously, data regarding the characteristics of true biological aerosol releases is largely unknown. This merely serves as an illustration of the dependence of particle collection on particle size and collector efficiency.

An effective mass collection rate for the original collector is expressed

$$\dot{m}_0 = Q_0 \cdot C_T \int_0^\infty f_m(d_p) \cdot \eta_0(d_p) \cdot dd_p \tag{1.47}$$

where $Q_0$ is the collector air flow rate, and $C_T$ and $f_m$ represent the total aerosol concentration and mass based particle size probability density function. The effective mass collection rate for the improved collector is expressed similarly by replacing the flow rate and efficiency function. A comparison of the collectors can be made from the ratio of the effective mass collection rates

$$R = \frac{\dot{m}}{\dot{m}_0} = \frac{\int_0^\infty f_m(d_p) \cdot \eta(d_p) \cdot dd_p}{\int_0^\infty f_m(d_p) \cdot \eta_0(d_p) \cdot dd_p} \tag{1.48}$$

where the total concentrations and collector air flow rates are assumed equal. Figure 1.31 shows the product of the original collector efficiency and mass based PSD, $\phi_0 = f_m(d_p) \cdot \eta_0(d_p)$. The shaded area under the curve is the integral in the denominator of (1.48) and is proportional to the effective mass collection rate. Figure 1.32 shows the same analysis for the upgrade collector. The ratio of effective mass collection rates is greater than one as observed by visual comparison of the shaded areas. In fact, for this PSD and these hypothetical collectors, the improved collector has an effective mass collection rate 3.2 times higher than the original collector. The detection mass advantaged realized from extension of the dynamic range (1-30 micrometers AD) significantly increases the probability of detection and reduces the likelihood of a false negative.

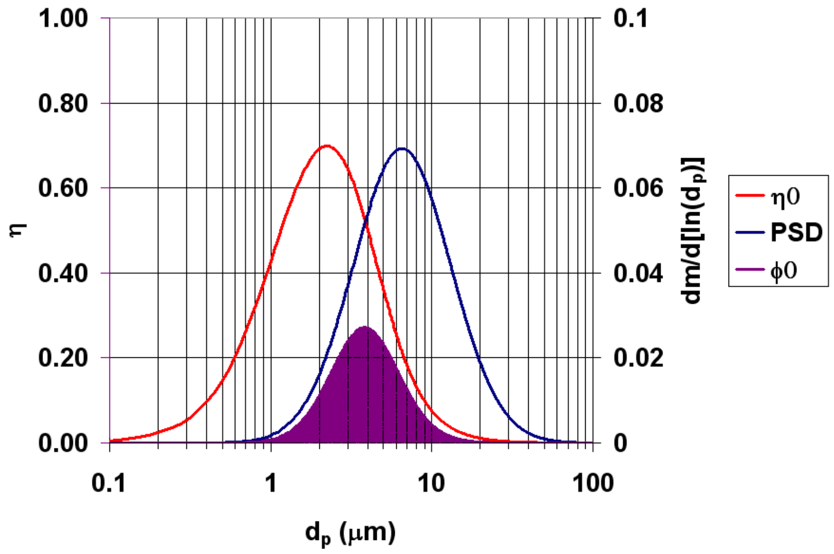

Figure 1.31: Mass based particle size distribution for CMAD 2.5 micrometers and GSD 2.0, hypothetical collector efficiency for original collector “0”, and product of PSD and collector efficiency

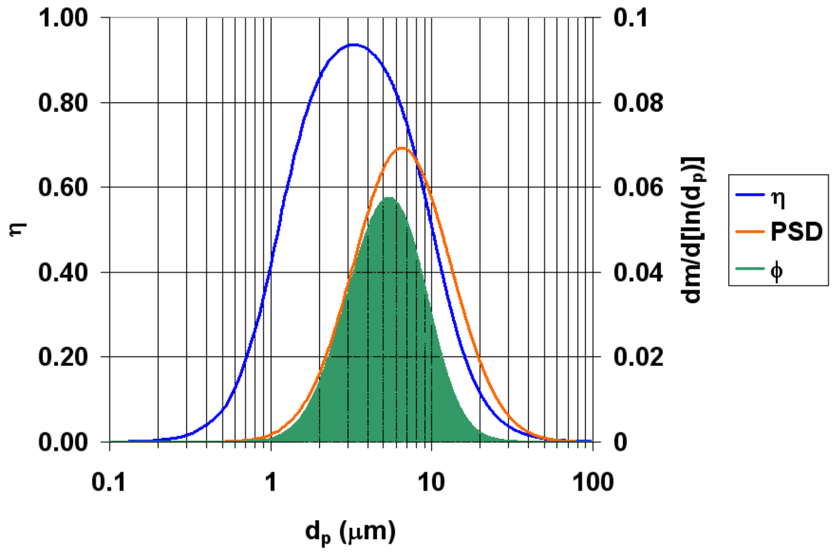

Figure 1.32: Mass based particle size distribution for CMAD 2.5 micrometers and GSD 2.0, hypothetical collector efficiency for upgrade collector, and product of PSD and collector efficiency

### 1.8.3. ANALYSIS OF CONVECTION-DIFFUSION-SEDIMENTATION MODEL DATA

Numerical simulations of atmospheric aerosol dispersion were used to assess the net benefit resulting from an extension the collector dynamic range to 1-30 micrometers AD. Table 1.6 shows the ratios of effective mass collection rates at 5 kilometers from the source for the 27 numerical simulations described in this study. The original and upgrade collector efficiency curves shown in Figure 1.30 were used in calculations. The ratio of effective mass collection rates for the initial size distribution is also given in the table. A net benefit, detection mass advantage, is obtained for all particle size distributions and atmospheric conditions.

Trends observed in $R_{5000}$ are similar to those for MMAD provided in Table 1.5. Changes in the effective mass collection ratio are negligible for small particle Peclet numbers. The particle size distribution changes little with distance from the source as particle settling becomes negligible with respect to atmospheric mixing. For some cases of fixed initial aerodynamic diameter and atmospheric conditions, $R_{5000}$ is observed to decrease with increasing GSD (e.g. CMAD$_0$ 10 micrometers in extremely stable atmospheric conditions). This is the result of shrinking overlap between the particle size distribution and collector efficiency curve as sedimentation dominates large particulate transport. In other cases, such as CMAD$_0$ 10 micrometers in neutral conditions, $R_{5000}$ increases with increasing GSD because aerosol mass in the 10-30 micrometer AD range increases with increasing AD.

| Initial PSD | | | $R_{5000}$ | | |
|---|---|---|---|---|---|
| **$CMAD_0$** | **$GSD_0$** | **$R_0$** | **No-mixing** | **Stable** | **Neutral** |
| 2.5 | 1.2 | 1.4 | 1.4 | 1.4 | 1.4 |
| 2.5 | 1.6 | 2.1 | 1.6 | 2.1 | 2.1 |
| 2.5 | 2.0 | 3.2 | 1.7 | 3.2 | 3.2 |
| 10.0 | 1.2 | 7.0 | 4.2 | 7.0 | 7.0 |
| 10.0 | 1.6 | 7.4 | 2.6 | 7.1 | 7.2 |
| 10.0 | 2.0 | 7.8 | 2.2 | 7.3 | 7.6 |
| 40.0 | 1.2 | 36.1 | 11.1 | 11.5 | 11.5 |
| 40.0 | 1.6 | 11.6 | 6.1 | 11.1 | 11.3 |
| 40.0 | 2.0 | 10.8 | 1.8 | 10.5 | 10.9 |

Table 1.6:Ratio of upgrade to original collector effective mass collection rates, for various initial PSD and atmospheric stability classes, at 5,000 meters from the source determined with simple convection-diffusion-sedimentation model

## 1.9. Summary

Atmospheric dispersion modeling is an important tool for the United States Biodefense Program. Planning and emergency preparedness are crucial. Forecasting the spread of an aerosol release facilitates the construction of effective surveillance and detection networks. It also enables response protocols to be implemented in advance of an attack. I have performed the following set of actions, and arrived at the accompanying conclusions, to strengthen our biodefense infrastructure:

- formulated simple convection-diffusion-sedimentation model to study the physics of coarse particulate transport in the atmospheric surface layer
- studied the relevance of particle inertia in atmospheric turbulent transport and established criteria under which the crossing trajectories effect can be neglected
- wrote transient and steady-state solvers and post-processing code for dispersion model
- verified code for conservativeness, discretization error, and accuracy against benchmark solutions
- validated model results against experimental data for the deposition of heavy particles released from an elevated continuous point source
- simulated the evolution of aerosol puff particle size distributions containing coarse particulate under various initial and atmospheric conditions
- concluded particles 10-60 micrometers AD can be transported distances up to 5 kilometers from the source under certain conditions
- defined particle Peclet number as an indicator of the relative strength of gravitational settling with respect to turbulent diffusion

- analyzed effects of bioaerosol sampler design on real-time bioaerosol detection
- recommended extending the dynamic range of bioaerosol samplers to 1-30 micrometers AD to capitalize on the mass collection advantage

## 1.10. Future Works

Additional work is proposed to develop the atmospheric dispersion model described here. The deposition algorithm of Kim et al. (2001) is gaining acceptance and utilization in current research. It is recommended that the current model's deposition flux be modified to represent the model of Kim et al. This could be achieved by imposing boundary conditions which match the diffusive and inertial fluxes given in (1.11) and (1.12), respectively.

Analysis of particle inertial effects suggested the crossing trajectories effect becomes non-negligible for particles larger than approximately 60 micrometers AD. The diffusivity reduction factor proposed by Csanady (1.10) should be incorporated to make the model more accurate for particles with large inertia.

Additional validation should be performed with available experimental data (Walker, 1965; Hage 1961; Doran et al., 1984; Doran and Horst, 1985). Comparisons to AERMOD predictions would be very useful to evaluate discrepancies between the two models. FDM comparisons are not recommended since the model is no longer supported by the EPA. As noted previously, source term errors are often the limiting factor for accurate modeling. The influence of source term error on convection-diffusion-sedimentation model predictions should be analyzed.

Parametric studies should be conducted to evaluate the effects of various model input parameters: surface layer height, release characteristics (e.g. height, magnitude, shape, size), and sampling location. Data from the current study shows significant dependence of downwind transport on the proximity of release to the ground. Data showing the relative effects of sedimentation and turbulent diffusion, independent of release characteristics, would be valuable to a broad audience.

Preliminary analysis of model data showed the downwind dosage for all particle sizes and atmospheric conditions could be collapsed to a single function of distance from the source and particle Peclet number. In essence, the transport of any particle size distribution, in any atmosphere, could be predicted by a single equation. The final result would be a simple and useful tool for risk assessment and aerosol sampler evaluation. Additional simulations should be performed to expand on this concept.

Lastly, the current convection-diffusion-sedimentation model code is un-optimized for speed. To be truly useful, the numerical solution methods should be optimized so that a simulation could be performed quickly. An adaptive time step algorithm should be adopted for the transient code. Another potential source of time savings is to eliminate the sectional method used to discretize particle size distributions in model simulations. The Quadrature method of moments (QMOM) is an alternative method that would greatly reduce computation time and eliminate errors attributable to particle size distribution discretization (Upadhyay and Ezekoye, 2006; Marchisio et al. 2003).

# 2. EXPERIMENTAL CHARACTERIZATION OF LIQUID RECOVERY IN A FAMILY OF WETTED-WALL BIOAEROSOL SAMPLING CYCLONES

## 2.1. Background

Cyclonic air flow devices have been used as industrial particulate separators for many years. The first device to apply similar physical principals to bioaerosol sampling was designed by the Aerojet-General Corporation ca. 1969. Since then, many modifications have been made and a family of wetted-wall bioaerosol sampling cyclones (WWC) has emerged to meet the growing need to detect, in real-time, the presence of bioaerosols. The reader is referred to McFarland et al. (2009) for a historical review of WWC development. Figure 2.1 shows a drawing of the wetted-wall bioaerosol sampling cyclone which exists as three geometrically and dynamically scaled versions with nominal design air flow rates of 100, 400, and 1250 liters per minute (Lpm).

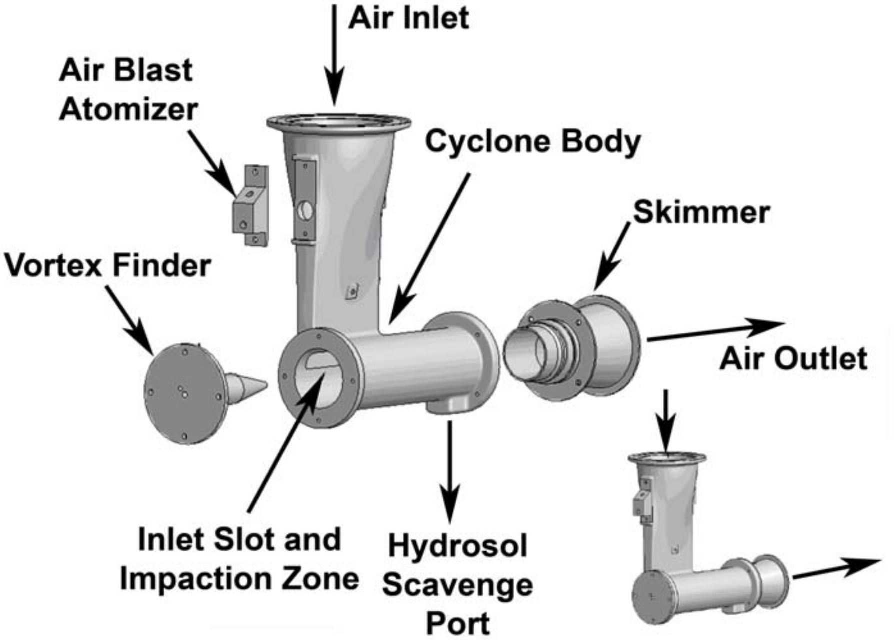

Figure 2.1: Wetted-Wall Bioaerosol Sampling Cyclone (WWC)

Air is sampled, accelerated through a converging inlet section, and enters the cyclone body through a rectangular inlet slot. The air velocity is tangential to the cyclone body at the inlet slot and results in a cyclonic flow with the aid of a coaxial shaft called the vortex finder. Aerosol particles attain speeds of approximately 40-50 meters per second in the inlet slot and impact the cyclone wall due to inertial separation from the flow. Slot velocities and cyclone dimensions are designed so that all three cyclones possess a characteristic aerodynamic particle cutpoint diameter of one micrometer, corresponding to the size of many bacterial spores. The aerodynamic cutpoint diameter is defined as the size at which half the particles impact the wall. The un-impacted particles follow the air streamlines and exit the cyclone with the air flow. Particles separated from the flow are continuously washed from the cyclone wall with liquid injected into the cyclone by an air-blast atomizer upstream of the slot and directed at the impaction zone.

The air-blast atomizer consists of 24 and 20 gage stainless steel hypodermic needles for liquid and air injection, respectively. The air needle is aligned at 45 degrees from horizontal directed down into the cyclone inlet. The liquid needle is aligned horizontal with the tip underneath the air-needle. A diaphragm pump (NF30-KPDC, KNF Neuberger Inc.) is used to provide pressurized air to the air needle at an approximate air flow rate of 0.275 Lpm. This air flow rate results in an exit air velocity of approximately 16 meters per second. A syringe pump (Cavro XCalibur, Tecan Group Ltd.) is used to provide a precise liquid input rate to the liquid needle. The atomized spray forms a cone directed into the inlet slot region that envelops the particle impaction zone. Biological particles are then entrained within a thin film hydrosol that covers the impaction zone which is subsequently driven downstream by aerodynamic forces at the air-liquid interface. The hydrosol is recovered at the downstream skimmer section after being separated from the exiting air stream.

The skimmer is a short concentric tube inside the cyclone with a thin gap between the outer diameter of the skimmer and inner diameter of the cyclone.  The liquid transported from the impaction zone flows into the gap, where it is then siphoned from the cyclone body through the scavenge port.  The air stream flows through the center of the skimmer tube and the liquid containing the collected particles is effectively separated from the air stream.  The collected hydrosol is then ready to be tested for analytes with biological detection methods like real-time polymerase chain reaction.

Effective coupling of these wetted-wall bioaerosol sampling cyclones with microfluidic detection technologies is achieved by delivering highly concentrated hydrosols.  Reducing the liquid volume to be analyzed decreases time to detection, eliminates intermediate liquid concentration processes, enhances limits of detection, and reduces the consumption of costly reagents (de Mello and Beard, 2003; Fair et al., 2007). However, achieving accurate and precise liquid output rates on the order of tens of microliters per minute (μL/min) requires understanding of the liquid evaporative behavior occurring within the cyclone.  Evaporation rates are observed to vary widely with inlet air temperature and relative humidity, and delivering constant microfluidic output rates can only be achieved by adjustment of the liquid input rate to offset the effects of evaporation.  The purpose of this study is to present the liquid mass transfer behavior (evaporation) for a family of wetted-wall cyclones as well as a systematic analysis of internal multi-phase flow and mass transfer phenomena.

## 2.2. WWC Gravimetric Liquid Recovery Study

### 2.2.1. EXPERIMENTAL APPARATUS

#### 2.2.1.1. Air Conditioning

Figure 2.2 shows the experimental cyclone inlet air conditioning test setup. A three module air conditioning system was built to provide control over the inlet air temperature and relative humidity. The three modules provided either desiccation, humidification, or heating to the ambient air. A wide range of air conditions were achieved by manually varying the degrees to which desiccant, vapor, and heating modules were used to alter laboratory air conditions.

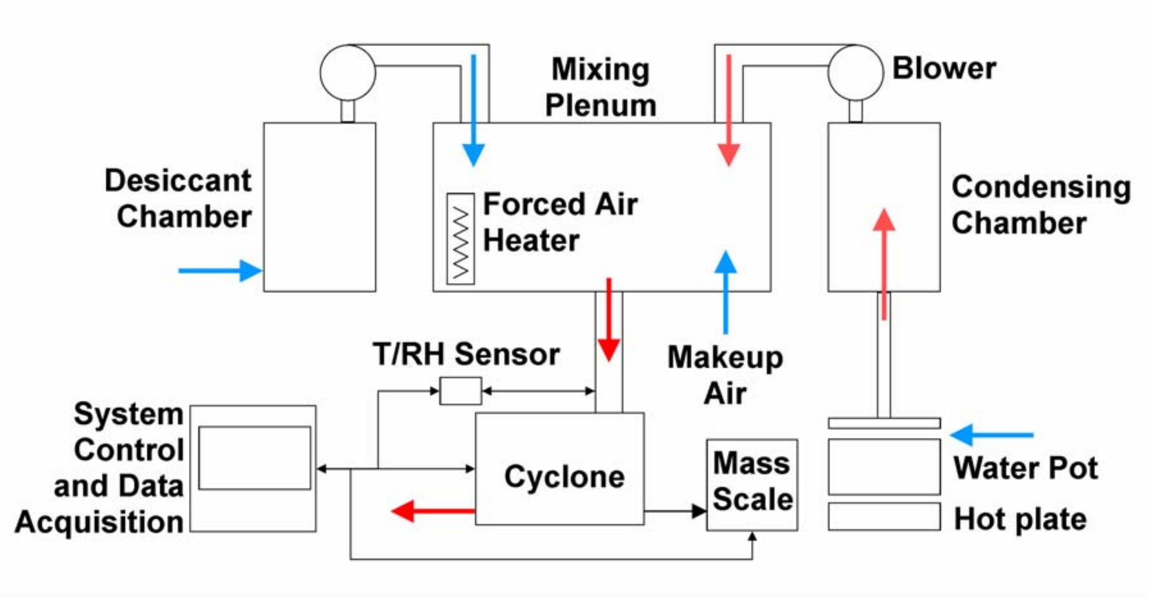

Figure 2.2: Experimental apparatus for controlling sampled air conditions and determining the liquid collection rate for the wetted wall cyclone bioaerosol sampling system

The desiccant module removed water vapor from laboratory air. Air was drawn through a 5 gallon bucket containing a granular desiccant (DuCal Drierite, W.A.

Hammond Drierite Co., LTD.) and into a mixing plenum. A blower (Ametek 119104-01) blower with approximately 119 cfm capacity was used to overcome the large pressure drop experienced within the desiccant bucket. The adjustable motor potentiometer was used to vary the air flow rate as needed for individual experiments. Relative humidity, at laboratory air temperature, could be reduced to approximately 10-20%, at an air flow rate of 100 Lpm, with quasi-steady-state conditions maintained for approximately 4 to 6 hours. The desiccation process was exothermic, thus, air temperature was observed to increase several degrees over the course of an hour. The desiccant module was less effective at larger air flow rates due to the small air residence time within the bucket.

A vapor module was also included to simulate moist sampling environments. A 4 quart stock pot containing liquid water was placed on a hot plate set to the lowest heating power. Air was then drawn over the warm water surface through a hole in the center of the pot lid. The lid was raised approximately 1 inch from the top of the pot to allow air to flow over the surface without significant loss of water vapor to the surroundings. A blower (Ametek 119498) was used to draw air over the water surface. The supply voltage was adjusted to control the air flow rate into the mixing plenum. Condensation of water in this module was typical as the air cooled on its way to the mixing plenum. To prevent droplet condensation on flow lines, the moist air was drawn through an empty 5 gallon bucket which served as a condensing chamber. This configuration allowed air temperature to stabilize prior to being introduced to the mixing plenum.

A forced air heater was mounted within the mixing plenum for tests in which elevated air temperatures were desired. A stand alone temperature controller (PXR3RCY1-4V0A1, Fuji Electric Systems Group, Inc.) was used to control the duty cycle of the heater and maintain the air temperature within the mixing plenum. Air was drawn from the mixing plenum by the blower of the wetted-wall bioaerosol collector system.  The mixing plenum was maintained at zero gage pressure to ensure the collector system air flow rates were unchanged by the presence of the air conditioning system.

#### 2.2.1.2. Data Acquisition and WWC Control

A wetted-wall cyclone system controller and data acquisition (DAQ) application was written in the C# programming language (Microsoft Visual Studio).  The controller software managed operation of the syringe pump based on user specified inputs such as the liquid input rate and sample time.  The controller application sent a command string to the syringe pump which in turn controlled sampling system components like the blower, scavenge pump, and atomizer pump, during each sample.  The controller also acquired real-time data from the air temperature and relative humidity probe (iTHX-W-DB9, Newport Electronics, Inc.) throughout the course of a sample.  A query command was sent to each of these devices on a one second interval.  The transient mass collected was recorded as a function of elapsed sample time by querying the mass scale (AB104-S/FACT, Mettler-Toledo International Inc.) on a one second interval.  Sample summary statistics, to be described below, were calculated internal to the DAQ software after the sample and all data written to a file for subsequent analysis.  The controller was programmed to include an interval of 5 minutes between successive samples.

#### 2.2.1.3. Wetted-Wall Bioaerosol Sampling Cyclone Systems

Experiments were conducted with wetted-wall bioaerosol sampling cyclones manufactured by TSI Inc. (St. Paul, Minnesota).  Version numbers, collector numbers (Applied Research Laboratories inventory number), and design dimensions are given in Table 2.1.  The WWC-1250 and WWC-100 bioaerosol collector systems are shown in Figure 2.3.

|  | WWC-100-v2.2-n6 |  | WWC-400-v3.2-n2 |  | WWC-1250-v3.3-n4 |  |
|---|---|---|---|---|---|---|
|  | (in) | (m) | (in) | (m) | (in) | (m) |
| bore diameter | 0.687 | 0.017 | 1.025 | 0.026 | 1.500 | 0.038 |
| slot length | 1.080 | 0.027 | 1.700 | 0.043 | 2.500 | 0.064 |
| slot width | 0.077 | 0.002 | 0.170 | 0.004 | 0.250 | 0.006 |
| wetted length | 2.272 | 0.058 | 2.778 | 0.071 | 4.276 | 0.109 |
| skimmer gap | 0.101 | 0.003 | 0.142 | 0.004 | 0.149 | 0.004 |

Table 2.1: Experimental wetted-wall bioaerosol sampling cyclone dimensions

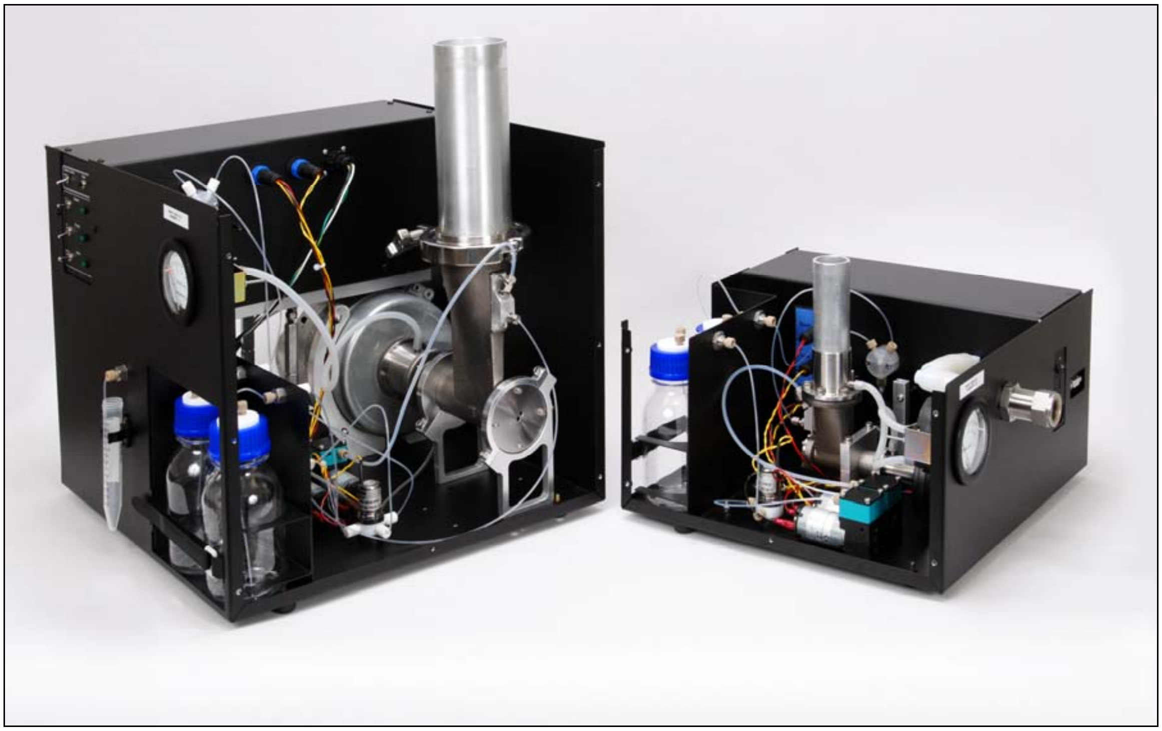

Figure 2.3: WWC-1250 (left) and WWC-100 (right) bioaerosol collector systems utilized in research studies

The units described above come equipped with diaphragm scavenge pumps with an approximate air flow rate of 0.275 Lpm. Using these pumps for liquid collection experiments presented several challenges. First, the air flow from the scavenge line impinged on the collection vial and caused a mass scale deflection of approximately 0.2 grams. In addition, the air flow from the diaphragm pump over the liquid reservoir resulted in non-negligible evaporation in the sample vial. These two effects complicated both data analysis and measurement, and the diaphragm pumps were replaced with peristaltic scavenge pumps. An Instech Laboratories P625/275 peristaltic pump with 0.062” tube set was used in WWC-100 and WWC-400 experiments. The maximum flow capacity, 3400 μL/min, was used for all tests and set by a power supply voltage of 12VDC. A medium flow peristaltic pump (3386, Control Company) with 0.0625” tube set, was used in WWC-1250 experiments. The maximum flow rate setting was approximately 12 milliliters per minute for the medium flow peristaltic pump. Use of the peristaltic pumps did not cause significant evaporation or liquid reservoir mass scale deflection. Liquid input and collection rates did not exceed the pumping capacity as witnessed by a large proportion of air (>50%) in the scavenge lines during experiments. The pumping rate was therefore not considered to affect the measured collection rates to be presented.

System air flow rates were verified prior to experimentation. The pressure drop across the cyclone body was measured with static pressure taps, one located upstream of the cyclone inlet and the other in the skimmer section. The pressure drop ($\Delta P$) was then experimentally correlated to the air flow rate through the pressure loss coefficient:

$$K = \frac{\Delta P}{\rho U^2 / 2} \tag{2.1}$$

where $U$ is the slot velocity. This method assumes that $K$ is independent of the Reynolds number. The use of (2.1) to calculate the air flow rate, $Q_a = UA$, was necessary because addition of a flow meter to the system altered the system air flow rate.

Measurements of the pressure drop and air flow rate were used to calculate $K$. The flow meter was then removed and the pressure loss coefficient was used to calculate the slot velocity and air flow rate according to design slot dimensions. Measured pressure loss coefficients, pressure drops, and corresponding air flow rates for the WWC-

100 and WWC-400 are given in Table 2.2. A thermal mass flow meter (Sage Metering, Inc.) was used to determine the pressure drop across the WWC-1250 at which the flow rate was 1250 Lpm, $\Delta P = 21$ inches of water. The flow meter was then removed from the system and the pressure drop was restored to 21 inches of water by adjustment of the blower speed.

| | **WWC-100-v2.2-n6** | **WWC-400-v3.2-n2** | **WWC-1250-v3.3-n4** |
|---|---|---|---|
| ΔP (in H2O) | 9.4 | 16.8 | 21.0 |
| K | 3.7 | 4.7 | 3.4 |
| Q (Lpm) | 103 | 430 | 1250 |

Table 2.2: Pressure drop, minor loss coefficient, and air flow rate for experimental WWC systems

Distilled water was used as the liquid input for all data in Sections 2.2 through 2.5. Liquid with small concentrations of surfactant are typically used in WWC to aid in biological particle removal from cyclone surfaces. Surfactant was not included here since the initial focus was to study the fundamental effects of air flow rate and ambient conditions on liquid collection and evaporation. Preliminary investigations into the effects of liquid chemical composition are discussed in Section 2.6.

### 2.2.2. EXPERIMENTAL PROCEDURE

Figure 2.4 shows the transient mass collection profile from a single liquid collection sample for the WWC-100, with a liquid input rate of 1000 μL/min, for air conditions of 21°C and 49% relative humidity. The elapsed sample time was measured relative to the time when the DAQ application sent the sample command string to the syringe pump. Typically, liquid mass recovered from the scavenge port was not recognized at the mass scale until some finite time had elapsed. This lag was defined as the latency period, $\tau$, and represents the time required from the start of liquid injection to the time at which liquid appears at the scavenge port for subsequent analysis. This measurement assumes that the wetted-wall cyclone is idle at the time it is triggered, thus, the internal cyclone walls are dry. The latency period was defined experimentally as the time at which 15 microliters (0.015 g) of liquid was recovered at the mass scale. This criterion was defined to reduce "false recognition" of liquid mass due to residual liquid within the sample lines at the start of a sample. The mass measurement at time $t_1 = \tau$ was stored in memory as $m_1$. The mass collection rate was observed to be constant after the latency period. A second mass reading, $m_2$, was recorded at the end of the 5 minute sample duration, $t_2 = 300$ seconds, and the steady state mass collection rate was calculated from the two points as $\left(m_2 - m_1\right)/\left(t_2 - t_1\right)$. The blower and scavenge pump remained operational for an additional 90 seconds to clear the system of any residual liquid after the sample period. The plateau in the mass collection profile near 325 seconds represents the point at which all hydrosol was recovered from the system.

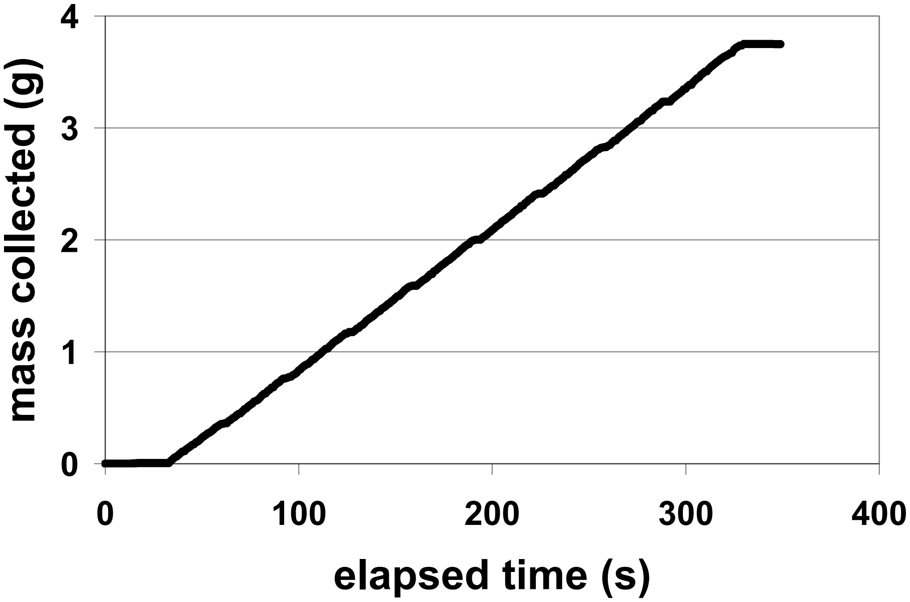

Figure 2.4: Hydrosol mass collected (g) versus elapsed sample time (s) for air conditions 21 °C and 49% RH at 1000 μL/min liquid input rate

The controller program then allowed a five minute sample interval, i.e. time between samples, to elapse, changed the liquid input rate setting, and sent the next sample command. The system control software ran through approximately five to eight sequential liquid input rate settings ranging from approximately 100 to 2000 μL/min depending on the cyclone air flow rate and air conditions. The lower limit on test liquid input rate was determined by trial and error on a per experiment basis. The upper limit was set at 1000 μL/min for the WWC-100 and 2000 μL/min for the WWC-400 and WWC-1250 from knowledge of typical WWC field operational settings. The liquid input rate sequence was selected such that the first four input rates were spaced closely to the minimum, and the remaining spanning the remainder of the test range, e.g. 100, 125, 150, 200, 500, 750, 1000 μL/min. Each liquid input rate sequence was repeated three times for a single combination of inlet air temperature and relative humidity.

Figure 2.5 shows the steady-state liquid output rates for multiple liquid input rates while sampling air at 21°C and 49% relative humidity with the WWC-100. The liquid output rate data were very repeatable over the entire range of liquid input rates. This data set shows the liquid output rate, $Q_o$, is linearly related to the liquid input rate, $Q_i$,

$$Q_o = m \cdot Q_i + b \tag{2.2}$$

where the standard form of a line, $y = m \cdot x + b$, was adopted which has slope '$m$'and y-intercept '$b$'. Figure 2.5 shows the slope of the liquid collection line is approximately 0.91 at these air conditions for the WWC-100. This slope, called the fractional collection, implies the liquid output rate was 91% of the liquid input rate during steady-state operation. The slope is expected to approach one in the limit of no evaporation, e.g. saturated air, and zero for total evaporation of the injected liquid.

The y-intercept has little physical significance until combined with the slope to calculate the x-intercept, $-b/m$, which was called the critical liquid input rate, $Q_c$. The critical liquid input rate corresponds to the minimum liquid input rate required to obtain any liquid output. It may also be considered the liquid input rate at which all injected liquid evaporates prior to reaching the skimmer section. The critical liquid input rate for the conditions represented in Figure 2.5 was 100 μL/min. This suggests an absolute lower limit on the liquid input rate for the wetted wall cyclone user. No sample will be recovered below this point. From a purely theoretical standpoint, the critical liquid input rate is expected to approach zero for saturated air conditions and increase as the evaporative capacity of the air increases.

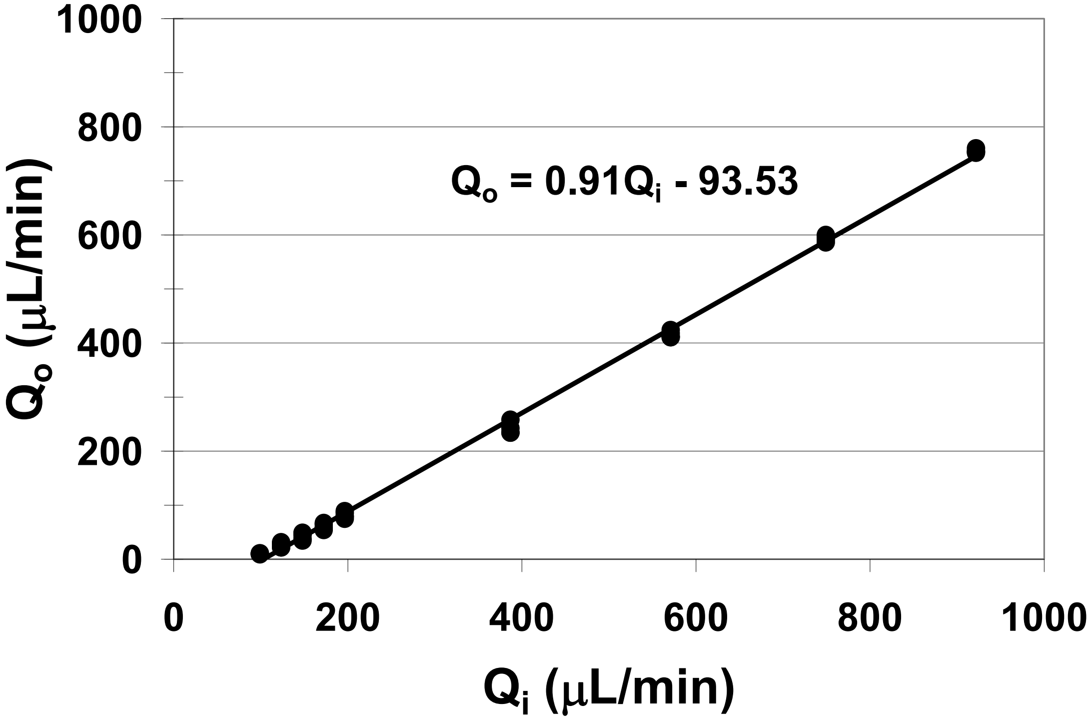

Figure 2.5: Steady-state liquid output rate versus liquid input rate for laboratory air conditions 21°C and 49% RH

### 2.2.3. DATA

#### 2.2.3.1. Air conditions

The experimental temperature and relative humidity test points, for all three cyclones, are shown in Figure 2.6. The temperatures ranged from approximately 280 to 320 Kelvin with relative humidity of 10% to 90%.

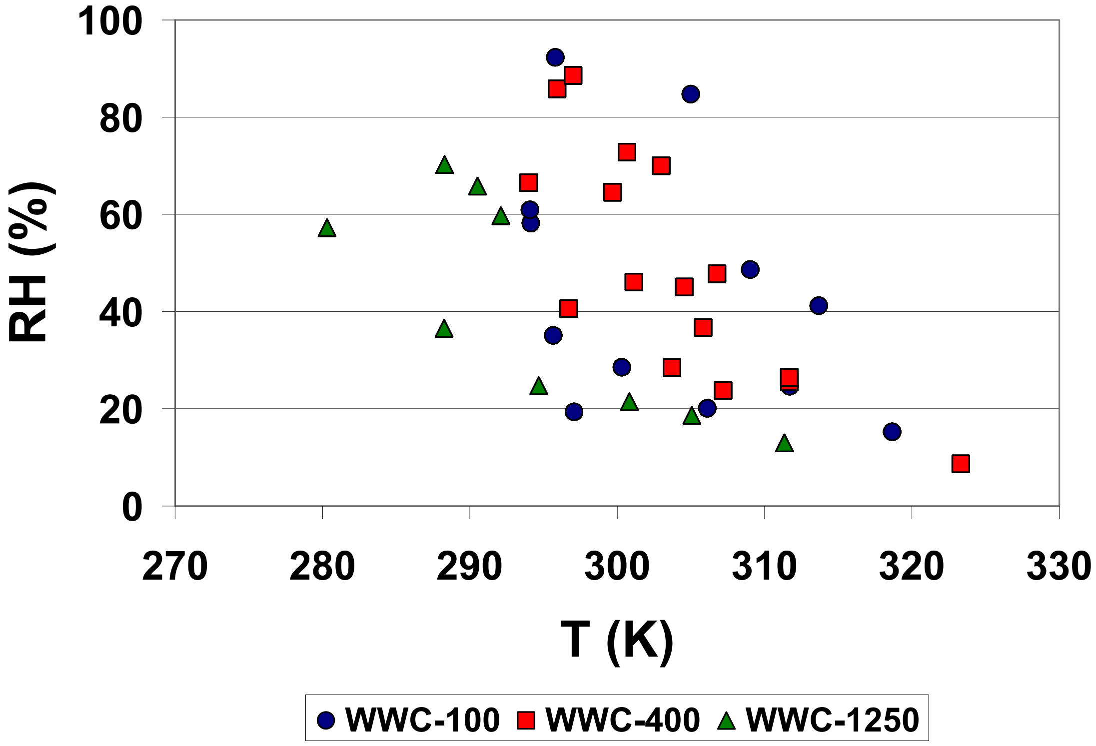

Figure 2.6: Laboratory Automated Liquid Collection Test air conditions for WWC-100, WWC-400, and WWC-1250

The air conditioning system described above was used to supply conditioned inlet air to the WWC-100, and WWC-400 for experiments. High relative humidity was more easily achieved at lower temperatures and ranged from 20% to 90% at standard room temperature (290 K) with a decreasing range as the temperature increased. High temperature, high relative humidity test points would require an alteration to the air conditioning system. The relative humidity decreased from saturated conditions (in the vapor module) upon being heated in the mixing plenum. The air would need to be heated prior to the vapor module to achieve high temperature, high relative humidity test points. This would be problematic due to condensation of water vapor in the remainder of the air conditioning system and within the cyclone body. Furthermore, ambient conditions seldom attain such high temperature and relative humidity combinations, reducing the need to gather data in that region.

The vapor and desiccant modules were insufficient to provide air conditioning at an air flow rate of 1250 Lpm. However, the heating module was utilized for WWC-1250 experiments. Relatively low temperatures observed for WWC-1250 tests were a result of the experiments being conducted in an annexed lab building with poor insulation during wintertime conditions.

#### 2.2.3.2. Steady-state liquid output rate

Figure 2.7 through Figure 2.9 show the measured steady-state liquid output rates for the 100, 400, and 1250 liter per minute cyclones, respectively. Each series of points represents a single temperature (K) and relative humidity (%) condition as given in the chart legends.

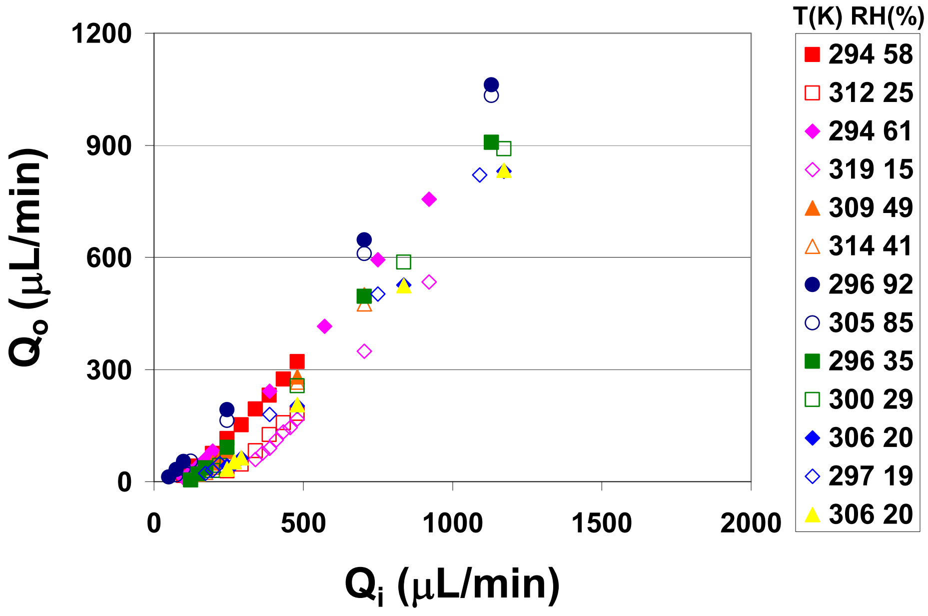

Figure 2.7: WWC-100 steady-state liquid output rate versus liquid input rate (μL/min) for various air temperature (K) and relative humidity (%)

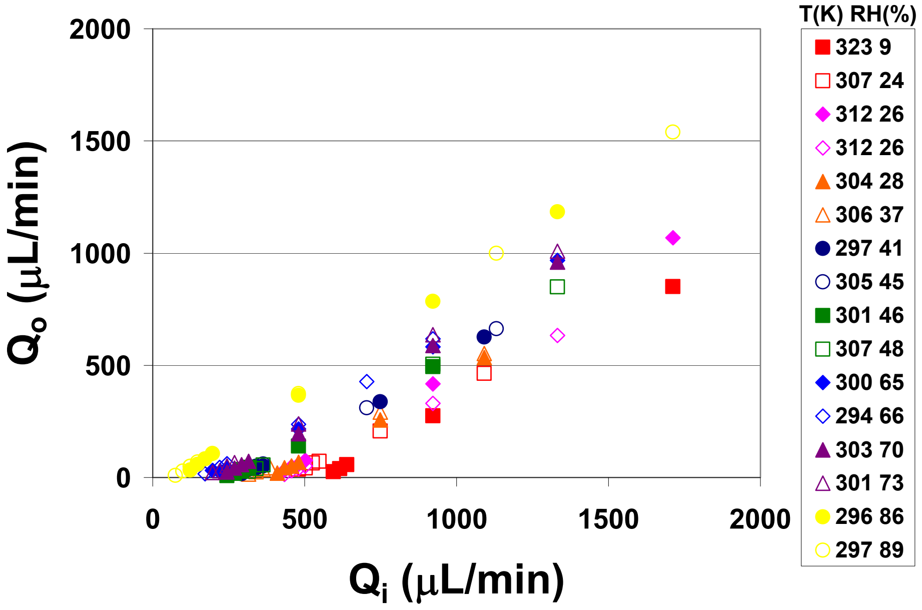

Figure 2.8: WWC-400 steady-state liquid output rate versus liquid input rate (μL/min) for various air temperature (K) and relative humidity (%)

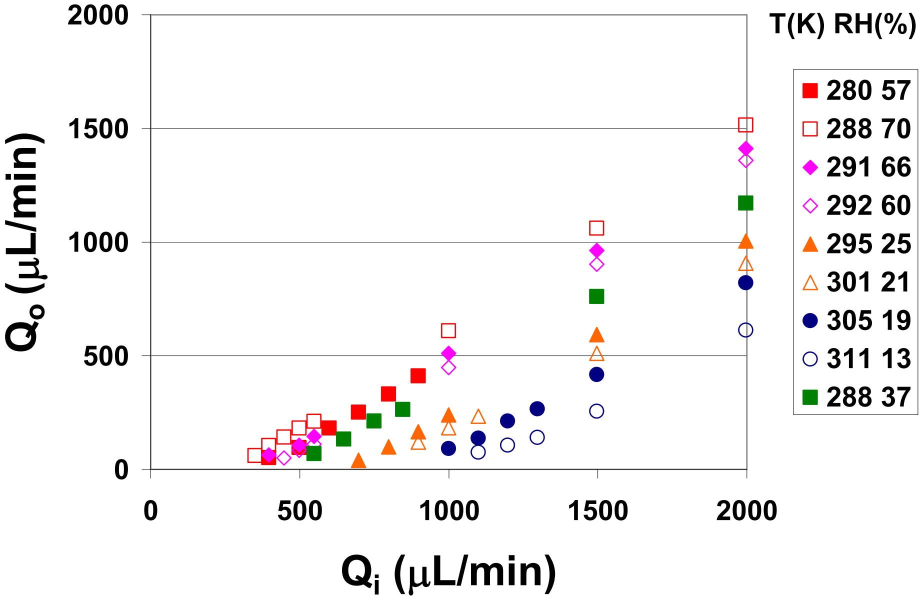

Figure 2.9: WWC-1250 steady-state liquid output rate versus liquid input rate (µL/min) for various air temperature (K) and relative humidity (%)

Uncertainty in the steady-state liquid output rate arises from using the two point measurement $\left(m_2 - m_1\right)/\left(t_2 - t_1\right)$ to calculate the steady-state liquid mass collection rate. With respect to Figure 2.4, liquid output rates were calculated from points at $t_1 = \tau \pm 5$ seconds and $t_2 = 300 \pm 5$ seconds. A least squares linear regression of the mass collected curve from $\tau \le t \le 300$ seconds was also performed and compared to the two point calculations. The estimated uncertainty in steady-state liquid output rate is approximately $\pm 2\%$.

### 2.2.3.3. Latency period

Figure 2.10 through Figure 2.12 show the latency period as a function of liquid input rate for 100, 400, and 1250 Lpm cyclones, respectively. Each individual point represents the average of three measurements at specific air conditions. Each series of points represents a different set of inlet air conditions. By definition the latency period is infinite at the critical liquid input rate and then decreases as the liquid input rate increases.  The latency period also increases with increasing air temperature and decreasing relative humidity.

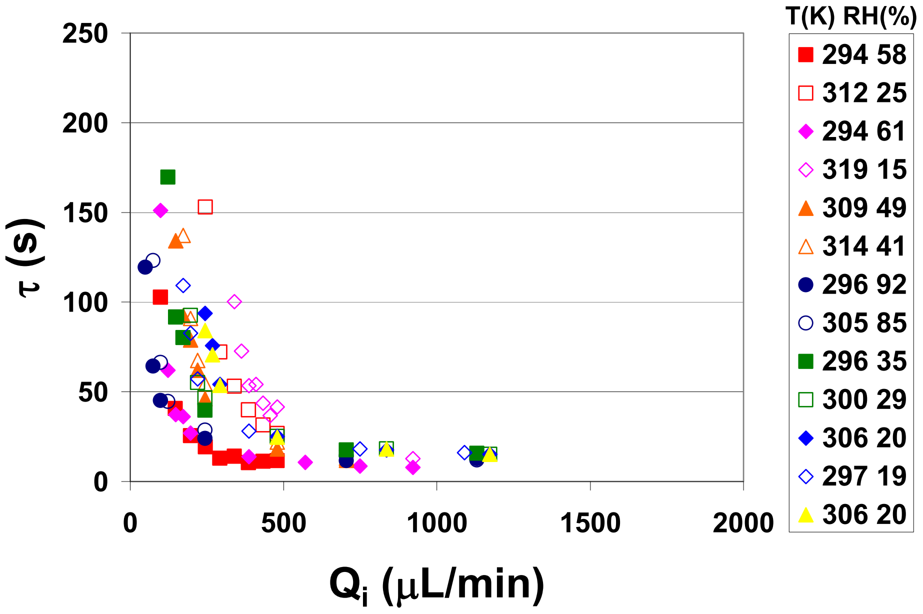

Figure 2.10: WWC-100 latency period (s) versus liquid input rate (μL/min) for various air temperature (K) and relative humidity (%)

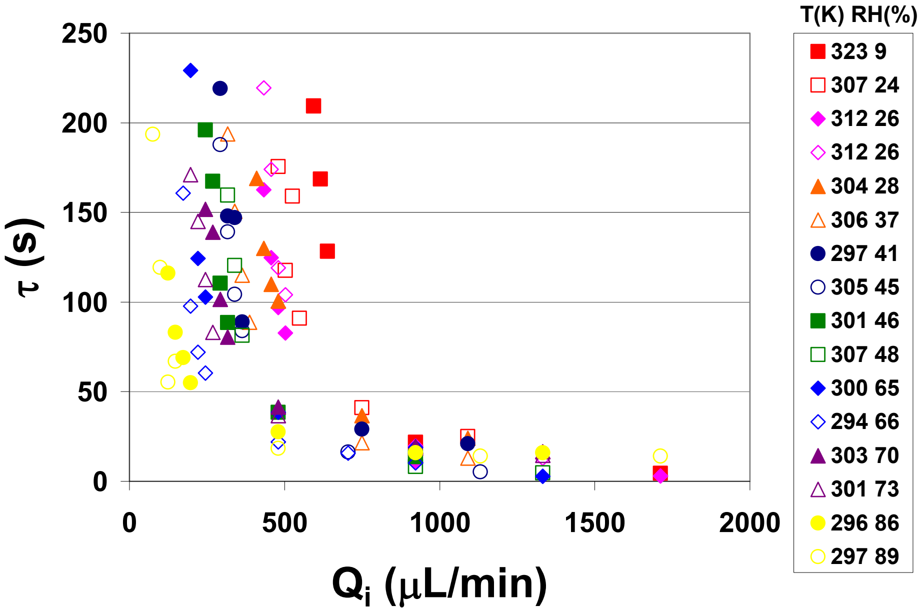

Figure 2.11: WWC-400 latency period (s) versus liquid input rate (μL/min) for various air temperature (K) and relative humidity (%)

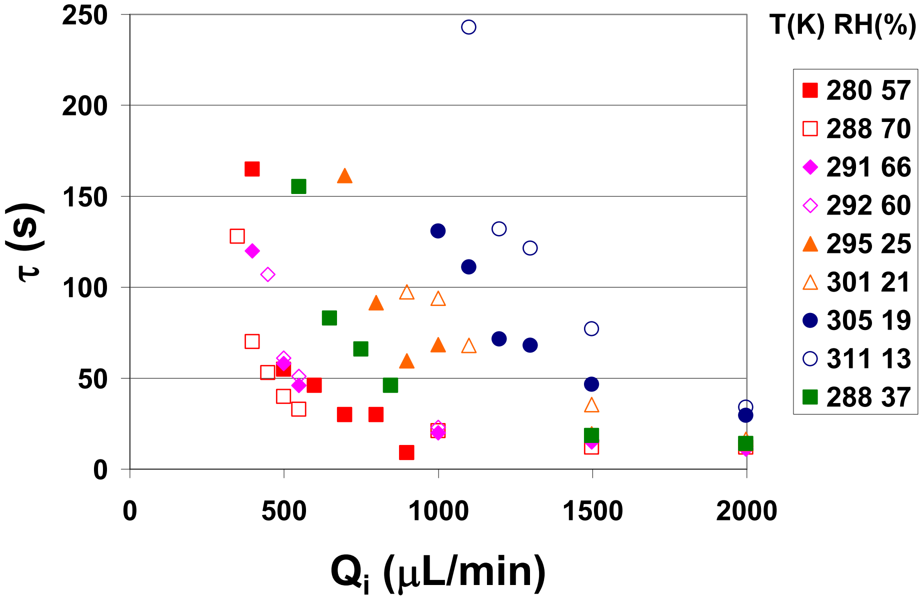

Figure 2.12: WWC-1250 latency period (s) versus liquid input rate (μL/min) for various air temperature (K) and relative humidity (%)

Each latency period data point in the above figures is the average of three individual measurements at the specified air conditions. Although not shown here, the standard deviation of those measurements increased as the liquid input rate approached the critical liquid input rate. The coefficient of variation (COV) is defined as the standard deviation of a data set divided by its average. Coefficients of variation near the critical liquid input rate were approximately 20-25%, i.e. standard deviations of 30-40 seconds. The COV then decreased to approximately 2% at large liquid input rates. This was observed for all air conditions and cyclones.

With respect to Figure 2.10, measured latency periods were typically 26 seconds greater than values shown in the figure. This was a result of using peristaltic scavenge pumps (experimental device) instead of the diaphragm scavenge pump (actual system device) to move the liquid through approximately 16 inches of tubing from the scavenge port to the mass scale. The value of 12 seconds, at $Q_l \approx 1200$ μL/min, was determined from fluorescent tracer studies described in Section 2.4.3. The actual system diaphragm scavenge pump and shorter scavenge lines were used to minimize the time required to travel from the scavenge port to the experimental measurement device. Measured latency periods were offset by a negative 26 seconds for the WWC-100 and WWC-400 since the same scavenge pump apparatus was used. WWC-1250 experiments were conducted with a larger peristaltic pump so the resulting time lag, and offset, was reduced to 10 seconds to match the minimum latency period of 12 seconds to the WWC-100 and WWC-400. One might expect the minimum latency period to be a function of cyclone geometry and air flow rate. However, dynamic scaling between all systems, and similarity between the 100 and 400 liter per minute system data suggest the WWC-1250 system should behave similarly. In conclusion, latency periods shown in Figure 2.10 through Figure 2.12 are representative of the deployed systems' performance, not the experimental systems.

### 2.2.3.4. Critical liquid input rate

A linear relationship between $Q_o$ and $Q_i$ is assumed for Figure 2.5. This assumption can cause error in the estimation of $m$, $b$, and $Q_c$ if not considered carefully. Slightly non-linear behavior near the critical liquid input rate causes the slope to be less than 0.91 in this region. Table 2.3 gives the linear regression parameters for regressions performed over different ranges of liquid input rates. The slope of the line is 0.73 when only $100 < Q_i < 200$ μL/min data are considered. The slope gradually increases as the regression is performed over a wider range of liquid input rates. All subsequent analyses for $m$, $b$, and $Q_c$ are based on data within the first 200-400 μL/min in excess of the critical liquid input rate. Using data in the low liquid input rate regime provides the most accurate estimation of the critical liquid input rate, the most critical parameter in describing WWC performance.

| $Q_i$ (μL/min) | m | b | $Q_c$ (μL/min) | dQc(%) |
|---|---|---|---|---|
| 100-1000 | 0.91 | -94 | 103 | 18 |
| 100-800 | 0.90 | -91 | 101 | 16 |
| 100-600 | 0.87 | -85 | 98 | 12 |
| 100-400 | 0.82 | -76 | 94 | 7 |
| **100-200** | **0.73** | **-63** | **87** | **0** |

Table 2.3: Error in m and b parameters associated with assumption of linear relationship between liquid input rate and output rate

Table 2.4 gives measured values of $m$, $b$, and $Q_c$ for the 100, 400, and 1250 Lpm cyclones, respectively, at each of the tested air conditions. Tables are sorted in order of increasing critical liquid input rate. The fractional collection, $m$, decreases as the air becomes hotter and drier with a nominal range of 50-90% for all cyclone air flow rates. The critical liquid input rate increases with increasing air temperature and air flow rate, and decreasing relative humidity. Measured ranges of the critical liquid input rate are $40 < Q_c < 265$, $90 < Q_c < 556$, and $291 < Q_c < 1016$ μL/min for the 100, 400, and 1250 liter per minute cyclones, respectively.

| WWC-100 | | | | |
|---|---|---|---|---|
| T (K) | RH (%) | m | b | $Q_c$ (μL/min) |
| 296 | 92 | 0.93 | -36 | 39 |
| 305 | 85 | 0.87 | -51 | 58 |
| 294 | 61 | 0.87 | -85 | 98 |
| 294 | 58 | 0.84 | -89 | 106 |
| 296 | 35 | 0.72 | -85 | 119 |
| 308 | 51 | 0.81 | -108 | 135 |
| 314 | 41 | 0.79 | -117 | 148 |
| 297 | 19 | 0.76 | -114 | 151 |
| 306 | 36 | 0.72 | -114 | 159 |
| 300 | 29 | 0.81 | -134 | 165 |
| 306 | 20 | 0.71 | -139 | 196 |
| 306 | 20 | 0.73 | -146 | 200 |
| 312 | 25 | 0.71 | -153 | 216 |
| 319 | 15 | 0.77 | -203 | 265 |

| WWC-400 | | | | |
|---|---|---|---|---|
| T (K) | RH (%) | m | b | $Q_c$ (μL/min) |
| 296 | 86 | 0.76 | -68 | 90 |
| 297 | 89 | 0.79 | -73 | 92 |
| 294 | 66 | 0.60 | -75 | 125 |
| 294 | 66 | 0.60 | -75 | 125 |
| 301 | 73 | 0.74 | -117 | 159 |
| 300 | 65 | 0.67 | -119 | 177 |
| 303 | 70 | 0.75 | -137 | 182 |
| 297 | 41 | 0.47 | -123 | 261 |
| 301 | 46 | 0.57 | -150 | 263 |
| 307 | 48 | 0.66 | -189 | 287 |
| 305 | 45 | 0.61 | -176 | 288 |
| 306 | 37 | 0.57 | -194 | 338 |
| 304 | 28 | 0.49 | -188 | 383 |
| 312 | 26 | 0.59 | -248 | 422 |
| 312 | 26 | 0.58 | -249 | 428 |
| 307 | 24 | 0.51 | -218 | 430 |
| 323 | 9 | 0.63 | -352 | 556 |

| **WWC-1250** | | | | |
|---|---|---|---|---|
| T (K) | RH (%) | m | b | $Q_c$ (μL/min) |
| 288 | 70 | 0.88 | -257 | 291 |
| 290 | 66 | 0.84 | -291 | 346 |
| 280 | 57 | 0.73 | -258 | 356 |
| 292 | 60 | 0.84 | -350 | 414 |
| 288 | 37 | 0.71 | -327 | 460 |
| 295 | 25 | 0.72 | -475 | 659 |
| 301 | 21 | 0.69 | -508 | 739 |
| 305 | 19 | 0.70 | -629 | 895 |
| 311 | 13 | 0.55 | -561 | 1016 |

Table 2.4: Fractional collection, $m$, and critical liquid input rate, $Q_c$, for all air temperature and relative humidity test conditions for the WWC-100, WWC-400, and WWC-1250

### 2.2.4. EMPIRICAL CORRELATIONS

Dimensionless performance parameters are formed from the critical liquid input rate. The dimensionless liquid output rate is given by

$$Q_o^* = \frac{Q_o}{Q_c} \tag{2.3}$$

and will be referred to as the collection ratio. The dimensionless liquid input rate

$$Q_i^* = \frac{Q_i - Q_c}{Q_c} \tag{2.4}$$

is formed as the dimensionless liquid input rate in excess of the critical liquid input rate. The actual liquid output rate is zero at $Q_i = Q_c$, thus $Q_o^* = 0$ at $Q_i^* = 0$. The physical significance of the excess liquid input rate is discussed in Chapter 4 in light of in-situ video observations of WWC internal multiphase flow patterns.

#### 2.2.4.1. Collection ratio

The collection ratio is plotted against the dimensionless liquid input rate in Figure 2.13 for all experimental data. Self similar behavior is observed. Rewriting (2.2) in terms of dimensionless parameters gives

$$Q_o^* = m \cdot Q_i^* \tag{2.5}$$

and provides the form of the fitting equation. The fractional collection, $m$, appears uncorrelated when plotted against the variables used here, e.g. $Q_i^*$, $Q_i - Q_c$, and air flow rate. More work is needed to determine the factors which influence the fractional collection. However, the dependence of $Q_o^*$ on the critical liquid input rate is much greater than the fractional collection and hence only an approximation to $m$ is required. A least squares regression of the data gives

$$Q_o^* = \left(0.7 + 0.01 \cdot Q_i^*\right) \cdot Q_i^* \tag{2.6}$$

where the fractional collection is weakly dependent on the dimensionless liquid input rate, $m\left(Q_i^*\right) = 0.7 + 0.01 \cdot Q_i^*$. The empirical correlation represents the data well with a coefficient of determination of $R^2 = 0.99$. A 95% confidence interval about the mean response is shown as a set of dashed lines in Figure 2.13 and has an average width of 0.06.

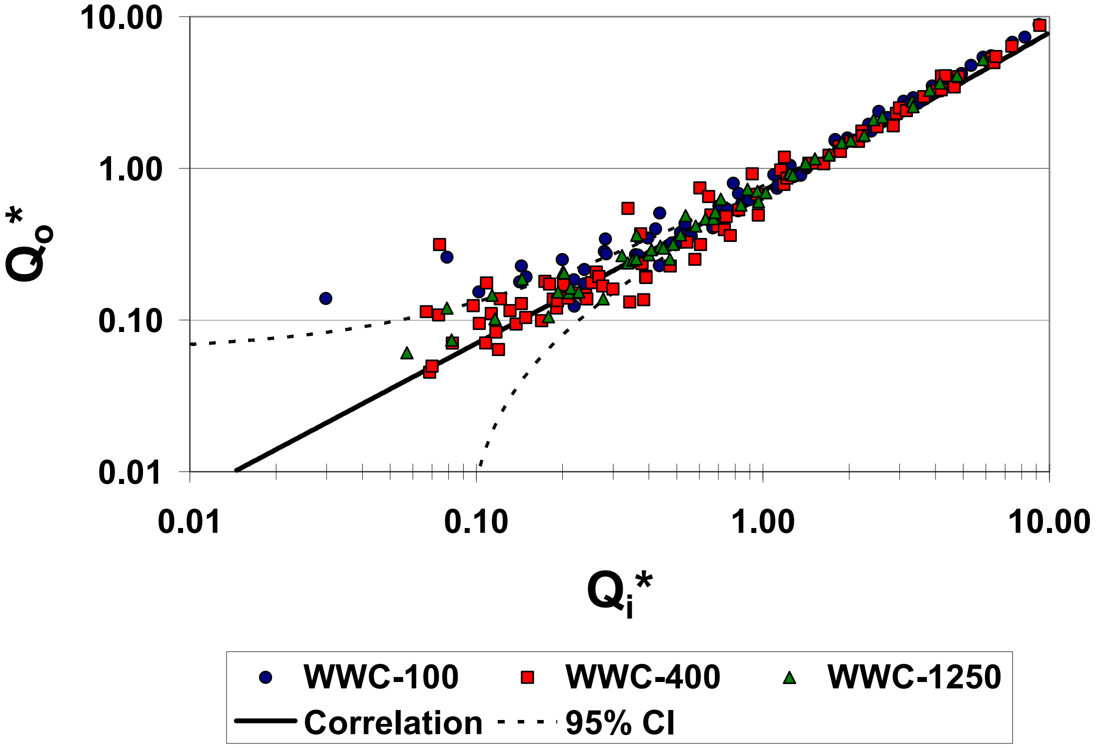

Figure 2.13: Collection ratio vs. dimensionless liquid input rate for WWC-100, WWC-400, and WWC-1250

### 2.2.4.2. Latency period

Self similar behavior is observed for latency period data plotted against the dimensionless liquid input rate in Figure 2.14. The latency period is infinite at $Q_i = Q_c$ or $Q_i^* = 0$. Hence, a fitting equation inversely proportional to the dimensionless liquid input rate was chosen to represent the data. A least squares regression on the latency period gives

$$\tau = \frac{22}{Q_i^*} + 9 \tag{2.7}$$

where the asymptotic value of 9 seconds was chosen such that the latency period at $Q_i^* = 10$ was 12 seconds in agreement with other experiments (Section 2.4.3).

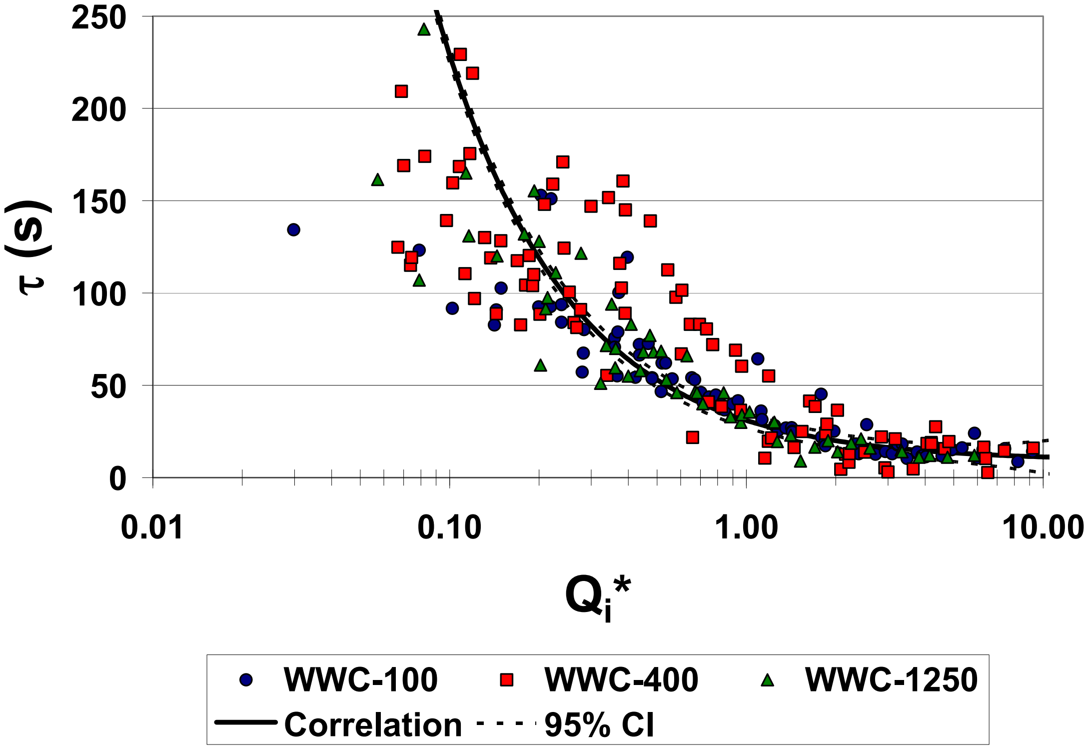

Figure 2.14: Latency period (s) vs. dimensionless liquid input rate for WWC-100, WWC-400, and WWC-1250

The coefficient of determination, $R^2$, for the latency correlation is 0.73. Points with $Q_i^* < 0.10$ were excluded from the analysis of $R^2$ due to infinite values of latency period near $Q_i^* = 0$ in the fitting equation. Errors between the experimental values and regression line were very large in this region and therefore excluded. A 95% confidence interval about the regression line is shown as dashed lines and has an average width of 10 seconds. However, significant variability is apparent near $Q_i^* = 0$. The standardized error of the regression line is approximately ± 50%. This error can be attributed to a lack of repeatability at fixed environmental conditions as well as the accuracy with which the critical liquid input rate is estimated.

Physical processes occurring at the solid-liquid and liquid-gas interfaces affect transient characteristics like the latency period. Contact angle hysteresis and the quasi-random nature of liquid travel along an imperfect surface are likely to cause significant variability in the latency period for constant air conditions as previously noted by COV's of 20-25% near $Q_i^* = 0$. This effect becomes insignificant as the excess liquid input rate becomes large. Section 2.4.2 and Chapter 4 provide more detailed descriptions of these effects. The accuracy with which the critical liquid input rate is predicted can also cause scatter about the empirical correlation shown in Figure 2.14. The magnitude of this error will be evaluated in the next section.

WWC-400 data exhibit greater variability compared to the 100 and 1250 liter per minute cyclones. Intermittent partial liquid bypass is a low probability, and largely unexplained, phenomena that can occur when liquid short circuits the skimmer and exits with the air stream rather than being siphoned at the scavenge port. Intermittent liquid bypass could be a random error associated with WWC-400 experiments. Inaccuracy in estimating the critical liquid input rate for the WWC-400 could also cause a higher degree of scatter. Under-estimation of the critical liquid input rate could cause $Q_i^*$ to shift to the right and would be a likely complication of erratic behavior due to intermittent partial bypass. Although low, the probability of intermittent liquid bypass should be studied in future works.

#### 2.2.4.3. Fractional collection and critical liquid input rate

Empirical correlations show the collection ratio and latency period can be described, for all air conditions and cyclone air flow rates, by characterizing the dependence of critical liquid input rate on these parameters. Multivariate linear regressions were performed on $m$, $b$, and $Q_c$ over air temperature (K) and relative humidity (%) for the each of the individual sets of cyclone data given in Table 2.4. For each cyclone, the parameters were assumed to be linear functions of temperature and relative humidity

$$m = C_1 \cdot T + C_2 \cdot RH + C_3 \tag{2.8}$$

$$b = C_4 \cdot T + C_5 \cdot RH + C_6 \tag{2.9}$$

$$Q_c = C_7 \cdot T + C_8 \cdot RH + C_9 \tag{2.10}$$

where the $C$'s are constants. The matrix based method of least squares regression described in Montgomery and Runger (2003) was used to determine the partial regression coefficients $C_1$ through $C_9$ from the data. The regression constants are given in Table 2.5. Only the regression for $Q_c$ will be discussed here since it is of most value in describing the overall liquid collection behavior through empirical correlations (2.6) and (2.7).

| | WWC-100 | WWC-400 | WWC-1250 | |
|---|---|---|---|---|
| $C_1$ | -0.00029 | 0.01389 | 0.00121 | **m** |
| $C_2$ | 0.00246 | 0.00654 | 0.00436 | |
| $C_3$ | 0.77175 | -3.91897 | 0.20640 | |
| $R^2$ | 0.75 | 1.00 | 0.77 | |
| $\sigma$ | 0.04 | 0.00 | 0.06 | |
| $C_4$ | -2.13497 | -7.37303 | -7.39956 | **b** |
| $C_5$ | 1.25049 | 1.07730 | 3.13444 | |
| $C_6$ | 483.63354 | 2022.12762 | 1645.70096 | |
| $R^2$ | 0.89 | 1.00 | 0.92 | |
| $\sigma$ | 15.1 | 35.9 | 44.6 | |
| $C_7$ | 2.89833 | 6.64500 | 13.96400 | **$Q_c$** |
| $C_8$ | -1.87786 | -4.07200 | -6.20600 | |
| $C_9$ | -654.96255 | -1543.00000 | -3285.00000 | |
| $R^2$ | 0.93 | 0.99 | 0.97 | |
| $\sigma$ | 17.1 | 15.2 | 49.6 | |

Table 2.5: Multivariate linear regression coefficients, coefficients of determination, and standard deviations for $m$, $b$, and $Q_c$ for the WWC-100, WWC-400, and WWC-1250

The total derivative of the critical liquid input rate,

$$dQ_c = \frac{\partial Q_c}{\partial T} dT + \frac{\partial Q_c}{\partial RH} dRH \tag{2.11}$$

contains partial derivatives that give the relative rates of change of $Q_c$ corresponding to unit changes in the independent variables, $T$ and $RH$. An increase in air temperature increases the critical liquid input rate, $\partial Q_c / \partial T > 0$. Increasing relative humidity results in reduced evaporative effects, hence $\partial Q_c / \partial RH < 0$. A ratio of the partial derivatives shows a unit change in temperature results in a 1.5-2.25 times greater change in the critical liquid input rate than a unit change in relative humidity. However, a 10 Kelvin change in ambient air temperature represents a significant change whereas a 10% change in relative humidity is relatively modest. This analysis suggests diurnal changes in relative humidity will affect liquid collection to a greater degree than temperature.

Coefficients of multiple determination, $R^2$ were determined to be 0.93, 0.99, and 0.97, for the 100, 400, and 1250 Lpm cyclones, respectively. High coefficients of multiple determination indicate that temperature and relative humidity are an adequate set of parameters, for fixed air flow rate, to characterize the critical liquid input rate. The standard deviations of model error are also given in Table 2.5. Empirical correlation error for $Q_c$ is approximately 10-20% and affects calculations of $Q_i^*$. Thus, scatter in Figure 2.14 caused by $Q_c$ prediction is of similar magnitude to variability in latency period measurements.

Multivariate linear regression models were evaluated by their standardized residuals, $d_i = e_i / \sigma$, where $e_i$ is the difference in data and model prediction, and $\sigma$ is the error standard deviation. All values fell between $-2 < d_i < 2$ indicating the absence of outliers. Standardized residuals are traditionally plotted against the independent variable to identify trends which may identify model insufficiency. The effects of temperature and relative humidity are not easily decoupled. Thus, the dimensionless critical liquid input rate is plotted on the abscissa because it is a joint measure of air conditions. For example, with respect to Table 2.4, the standardized residual for $Q_c = 39$ was plotted at $Q_c{*} = 39/265$. Plots of the standardized residuals for the WWC-100 and WWC-1250 appear to be approximately normally distributed about zero. This implies no higher order terms were required to describe the behavior. The linear model adopted here was reasonably justified given the data. However, the WWC-400 data could be described as possessing a modest “u” shape which could imply model inadequacy. It is doubtful the WWC-100 and WWC-1250 data could be explained with linear models whereas non-linear behavior exists in the WWC-400. The occurrence of intermittent partial liquid bypass may be responsible for the trend observed here.

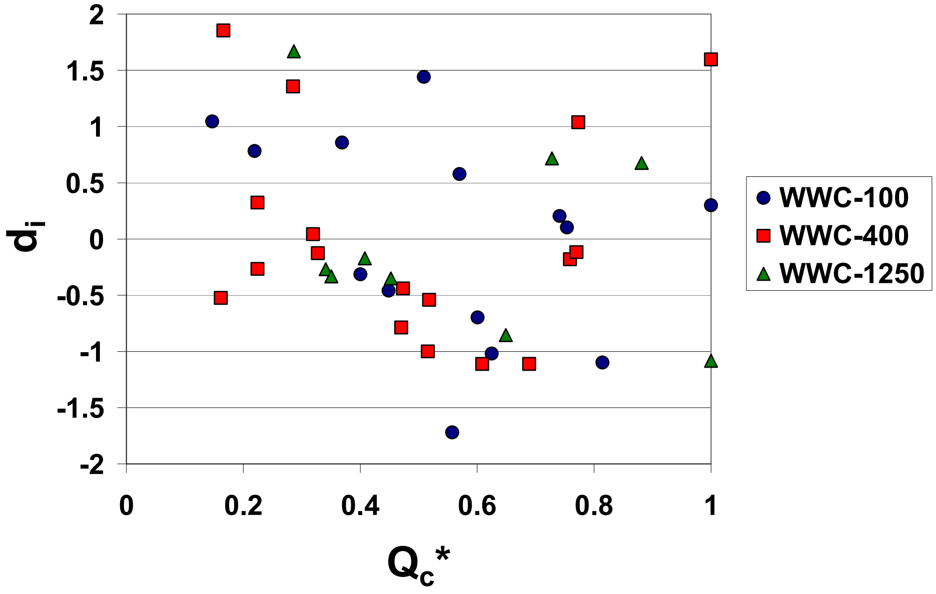

Figure 2.15: Standardized residuals for multivariate linear regressions performed on the critical liquid input rate over temperature and relative humidity

Figure 2.16 shows experimental $Q_c$ data points as well as regression planes plotted for $280 < T < 320$ K, and $0 < RH < 100$ % with the 100, 400, and 1250 Lpm cyclones taking on values from smallest to largest, respectively. The regression planes predict critical liquid input rate minima of 0, -25, and 150 μL/min and maxima of 250, 600, and 1200 μL/min for the 100, 400, and 1250 Lpm cyclones, respectively. The empirical model does not adequately describe behavior near saturated conditions since data points are absent in this region. The critical liquid input rate is expected to approach zero for saturated conditions, $RH = 100\%$.

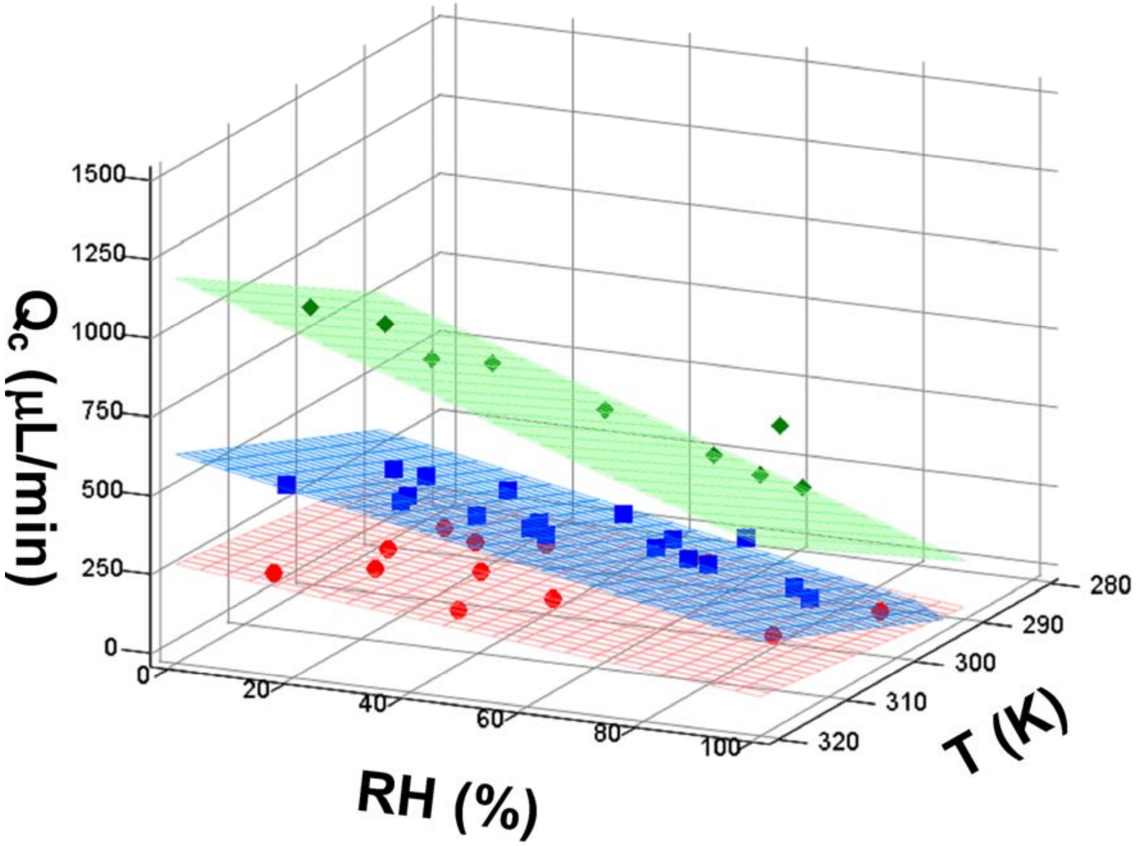

Figure 2.16: Critical liquid input rate (µL/min) vs. air temperature (K) and relative humidity (%): Experimental data points and multivariate linear regression planes for WWC-100, WWC-400, and WWC-1250

## 2.3. WWC-100 Autonomous Ambient Air Sampling

The practical utility of the empirical models described above is their ability to provide autonomous system control over the desired liquid output rate, $Q_{o,desired}$, by adjusting the required liquid input rate, $Q_{i,required}$. Rearranging (2.2) for the liquid input rate gives

$$Q_{i,required}(T,RH,Q_{air}) = \frac{Q_{o,desired} - b(T,RH,Q_{air})}{m(T,RH,Q_{air})} \tag{2.12}$$

where the regression parameters account for the conditions of the sampled air and air flow rate of the cyclone. Cyclone system control software was updated to take measurements of air temperature and humidity, determine the regression parameters from the coefficients listed in Table 2.5, and adjust the liquid input rate to obtain a specified liquid output rate. These system modifications enable constant liquid output rate delivery over a wide range of air conditions that are typically experienced during the diurnal cycle.

### 2.3.1. EXPERIMENTAL APPARATUS

System controller and data acquisition software described above was modified to autonomously calculate the required liquid input rate according to (2.12), execute a sample, and measure the liquid output rate while sampling ambient air. The WWC-100 inlet was vented to the outside of the laboratory building with 3 inch flexible duct and window mounted duct fittings. A sensor housing was constructed out of 3 inch PVC connected directly upstream of the cyclone inlet with PVC reducers and flexible couplers. The temperature probe was inserted through the side of the sensor housing perpendicular to the direction of air flow. This experiment was only performed on the WWC-100 system as a proof-of-concept for controlling the liquid output rate based on the empirical model.

### 2.3.2. EXPERIMENTAL PROCEDURE

The desired liquid output rate was specified at the beginning of each set of trials. Microfluidic output rates of 50, 40, and 25 μL/min were specifically chosen to determine the capability of the empirical model to deliver highly concentrated hydrosols. The blower was turned on three minutes prior to each sample and allowed the temperature and relative humidity probe to equilibrate to the air conditions flowing through the inlet duct and sensor housing. The WWC controller calculated the liquid input rate required and executed a 5 minute liquid collection sample. The latency period and liquid output rate were calculated after each sample and the controller waited 30 minutes to repeat the sampling procedure.

Several inlet air filters were tested to minimize accumulation of ambient dust and dirt inside the cyclone. However, including filters required system modifications, i.e. blower replacement and air flow rate matching to the original system. This was viewed as a non-negligible departure from the system as characterized experimentally. Therefore, filters were omitted and the cyclone was disassembled and cleaned after each set of trials.

### 2.3.3. DATA

Figure 2.17 shows the actual liquid output rate obtained versus sample number for the test in which the desired liquid output rate was 25 μL/min. Air temperatures, relative humidity, and dew point temperatures are observed to vary during the diurnal cycle. The system controller adjusted the liquid input rate, prior to the start of each sample, to maintain the desired output rate in spite of changing air conditions. The algorithm successfully maintained the desired liquid output rate over a wide range of ambient conditions.

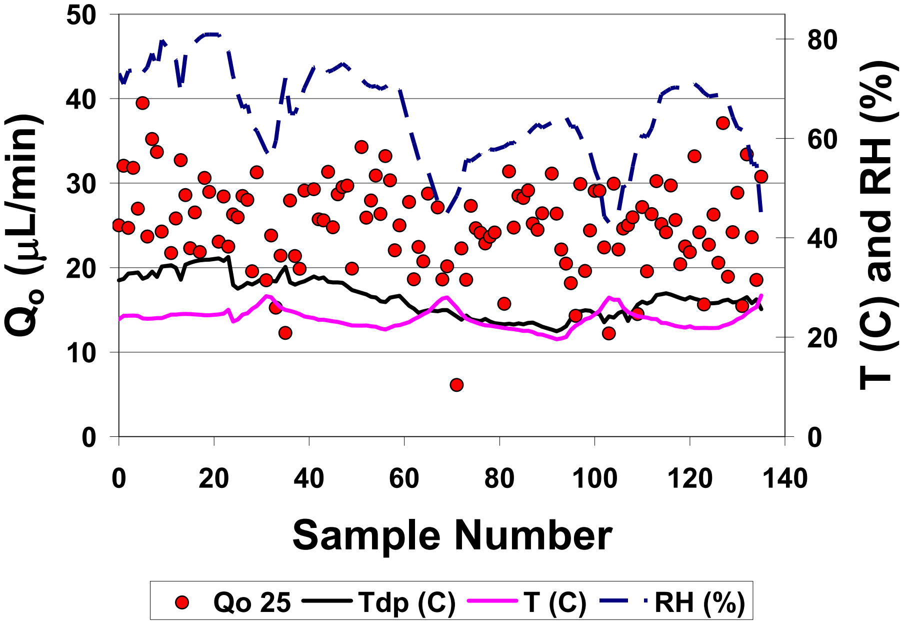

Figure 2.17: Actual liquid output rate obtained with the WWC-100 while sampling ambient air with a specified desired liquid output rate of 25 μL/min

Table 2.6 gives summary statistics for all ambient air sampling tests. A total of 307 individual liquid collection samples were executed for desired liquid output rates of 50, 40, and 25 μL/min. The set of air temperatures and relative humidity experienced during sampling was broad, 16.8 to 29.9°C, and 10.3 to 80.9%. These conditions correspond to dew point temperature minimum and maximum of -5.9 and 21.3. The latency period ranged from 87.0 and 261.6 seconds. The required liquid input rates ranged from 84 to 264 μL/min corresponding to collection ratios of 0.1 to 0.3, respectively. The mean, actual liquid output rates for desired output rates of 50, 40, and 25 μL/min were 47.5, 46.5, and 25.1 μL/min, respectively; excellent control over liquid output rate was achieved.

|  | $Q_{o,desired}$ (μL/min) |  |  |
|---|---|---|---|
|  | 50 | 40 | 25 |
| Number of Samples |  |  |  |
|  | 109 | 72 | 126 |
| Air Temperature (C) |  |  |  |
| Mean | 24.6 | 21.1 | 23.7 |
| Standard Deviation | 1.9 | 3.4 | 1.9 |
| Range | [21.4,29.9] | [16.8,29.3] | [19.6,28.4] |
| Relative Humidity (%) |  |  |  |
| Mean | 58.0 | 25.4 | 64.8 |
| Standard Deviation | 8.4 | 7.5 | 9.3 |
| Range | [39.6,71.0] | [10.3,36.6] | [43.1,80.9] |
| Dew Point Temperature (C) |  |  |  |
| Mean | 15.6 | -0.3 | 16.5 |
| Standard Deviation | 1.8 | 2.2 | 2.3 |
| Range | [11.5,18.6] | [-5.9,3.5] | [12.5,21.3] |
| Latency period (s) |  |  |  |
| Mean | 110.7 | 125.8 | 190.3 |
| Standard Deviation | 12.1 | 16.3 | 27.1 |
| Range | [87.0,155.9] | [94.0,168.1] | [126.0,261.3] |
| $Q_{i,required}$ (μL/min) |  |  |  |
| Mean | 153.8 | 201.0 | 108.9 |
| Standard Deviation | 20.7 | 27.8 | 19.8 |
| Range | [128.4,201.2] | [162.6,263.9] | [84.4,162.6] |
| $Q_{o,actual}$ (μL/min) |  |  |  |
| Mean | 47.5 | 46.5 | 25.1 |
| Standard Deviation | 4.9 | 5.0 | 5.4 |
| Range | [31.9,57.9] | [30.6,55.4] | [6.1,39.5] |
| $\Delta Q_{out}/\sigma Q_{out}$ |  |  |  |
| Mean | 0.0 | -1.8 | 0.5 |
| Range | [-2.1,3.1] | [-3.8,1.3] | [-2.8,3.1] |

Table 2.6: Test data for WWC-100 ambient air sampling trials with specified desired liquid output rates of 50, 40, and 25 μL/min

The mean standardized residuals, $d_i$, were calculated for each set of data to provide an overall estimate of performance. The data sets for desired liquid output rates of 50 and 25 μL/min show excellent effectiveness, $|d_i| < 0.5$, of the control algorithm. The accuracy error associated with the 40 microliter per minute desired output rate is somewhat higher than the others although still considerably close to the specified target.

This may be attributable to lower dew point temperatures experienced for this particular test.

Data for all desired liquid output rates were plotted against the dew point temperature in Figure 2.18. The vertical dashed lines represent the dew point temperature limits of laboratory experiments, 29.0 and -1.0°C. The control algorithm was based on measurements within these limits. Dew point temperatures experienced during the $Q_{o,desired} = 40$ ambient air tests were close to, or below, the temperatures on which the algorithm was based. Additional regression points for cool and dry air conditions would increase accuracy in this range and would most likely have brought the mean, actual liquid output rate closer to 40 μL/min.

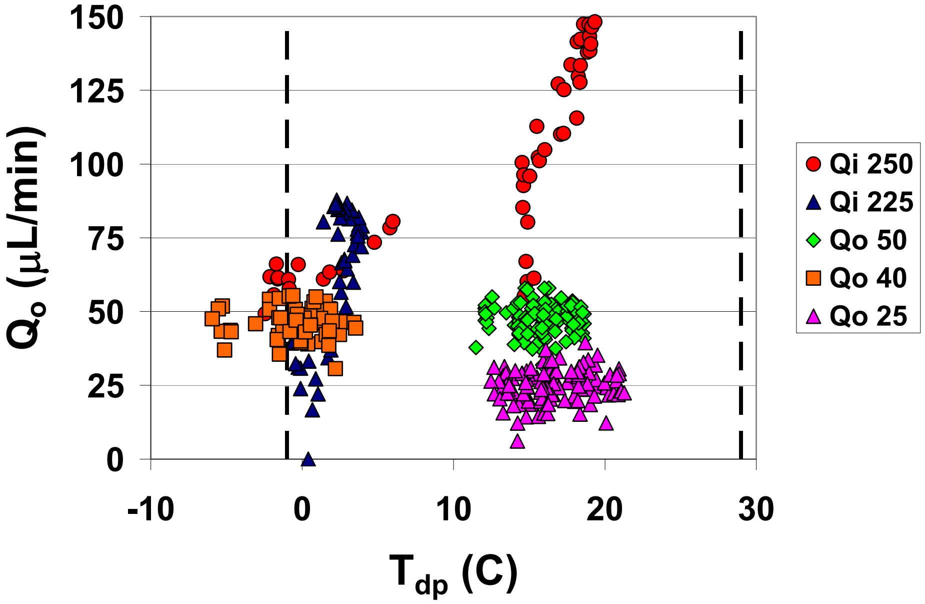

Figure 2.18: Actual liquid output rates for controlled experiments with specified output rates of 50, 40, and 25 μL/min, and uncontrolled experiments with specified liquid input rates of 250 and 225 μL/min

Additional ambient air sampling tests were conducted without the use of the liquid input rate control algorithm. This is equivalent to the user arbitrarily choosing a liquid input rate and accepting the liquid output rates as affected by ambient air conditions. Figure 2.18 shows data for two experiments in which constant liquid input rates of 250 and 225 μL/min were specified knowing these input rates would produce liquid output rates on the order of 50 μL/min for some air conditions.

### 2.3.4. ANALYSIS

Figure 2.18 illustrates the advantage of implementing open loop control from WWC-100 empirical models. Liquid output rates for the uncontrolled device are as high as 150 μL/min. Delivering hydrosols of substantially reduced bioagent concentration (~1/6) reduces the probability of detection. Some proportion of hydrosol would likely go unanalyzed or necessitate the addition of a pre-detector hydrosol concentration stage, adding to the complexity of the detector, delaying the response time, and forcing viable organisms to go through additional system components. Several liquid collection samples at low relative humidity also failed to deliver liquid output. This result is seen as a system failure since hydrosol must be collected for subsequent analysis.

Ambient air sampling test data are compared to empirical self-similar profiles in Figure 2.19 and Figure 2.20. Dimensionless liquid input rates for ambient automated tests were between 0.2 and 0.8. The latency periods from ambient tests appear slightly shifted to the right of points from the laboratory tests. However, the degree of scatter is well within that expected from analysis of experimental data. One possible explanation is that the system air flow rate was adjusted and reset from laboratory to ambient air tests. The speed with which liquid moves through the cyclone is governed by the air flow field and surface physics. Although minor, differences in air flow rate could have non-trivial effects on transient multiphase flow characteristics like the latency period. The ambient air sampling test collection ratio data, Figure 2.20, are more evenly scattered about the regression line.

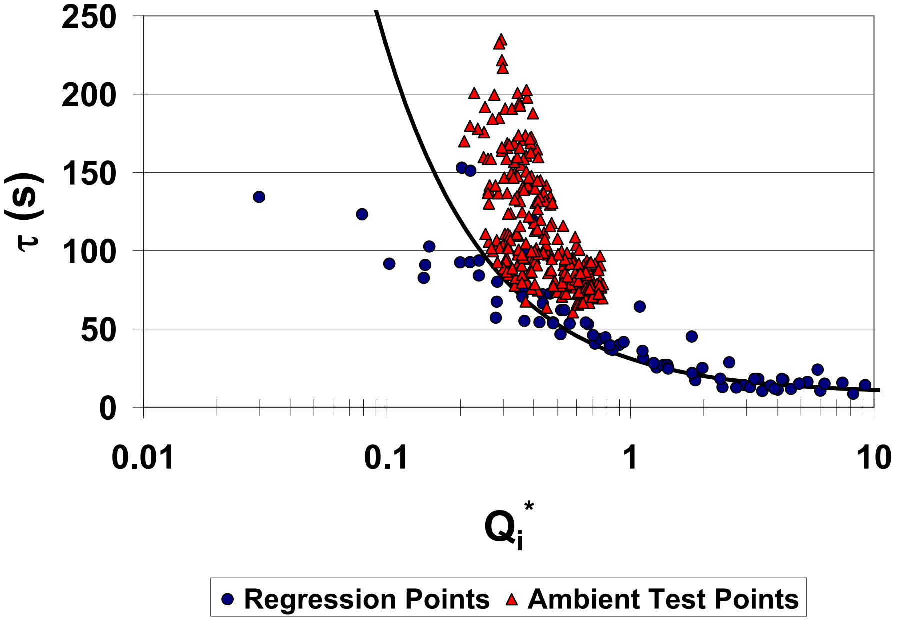

Figure 2.19: WWC-100 ambient automated test latency periods and laboratory automated test latency periods plotted against the dimensionless liquid input rate

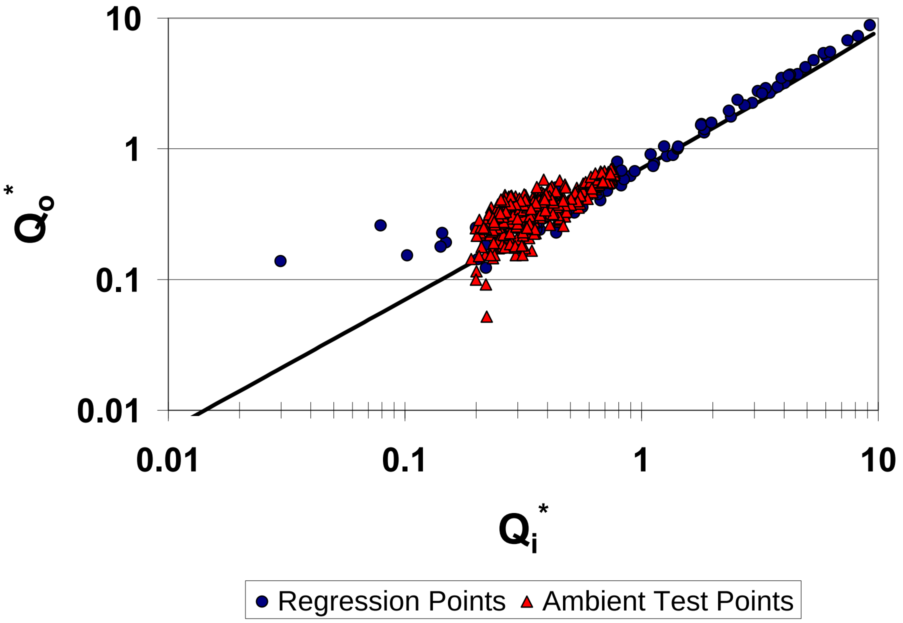

Figure 2.20: WWC-100 ambient automated collection ratios and laboratory automated collection ratios plotted against the dimensionless liquid input rate

Ambient air sampling test data were used to supplement data taken in the laboratory. Critical liquid input rate data from laboratory experiments are shown in Figure 2.16. The fourteen measurements taken in the laboratory represent a significant time investment since the air conditioning system had to be manipulated and brought to steady-state operation prior to each test. Utilizing changes in ambient air conditions provided a broad range of test points and was achieved without experimenter interaction. Equation (2.6) was rearranged for $Q_i^*$ and the critical liquid input rate was calculated for each of the ambient automated test data points. Figure 2.21 shows back-calculated ambient air sampling test $Q_c$ data plotted along with the laboratory test data and multivariate regression plane. Multiple samples performed over a large span of air conditions, some difficult to produce experimentally, are easily achieved by taking advantage of atmospheric air conditioning.

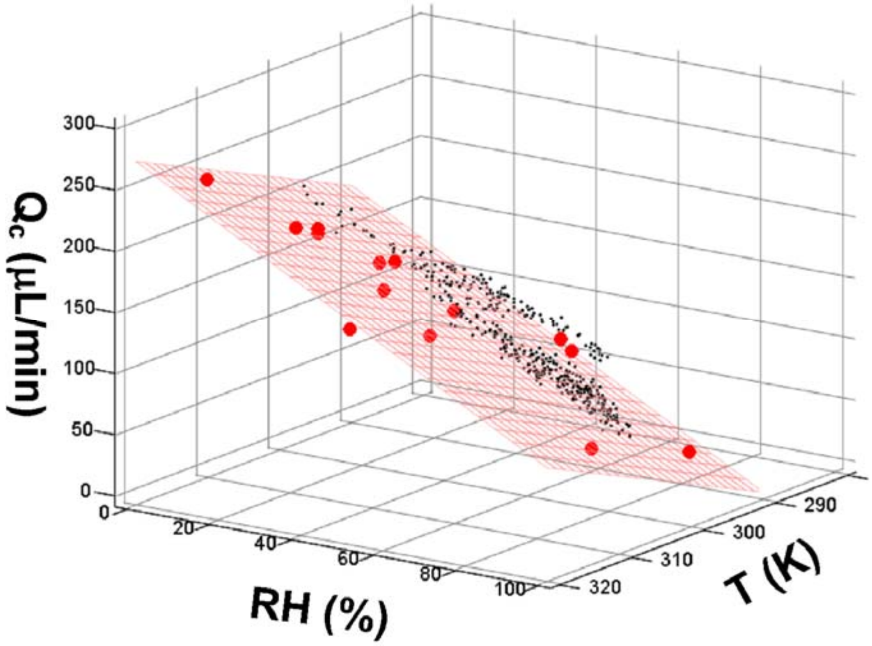

Figure 2.21: Back calculated critical liquid input rate values from WWC-100 ambient automated tests

Finally, a unique and advantageous characteristic of the WWC-100 was discovered when transient mass collection profiles were plotted for 50 and 25 microliter per minute output ambient air sampling tests. Figure 2.22 shows the discrete nature of liquid output. Liquid output is a series of droplets rather than a continuous stream. The steady-state liquid output rate can still be reasonably approximated as steady due to the consistent time period between droplets. Liquid output rates of 50 and 25 µL/min correspond to total collection volumes of approximately 225 and 95 microliters, respectively, for these two samples. The total volumes are quantized into roughly 30 and 10 droplets, respectively, providing an average hydrosol droplet volume of 7 to 10 microliters delivered at an accurate and precise rate. This is a very promising discovery when considering the ability of Lab on chip (LoC) devices to process discrete droplets quickly and efficiently.

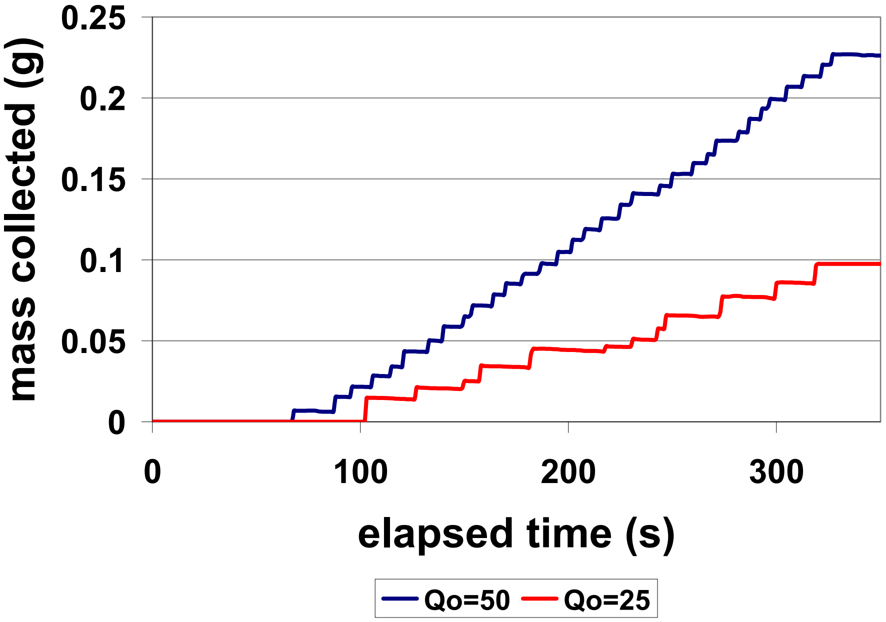

Figure 2.22: Transient mass collection profiles for liquid collection rates of 50 and 25 μL/min from WWC-100 ambient tests

Accurate and precise microfluidic output rate control demonstrated here lends to a comparison of the WWC-100 system to other advanced bioaerosol wet collectors. The concentration rate (min$^{-1}$) is a parameter defined as the ratio of bioaerosol concentrations in the liquid sample and air stream per unit time of air sampling. This is reasonably approximated as the collector air flow rate multiplied by the collector efficiency divided by the sample volume, or the ratio of the air flow and liquid output rates. Bioaerosol collector systems with varying air flow rates and liquid sample volumes are compared with this parameter. Han and Mainelis (2008) give a review of the concentration rates for commercially available bioaerosol collectors, e.g. Biosampler (SKC Inc.). Their calculations show concentration rates on the order of 100 to 100,000 for commercially available portable systems, and a substantial increase to rates above 1,000,000 with their super-hydrophobic electrostatic precipitator. Theoretical WWC-100 maximum concentration rates can be calculated for liquid output rates of 50 and 25 μL/min. Concentration rates for these samples would be on the order of 1,000,000-2,000,000. This is a substantial increase over the portable samplers referenced by Han and Mainelis (2008) and on par with their super-hydrophobic electrostatic precipitator.

## 2.4. WWC-100 Fluorometric Liquid Recovery Study

### 2.4.1. FILM ENTRAINMENT

Liquid mass transfer in the wetted-wall cyclone has been largely attributed to evaporation at the air-water interface. Anecdotal evidence suggests there may be other mechanisms responsible for incomplete recovery of the collection liquid. In situ visual observations of the multiphase flow have been made using a borescope (Hawkeye Slim, Gradient Lens Corporation). Liquid has been observed to collect on the backside of the inlet slot and appears to be sheared off by the air flow. This is referred to as liquid reaerosolization. Liquid reaerosolized into the gas core could contribute to incomplete hydrosol recovery and was therefore studied.

A review of the literature provides evidence of liquid entrainment in two-phase co-annular film flows. This field of study is primarily concerned with correlating entrainment and deposition rates of droplets from the core of gas-film flows. Empirical models have been developed for heat and mass transfer augmentation, critical heat flux (CHF), and post dryout heat transfer, for nuclear power applications (Chun et al., 2006). The seminal work of Ishii and Grolmes proposed liquid entrainment from the film surface was mostly attributed to the shearing off of roll wave crests by the gas phase (1975).

Wave under-cutting and bubble bursting can also occur in other flows due to the complex transfer of momentum between the liquid and gas phases (Ishii and Grolmes, 1975; Kim and Peterson, 1995). Entrainment inception criteria and equilibrium entrainment fractions are well correlated to dimensionless parameters such as the film Reynolds number, $Re_f$, a ratio of inertial to viscous forces in the liquid, and the gas phase Weber number, $We$, a ratio of gas phase inertial forces to surface tension forces (Ishii and Grolmes, 1975; Sawant et al. 2008; Katoaka et al., 2000).

A study was designed to determine the relative magnitudes of evaporation and the combined effects of reaerosolization and entrainment. The double film extraction method is sometimes used for such a study (Okawa et al., 2005). However, less intrusive tracer methods can be used to perform mass balances that quantify the relative fractions of liquid lost to latent heat transfer and entrainment. This was accomplished here by tagging the liquid input with a fluorescent tracer similar to the work of Schadel et al. (1990). For example, 10 mL of tagged liquid are injected into the cyclone and 5 mL are recovered. A recovered liquid concentration twice that of the input would reveal no entrainment occurred and the solute remained in the film while the solvent evaporated into the air-stream. The outlet air-stream was filtered in this study to ensure a complete accounting of fluorescent tracer mass. Only the WWC-100 was studied here due to time constraints. Similar behavior is expected in the WWC-400 and WWC-1250 because of similarity observed in gravimetric liquid collection experiments.

#### 2.4.1.1. Experiment

Cyclone liquid input was tagged with fluorescein disodium salt (Acros 17324-1000), commonly known as uranine or sodium fluorescein. This particular form of sodium fluorescein was chosen for its solubility in water. A sodium fluorescein solution with concentration of 0.3 μM was prepared with distilled water. The test solution was then atomized into the cyclone at liquid input rates ranging from 200-1000 μL/min. Hydrosol recovery, by volume or rate, is significantly lower in the low liquid input rate range, and was therefore emphasized to provide the highest probability of quantifying tracer loss and liquid entrainment.  A 47 mm in-line aluminum filter holder (1235, Pall Corporation) and 47 mm A/D fiberglass filter (66224, Pall Corporation) were integrated into the system in between the cyclone exhaust and blower inlet to capture any entrained droplets or solute condensation nuclei.  The original cyclone system blower was replaced with a larger model to ensure the flow rate was equal to the original system with the added pressure drop of the filter.

Each test consisted of two parts: one sample with 20 mL of tagged liquid injected at a constant rate ranging from 200-1000 μL/min, and a second sample with 15 mL untagged distilled water injected at 1000 μL/min to wash the cyclone of any residual tracer.  Large tagged liquid input volumes were required to produce samples of at least 10 mL for subsequent analysis without additional dilution.  Liquid samples recovered from the skimmer section were collected in 15 mL test tubes and the total mass of liquid recovered was measured with the AB104-S mass scale.  The liquid sample was then divvied up into 3 mL aliquots in 12 mm glass culture tubes for fluorometric analysis. The outlet filters were placed in 60 mL wide mouth jars and eluted with 10 mL of water for 12 hours.  The resulting filter solutions were also divided into 3 mL aliquots and placed in culture tubes.

The dependence of uranine fluorescence on pH was witnessed here during data analysis.  Dissolution of dirt or trace gases in the sample liquid most likely caused small changes in sample pH and ultimately led to unexplainable mass imbalances on the order of -30%.  Kesavan et al. show the fluorescent intensity to be highly dependent on pH near neutral conditions (2001).  Fluorescence reaches its asymptotic maximum near a pH of 8 with near constant fluorescence at greater pH. Thirty microliters of 0.01M NaOH were added to each sample culture tube to force the pH to 10 and ensure all samples were out of the range of pH dependence.

A digital filter fluorometer (FM109535, Turner Quantech) was used to measure the mass concentration of sodium fluorescein in all liquid samples. The maximum excitation wavelength of sodium fluorescein is approximately 490 nm, therefore, a narrow band 490 nm wavelength excitation filter (NB490, Turner Quantech) was used in the fluorometer. The maximum emission wavelength of sodium fluorescein is approximately 515 nm. A sharp-cut, long-pass, 515 nm wavelength filter (SC515, Turner Quantech) was used as the emission filter. The fluorometer was used on the raw fluorescence (mode II) setting. This setting eliminates the need for formal calibration curves to known mass concentrations by providing all measurements of fluorescent intensity units ( $FIU$ ) relative to a reference solution. The reference solution was chosen with concentration approximately 16 times the injected test solution such that no test samples would exceed the reference. The fluorometer automatically sets the internal gain according to the concentration of the reference. Distilled water was used as the blank reference.

The intensity of the fluorescent signal is proportional to the sodium fluorescein mass concentration in the absence of multiple scattering. This is a reasonable assumption for dilute solutions and was checked by preparing serial dilutions of the test solution. All collected samples were compared to the liquid input as the ratio of sodium fluorescein mass in the sample and input solutions,

$$\eta = \frac{C_s \cdot m_s}{C_i \cdot m_i} = \frac{FIU_s \cdot m_s}{FIU_i \cdot m_i} \tag{2.13}$$

where $m$ and $C$ represent mass and mass concentration, and the subscripts $i$ and $s$ refer to input and sample solutions, respectively. This computation provides the percentage of tracer mass in an unknown sample with respect to the total tracer mass injected into the cyclone and will be referred to as the uranine mass fraction.

#### 2.4.1.2. Data

Figure 2.23 and Figure 2.24 show the average liquid volume fractions and average uranine mass fractions for the tests described above. Two tests each were conducted at liquid input rates of 200, 250, 300, and 400 μL/min and four tests at 1000 μL/min. The recovered liquid mass was measured and divided by the input liquid mass to form the liquid recovered volume fraction presented in Figure 2.23.

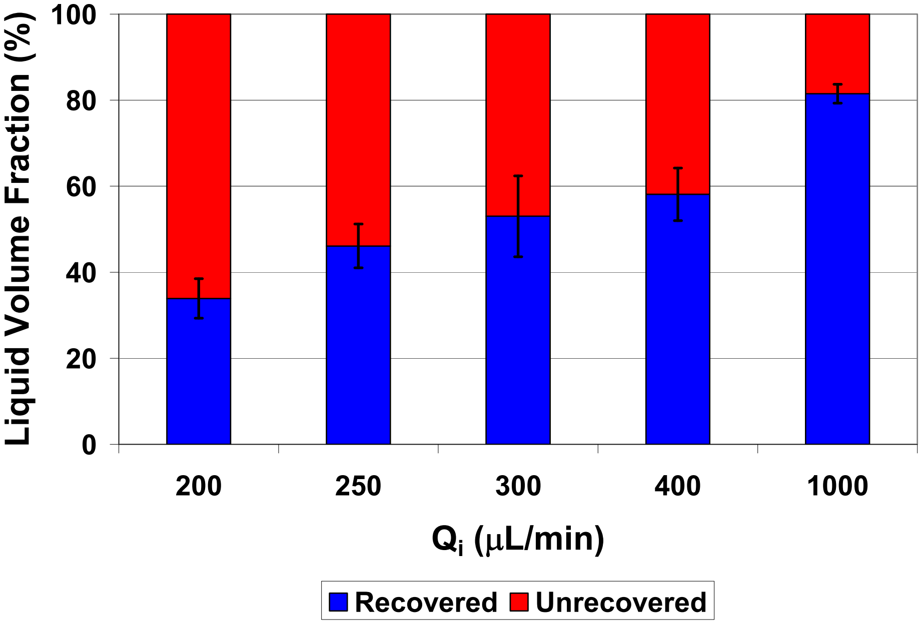

Figure 2.23: Liquid volume fraction recovered and non-recovered (%) for WWC-100 fluorometric liquid collection characterization study

Total solvent volume recovered and unrecovered can be seen here. Liquid recovery is observed to increase with increasing liquid input rate similar to collection ratio data taken in other experiments. Approximately 30-40% liquid recovery, or 60-70% liquid unrecovered, by volume is observed at 200 μL/min. Error bars corresponding to the standard deviations are included and reflect changes in air conditions throughout the course of testing. Liquid input rates were sequentially staggered during testing and laboratory air temperatures increased approximately 10 degrees Celsius from the first to second test at each liquid input rate. The liquid recovery volume fraction increases to approximately 80-90% at 1000 μL/min. The unrecovered fractions were calculated by subtracting the recovered fraction from 100%. Similar trends in uranine mass recovery would imply the unrecovered liquid exited the cyclone in the air-stream as a consequence of reaerosolization or entrainment.

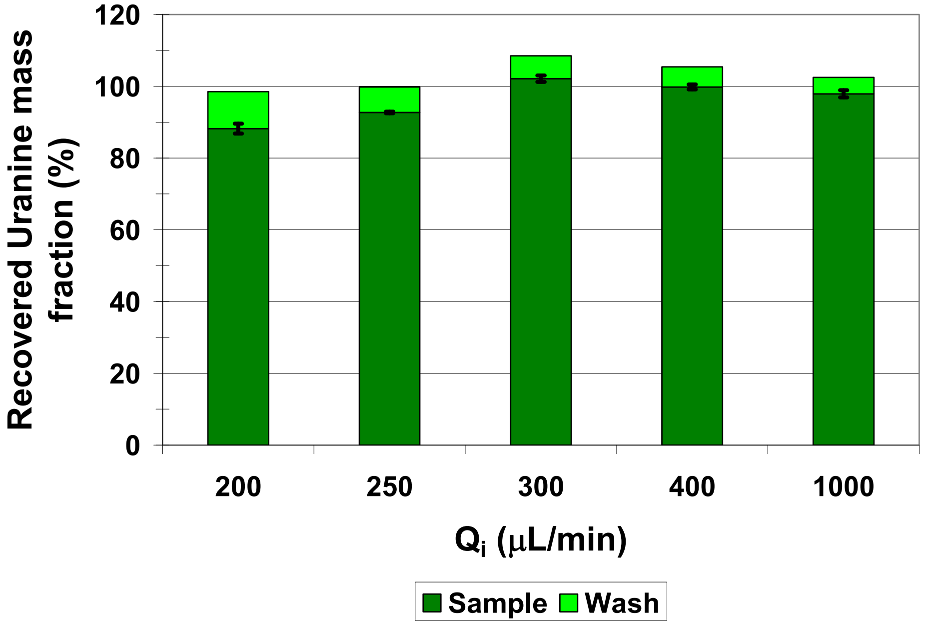

Figure 2.24: Uranine mass fraction (%) collected in sample and wash cycles for WWC-100 fluorometric liquid collection characterization study

Figure 2.24 shows the results of fluorometric analysis on each liquid sample. Only 30% of the liquid input volume was recovered at a liquid input rate of 200 μL/min. However, 88% of the input uranine mass was recovered in the sample with an additional 10% recovered in the subsequent wash with distilled water. No traces of uranine were discovered in the filter solutions for any test. Random swabs of the inner cyclone surfaces (e.g. inlet section, slot, cyclone bore, skimmer, exit tube) failed to reveal any traces of uranine. The wash cycles removed residual uranine effectively. Higher liquid input rates reduced the amount of tracer recovered in the wash. Partial film wetting and dryout at low liquid input rates most likely resulted in residue formation on the cyclone walls. The most significant source of error for each of these tests was repeatability of the fluorometer reading (~5%). The sum of the recovered mass fractions in samples and washes was approximately $100 \pm 5\%$ for all liquid input rates.

#### 2.4.1.3. Analysis

Although significant liquid losses occur, e.g. nearly 70% by volume at 200 μL/min input, the solute remained within the cyclone to be scavenged at the skimmer section. These data suggest liquid losses are due to evaporative mass transfer at the air-liquid interface and are not a consequence of reaerosolization or entrainment. Dimensionless analysis of the air-film flow and inception criteria from the literature support this result.

Entrainment from the shearing off of roll wave crests can be correlated to the film Reynolds number

$$Re_f = 4\Gamma / \nu_f \tag{2.14}$$

where $\Gamma$ is the volumetric film flow rate per unit wetted perimeter, and $\nu_f$ is the kinematic viscosity of the film. Ishii and Grolmes originally proposed no entrainment occurs by wave crest shearing for $Re_f < 160$ in forced air flows (1975). Stabilization of the film flow and reduction in the disturbance growth factor lead to the disappearance of interfacial waves and thus the primary mechanism for entrainment. Analysis of the experimental parameters described above shows $Re_f \sim 1$, which is two orders of magnitude less than the critical Reynolds film number for entrainment by the shearing of wave crests. This places the cyclone film flows into the limiting case of low Reynolds number film flow. Inception criteria suggest critical gas velocities would have to exceed 100 meters per second for entrainment to occur for wave crest shearing. However, entrainment may still occur as a result of wave undercutting as the gas flow rate increases.

The effect of gas flow rate on entrainment is determined by the magnitude of the Weber number

$$We = \rho_g V_g{}^2 \delta_f / \sigma_f \tag{2.15}$$

where $\rho_g$, $V_g$, $\delta_f$, and $\sigma_f$ represent the gas density, gas velocity, film thickness, and surface tension, respectively. This parameter shows the relative size of the destabilizing gas phase inertial force with respect to the stabilizing surface tension force of the film. Pressure asymmetry on the wave induced by boundary separation results in the formation and detachment of liquid bulges by the gas phase. This mechanism is called wave undercutting and is negligible for $We < 17$ (Kim and Peterson, 1995). An assumed film thickness of 1 millimeter gives $We \sim 1$ and suggests wave undercutting is not a potential source of entrainment due to the dominance of surface tension forces over gas phase inertial forces. Theoretical analysis of the gas-film flow supports the experimental observation that no entrainment occurs; unrecovered liquid is lost to latent heat and mass transfer at the air-film interface.

### 2.4.2. STEADY-STATE SYSTEM RESPONSE TIME

The wetted-wall bioaerosol sampling cyclone can be operated continuously rather than in discrete liquid samples as described above. In continuous mode the liquid output stream would only be analyzed upon recognition of some signal, e.g. an impulse from an optical device located in the collector inlet. At that point the liquid output stream would be diverted to analysis hardware, minimizing the amount of liquid analyzed and reagents consumed. The latency period data presented in Section 2.2 are representative of a system triggered from rest (idle system) not a system triggered during steady-state operation. A transient period exists in which the cyclone walls become wetted when the system is triggered from an idle state. Once the walls are wetted the cyclone behavior can be considered steady-state. The steady-state latency period is significantly different than the idle latency period. The response time is reduced once the system attains steady-state operation because liquid motion is less impeded by interfacial forces occurring at the dry wall solid-liquid interface. Once the surface is wetted, liquid is envisioned to flow on top of a quasi-stationary microscopic film layer which offers much less resistance to motion and results in faster liquid transport from the inlet slot to the scavenge port. Fluorometric analysis techniques were used to determine the steady-state latency period.

#### 2.4.2.1. Experimental Apparatus

The steady-state latency period of the WWC-100 was quantified by tagging the liquid input with uranine and making real-time measurements of output sample concentration. The fluorescently tagged output stream was directly routed from the scavenge port to the Turner Digital Fluorometer (FM109535) with a high flow diaphragm pump (0.275 Lpm). The scavenge rate of the diaphragm pump is significantly (~150x) higher than the peristaltic pump used in laboratory liquid collection experiments. Thus, the time required for liquid to traverse approximately 12” of 1/32” scavenge tube is considered negligible.

A simple flow cell was created from a 12 mm culture tube, silicon stopper, and 4.5 mL of distilled water as shown in Figure 2.25. Two 1/32” holes were drilled through the stopper. Air bubbles from the scavenge pump created substantial signal noise as they traversed the fluorometer illumination window. Therefore, the bottom of the WWC-100 liquid output line was placed approximately 25 mm from the bottom of the culture tube. This separation distance minimized signal noise and maximized liquid mixing within the fluorometer viewing window. The diaphragm pump created positive pressure within the flow cell. Liquid bubbled up to the flow cell exhaust tube, 5 mm underneath the stopper, when the pump was operational.

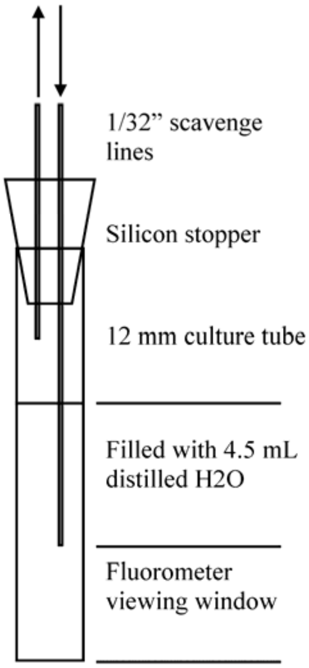

Figure 2.25: Simple flow through cell created to measure the steady-state response time of the WWC-100 using fluorescent liquid input and real-time fluorometer measurements

A three port distribution valve (Tecan Systems 20736615) was installed on the cavro pump. This allowed the cavro pump to draw from two different liquid input reservoirs during continuous operation: distilled water and 0.3 μM uranine solution. The fluorometer was set to raw fluorescence (mode II) and setup according to procedures described in 2.4.1.1. The fluorometer RS-232 port was connected to a Windows based PC and Hyperterminal was used to acquire and record real time measurements of fluorescent intensity. Fluorometer output readings were recorded on a 1 second time interval.

#### 2.4.2.2. Experimental Procedure

Figure 2.26 shows the real-time fluorescent intensity for a single steady-state response time experiment. The liquid input rate for the figure was 150 μL/min. The flow cell was initially filled (4.5 mL) with distilled water and the FIU was zero. Data was recorded continuously and visual observations were used to link sample times with individual data points recorded in Hyperterminal. Five hundred microliters (0.5 mL) of distilled water were injected into the cyclone at a fixed liquid input rate. The start of the cavro dispense cycle was observed visually and the corresponding Hyperterminal time was recorded.

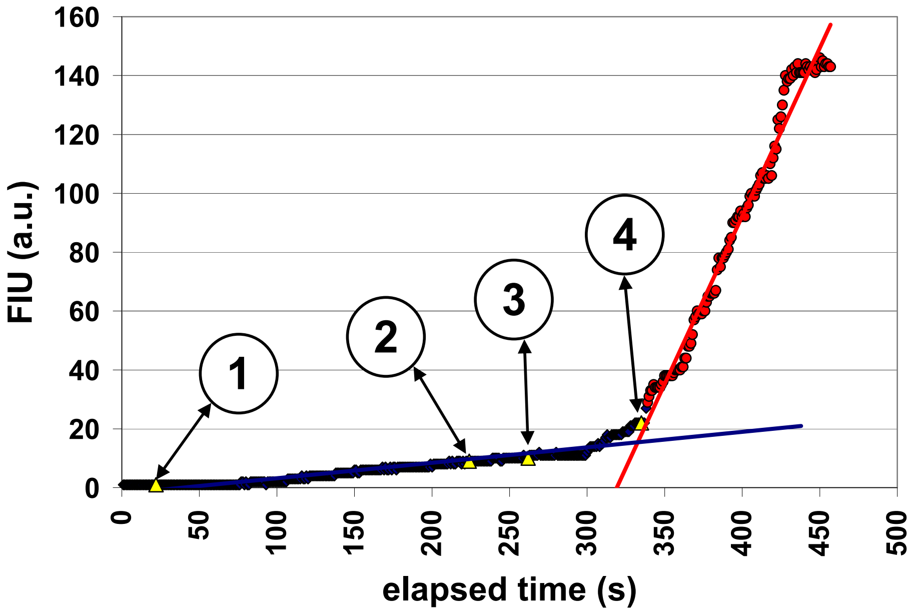

Figure 2.26: Real-time fluorescent intensity data used to determine the steady-state response time of the WWC-100 using a flow through cell and fluorometer

Point 1 in Figure 2.26 marks the start of injection of distilled water. Approximately 200 seconds elapsed and steady-state operation was established. The cavro pump valve was automatically switched to the tagged reservoir and 0.5 mL of tagged liquid was injected. Point 2 marks the beginning of tagged liquid injection as witnessed visually. A dead volume of approximately 100 microliters was calculated for the length of 1/32” tubing from the cavro pump to the air-blast atomizer. Point 3 shows the time at which tagged liquid actually entered the cyclone as calculated with the line dead volume and liquid input rate. An abrupt change in slope (FIU/s) was observed after some finite time and marked as point 4 in the figure. This signifies the arrival of tagged liquid at the flow cell. The elapsed time between points 3 and 4 is the steady-state latency period of the WWC-100. Cyclone wash samples were conducted after each experiment to clean out any residual fluorescent material. Ten milliliters of distilled water were injected at a rate of 1000 μL/min. The culture tube and remaining liquid were discarded. Clean culture tubes with 4.5 mL of distilled water were placed inside the fluorometer for successive experiments.

### 2.4.2.3. Data

Air temperature and relative humidity were recorded at the start of each experiment. The empirical critical liquid input rate correlation was used to convert actual liquid input rates to dimensionless liquid input rates. Steady-state response time experiments were repeated three times for actual liquid input rates of 125, 150, 175, 250, 500, and 1000 μL/min. Error of approximately ±5 seconds was estimated from the dependence of data on visual observations and the determination of Point 4 by the change in slope of Figure 2.26. Figure 2.27 shows the calculated steady-state latency periods, $\tau_{ss}$, along with the idle latency period, $\tau$, regression line (2.7). The steady-state latency period is approximately 40-60 seconds less than the idle latency period near the critical liquid input rate ($Q_i^* \leq 1.5$) and 10 seconds less in the asymptotic limit ($Q_i^* \geq 3$).

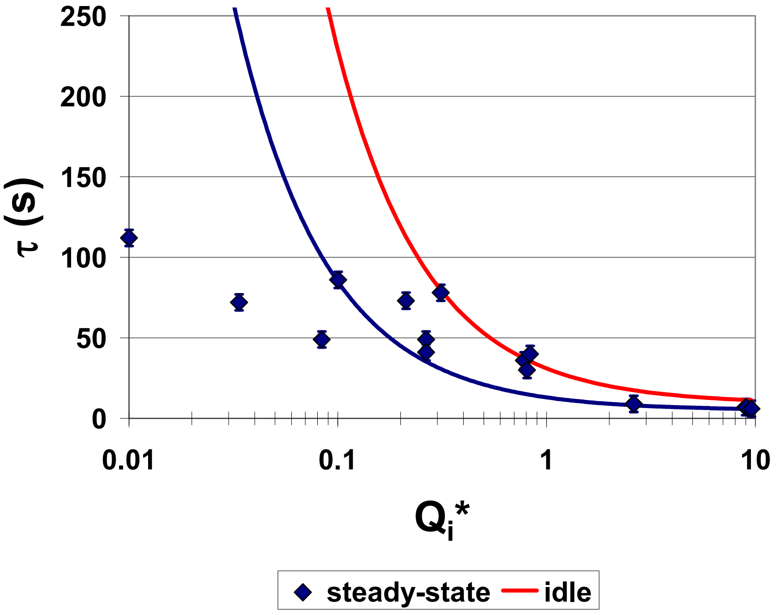

Figure 2.27: WWC-100 response time versus dimensionless liquid input rate for a system triggered from rest (dry) and triggered during steady-state operation (wet)

#### 2.4.2.4. Analysis

Least squares regression and the best judgment of the experimenter were used to fit the WWC-100 steady-state latency period, $\tau_{ss}$, as a function of the dimensionless liquid input rate. The form of (2.7) was used to obtain

$$\tau_{ss} = \frac{8}{Q_i^*} + 5 \tag{2.16}$$

with $R^2 = 0.7$. There are two major differences between steady-state and idle latency periods: the asymptotic latency period is slightly lower under steady-state conditions, and the steady-state system approaches its asymptotic latency period more rapidly than the idle system.

A qualitative physical model is adopted to explain the reduction in latency period under steady-state conditions. Liquid is observed to travel down the cyclone as discrete droplets approximately 1 mm in diameter. Contact angle hysteresis and contact line pinning contribute to the resistance of droplet motion. Microscopically the cyclone surface is composed of individual roughness elements and void spaces. Interactions between liquid droplets and the random solid surface structure are greatest for a dry surface. A microscopic film is proposed to fill the void spaces and span over the roughness elements, thereby reducing interactions between the droplet and surface, once steady-state conditions are reached. Droplets move along the wetted cyclone surface more rapidly and the latency period is reduced.

### 2.4.3. MINIMUM IDLE SYSTEM RESPONSE TIME

The real-time fluorometric procedure described above was used to quantify the response time of an idle WWC-100 system. In this case the walls were assumed dry and a single 5 minute sample command was executed. These conditions are identical to laboratory liquid collection data described in Section 2.2.3. The peristaltic pump flow rate, used in laboratory collection experiments, is much slower (~150x) than the diaphragm pump used in fluorometric experiments. The time required for liquid to traverse scavenge lines is negligible at diaphragm pump air flow rates. Time periods of approximately 20-30 seconds were required for liquid to be transported from the scavenge port to the mass scale in the laboratory experiments (peristaltic pump). Thus, uncorrected data from laboratory experiments were not truly representative of the actual system due to the use of the peristaltic pump. The minimum idle-system response time was quantified. Latency period data obtained in laboratory experiments were then corrected to remove the effects of using a peristaltic scavenge pump.

The experimental test apparatus and procedure are similar to those described for the WWC-100 steady-state response time. A five minute sample cycle was executed using only tagged liquid as input. The minimum latency period, for an idle system, was determined from real-time fluorometer measurements at $Q_i = 1000$ μL/min. Figure 2.28 shows three measurements which average to 12 seconds. Deployed WWC-100 systems would therefore have a minimum idle response time of 12 seconds for large liquid input rates, $Q_i^* > 5$. Data obtained from laboratory experiments of the idle system response time are also shown. The asymptotic limit is approximately 38 seconds. This time includes the lag time associated with using the peristaltic pump. All laboratory test experimental data were offset by -26 seconds to bring the asymptotic value to 12 seconds as measured in fluorometric experiments. The latency period empirical correlation (2.7) thus reflects actual system performance.

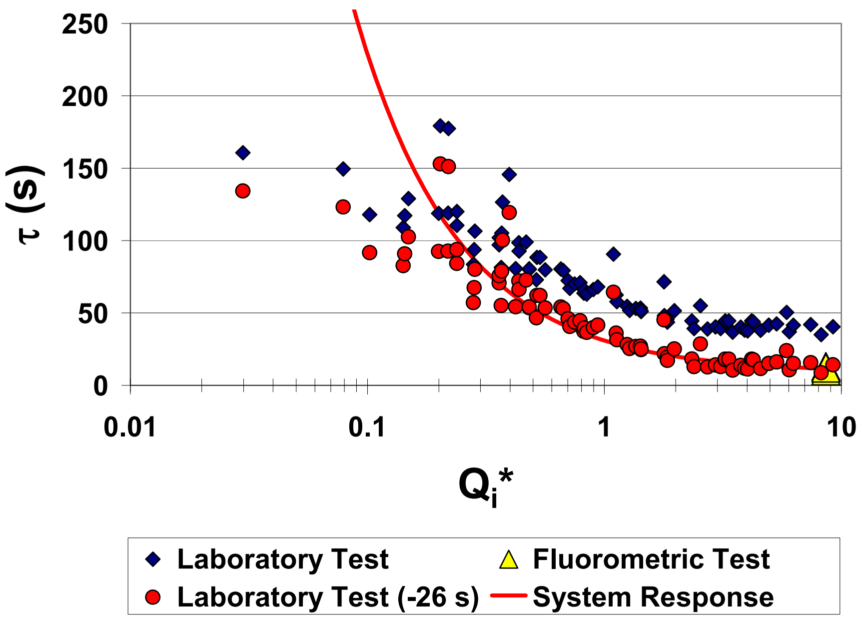

Figure 2.28: Latency period (s) plotted against the dimensionless liquid input rate for laboratory liquid collection characterization, asymptotic behavior from fluorometric liquid characterization, and resulting offset reflected in system latency period

## 2.5. Effects of air-blast atomizer

Two separate multi-phase flow regimes exist in the wetted-wall cyclone. Liquid is atomized in the cyclone inlet resulting in an entrained droplet flow. Droplets impact on the cyclone wall, form a thin film, and are subsequently driven downstream. Collection ratio data shown in Section 2.2.4.1 represent the net mass transfer occurring for the entire system. The relative importance of the two multiphase flow regimes on mass transfer rate was evaluated.

Low mass transfer rate theory can be used to determine the approximate lifetime of a droplet entrained in air flow for different air temperatures and relative humidity (Mills, 2001). Conditions corresponding to minimum droplet lifetimes are $T = 320\,\mathrm{K}$ and $RH = 0\%$. An empirical correlation for the spray size distribution from a plain jet air-blast atomizer suggests approximate droplet sizes of 100 to 200 μm for this atomizer (Rizk and Lefebvre, 1984). Approximate droplet lifetimes of 4 to 15 seconds correspond to these air conditions and droplet sizes. The inlet droplet residence time, 0.01 seconds, is formed as the ratio of atomizer to impaction zone distance to the atomizer exit air velocity. This is the approximate time period over which the liquid exists as entrained droplets. The droplet lifetime is on the order of 400 to 1500 times larger than the inlet droplet residence time for 100 and 200 μm droplets, respectively. Figure 2.14 shows overall system residence times (latency period) to be approximately 10-100 seconds. The time spent as entrained droplets is approximately 1,000 to 10,000 times less than the time spent in the cyclone body downstream of the inlet slot. Thus, it was concluded that effects of air-blast atomization on system mass transfer were less significant than processes occurring in the remainder of the system. Simple experiments were performed to confirm this hypothesis.

### 2.5.1. EXPERIMENT

Cyclone liquid input rates, as provided by the syringe pump, were first verified. Atomizer liquid needle discharge was collected into a container placed on the precision mass scale. Liquid mass output was measured over time with the atomizer air supply pump inoperable. The measured rate was $\pm 1\%$ of the specified syringe pump rate. This experiment showed that the liquid input rate used to characterize the cyclone systems, $Q_i$, was accurate. Two experiments were then performed to isolate the effects of air-blast atomization on WWC system evaporative mass transfer.

Liquid was atomized into a funnel with 6 cm opening as depicted in Figure 2.29A. The axis of the funnel was aligned with the air needle. The face of the atomizer block was flush with the funnel perimeter such that no spray went outside the funnel. The bottom of the funnel was plugged with a 1 cm silicon stopper. A liquid scavenge line was inserted into a hole drilled through the stopper. Collected liquid was siphoned off by a peristaltic pump and sent to a container on the precision mass scale. The distance from atomizer needle tips to silicon stopper was approximately 3 cm. The steady-state collection rate was measured for liquid input rates ranging from 200-1000 μL/min.

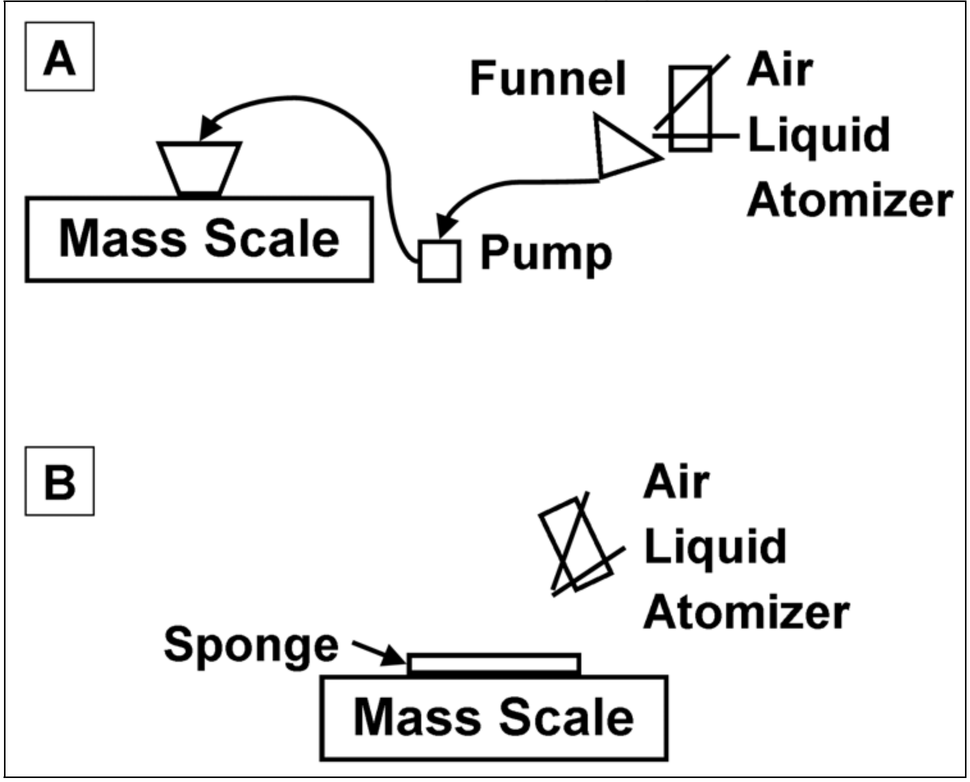

Figure 2.29: Experimental setup for study of evaporation of liquid attributable to air-blast atomizer with funnel (A) and sponge (B) liquid collectors

The funnel collector was replaced with a soldering iron sponge as depicted in Figure 2.29B and the experiment was repeated. The sponge was 6 cm square and placed on the mass scale approximately 2.5 cm underneath the atomizer needle tips. The atomizer was oriented such that the spray envelop was inside 1 cm sponge perimeter margins. The mass scale was tarred with the air pump turned on to account for the offset induced by aerodynamic forces on the sponge (~0.1 g). The forced air evaporation rate for a wet sponge with incident air jet was also measured as 35 ± 5 μL/min. The rate of liquid collection from the air-blast atomizer was measured for liquid input rates ranging from 200-1000 μL/min. The collection rates were then offset by the forced air evaporation rate to separate evaporative losses in the entrained droplet flow from those occurring at the sponge surface.

Figure 2.30 shows the calculated liquid evaporation rates for the funnel and sponge collectors. The evaporation rates range from approximately 20-70 μL/min with standard deviation of 10. These represent evaporative phenomena that occur upstream of the inlet slot for entrained droplet flow. The sponge collector evaporation rate is lower (~20 μL/min) than the funnel collector at low liquid input rates ($Q_i \approx 200$ μL/min). The discrepancy between the two measured evaporation rates becomes negligible as the liquid input rate becomes greater than 600 μL/min.

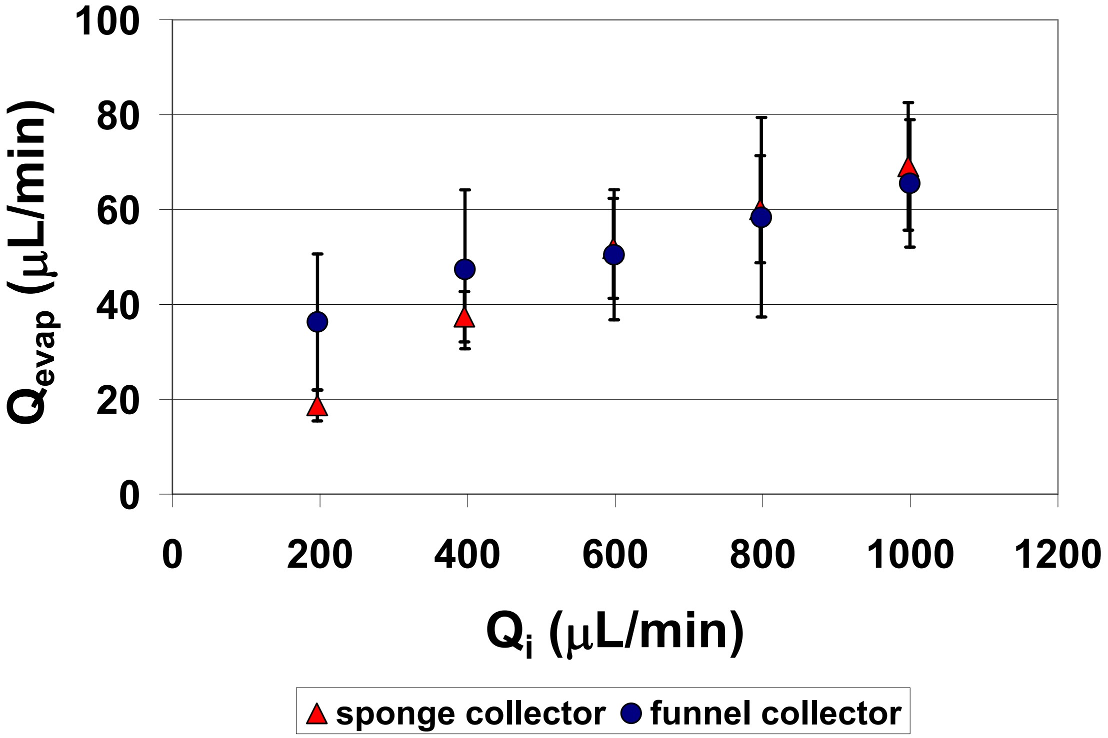

Figure 2.30: Volumetric evaporation rate (μL/min) attributed to air-jet atomization vs. actual liquid input rate for spray collection with sponge and funnel collectors

### 2.5.2. ANALYSIS

These simple experiments provided significant insight into the physical behavior of the wetted-wall cyclone system. Naturally occurring cyclone inlet phenomena were observed in the funnel collector. Figure 2.31 shows a diagram of the inlet slot as seen by looking into the cyclone inlet in the same direction as air flow. Air flow and atomized liquid are directed into the plane. The air-blast atomizer creates a cone jet of fine liquid droplets. The cone encompasses the inlet slot and overlaps onto surfaces of the converging cyclone inlet. The spray impacts on inlet surfaces and coalesces into droplets. These pendant shaped droplets remain stationary until they reach a point at which gravity overcomes surface adhesion and they slide into the inlet slot. The growth and detachment of these droplets on the walls takes longer at low liquid input rates. This helps explain the difference in evaporation rates measured for the funnel and sponge collectors. The droplets grow, coalesce, and slide down the funnel walls more quickly as the liquid input increases. The time spent as pendant shaped droplets increases the time period over which forced convection occurs. This is judged to be the primary reason funnel collector evaporation rates are higher than the sponge collector.

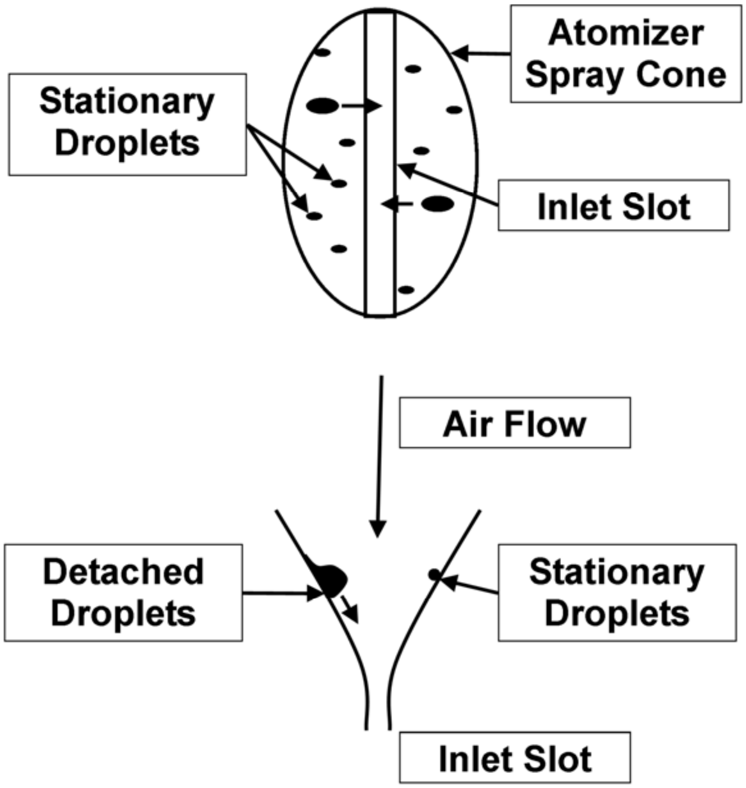

Figure 2.31: Drawing of cyclone inlet section, with airflow and atomized spray directed into the plane, and incident spray cone resulting in quasi-stationary pendant shaped droplets subject to interfacial and gravitational forces

## 2.6. Effects of liquid chemical composition

A small percentage (volume/volume) of surfactant is generally added to WWC liquid input. Surfactant enhances the removal of biological particles from internal cyclone surfaces. Experiments conducted at Texas A&M University suggest this percentage is on the order of 0.02% or less, for Tween 20 surfactant, to be effective. Peculiarities in liquid collection behavior have been noted by users of field tested WWC-1250 systems. PBST solution is commonly used as liquid input and consists of a phosphate buffer solution (PBS) with 0.1% (volume/volume) Triton X-100 surfactant concentration. Buffer solution maintains organism viability over prolonged periods between collection and analysis.

### 2.6.1. EXPERIMENT

PBST solution was prepared according to the mass breakdown presented in Table 2.7. Laboratory liquid collection experiments were performed for the WWC-1250 as described in Section 2.2 to determine the effects of liquid input composition on evaporation.

| | **mass (g)** | **molecular weight (g/mol)** | **mol** | **mol fraction (%)** | **solubility (g/L)** |
|---|---|---|---|---|---|
| NaCl | 7 | 58 | 1.21E-01 | 2.17E-03 | 359 |
| KCl | 0.2 | 75 | 2.67E-03 | 4.79E-05 | 340 |
| $Na_2HPO_4$ | 1.2 | 142 | 8.45E-03 | 1.52E-04 | 77 |
| $KH_2PO_4$ | 0.2 | 136 | 1.47E-03 | 2.64E-05 | 220 |
| $H_2O$ | 1000 | 18 | 5.56E+01 | 9.98E-01 | |

Table 2.7: Mass and molar breakdown of phosphate buffer solution (PBS)

In the first experiment, the liquid input line was switched between distilled water and PBST reservoirs after 10 samples were collected at a liquid input rate of 2250 μL/min. The collection ratio dropped from 0.7 to 0.15 immediately after the liquid input switch to PBST from distilled water. A collection ratio of 0.15 typically indicates liquid bypass. The liquid line was switched back to distilled water after 10 PBST samples and the collection ratio was highly erratic ($0 \le Q_o^* < 0.7$) for 20 succeeding samples. The test was repeated after disassembling and washing the cyclone thoroughly with distilled water. Subsequent data showed only a modest drop in collection ratio from 0.7 to 0.55 with no indication of bypass. Bypass occurring for the first test was concluded to be a random occurrence and not explicitly attributable to the use of PBST. It is unknown whether PBST increases the probability of bypass and should be investigated in future studies since it represents a system failure.

Similar tests were conducted with distilled water and 0.02% Tween 20 solution. No difference in collection ratio was observed. The 15% increase in evaporation of PBST solution was accredited to differences in chemical composition. Two experiments were performed to separately analyze the effects of adding salts (phosphate buffer solution) and Triton X-100 surfactant to liquid input.

Figure 2.32 shows the collection ratio as a function of liquid input rate for PBS and distilled water inputs. Five samples, with sequentially increasing liquid input rates, were collected with distilled water. The input reservoir was then changed to PBS for five additional samples at the same set of liquid input rates. The ten sample series was then repeated. Differences in collection ratio were negligible away from the critical liquid input rate. However, no distilled water was collected at $Q_i = 800$ μL/min where approximately 50 μL/min was collected for PBS at the same liquid input rate.

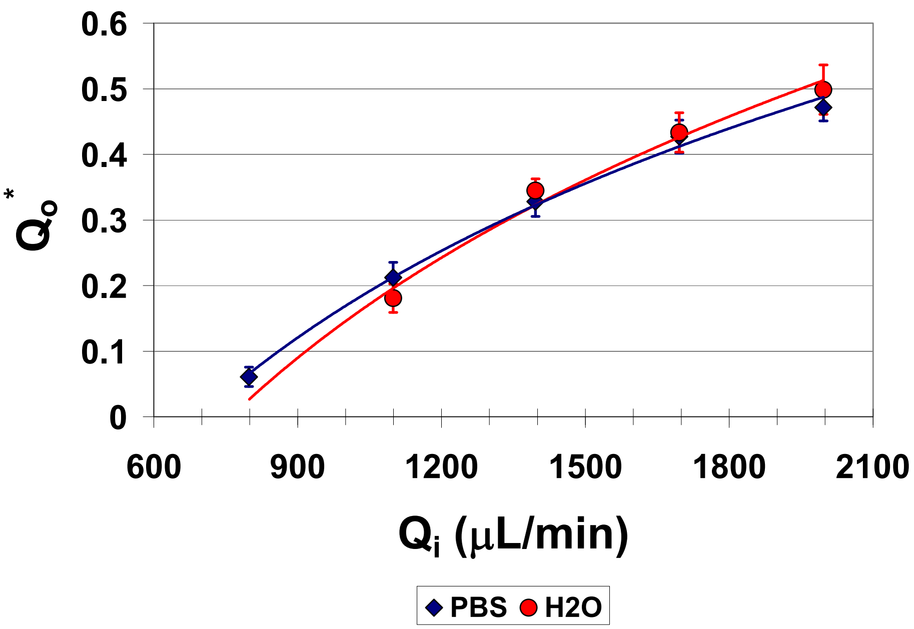

Figure 2.32: Collection ratio vs. liquid input rate for WWC-1250 with PBS and distilled water

The experiment described above was repeated with liquid input pairs of distilled water and 0.1% Triton X-100 solution, and distilled water and 0.02% Triton X-100 solution. These were performed to isolate the effects of PBS from Triton X-100 (in PBST) as well as quantify the effects of Triton X-100 surfactant concentration. Figure 2.33 shows the WWC-1250 collection ratio for distilled water and 0.1% Triton X-100 solution. A 16% reduction in collection, for all liquid input rates, was observed between series 1 and series 2 upon the switch to 0.1% Triton X-100. The collection ratio did not return to its previous values when the liquid input was returned to distilled water. An additional reduction of 12% was observed between series 3 and series 4. Fifteen wash cycles ($Q_i = 2000$ μL/min) were executed after the last set of 0.1% Triton X-100 collection samples. The collection ratio immediately returned to its original value for washes with large liquid input rate.

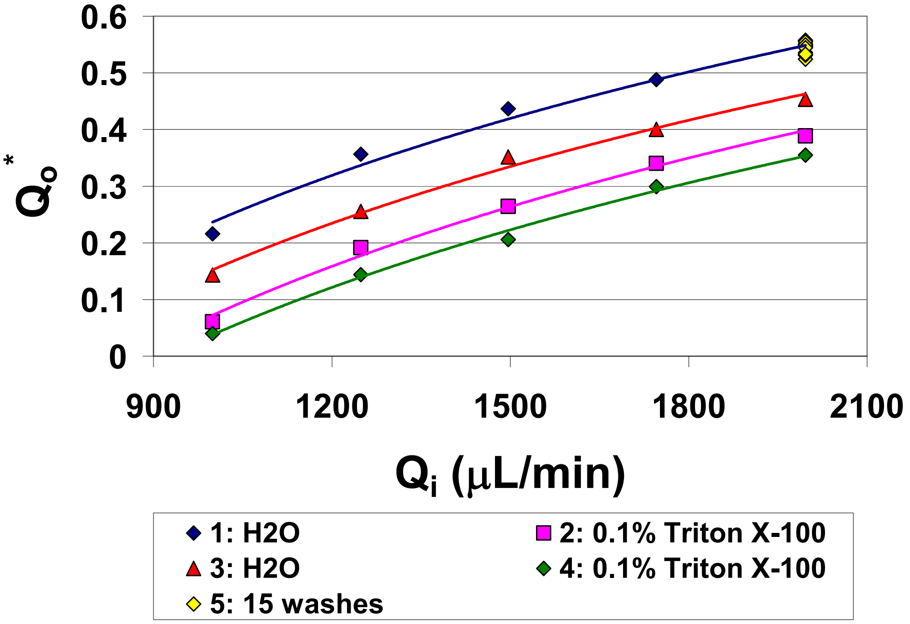

Figure 2.33: WWC-1250 Collection ratio with increasing liquid input rate for distilled water and 0.1% (v/v) Triton X-100 solution

No differences in evaporation have been observed for distilled water and 0.02% Tween 20 solution. The Triton X-100 experiment was repeated with distilled water and 0.02% Triton X-100 solution to determine if high Triton X-100 concentration was responsible for the increase in evaporation. Figure 2.34 shows a similar 15% reduction in collection ratio for 0.02% Triton X-100 solution. However, the carryover effect observed for 0.1% Triton X-100 solution is not as distinct for 0.02% solution.

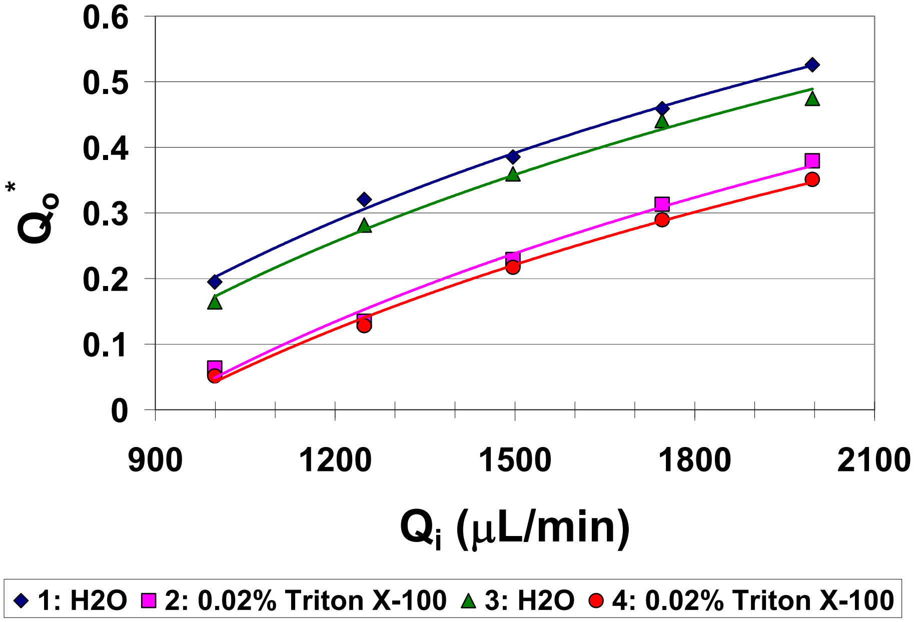

Figure 2.34: WWC-1250 Collection ratio with increasing liquid input rate for distilled water and 0.02% (v/v) Triton X-100 solution

### 2.6.2. ANALYSIS

Water/PBS experiments suggest the addition of salts does not broadly effect evaporation although it may suppress evaporation at low liquid input rates. Raoult's law was used to predict the reduction in vapor pressure above an idealized solution of PBS. The solution saturation vapor pressure is reduced by approximately 5% with respect to distilled water. Physically this means the vapor mass fraction difference, i.e. the mass transfer driving force, is reduced by roughly the same percentage. Trend lines in Figure 2.32 were compared at $Q_i = 800$ μL/min and show a reduction in collection ratio of approximately 5% when PBS is used. This supports the idea that film surface vapor pressure depression could reduce evaporation.

Figure 2.33 and Figure 2.34 show Triton X-100 surfactant is the component of PBST responsible for the reduction in collection ratio, i.e. increased evaporation. These figures also show a dependence on surfactant concentration. At 0.1%, Triton X-100 appears to have a residual effect even when the liquid input is switched back to distilled water. It is likely that some of the surfactant adheres to the surface and must be rinsed thoroughly to eliminate undesirable effects. Otherwise there is a cumulative effect of increasing evaporation. This effect is not as distinct when the Triton X-100 concentration is reduced to 0.02%. It is unknown whether the concentration of Triton X-100 needs to be 0.1% or if a reduced concentration would be effective at biological particle removal. Tween 20 is effective at concentrations of 0.02% and does not affect the collection ratio.

The significance of surface physics on evaporative effects has been briefly mentioned. These effects are highlighted here by increased evaporation for Triton X-100 solution and PBST with respect to distilled water. Surfactant acts to reduce the surface tension of a droplet. Liquid flowing along the cyclone wall is driven downstream by aerodynamic forces at the air-liquid interface. Decreasing surface tension and increasing spreading is hypothesized to reduce the liquid height above the surface thereby reducing drag by dropping it further into the boundary layer. A reduction in drag forces could be responsible for slowing the transport of liquid through the system. This would prolong liquid exposure to forced convection heat and mass transfer. Increased spreading could also create an increase in surface area over which heat and mass transfer occur. This is another plausible explanation for the increase in evaporation. The hypothesis that liquid transport is retarded by the inclusion of Triton X-100 could be explored through latency period studies for idle and steady-state systems. This is recommended for future studies.

Critical differences are observed between Tween 20 and Triton X-100 although both are non-ionic surfactants. Tween 20 has a molecular weight of 1227 g/mol whereas Triton X-100 is 625 g/mol. The more distinguishing characteristic is the critical micelle concentration (CMC), 0.3 mM (0.018% v/v) and 0.006 mM (0.006% v/v), for Triton X-100 and Tween 20, respectively. At these molarities individual surfactant molecules aggregate to form structures called micelles. It should be noted that 0.02% Tween 20 and 0.1% Triton X-100 solutions have sufficiently large concentrations (1-5 x CMC) that micelles are present. This enables efficient removal of biological particles from cyclone surfaces as the micelles encapsulate biological particles. There is evidence that the chemical structure of non-ionic surfactant solutions strongly influences interfacial and liquid flow characteristics in co-current gas-liquid flows. Lioumbas et al. suggest surfactant molecules are concentrated near the liquid gas interface thereby forming a protective layer which reduces the mean liquid axial velocity and pressure drop in two-phase turbulent flows (2006). These effects should be analyzed in future studies with respect to their influence on evaporative mass transfer.

## 2.7. Summary

A family of wetted-wall bioaerosol sampling cyclones (WWC) was developed to meet the growing need for surveillance and detection systems. The following set of activities were performed to enhance the capabilities of this system to provide real-time detection of airborne pathogens:

- developed Windows application to perform simultaneous WWC control, data acquisition, and data analysis
- constructed test apparatus to condition laboratory air to simulate ambient aerosol sampling in many environmental conditions
- measured dependence of response time and liquid recovery rate on environmental conditions
- formulated empirical performance correlations for system response time and liquid recovery rate that enable effective use of WWC
- developed open-loop control algorithm to deliver highly concentrated liquid samples independent of sampling environment
- validated control algorithm by performing ambient air sampling tests and achieving constant, microfluidic liquid output rates of $25 \pm 5$ μL/min corresponding to a concentration factor of 2,000,000
- quantified WWC liquid mass transfer mechanisms with fluorescent tracer studies and attributed performance to evaporative effects
- investigated system performance changes due to surface physics and the addition of surfactants commonly used in biological aerosol collection

## 2.8. Future Works

Multiphase flow internal to the WWC has a significant impact on sampler performance. Steady-state evaporation and sampler response time should not be analyzed without regard for complex interactions occurring at the solid-liquid and gas-liquid interfaces. Multiphase flow visualization studies are planned for the 100 liter per minute wetted-wall bioaerosol sampling cyclone. A borescope and high speed video camera system will be used to capture images of cyclone co-annular air-liquid flows. MATLAB Image Processing Toolbox will then be used to analyze image sequences and determine characteristics such as liquid surface area coverage and liquid droplet trajectories. The dependence of droplet motion on air flow rate will be studied. The effects of liquid chemical composition will also be examined through the addition of Tween 20 and Triton X-100 surfactants at various concentrations above and below the critical micelle concentration. Lastly, steady-state evaporation and sampler response time will be analyzed in light of qualitative and quantitative multiphase flow descriptions.

# 3. MODELING TWO-PHASE HEAT AND MASS TRANSFER IN A FAMILY OF WETTED-WALL BIOAEROSOL SAMPLING CYCLONES

## 3.1. Background

It has been shown experimentally that collection ratios and latency periods for all wetted-wall bioaerosol sampling cyclones collapse when plotted as a function of the dimensionless liquid input rate. Thus, knowledge of the critical liquid input rate allows performance to be predicted for any air conditions or air flow rate. Empirical correlations for the critical liquid input rate were developed in 2.2.4. These models were successfully integrated into an open-loop control algorithm for WWC-100 delivery of constant microfluidic output rates. However, these models lacked proper asymptotic behavior at saturated air conditions due to a lack of experimental data for these conditions. The critical liquid input rate was also assumed to be a linear function of both ambient air temperature and relative humidity. Extrapolation from the empirical model could result in significant error due to the linear assumption. A numerical model was developed to improve the accuracy and reliability of critical liquid input rate predictions. The true functionality of critical liquid input rate on air conditions and air flow rate, and proper physical behavior are shown.

## 3.2. Conservation Equations

Multiphase flow inside the wetted-wall cyclone is modeled as co-annular air-film flow as shown in Figure 3.1. Control volumes surround the air-vapor mixture and liquid film. One-dimensional plug flow in the longitudinal ($x$) direction is assumed for the air-vapor mixture. The air-vapor mixture is described by the mixture mass flow rate, $\dot{m}$, vapor and air mass fractions, $Y_v$ and $Y_a$, and the mixture enthalpy, $h$. Energy transfer to and from the liquid film surface to the air-vapor mixture is a result of forced convection heat transfer. Newton's Law of cooling is used to specify the heat transfer rate. Mass transfer and the accompanying latent energy transfer also occur as the liquid film evaporates into the mixture. A control surface is drawn around the liquid film and air-vapor mixture interface which is assumed to be in equilibrium.

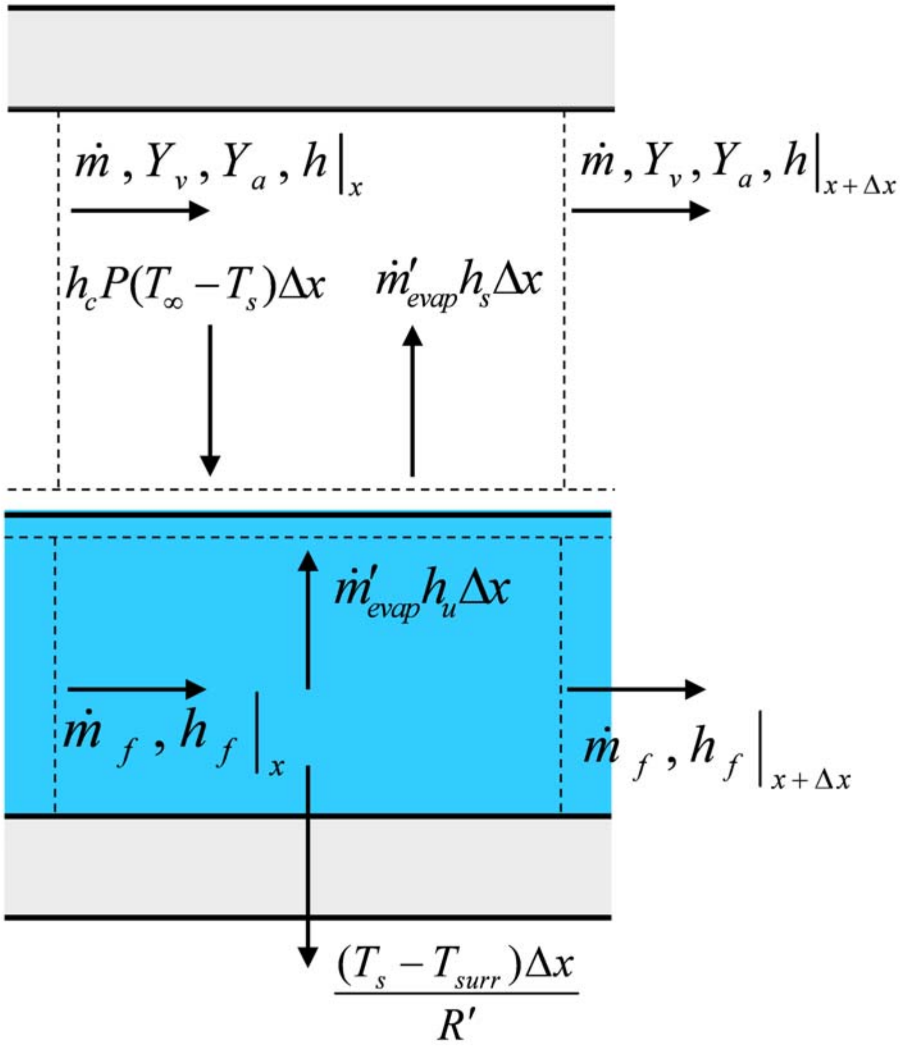

Figure 3.1: Multiphase flow inside the wetted-wall cyclone modeled as co-annular air-film flow

The liquid film is also modeled as a one-dimensional plug flow in the $x$ direction. The film is characterized by the film mass flow rate and enthalpy, $\dot{m}_f$ and $h_f$, respectively. Heat transfer to or from the film to the external surroundings, through the cyclone wall, is modeled with the resistance analogy. This model feature is unique in that it allows for detailed studies of the effects of external heating and cooling on internal heat and mass transfer.

The derivation of governing heat and mass transfer equations is greatly simplified by working with each control volume and control surface independently. The results are then combined to obtain the final set of coupled equations. These equations must be solved numerically in most cases. However, approximate analytical solutions will be derived under the assumptions of an adiabatic wall and constant liquid film temperature.

### 3.2.1. AIR-VAPOR MIXTURE

Mixture mass, vapor mass, and energy balances can be written for the air-vapor mixture control volume. The mixture mass balance is

$$\frac{d\dot{m}}{dx} = \dot{m}'_{evap} \tag{3.1}$$

where $\dot{m}'_{evap}$ is the film mass evaporation rate per unit length in the longitudinal direction. The liquid film interface is assumed impermeable to air, thus the air mass flow rate remains constant and (3.1) can be rewritten as a vapor mass balance

$$\frac{d\left(\dot{m}Y_{v\infty}\right)}{dx} = \dot{m}'_{evap} \tag{3.2}$$

where the vapor mass flow rate is expressed as a product of the mixture mass flow rate and vapor mass fraction, $\dot{m}_v = \dot{m}Y_{v\infty}$. The evaporation rate per unit length is modeled with low mass transfer rate theory (Mills 2001). The net rate of mass transfer is the product of the mass transfer conductance, $g_m$, wetted perimeter, $\mathrm{P}$ , and difference in surface and free-stream vapor mass fractions, $Y_{vs} - Y_{v\infty}$ ,

$$\dot{m}'_{evap} = g_m \mathrm{P}\, (Y_{vs} - Y_{v\infty}) \tag{3.3}$$

where the mass transfer conductance plays an analogous role to the heat transfer coefficient, $h_c$, in Newton's law of cooling. Model calculations will confirm that low mass transfer rate theory is appropriate for the physics to be modeled here $(Y_{vs} - Y_{v\infty} < 0.1)$.

The heat and mass transfer analogy, and assumption of Lewis number $(Le)$ of one, provide an approximation for the mass transfer conductance, $g_m = h_c / C_p$, where $C_p$ is the mixture specific heat (Incropera and Dewitt, 2002). The latter assumption $(Le = 1)$ is widely utilized for dilute air-vapor mixtures although the Chilton-Colburn equation, $h_c / g_m = C_p Le^{2/3}$, shows the mass transfer conductance is underestimated by approximately 10%. Changes in the mixture specific heat due to increasing vapor content are included in the model although negligibly small (<1%). Neglecting changes in the Lewis number due to air conditions is justified since the flows considered here are turbulent; eddy mixing overwhelms molecular diffusion and the effective diffusivities of heat and mass are approximately equal (Cengel, 2003). Combining Equations (3.2) and (3.3) gives the final form of vapor mass continuity.

$$\frac{d\left(\dot{m}Y_{v\infty}\right)}{dx} = \frac{h_c \mathrm{P}}{C_p}(Y_{vs} - Y_{v\infty}) \tag{3.4}$$

An energy balance on the air-vapor mixture is

$$\frac{d(\dot{m}h)}{dx} = -\dot{q}'_s + \dot{m}'_{evap} h_s \tag{3.5}$$

where convection heat transfer to the liquid surface, per unit longitudinal length, is denoted $\dot{q}'_s$. Latent energy transfer due to evaporation is $\dot{m}'_{evap}h_s$ where $h_s$ is the enthalpy at control surface '$s$' which exists as a saturated vapor. Newton's Law of cooling is used to specify $\dot{q}'_s$. The final differential form of the conservation of mixture energy is

$$\frac{d(\dot{m}h)}{dx} = -h_c \mathrm{P}\,(T_\infty - T_s) + \frac{h_c \mathrm{P}}{C_p}(Y_{vs} - Y_{v\infty})h_s \tag{3.6}$$

where $h$ represents the mass averaged air-vapor mixture enthalpy.

### 3.2.2. LIQUID FILM

The differential form of liquid film continuity is

$$\frac{d\dot{m}_f}{dx} = -\dot{m}'_{evap} \tag{3.7}$$

where the evaporation rate per unit length is the same as above. An energy balance on the film flow yields

$$\frac{d\left(\dot{m}_f h_f\right)}{dx} = -\dot{m}'_{evap}h_u - \dot{q}'_{surr} \tag{3.8}$$

where $\dot{q}'_{surr}$ denotes heat transferred to the external surroundings, per unit longitudinal length, and subscript '$u$' denotes the value at the control surface just below the film interface. The '$u$' surface state is assumed to be saturated liquid. Heat transfer to the external surroundings is expressed using the resistance analogy

$$\dot{q}'_{surr} = \frac{(T_s - T_{surr})}{R'} \tag{3.9}$$

where $R'$ is an effective series resistance for conduction through the wall and subsequent convection to the cyclone surroundings. The '$u$' surface enthalpy, $h_u$, is eliminated from (3.8) by writing the surface energy balance at the film-mixture interface

$$\dot{m}'_{evap} h_u = \dot{m}'_{evap} h_s - h_c \mathrm{P}\,(T_\infty - T_s) \tag{3.10}$$

for an incremental length $\Delta x$. The film is assumed to be perfectly mixed at temperature $T_s$. No temperature gradient exists at the '$u$' surface under this assumption therefore no conduction term is included as in more complicated formulations. Combining the above equations gives the final form of the differential conservation of film energy

$$\dot{m}_f C_{pf} \frac{dT_s}{dx} = -\frac{h_c \mathrm{P}}{C_p}(Y_{vs} - Y_{v\infty}) h_{fg} + h_c \mathrm{P}\,(T_\infty - T_s) - \frac{(T_s - T_{surr})}{R'} \tag{3.11}$$

where the familiar enthalpy of vaporization, $h_{fg}$, appears as a consequence of applying the chain rule and incompressible substance model, $dh_f = C_{pf} dT_s$, to the left hand side.

The equivalent resistance from the film to the external surroundings is represented as the sum of radial conduction and external convection resistances, $R' = R'_{cond} + R'_{conv}$, or

$$R' = \frac{\ln(r_o / r_i)}{2\pi \cdot k_s} + \frac{1}{h_{ext} \cdot 2\pi \cdot r_o} \tag{3.12}$$

where $k_s$, $h_{ext}$, $r_o$, and $r_i$ represent the thermal conductivity of steel, external heat transfer coefficient, and outer and inner cyclone radii, respectively.

## 3.3. Numerical Methods

### 3.3.1. ENTHALPY MODELS

Numerical solutions to the coupled heat and mass transfer equations require a formulation of air, water vapor, and liquid water enthalpies. The ideal gas model and incompressible liquid model with reference temperature at $0°C$ are used here. Vapor, air, and film enthalpies are given by

$$h_v = C_{pv} T_v + h_{fg,0} \tag{3.13}$$

$$h_a = C_{pa} T_a \tag{3.14}$$

and

$$h_f = C_{pf} T_f \tag{3.15}$$

respectively, where $C_{pv} = 1862$ (J/kgK), $C_{pa} = 1007$ (J/kgK), $C_{pf} = 4179$ (J/kgK), and $h_{fg,0} = 2.5013 \cdot 10^6$ (J/kg). The air-vapor mixture enthalpy,

$$h = Y_v (C_{pv} T_v + h_{fg,0}) + Y_a C_{pa} T_a \tag{3.16}$$

is calculated as the mass averaged mixture enthalpy. Lastly, liquid film and vapor enthalpies are combined to get the linear form of the enthalpy of vaporization,

$$h_{fg} = (C_{pv} - C_{pf}) T + h_{fg,0} \tag{3.17}$$

which is only a function of liquid temperature.

### 3.3.2. SOLUTION PROCEDURE

The mixture mass, vapor mass, and mixture energy conservation equations (3.1), (3.2), and (3.6) are written with source per unit length terms, $S'_m$ and $S'_t$,

$$\frac{d\dot{m}}{dx} = S'_m \tag{3.18}$$

$$\frac{d\left(\dot{m} Y_{v\infty}\right)}{dx} = S'_m \tag{3.19}$$

$$\frac{d(\dot{m} h)}{dx} = S'_t \tag{3.20}$$

where subscripts '$m$' and '$t$' denote mass and energy sources, respectively. The upwind convection scheme (Patankar 1980) is used to formulate the set of discretized equations. This scheme assumes diffusive fluxes are negligible with respect to convective fluxes and is valid for large Peclet number flows such as the one modeled herein. The discretized form of (3.19) is

$$\dot{m}_v\big|_P = \dot{m}_v\big|_W + S'_m\big|_P \,\Delta x \tag{3.21}$$

where the vapor mass flow rate at point ‘ $P$ ’ is the sum of the value at the upwind node ‘$W$ ’ and the contribution from mass source term. The new mixture mass flow rate is subsequently determined since the air mass flow rate is constant.

$$\dot{m}\big|_P = \dot{m}_a\big|_P + \dot{m}_v\big|_P \tag{3.22}$$

The vapor mass fraction at ‘ $P$ ’ is also found from the discretized form of (3.19)

$$Y_v\big|_P = \frac{S'_m\big|_P \,\Delta x + \dot{m}Y_v\big|_W}{\dot{m}\big|_P} \tag{3.23}$$

where the vapor mass flow rate is expressed as the product of mixture mass flow rate and vapor mass fraction. The air mass fraction is determined from the definition of mass fraction

$$Y_a\big|_P = 1 - Y_v\big|_P \tag{3.24}$$

and enables the calculation of the mass averaged mixture specific heat.

$$C_p\big|_P = Y_a C_{pa}\big|_P + Y_v C_{pv}\big|_P \tag{3.25}$$

The discretized form of the mixture energy equation is

$$\dot{m}h\big|_P = \dot{m}h\big|_W + S'_t\big|_P \tag{3.26}$$

where mass flow rates and enthalpies are mixture values.

The mass and energy source terms must be calculated to solve the set of discretized air-vapor mixture equations. Both terms are determined from the solution to the discretized form of the film energy conservation equation (3.11)

$$\dot{m}_f h_f\Big|_P - \dot{m}_f h_f\Big|_W = -\dot{m}_{evap} h_s + h_c \mathrm{P}\,\Delta x (T_\infty - T_s) - \frac{(T_s - T_{surr})}{R'}\Delta x \tag{3.27}$$

and film continuity equation (3.7).

$$\dot{m}_f\Big|_P = \dot{m}_f\Big|_W - \dot{m}_{evap} \tag{3.28}$$

The unknown $\dot{m}_f\big|_P$ is eliminated from (3.27) upon substitution of (3.28). The '$s$' surface enthalpy is assumed to be saturated vapor at $T_s$ and $h_f\big|_P$ is specified by assuming a saturated liquid at $T_s$. Collecting like terms and substituting the incompressible liquid film enthalpy model gives

$$\begin{aligned} &\dot{m}_f\Big|_W C_{pf}(T_{s,W} - T_{s,P}) + \frac{h_c \mathrm{P}}{C_p}\Delta x (Y_{vs}(T_{s,P}) - Y_{v\infty,P}) h_{fg}(T_{s,P}) \\ &\qquad - \frac{(T_{s,P} - T_{surr})}{R'}\Delta x + h_c \mathrm{P}\,\Delta x (T_{\infty,P} - T_{s,P}) = 0 \end{aligned} \tag{3.29}$$

where $T_s$ is the only unknown value. Definitions of mol fraction, mixture molecular weight, and partial pressure from the Dalton model of ideal gases are used to derive the functional dependence of saturated vapor mass fraction on temperature $T_s$

$$Y_{vs} = \frac{P_{v,sat}(T_s)}{1.6086 P_{atm} - 0.6086 P_{v,sat}(T_s)} \tag{3.30}$$

where $P_{v,sat}$ is the saturated vapor pressure. An empirical correlation

$$\ln\left(\frac{P_{v,sat}(T_s)}{P_c}\right) = \frac{T_c}{T_s}(a_1 \cdot \tau + a_2 \cdot \tau^{1.5} + a_3 \cdot \tau^3 + a_4 \cdot \tau^{3.5} + a_5 \cdot \tau^4 + a_6 \cdot \tau^{7.5}) \tag{3.31}$$

is used to calculate the saturated vapor pressure at $T_s$ where $\tau = 1 - T_s / T_c$, and $P_c$, $T_c$ are the critical pressure and temperature of water, respectively (Wagner 1993). The solution to the set of (3.29) through (3.31) determines the value of $T_s$. Newton-Raphson iteration (Stoecker 1989) was used to solve for $T_s$. Saturated vapor pressure and saturated vapor mass fraction, $P_{v,sat}(T_s)$ and $Y_{vs}(T_s)$, were then calculated to determine the magnitudes of the mass and energy source terms.

The model was implemented in the Visual Studio C# programming language. This allowed for a windows based application to be developed in which model inputs were easily changed and outputs could be plotted without post-processing. This was most advantageous in model and computational debugging stages. The user first specifies input parameters such as sampled air stream temperature and relative humidity, cyclone internal and external heat transfer coefficients, air sampling mass flow rate, and liquid input rate. One-dimensional arrays for solution parameters, e.g. mixture vapor mass fraction, are filled with initial values calculated from model inputs. The code begins calculations at the first node. Newton-Raphson iteration is used to determine the film surface temperature and resulting source terms. A relaxation factor of 0.2 was used to slow convergence due to large source terms that caused divergence for certain initial conditions. Arrays representing mixture, air, and vapor mass flow rates, air and vapor mass fractions, and mixture specific heat at the node were updated according to the discretized equations. The film mass flow rate was also updated to reflect liquid mass transfer to the air-vapor mixture. The energy source term was used to determine an intermediate value of air-vapor mixture temperature from rearranging (3.29). This procedure was then repeated until the solution at node '$P$' converged. Three convergence criteria were employed: relative changes in mixture temperature and mixture vapor mass fraction were negligible and (3.29) was satisfied to ensure the solution values conserved mass and energy.

The solution procedure was repeated at the downwind node after convergence at the previous node. The upwind scheme effectively makes the solution at '*P*' independent of downstream conditions, therefore the solver marched longitudinally until there were no additional downstream nodes for which a solution was required. Summary parameters like total mass evaporation rate, heat transfer to the surroundings, and air-vapor mixture output temperature and relative humidity were calculated and included in the model output GUI.

### 3.3.3. CODE VERIFICATION

Global mass

$$\Delta\dot{m} = \left[\dot{m}_v + \dot{m}_f\right]_{x=0} - \left[\dot{m}_v + \dot{m}_f\right]_{x=L} \tag{3.32}$$

and energy balances

$$\Delta E = \left[\dot{m}h + \dot{m}_f h_f\right]_{x=0} - \left[\dot{m}h + \dot{m}_f h_f\right]_{x=L} + \dot{q}_s \tag{3.33}$$

were calculated to check each solution for energy and mass conservation. Typical values of the differences were approximately $\Delta\dot{m} = 10^{-20}$ and $\Delta E = 10^{-5}$. Solutions profiles were also examined for proper physical behavior. The mixture relative humidity did not exceed 100%. Liquid film and air-vapor mixture temperature and vapor mass fractions also become equal as the film becomes infinitely long.

## 3.4. WWC Internal Heat Transfer Coefficient

The numerical two-phase heat and mass transfer model requires an estimate of the internal heat transfer coefficient. The Dittus-Boelter Equation,

$$N_{u_D} = \frac{h_c D}{k} = 0.023 Re_D{}^{0.8} Pr^{0.4} \tag{3.34}$$

is an empirical relationship which describes turbulent heat transfer coefficients for internal flows where the diameter $D$ is the hydraulic diameter, $D_h = 4A_c / P$. Air enters the cyclone through a rectangular slot where the flow is most geometrically constricted. An air stream tube with dimensions equal to the slot is envisioned to spiral down the bore of the cyclone. The hydraulic diameter is calculated from slot dimensions. Measured WWC air flow rates, corresponding slot air velocities, Reynolds and Nuesselt numbers, and convection heat transfer coefficients were calculated. An average heat transfer coefficient of $195 \pm 15$ W/m$^2$K is predicted from (3.34).

Experiments have been conducted in which the WWC-100 cyclone body was submerged in a vigorously stirred chilled water bath. The inlet and outlet air temperatures were measured along with the water bath temperature. The cyclone wall temperature is approximated by the water bath temperature under the assumption of a large forced convection coefficient within the chilled water bath. One data point from this study was used to approximate the internal heat transfer coefficient of the WWC-100. A simple, internal flow, constant surface temperature energy analysis is described by Incropera and Dewitt (2002). This solution was used to determine the net heat transfer, log-mean temperature difference, and average internal convection coefficient. The mean inlet and outlet air temperatures were $31.5°C$ and $26.3°C$ when the water bath was held at $T_s = 20.3°C$. The internal heat transfer coefficient required to transfer this amount of energy to the water bath from the air is approximately 260 W/m$^2$K. The surface area used in this calculation was based on the internal cyclone bore. The actual experimentally chilled surface area was larger because portions of the cyclone inlet and skimmer were also submerged in the bath. Underestimating the chilled surface area by

25% would result in an overestimate of the heat transfer coefficient by 25%. After accounting for this error, the Dittus-Boelter prediction for internal heat transfer coefficient based on slot dimensions (195 W/m$^2$K) is verified. The average internal heat transfer coefficient should be approximately equal to the coefficient in the inlet slot as predicted by the Dittus-Boelter equation.

## 3.5. Adiabatic Wall Model

### 3.5.1. APPROXIMATE ANALYTICAL SOLUTION

#### 3.5.1.1. Vapor Mass Fraction and Temperature Profiles

Governing heat and mass transfer equations were simplified to obtain approximate analytical solutions for the temperature and vapor mass fraction profiles in the $x$ direction. Heat transfer from the film to the cyclone surroundings is neglected. The appropriateness of this assumption is evaluated by comparing heat transfer resistances from the film to the internal flow, and film to the cyclone surroundings. The internal convection heat transfer coefficient is approximately 180 W/m$^2$K as will be shown later. The natural convection coefficient on the exterior of the cyclone is approximately 1-10 W/m$^2$K. The ratio of heat transfer coefficients (20-200) is equal to the ratio of heat transfer resistances if the cylinder is assumed to have negligible thickness. Heat transfer to the surroundings is therefore negligible with respect to internal heat transfer. Physically this means the cyclone body can be assumed adiabatic even though it is not insulated from its environment. The chain rule applied to the left hand side of (3.6) gives

$$\dot{m}C_p \frac{dT_\infty}{dx} = -h_c \mathrm{P}\,\Delta T + \frac{h_c \mathrm{P}}{C_p}\Delta Y_v (h_s - h) \tag{3.35}$$

where $\Delta Y_v = Y_{vs}(x) - Y_{v\infty}(x)$ and $\Delta T = T_\infty(x) - T_s(x)$. The mixture enthalpy is expressed with the ideal gas model assuming constant specific heat. This term appears on the right hand side as a difference with respect to the film surface saturated vapor enthalpy. Gathering like terms results a relationship for the change in mixture temperature with longitudinal distance.

$$\frac{dT_\infty}{dx} = \frac{h_c \mathrm{P}}{\dot{m} C_p}\left[-\Delta T + \frac{(h_s - h)}{C_p}\Delta Y_v\right] \tag{3.36}$$

A similar expression is derived from (3.11) for the change in liquid film surface temperature.

$$\frac{dT_s}{dx} = \frac{h_c \mathrm{P}}{\dot{m}_f C_{pf}}\left[\Delta T - \frac{h_{fg}}{C_p}\Delta Y_v\right] \tag{3.37}$$

The rate of change of the temperature difference is determined by subtracting (3.37) from (3.36)

$$\frac{d\Delta T}{dx} = \frac{h_c \mathrm{P}}{\dot{m}_f C_{pf}}\left[-\Delta T\left(\frac{\dot{m}_f C_{pf}}{\dot{m} C_p} + 1\right) + \frac{\Delta Y_v}{C_p}\left(\frac{\dot{m}_f C_{pf}}{\dot{m} C_p}(h_s - h) + h_{fg}\right)\right] \tag{3.38}$$

where the ratio of film to mixture thermal flow capacities appears. Co-annular film flows considered here lie in the range $0.001 < \left(\dot{m}_f C_{pf} / \dot{m} C_p\right) < 0.01$. The temperature difference reduces to

$$\frac{d\Delta T}{dx} = \frac{h_c \mathrm{P}}{\dot{m}_f C_{pf}}\left(-\Delta T + \Delta Y_v \frac{h_{fg}}{C_p}\right) \tag{3.39}$$

when the ratio of thermal flow capacities is small. The term $(h_s - h)$ conveniently drops out of the equation since the enthalpy differences are of the same order of magnitude for typical air and film temperatures ($280 < T < 330K$) and the ratio of thermal flow capacities is small. Dimensionless temperature and vapor mass fraction differences are defined as

$$\theta = \frac{T_\infty(x) - T_s(x)}{\Delta T_c} \tag{3.40}$$

and

$$\beta = \frac{Y_{vs}(x) - Y_{v\infty}(x)}{\Delta Y_{vc}} \tag{3.41}$$

respectively, where characteristic temperature and vapor mass fraction differences are written succinctly as $\Delta T_c$ and $\Delta Y_{vc}$. The dimensionless form of (3.39) is

$$\frac{d\theta}{d\eta} = \frac{h_c \mathrm{P} L}{\dot{m}_f C_{pf}} \left( -\theta + \frac{\Delta Y_{vc}}{\Delta T_c} \frac{h_{fg}}{C_p} \beta \right) \tag{3.42}$$

where the dimensionless longitudinal length is expressed as $\eta = x / L$. The solution to the dimensionless temperature difference profile is a function of the dimensionless vapor mass fraction.

The conservation of mixture vapor mass, (3.4), is simplified by applying the chain rule to the left hand side.

$$\dot{m} \frac{dY_{v\infty}}{dx} = (1 - Y_{v\infty}) \frac{h_c \mathrm{P}}{C_p} \Delta Y_v \tag{3.43}$$

The mixture vapor mass fraction is generally on the order of a few percent, $Y_{v\infty} << 1$, for moist air near standard temperature and pressure. Thus, the $Y_{v\infty}$ term drops out. Algebraic manipulation of Equation (3.43) under the assumption that $\frac{dY_{vs}}{dx}$ is negligible gives an interesting result.

$$\dot{m} \frac{d\Delta Y_v}{dx} = -\frac{h_c \mathrm{P}}{C_p} \Delta Y_v \tag{3.44}$$

This assumption is only appropriate when the film surface quickly attains its equilibrium temperature and remains constant. The saturated vapor mass fraction at the surface is then constant along $x$ as well. This occurs under steady-state conditions when no heat transfer occurs between the film and the external surroundings, i.e. adiabatic wall. No energy storage occurs under steady-state conditions. Furthermore, the small ratio of thermal flow capacities results in a rapid change in film temperature to its equilibrium, adiabatic saturation ($T_{as}$), state. The sensible and latent heat transfer rates from the film to the air-vapor mixture must be equal after the adiabatic saturation point is reached.

The simple ordinary differential equation (3.44) implies the vapor mass fraction difference is independent of the mixture-film temperature difference and liquid film thermal flow capacity

$$\beta = \exp\left(-\gamma\eta\right) \tag{3.45}$$

where $\gamma = \frac{h_c \mathrm{P} L}{\dot{m} C_p}$. This expression is substituted into (3.42) and the analytical solution to the dimensionless temperature difference

$$\theta = (1-C)\cdot exp\left(-\alpha\eta\right) + C\cdot exp\left(-\gamma\eta\right) \tag{3.46}$$

is derived where $\alpha = \frac{h_c \mathrm{P} L}{\dot{m}_f C_{pf}}$ and $C = \frac{\Delta Y_{vc}}{\Delta T_c}\frac{h_{fg}}{C_p}$. The first term, $exp\left(-\alpha\eta\right)$, decays much faster than the second, $exp\left(-\gamma\eta\right)$, due to the small ratio of thermal flow capacities. Both dimensionless temperature and vapor mass fraction differences are a function of the mixture mass flow rate and independent of the film mass flow rate. The functional group $\gamma$ shows a decrease in the mixture mass flow rate has the same effect as increasing the wetted surface area or heat transfer coefficient.

### 3.5.1.2. Heat and Mass Transfer Rates

The total film evaporation rate

$$\dot{m}_{evap} = \int_0^L \frac{h_c \mathrm{P}}{c_p} \left[ Y_{vs}(x) - Y_{v\infty}(x) \right] \cdot dx \tag{3.47}$$

is calculated by integrating equation (3.3) over the longitudinal length. The significance of equation (3.45) is now apparent. Upon substitution of (3.45) into (3.47), the total evaporation rate

$$\dot{m}_{evap} = \left[ \frac{h_c \mathrm{P} L}{c_p} \int_0^1 e^{-\gamma\eta} \cdot d\eta \right] \Delta Y_{vc} \tag{3.48}$$

is observed to be a constant product of geometrical and heat transfer properties, $C_c$, and the inlet vapor mass fraction difference, $\Delta Y_{vc}$.

$$\dot{m}_{evap} = C_c \cdot \Delta Y_{vc} \tag{3.49}$$

The total heat transfer rate can then be calculated from the evaporation rate and enthalpy of vaporization,

$$Q = \dot{m}_{evap} h_{fg} \tag{3.50}$$

since the film temperature is assumed constant and no heat transfer to the external surroundings occurs.

In summary, simple analytical solutions for the temperature and vapor mass fraction differences, and net heat and mass transfer rates, are derived under the assumptions of negligible heat transfer to the exterior surroundings, a small ratio of film to mixture thermal flow capacities, and constant liquid film temperature equal to the adiabatic saturation temperature. Specific heats, enthalpy of vaporization, and mass flow rates are also considered constant. Accuracy achieved under this set of assumptions will be evaluated from comparison of numerical and approximate analytical solutions.

#### 3.5.1.3. Adiabatic Saturation Temperature

The adiabatic saturation temperature is a critical parameter in the approximate analytical solutions derived above. A physical description of this temperature is useful in understanding why it is the asymptotic film temperature when the wall is adiabatic. Consider an insulated container enclosing both liquid water and an air-vapor mixture. Sensible heat will be transferred to the liquid water under non-equilibrium initial conditions. This sensible heat exchange must be balanced by latent energy transfer, evaporation, to the mixture since the container is adiabatic. Heat and mass transfer will continue to occur until the air becomes saturated at decreased temperature with respect to its initial temperature. At this point the liquid and air-vapor mixture will be isothermal with temperature defined as the adiabatic saturation temperature. This mixture property is often approximated by the wet bulb temperature although only valid for air-water vapor mixtures in the normal ranges of temperature and pressure for atmospheric air.

The adiabatic saturation temperature is a mixture property and therefore only dependent on the initial air temperature and vapor content. An energy balance on the film interface with an adiabatic wall condition gives

$$[T_\infty - T_{as}] - \frac{h_{fg}(T_{as})}{c_{p\infty}} \cdot [Y_{vs}(T_{as}) - Y_{v\infty}] = 0 \tag{3.51}$$

where no dependence on heat transfer coefficient or geometrical properties are observed. The adiabatic saturation temperature can also be determined from a thermodynamic analysis as presented by Moran and Shapiro (2000). The sensible and latent heat transfer rates are zero at the point of adiabatic saturation. Prior to saturation the latent and sensible heat transfer rates are equal and opposite. The adiabatic saturation temperature is shown in Figure 3.2 over a broad range of initial air temperature and relative humidity. As expected, the initial air temperature is equal to the adiabatic saturation temperature for initially saturated air. For the adiabatic case of an infinitely long film, the film temperature must go to the adiabatic saturation temperature as evaporation drives the mixture to saturated conditions.

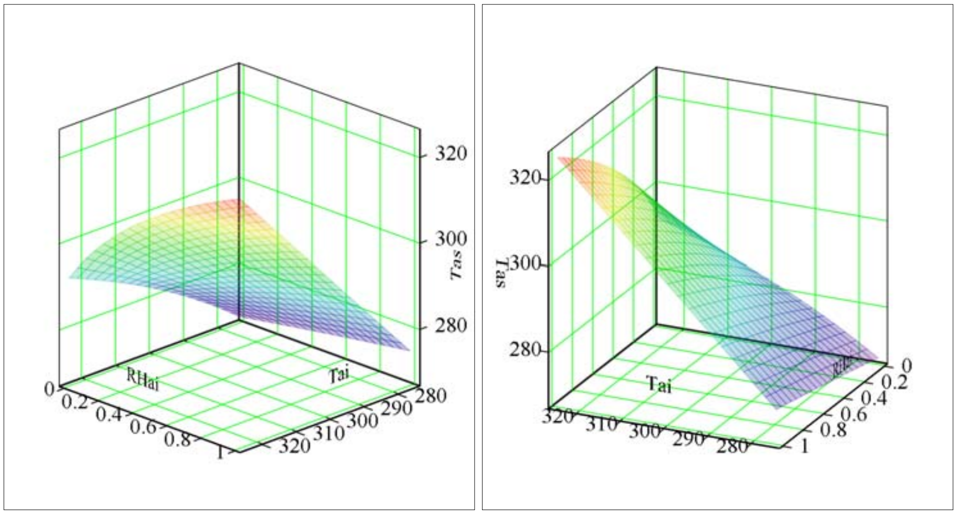

Figure 3.2: Adiabatic saturation temperature plotted against initial air temperature and relative humidity

### 3.5.2. SIMULATIONS OF HEAT AND MASS TRANSFER

Steady-state solutions of the evolving temperature and vapor mass fraction profiles were calculated for a variety of geometrical configurations, heat transfer properties, and initial conditions. Simulation parameter sets A through M are given in Table 3.1. The adiabatic wall condition was imposed by setting the external heat transfer coefficient to $10^{-6}$. Inlet air temperatures, relative humidity, and resulting adiabatic saturation temperatures ranged from 290 to 320 K, 0% to 75%, and 275 to 315 K, respectively. The wetted-perimeter corresponded to the inside diameter of the WWC-

100. Lengths from 1.0 to 2.0 meters were used to attain equilibrium conditions for some cases. The air flow rate and film flow rate were chosen as 250 Lpm and 2000 μL/min, respectively, to provide a ratio of thermal flow capacities much less than 1 ($\dot{m}_f C_{pf} / \dot{m} C_p = 0.007$). This was intentionally selected such that numerical results could be compared to approximate analytical solutions derived in Section 3.5.

| **$Q_a$ (Lpm)** | 250 |
|---|---|
| **$Q_f$ (μL/min)** | 2000 |

| Series | L (m) | Dia (m) | $h_c$ (W/m$^2$K) | $T_{s,i}$ (K) | $T_{inf,i}$ (K) | $RH_i$ | $T_{as}$ (K) |
|---|---|---|---|---|---|---|---|
| A | 1.0 | 0.015 | 150 | 290 | 290 | 0.00 | 277.4 |
| B | 1.5 | 0.015 | 150 | 290 | 290 | 0.35 | 282.4 |
| C | 2.0 | 0.015 | 150 | 290 | 290 | 0.70 | 286.7 |
| D | 1.0 | 0.020 | 200 | 300 | 300 | 0.00 | 282.3 |
| E | 1.5 | 0.020 | 200 | 300 | 300 | 0.35 | 289.9 |
| F | 2.0 | 0.020 | 200 | 300 | 300 | 0.70 | 295.8 |
| G | 1.0 | 0.025 | 250 | 280 | 310 | 0.00 | 286.6 |
| H | 1.5 | 0.025 | 250 | 280 | 310 | 0.35 | 297.3 |
| I | 2.0 | 0.025 | 250 | 280 | 310 | 0.70 | 304.9 |
| J | 1.0 | 0.010 | 100 | 290 | 290 | 0.00 | 277.4 |
| K | 1.5 | 0.010 | 100 | 290 | 290 | 0.35 | 282.4 |
| L | 2.0 | 0.010 | 100 | 290 | 290 | 0.70 | 286.7 |
| M | 1.0 | 0.015 | 200 | 290 | 285 | 0.00 | 274.6 |
| N | 1.0 | 0.015 | 200 | 290 | 285 | 0.25 | 277.5 |
| O | 1.0 | 0.015 | 200 | 290 | 285 | 0.50 | 280.2 |
| P | 1.0 | 0.015 | 200 | 290 | 285 | 0.75 | 282.7 |
| Q | 1.0 | 0.015 | 200 | 290 | 320 | 0.25 | 301.5 |
| R | 1.0 | 0.015 | 200 | 290 | 320 | 0.50 | 309.2 |
| S | 1.0 | 0.015 | 200 | 290 | 320 | 0.75 | 315.2 |

Table 3.1: Input parameters for simulation of coupled heat and mass transfer from a thin liquid film with adiabatic wall condition

Liquid film surface and air-vapor mixture temperatures are plotted against longitudinal distance in Figure 3.3 for parameter sets A through L. Each color represents one set of simulation parameters. The liquid surface temperature profiles do not change significantly after approximately the first 5 centimeters. Equilibrium liquid film surface temperatures are the adiabatic saturation temperatures corresponding to initial air conditions. Temperature profiles for simulation G terminate prior to the final length of one meter. This is the result of complete evaporation, $\dot{m}_f = 0$, having occurred at a length of 40 centimeters. Mixture and film temperatures converge with sufficient length. Figure 3.4 shows the vapor mass fraction profiles for simulations A through L. The film surface vapor mass fraction is constant once the adiabatic saturation temperature has been reached.

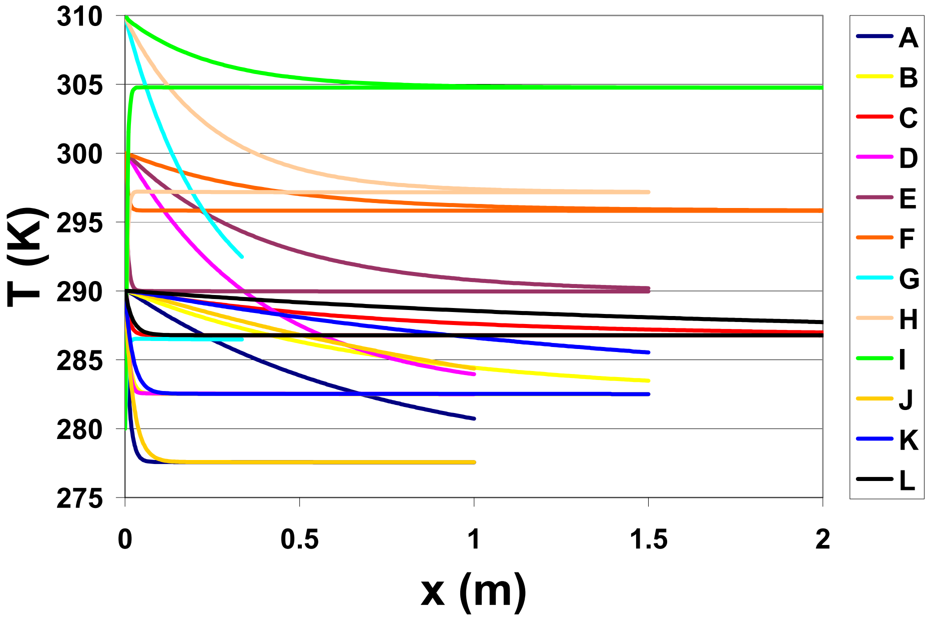

Figure 3.3: Numerical solutions for air-vapor mixture and film temperatures (K) versus axial length for adiabatic wall condition and various inlet conditions

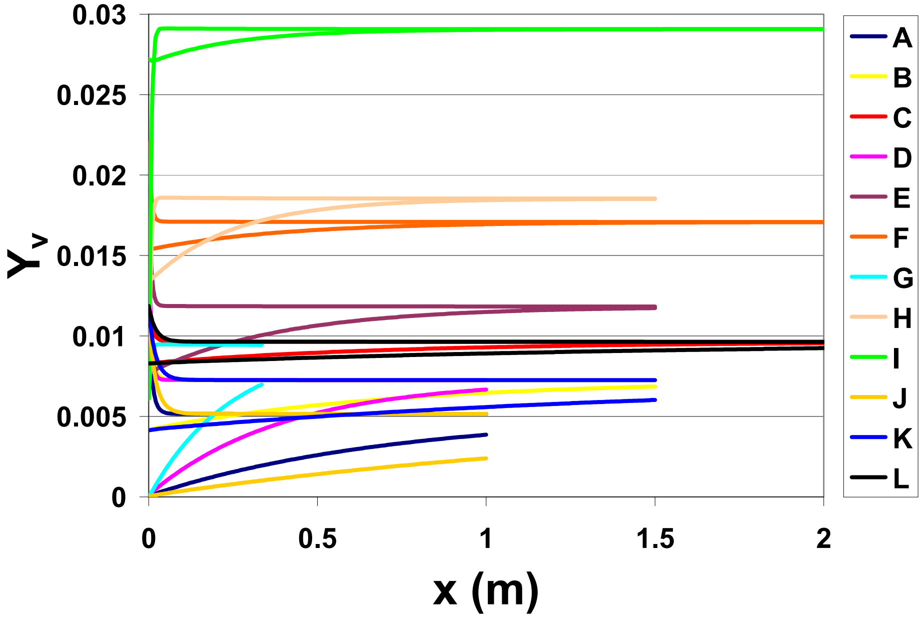

Figure 3.4: Numerical solutions for air-vapor mixture and liquid film surface vapor mass fraction versus axial length for adiabatic wall condition and various inlet conditions

Characteristic temperature and vapor mass fractions are expressed as differences in initial, "$i$", and adiabatic saturation, "$as$", conditions, $\Delta T_c = T_{\infty,i} - T_{as}$ and $\Delta Y_{vc} = Y_{vs,as} - Y_{v\infty,i}$. Dimensionless temperature and vapor mass fraction differences, $\theta$ and $\beta$, are shown in Figure 3.5 and Figure 3.6 for simulations A through L. Numerical solutions are shown as hollow symbols. Profiles from the approximate analytical solutions, (3.45) and (3.46), are also shown in the figures as solid lines. Good agreement $(\pm 5\%)$ is observed for $\eta > 0.05$. The assumption of $\frac{dY_{vs}}{dx} = 0$ used in the derivation of the analytical solutions is valid after a brief entrance region in which the liquid film attains the adiabatic saturation temperature. This is the reason numerical solutions profiles start at values of $\theta$ and $\beta$ not equal to 1. Analytical and numerical profiles demonstrate good agreement, irrespective of initial conditions, once this assumption becomes valid.

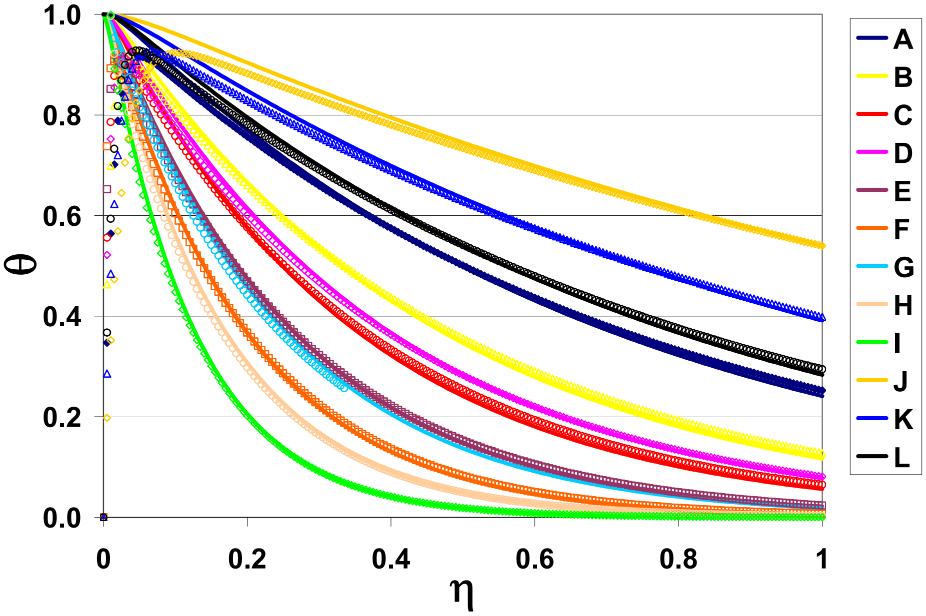

Figure 3.5: Dimensionless temperature difference plotted against the dimensionless longitudinal length for full numerical model and approximate analytical solution

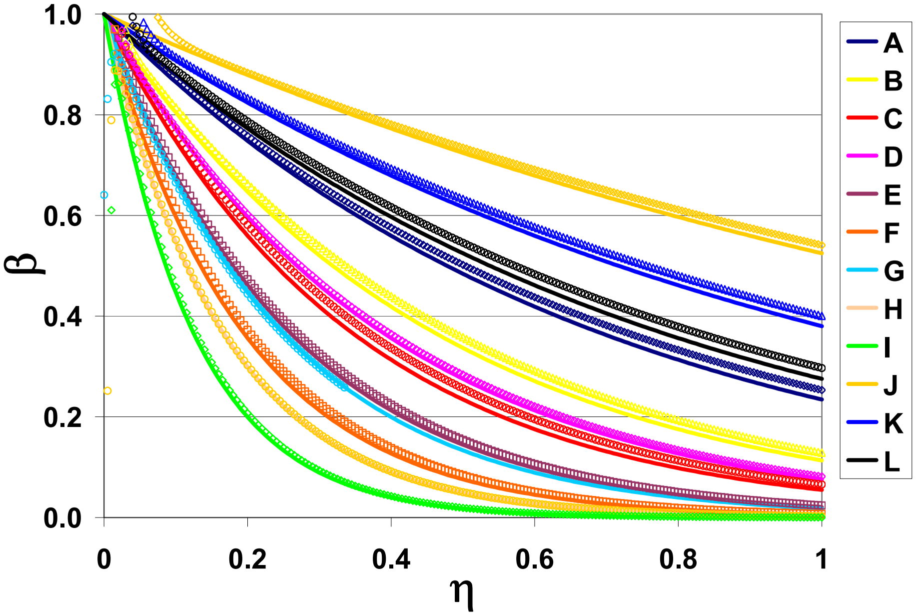

Figure 3.6: Dimensionless vapor mass fraction difference plotted against the dimensionless longitudinal length for full numerical model and approximate analytical solution

Net evaporation rates (μL/min) and heat transfer rates (W) are given in Table 3.1. Errors in the net rates of heat and mass transfer predicted by the analytical solution are approximately $\pm 10\%$, with respect to the numerical solution, for a wide range of simulation parameters. The error magnitude is dependent on the entrance length and increases with increasing difference between initial and adiabatic saturation conditions. The majority of simulations A through L have zero initial temperature difference. Simulations M through S were performed to evaluate the effects of growing entrance length (i.e. increasing range of $\theta_i$ and $\beta_i$) on the accuracy of the analytical solutions. Good accuracy ($\pm 10\%$) is achieved for $|\theta_i| < 10$ and $|\beta_i| < 10$.

These simulations illustrate the accuracy with which heat and mass transfer rates can be approximated from the approximate analytical solution when no heat transfer to the external surroundings is considered. The rates are only dependent upon the initial air conditions and geometrical and heat transfer properties. Two-phase heat and mass transfer rates can be calculated within $\pm 10\%$ without significant computational cost.

|  |  |  | $Q_{evap}$ (μL/min) |  |  | Q (W) |  |  |
|---|---|---|---|---|---|---|---|---|
| **Series** | $\theta_i$ | $\beta_i$ | **Numerical** | **Analytical** | Δ(%) | **Numerical** | **Analytical** | Δ(%) |
| A | 0.00 | 2.33 | 1182 | 1133 | -4.1 | 47.2 | 47.0 | -0.5 |
| B | 0.00 | 2.51 | 833 | 791 | -5.1 | 33.3 | 32.7 | -1.9 |
| C | 0.00 | 2.70 | 386 | 364 | -5.6 | 15.4 | 15.0 | -2.7 |
| D | 0.00 | 3.07 | 1979 | 1922 | -2.9 | 79.2 | 79.4 | 0.3 |
| E | 0.00 | 3.47 | 1218 | 1176 | -3.4 | 48.5 | 48.3 | -0.5 |
| F | 0.00 | 3.85 | 518 | 499 | -3.7 | 20.5 | 20.4 | -0.8 |
| G | 1.28 | 0.64 | >2000 | 2721 |  | >86.3 | 112.0 |  |
| H | 2.37 | -1.41 | 1451 | 1512 | 4.2 | 65.8 | 61.6 | -6.3 |
| I | 5.89 | -9.99 | 539 | 613 | 13.8 | 31.1 | 24.8 | -20.2 |
| J | 0.00 | 2.33 | 733 | 703 | -4.1 | 28.6 | 29.2 | 1.8 |
| K | 0.00 | 2.51 | 578 | 554 | -4.2 | 22.8 | 22.9 | 0.4 |
| L | 0.00 | 2.70 | 292 | 279 | -4.5 | 11.6 | 11.5 | -0.7 |
| M | 4.49 | -2.27 | 1105 | 1039 | -6.0 | 43.8 | 43.2 | -1.3 |
| N | 5.55 | -3.10 | 800 | 749 | -6.4 | 31.0 | 31.1 | 0.3 |
| O | 7.65 | -4.75 | 517 | 480 | -7.2 | 19.6 | 19.9 | 1.6 |
| P | 13.89 | -9.70 | 255 | 231 | -9.2 | 9.0 | 9.6 | 5.9 |
| Q | -0.58 | 1.62 | 1806 | 1902 | 5.3 | 77.6 | 77.2 | -0.5 |
| R | -4.71 | 2.79 | 1023 | 1114 | 8.9 | 46.7 | 44.9 | -3.8 |
| S | -18.86 | 6.22 | 412 | 502 | 21.9 | 22.8 | 20.1 | -11.7 |

Table 3.2: Net evaporation rate (μL/min) and net heat transfer rate (Watts) for simulated co-current air-film flow with adiabatic wall condition as calculated with numerical code and approximate analytical solution

## 3.6. Modeling WWC Critical Liquid Input Rate

Wetted-wall cyclone performance for any air flow rate and air conditions can be predicted from the critical liquid input rate at those conditions. Experiments were conducted and multiple linear regression models were adopted for the critical liquid input rate at air flow rates of 100, 400, and 1250 Lpm. Better predictions of the critical liquid input rate were desired since experimental measurements were performed over a limited domain. Extrapolation would be required for some climates, e.g. very hot and dry. This could result in significant error since linear dependencies were assumed with respect to air conditions. The empirical models also fail to enforce proper physical behavior near saturated conditions. Analytical and numerical two-phase heat and mass transfer formulations described above were used to model the critical liquid input rate data and develop semi-empirical models with better accuracy, proper physical behavior, and more reliability for all air conditions.

### 3.6.1. APPROXIMATE ANALYTICAL SOLUTION

Equation (3.48) was used in preliminary predictions of liquid evaporation since it demonstrated good accuracy and computational efficiency. The approximate analytical solution does not require knowledge of the film mass flow rate since the ratio of thermal flow capacities was assumed negligibly small. The only unknown variable in the solution is the convection heat transfer coefficient. Evaporation rates corresponding to experimental air conditions were calculated for each of the wetted-wall cyclones assuming an arbitrary heat transfer coefficient of 195 W/m$^2$K. A least squares regression was then performed on the predicted and measured values of the critical liquid input rate. The coefficient of determination was maximized by optimizing the heat transfer coefficient. In other words, approximate analytical solutions for experimentally observed critical liquid input rates were optimized by finding the heat transfer coefficient required to produce said evaporation rates.

Figure 3.7 shows the analytical model error as a percent difference,

$$\Delta Q_c = \frac{Q_{c,data} - Q_{c,model}}{Q_{c,data}} \cdot 100\% \tag{3.52}$$

in measured, $Q_{c,data}$, and model, $Q_{c,model}$, critical liquid input rates for the WWC-100. The model error is plotted against the measured critical liquid input rate which increases with increasing temperature and decreasing relative humidity.

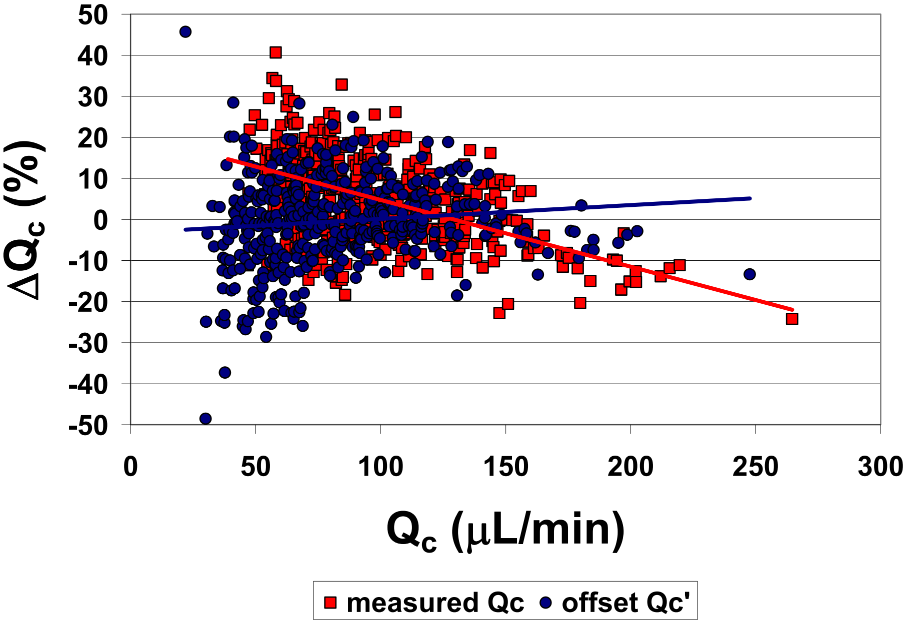

Figure 3.7: Analytical model critical liquid input rate error (%) versus critical liquid input rate (μL/min) for measured values of the WWC-100 critical liquid input rate as well as offset values to account for atomizer effects

Some dependence on critical liquid input rate is observed. The percent error is large and positive for small values of the critical liquid input rate (near saturated conditions). These errors correspond to absolute errors of approximately 20 μL/min. The percent error is large and negative for high critical liquid input rate, hot and dry conditions, and corresponds to absolute error of approximately 50 μL/min. One plausible explanation for this discrepancy is that atomizer effects are not properly modeled in the co-annular film flow model. Figure 2.30 shows the results of experiments conducted to quantify evaporative losses occurring upstream of the inlet slot. Liquid losses on the order of 20-80 μL/min were attributed to stationary pendant shaped droplets in the cyclone inlet. These losses represent phenomena that should not be included when modeling evaporative losses downstream of the slot when the flow more reasonably resembles co-current air-film flow. Hence, the measured critical liquid input rates were offset by a constant liquid flow rate, $Q_c' = Q_{c,data} - Q_{c,offset}$, to reflect only the losses occurring downstream of the slot where the model physics are most reflective of the true physics. This offset has a greater effect on the percent error near saturated conditions when its relative magnitude is significant with respect to the critical liquid input rate. For example, assume the critical liquid input rate for a single experiment is 50 μL/min. Of those 50 μL/min, 20 μL/min evaporate upstream of the slot, leaving only 30 μL/min to evaporate downstream of the slot. Net evaporation of 30 μL/min, not 50 μL/min, should be modeled with the film flow model. The relative magnitude of this offset is 40% compared to 10% when the critical liquid input rate is 200 μL/min (away from saturation).

The coefficient of determination was re-optimized on $h_c$ and $Q_{c,offset}$ and the percentage model error was recalculated with respect to offset critical liquid input rate data ($Q_c'$). The dependence of model error on critical liquid input rate was observed to decrease. Optimized model parameters providing the best fit to data are given in Table 3.3 for all three wetted-wall cyclones. The optimized heat transfer coefficients were all nominally 180 W/m$^2$K. Optimized offset liquid flow rates were 17, 53, and 109 μL/min for the 100, 400, and 1250 Lpm cyclones.

| WWC | 100 | 400 | 1250 |
|---|---|---|---|
| $h_c$ (W/m$^2$K) | 180 | 179 | 178 |
| offset (μL/min) | 17 | 53 | 109 |
| $\gamma$ | 0.154 | 0.121 | 0.092 |
| $R^2$ | 0.95 | 0.92 | 0.96 |

Table 3.3: Optimized heat transfer coefficients (W/m$^2$K) and rate offsets (μL/min) for analytical model predictions of critical liquid input rate for the WWC-100, WWC-400, and WWC-1250

Figure 3.8 shows the percentage error in the offset critical liquid input rate. The errors are approximately randomly distributed about 0. This shows the offsetting procedure reduced the dependence of model error on air conditions. The errors tend to decrease with increasing critical liquid input rate and range from 40% near the lower limit of critical liquid input rate and 10% in the upper limit. The minimum and maximum absolute errors are approximately 20 and 150 μL/min, respectively, and occur for the minimum and maximum offset critical liquid input rate.

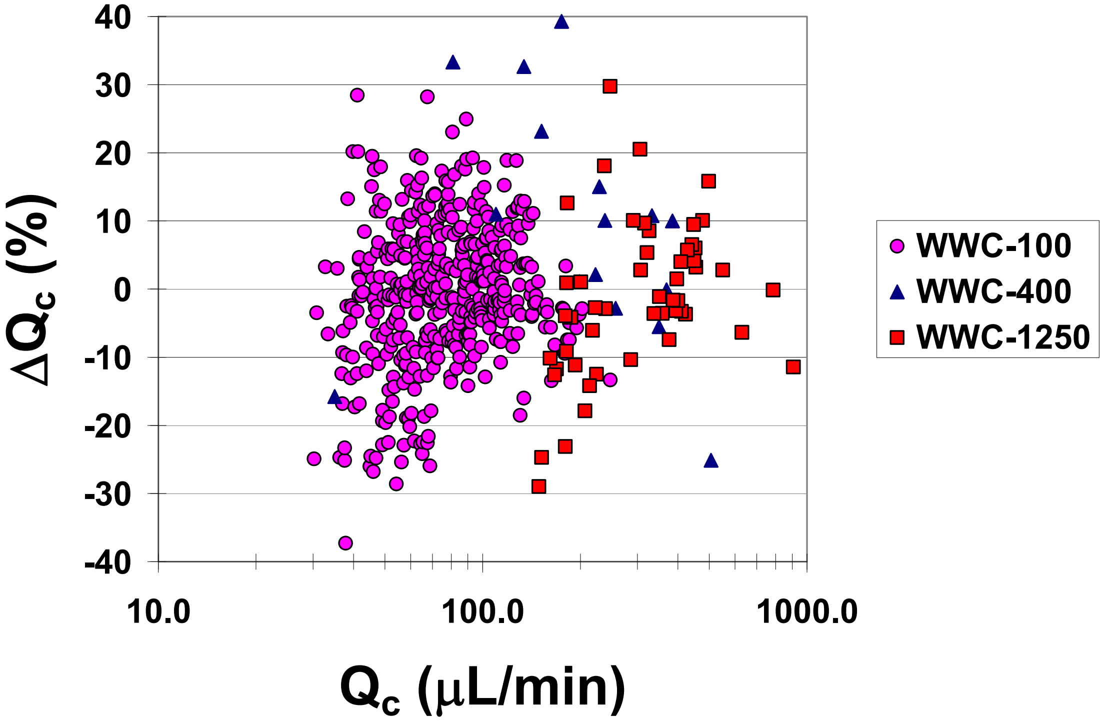

Figure 3.8: Error in analytical solution predictions of offset critical liquid input rate with optimized parameters: heat transfer coefficient ($W/m^2K$) and rate offset (μL/min)

Data from atomizer experiments, described in section 2.5, support the notion of increasing offset for the WWC-100, 400 and 1250. Non-film-evaporation losses increase with increasing liquid input rate. Therefore, the offset values are expected to increase because liquid injection rates increase with increasing air flow rate. More experiments are needed to accurately describe the physical nature of losses in the inlet section. The dependence of non-film-evaporation losses on air conditions and air flow rate is unknown.

The evaporation models developed here assume the entire cyclone surface is wetted. The true percentage of wetted area is unknown. Optimizing the convection heat transfer coefficient to match the data essentially counteracts any error inherent in this assumption. The Dittus-Boelter equation and experiments suggest a heat transfer coefficient of 195 W/m$^2$K. Optimized model heat transfer coefficients are 180 W/m$^2$K. Good agreement is observed which could imply the wetted surface area is approximately equal to the internal cyclone surface area.

### 3.6.2. SEMI-EMPIRICAL MODEL FOR CRITICAL LIQUID INPUT RATE

Predictions of the critical liquid input rate were made with the numerical model utilizing optimized heat transfer coefficients and offset liquid flow rates described above. The critical liquid input rate was modeled as the liquid input rate for which the film flow rate was non-zero over the entire length of the cyclone, i.e. onset of total evaporation. This was accomplished by sequentially increasing the numerical model liquid input rate until the film mass flow rate at $x = L$ became non-zero. Calculations were made for $275 < T_\infty < 330\,K$ and $0 < RH_\infty < 100\%$ at increments of $2.5\,K$ and $5\%$, respectively. The numerical model predictions were approximated by third order polynomials in Mathcad. Measured values of $Q_c'$ and numerically predicted contour surfaces are given in Figure 3.9A, B, and C, for the WWC-100, WWC-400, and WWC-1250, respectively. All three critical liquid input rate surfaces are plotted together in Figure 3.10 to show their relative magnitudes. Proper asymptotic behavior is observed as the air becomes saturated.

Maximum values of the critical liquid input rate are approximately 2000, 800, and 500 μL/min at $330\,K$ and $0\%$.

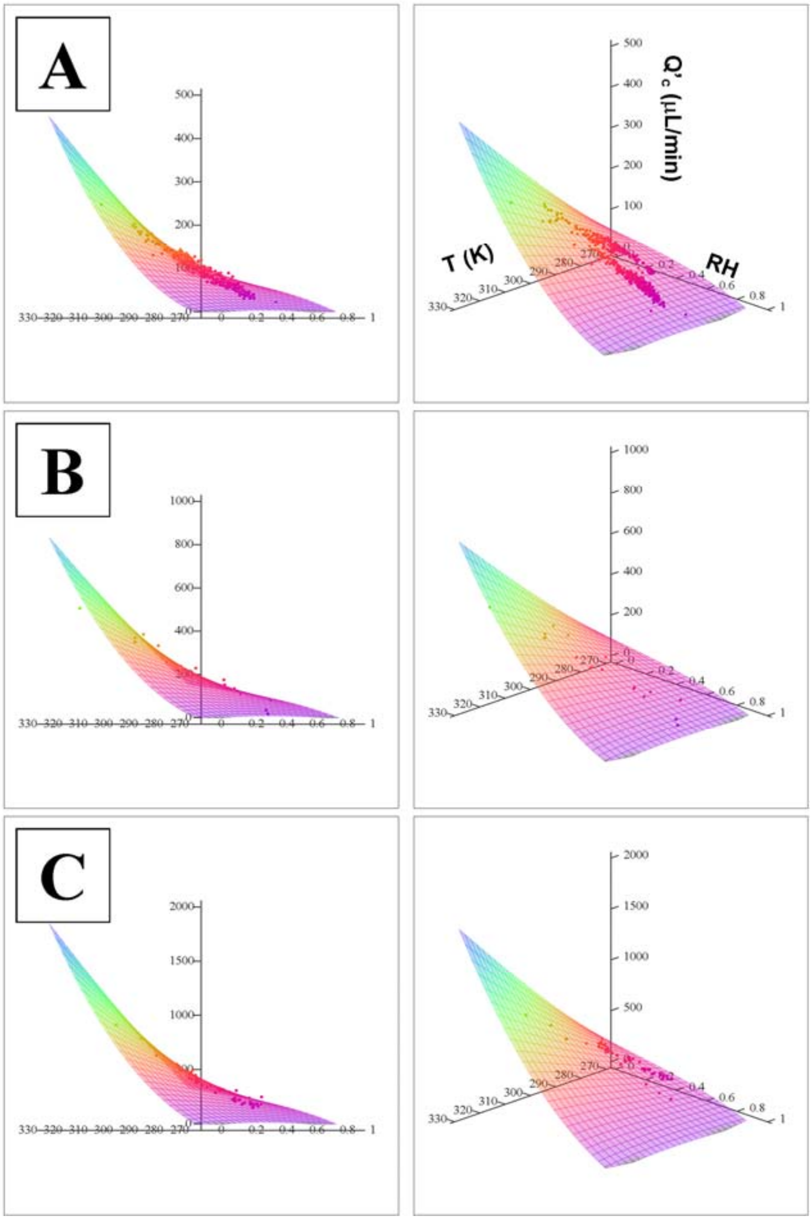

Figure 3.9: Numerical model predictions for offset critical liquid input rate (μL/min), and experimental offset critical liquid input rate data, versus air temperature (K) and relative humidity (decimal) for A) WWC-100, B) WWC-400, and C) WWC-1250

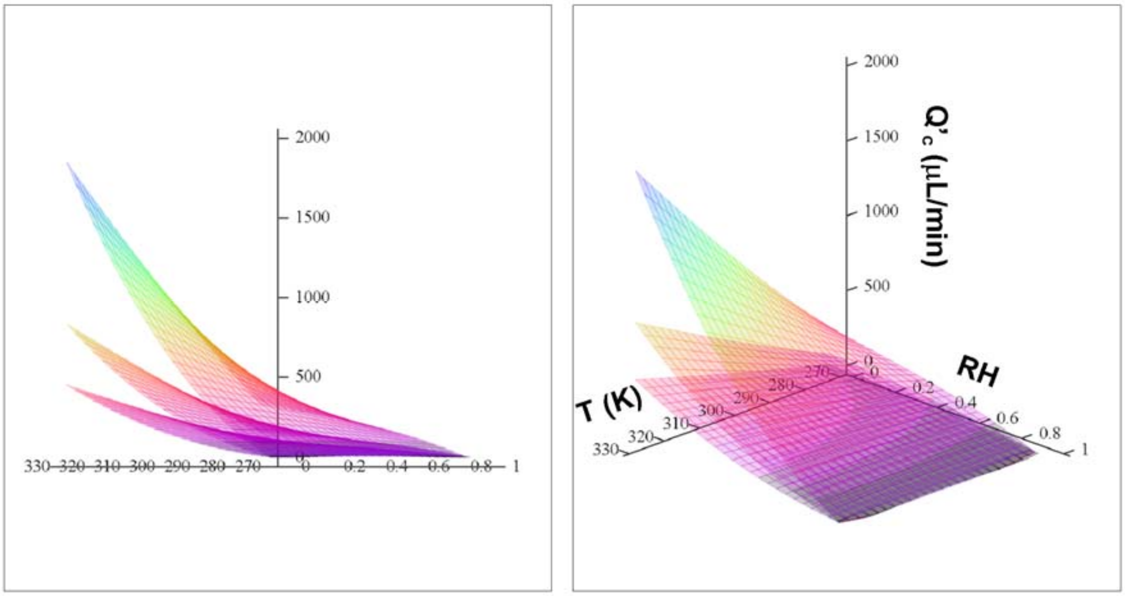

Figure 3.10: Numerical model predictions for offset critical liquid input rate (μL/min) versus air temperature (K) and relative humidity (decimal) for the WWC-100, WWC-400, and WWC-1250

The benefits derived from the semi-empirical model are easily observed in Figure 3.11. Empirical and semi-empirical offset critical liquid input rate surfaces are shown. Empirical model prediction errors are most likely to occur in the four corners of the temperature and relative humidity domain. For instance, if the WWC-100 were operated in a desert climate at 330 Kelvin and 0% relative humidity, the empirical model would predict an offset critical liquid input rate of 280 μL/min. A collector set to deliver 50 μL/min would fail to deliver a hydrosol sample since extrapolation from the empirical model is required. The semi-empirical model predicts an offset critical liquid input rate of 450 μL/min, nearly 200 μL/min higher than the empirical model prediction. Serious error would also occur for saturated conditions at high and low temperature, and low temperature, low humidity conditions.

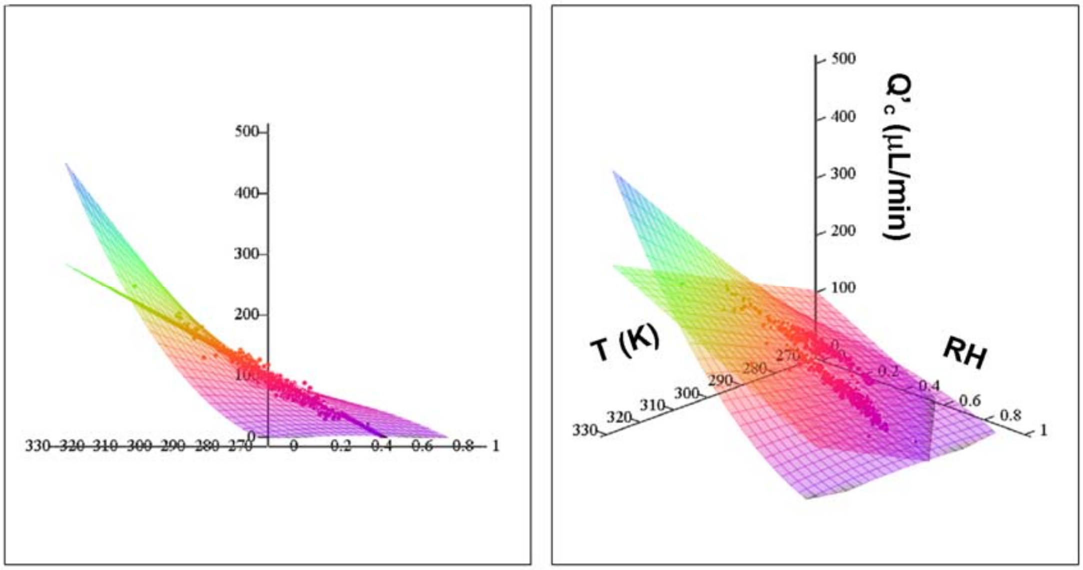

Figure 3.11: WWC-100 empirical and semi-empirical offset critical liquid input rate predictions

Non-physical behavior is predicted at low air temperatures. The model becomes invalid when the adiabatic saturation temperature drops below the freezing point of water, $273.15\,K$. A small region of the temperature and relative humidity domain falls under this category as shown in Figure 3.12 by the non-shaded area. The regression planes show non-zero values of the critical liquid input rate since the numerical model does not account for freezing and melting.

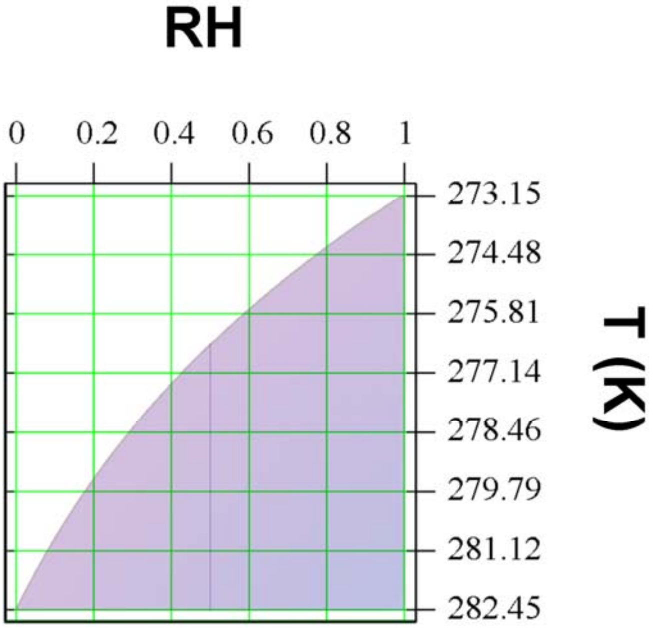

Figure 3.12: Initial conditions at which adiabatic saturation temperature falls below the freezing point of water

Table 3.6 gives the third order regression coefficients determined in Mathcad. A second order polynomial would be sufficient to describe the behavior far from saturation. However, a third order polynomial was necessary to get ‘flat’ behavior, $Q_c' = 0$, at $RH = 100\%$. The offset critical liquid input rate, for a constant air flow rate, is calculated as

$$Q_c'(T, RH) = \sum a_{n,m} \cdot T^n RH^m \tag{3.53}$$

where $T$ is in Kelvin and $RH$ is expressed as a decimal. The true critical liquid input rate can then be calculated by

$$Q_c(T, RH) = Q_c'(T, RH) + Q_{c,offset} \tag{3.54}$$

where $Q_{c,offset}$ are 17, 53, and 109 μL/min for the 100, 400, and 1250 Lpm cyclones, respectively.

| $T^nRH^m$ | | Regression Coefficients ($a_{n,m}$) | | |
|---|---|---|---|---|
| n | m | WWC-100 | WWC-400 | WWC-1250 |
| 0 | 0 | 2.67E+03 | 6.74E+03 | 1.63E+04 |
| 0 | 1 | 1.59E+03 | 2.40E+03 | 3.98E+03 |
| 0 | 2 | -2.09E+03 | -3.34E+03 | -6.90E+03 |
| 0 | 3 | -3.85E+01 | -7.68E+01 | -2.02E+02 |
| 1 | 0 | -3.36E+01 | -7.95E+01 | -1.87E+02 |
| 1 | 1 | 1.02E+00 | 3.88E+00 | 1.60E+01 |
| 1 | 2 | 7.56E+00 | 1.23E+01 | 2.55E+01 |
| 2 | 0 | 1.21E-01 | 2.79E-01 | 6.46E-01 |
| 2 | 1 | -2.53E-02 | -4.74E-02 | -1.14E-01 |
| 3 | 0 | -1.19E-04 | -2.79E-04 | -6.39E-04 |
| | $R^2$ | 0.90 | 0.92 | 0.92 |

Table 3.4: Semi-empirical regression coefficients for offset critical liquid input rate for the WWC-100, WWC-400, and WWC-1250

Future cyclone designs may utilize air flow rates other than those tested here. The semi-empirical model can be used for other designs if geometric and dynamic scaling is preserved. The air flow rate dependent offset critical liquid input rate is determined by

$$Q'_c(T, RH, Q_a) = \sum \left[ A_2 \cdot Q_a^{\,2} + A_1 \cdot Q_a + A_0 \right]_{n,m} \cdot T^n \cdot RH^m \qquad (3.55)$$

where $Q_a$ is in Lpm and regression coefficients given in Table 3.7. The true critical liquid input rate can then be found from (3.54) with an approximate offset, $Q_{c,offset} = 0.08 \cdot Q_a + 13$. Finally, the collection ratio and latency period for an actual system can be calculated from self-similar profiles (2.6) and (2.7).

| n | m | $A_2$ | $A_1$ | $A_0$ |
|---|---|---|---|---|
| 0 | 0 | -1.26E-04 | 1.20E+01 | 1.46E+03 |
| 0 | 1 | -3.87E-04 | 2.60E+00 | 1.33E+03 |
| 0 | 2 | -6.05E-04 | -3.36E+00 | -1.75E+03 |
| 0 | 3 | -3.68E-05 | -9.27E-02 | -2.89E+01 |
| 1 | 0 | 1.69E-06 | -1.36E-01 | -2.00E+01 |
| 1 | 1 | 5.65E-06 | 5.36E-03 | 4.29E-01 |
| 1 | 2 | 2.21E-06 | 1.27E-02 | 6.27E+00 |
| 2 | 0 | -1.09E-08 | 4.71E-04 | 7.36E-02 |
| 2 | 1 | -1.54E-08 | -5.67E-05 | -1.94E-02 |
| 3 | 0 | 2.40E-11 | -4.85E-07 | -7.07E-05 |

Table 3.5: Semi-empirical regression coefficients for offset critical liquid input rate for any air flow rate (Lpm) in a dynamically and geometrically similar wetted-wall cyclone

## 3.7. Constant Film Temperature Model

An experiment performed by Seo suggests chilling the WWC-100 wall to approximately $1°C$ reduced evaporation by 15% under typical laboratory air conditions (2007). Seo attributed the reduction in evaporation rate to the drop in liquid surface vapor pressure associated with cooling the liquid film. This data suggests it may be possible to control the liquid output rate by controlling the film temperature, i.e. evaporation rate, rather than adjusting the liquid input rate. Thermoelectric coolers could be applied to the cyclone body to maintain fixed surface temperature. Evaporation could theoretically be eliminated if the surface temperature were kept at the air dew point temperature. Furthermore, a surface temperature below the dew point should cause condensation on the cyclone wall. This method of operation would eliminate the need to re-supply the system with liquid inputs, a major limitation of the system for some applications. The numerical and analytical models were used to explore the effects of ambient air conditions and cyclone cooling on liquid evaporation and condensation.

### 3.7.1. NUMERICAL MODEL SIMULATIONS

Simulations of coupled heat and mass transfer from a thin film with constant surface temperature were performed. The external heat transfer resistance, $R'$, determines the effect of the surroundings temperature on the liquid film temperature. The surroundings act as a perfect source or sink of energy in the limit of zero resistance. The film would therefore have constant surface temperature at the surroundings temperature. Simulations A through I were performed with $T_{surr} = 285K$, $R' = 10^{-4} m \cdot K / W$, $Q_f = 5000 \mu L / min$, $Q_a = 250 Lpm$, $L = 1.0m$, and $D = 0.015m$. Heat transfer coefficients, inlet air conditions, and numerical model results for total evaporation and heat transfer rate to the surroundings are given in Table 3.6.

| | | | | | | | Numerical | | Analytical | | |
|---|---|---|---|---|---|---|---|---|---|---|---|
| **Series** | **$h_c$ ($W/m^2K$)** | **$T_{\infty,i}$ (K)** | **$RH_i$** | **Yvs** | **Yvinf** | **dYvc** | **$Q_{surr}$ (W)** | **$Q_{evap}$ (μL/min)** | **$\gamma$** | **$Q_{evap}$ (μL/min)** | **$\Delta Q_{evap}$ (%)** |
| A | 150 | 310.0 | 0.00 | 8.57E-03 | 0.00E+00 | 8.57E-03 | -14.1 | 1887 | 1.451 | 1904 | 0.9 |
| B | 150 | 300.0 | 0.00 | 8.57E-03 | 0.00E+00 | 8.57E-03 | 23.0 | 1921 | 1.451 | 1904 | -0.9 |
| C | 150 | 290.0 | 0.00 | 8.57E-03 | 0.00E+00 | 8.57E-03 | 61.4 | 1956 | 1.451 | 1904 | -2.7 |
| D | 200 | 310.0 | 0.35 | 8.57E-03 | 1.35E-02 | -4.92E-03 | -152.6 | -1204 | 1.934 | -1223 | 1.6 |
| E | 200 | 300.0 | 0.35 | 8.57E-03 | 7.63E-03 | 9.36E-04 | -53.3 | 235 | 1.934 | 233 | -1.2 |
| F | 200 | 290.0 | 0.35 | 8.57E-03 | 4.13E-03 | 4.43E-03 | 25.4 | 1138 | 1.934 | 1101 | -3.2 |
| G | 250 | 310.0 | 0.70 | 8.57E-03 | 2.72E-02 | -1.86E-02 | -308.7 | -4826 | 2.418 | -4929 | 2.1 |
| H | 250 | 300.0 | 0.70 | 8.57E-03 | 1.53E-02 | -6.76E-03 | -141.6 | -1804 | 2.418 | -1789 | -0.8 |
| I | 250 | 290.0 | 0.70 | 8.57E-03 | 8.29E-03 | 2.79E-04 | -19.8 | 77 | 2.418 | 74 | -3.9 |

Table 3.6**:** Simulation parameters for evaporation and condensation from a film with constant surface temperature of 285 Kelvin

Figure 3.13 and Figure 3.14 show the air-vapor mixture temperature and vapor mass fraction profiles, respectively. The surface temperature is maintained at 285 K by heat transfer to or from the surroundings. Figure 3.15 shows the heat transfer rate, per unit length, required to maintain the temperature at 285 K. Mass transfer rates range from 5000 (condensation) to 2000 (evaporation) μL/min depending on the temperature and moisture content of the inlet air stream. Heat transfer rates to the surroundings increase with increasing relative humidity for fixed inlet air temperature. Evaporation decreases with increasing relative humidity. Therefore, sensible heat transfer to the liquid film must be balanced by heat transfer to the surroundings when latent heat transfer becomes small.

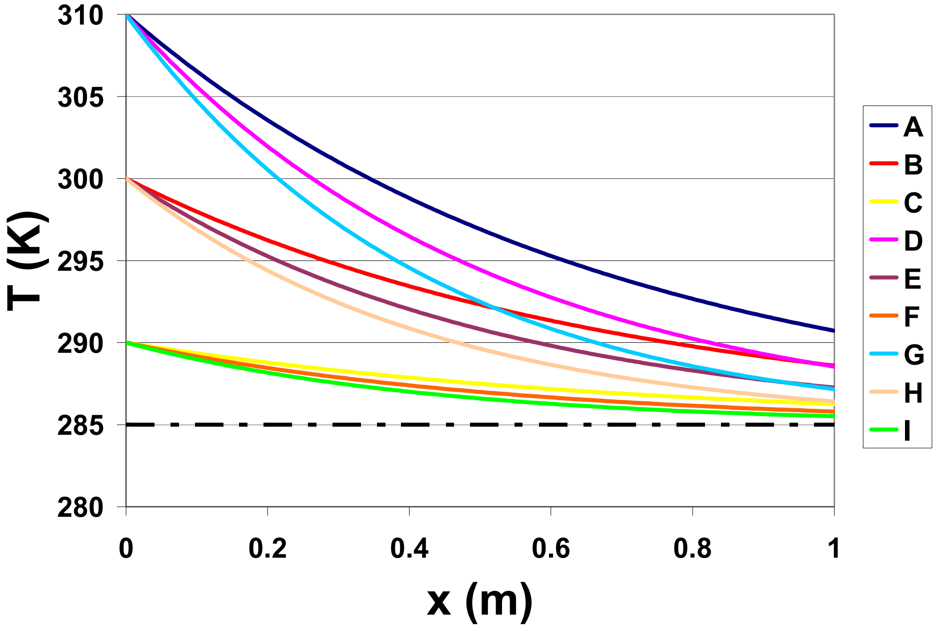

Figure 3.13: Air-vapor mixture temperature profiles for simulations of mass transfer from a water film with constant temperature of 285 K

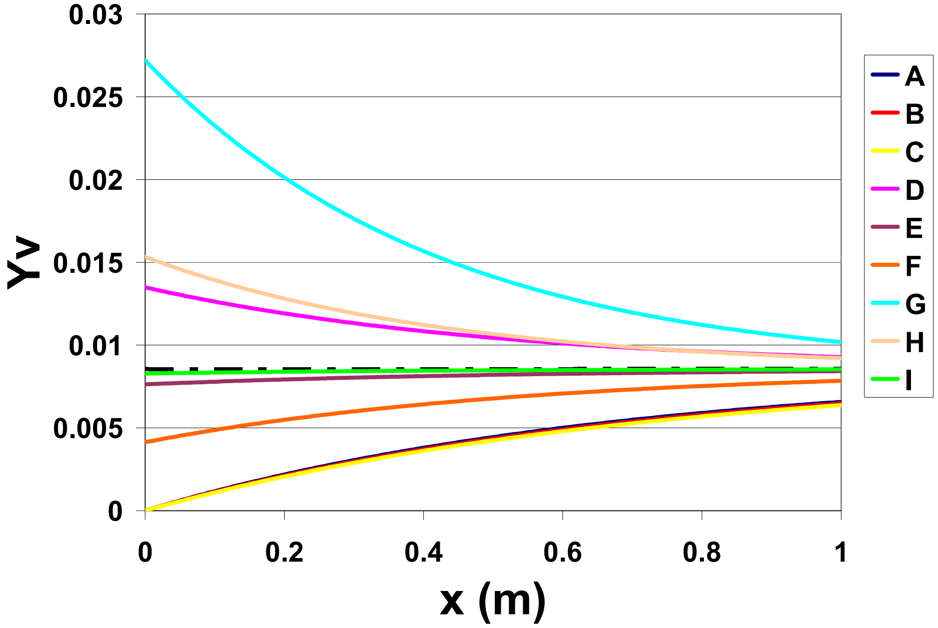

Figure 3.14: Vapor mass fraction profiles for simulations of mass transfer from a water film with constant temperature of 285 K

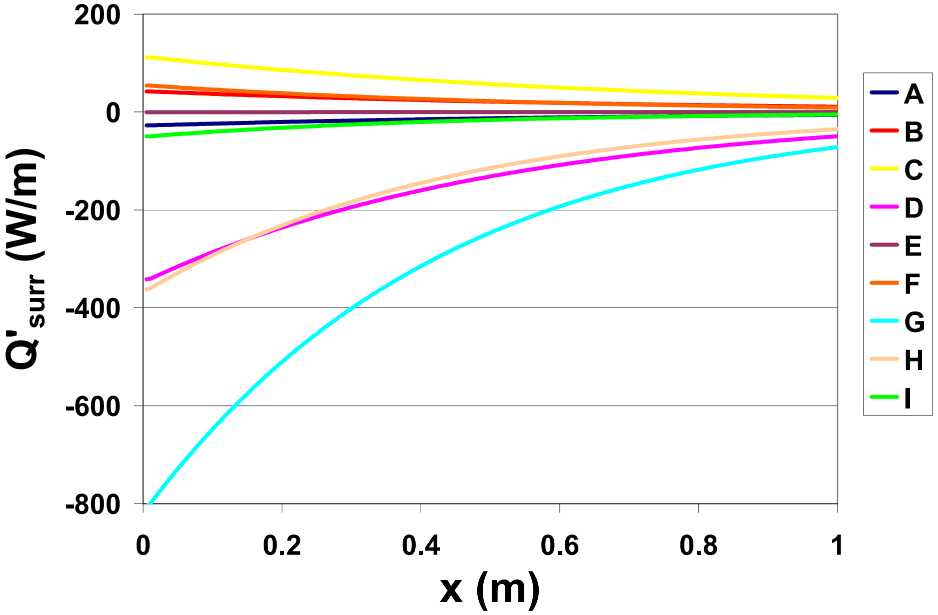

Figure 3.15: Heat transfer rate per unit length (W/m) required to maintain a constant surface film temperature of 285 K

### 3.7.2. APPROXIMATE ANALYTICAL MODEL

The approximate analytical models for heat and mass transfer rates developed in Section 3.5 were derived under the assumptions of negligible heat transfer to the surroundings, small ratio of thermal flow capacities, small mixture vapor mass fraction, and constant film surface temperature. All but the first assumption are valid for the case of constant surface temperature. The approximate analytical solution for temperature difference is invalid because the surroundings heat transfer term cannot be neglected. The magnitude of this term is unknown and cannot be expressed simply to derive an approximate solution. The heat transfer rate to the surroundings assumes the value required to maintain the surface temperature.

The approximate analytical solution for evaporation rate is still valid since the underlying assumptions are the same as the adiabatic case. Hence, a simple expression approximates the evolving dimensionless vapor mass fraction difference and resulting evaporation, or condensation, rate. The characteristic temperature and vapor mass fraction differences for this case are $\Delta T_c = T_{\infty,i} - T_s$ and $\Delta Y_{vc} = Y_{vs} - Y_{v\infty,i}$ where $T_s$ is the constant film surface temperature and $Y_{vs}$ is the corresponding saturated vapor mass fraction. Approximate analytical solutions for vapor mass fraction difference are plotted as solid lines in Figure 3.16 for simulations A through I.

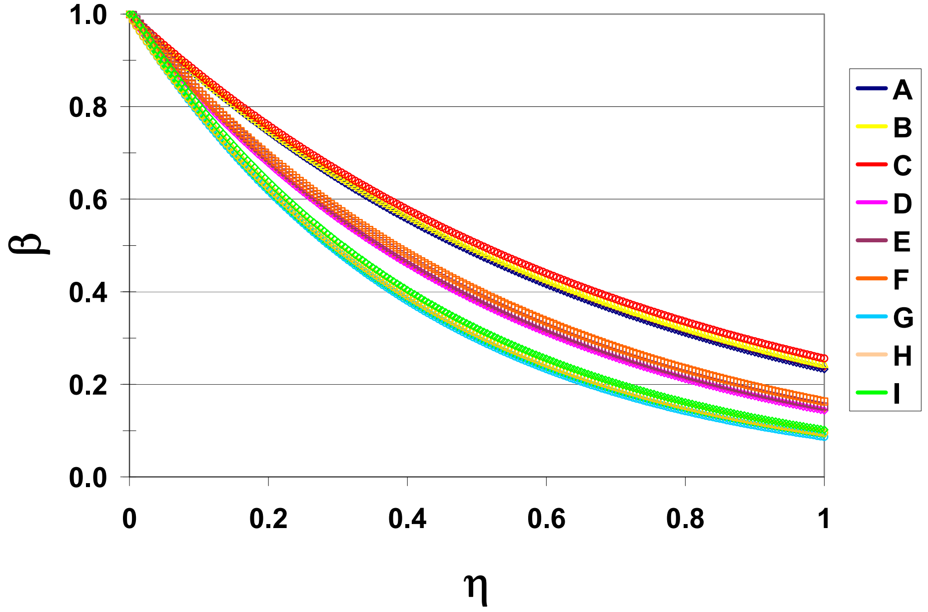

Figure 3.16: Dimensionless vapor mass fraction difference, simulations A through I, for evaporation and condensation from a water film with constant temperature of 285 Kelvin

Results from numerical simulations are shown as points. Excellent agreement is observed with maximum errors of ±10% at $\eta = 1$. The net mass transfer rates from numerical and analytical models are given in Table 3.6. Again, excellent agreement $(\pm 5\%)$ is observed for both evaporation and condensation rates. Error in the approximate analytical solution for constant surface temperature is smaller than in the adiabatic case because the assumption of $\frac{dY_{vs}}{dx} = 0$ is true over the entire length in the former.

Heat transfer rates for the constant film temperature case cannot be predicted by an approximate solution analogous to that derived for the adiabatic case. Latent and sensible energy transfer to and from the film are not balanced here and therefore cannot be expressed by the product of mass transfer rate and enthalpy of vaporization.

### 3.7.3. CHILLED WWC-100 FILM CONDENSATION EXPERIMENTS

Experiments have been conducted to determine the feasibility of chilling the WWC-100 to achieve control over the liquid output rate (Tucker, 2009). The WWC-100 was submerged in a liquid reservoir whose temperature was controlled to affect the cyclone wall temperature. Reservoir water was re-circulated through a separate ice water bath by a 2000 milliliters per minute peristaltic pump. The volumetric flow rate of the recirculation pump was manipulated to achieve different reservoir temperatures.

Simultaneous measurements of inlet air temperature, reservoir temperature, and inner cyclone wall temperature were made with type T thermocouples (Omega 5SRTC-TT-T-30-36) and data logger (Omega HH147). The thermocouples were embedded in the cyclone wall as close to the inner cyclone surface as possible. Figure 3.17 shows a schematic of a thermocouple 'pot' machined in the cyclone wall. A 0.032 inch thermocouple tip cavity was machined to maximum depth, according to the machinist's best judgment, without breaking the surface. A larger, 0.125", air void cavity was machined over the tip cavity to insulate the thermocouple tip from longitudinal conduction within the cyclone wall. A thermally conductive epoxy (Omega OB-101) was used to bond the thermocouple tip to the cyclone surface. Silicon adhesive was then used to create a seal over the air void cavity and protect the thermocouple from moisture.

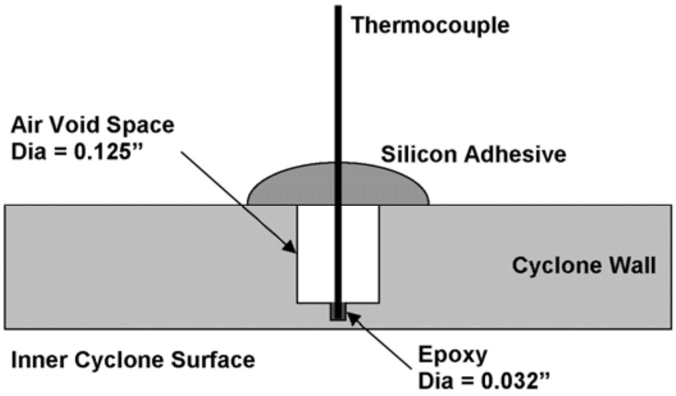

Figure 3.17: Diagram of embedded thermocouple in cyclone wall designed to measure the inner cyclone surface temperature for chilled WWC-100 experiments

#### 3.7.3.1. Experiment

Measurements of the liquid output rate were made for liquid input rates of 50 and 0 μL/min, under laboratory air conditions, with varying cyclone surface temperature. Figure 3.18 shows the rates of evaporation ($Q_{evap} > 0$) and condensation ($Q_{evap} < 0$) for both liquid input rates versus the characteristic vapor mass fraction difference. The $Q_i = 50$ microliter per minute experiments were performed with the cyclone surface temperature approximately equal to the dew point temperature, $\Delta Y_{vc} \approx 0$, to study the feasibility of eliminating evaporative effects thereby collecting liquid at a rate equal to the injection rate. Evaporation rates are expected to approach zero as $\Delta Y_{vc} \to 0$. The rates of evaporation show significant scatter ($\pm 25$ μL/min) for $-0.0006 < \Delta Y_{vc} < 0.0003$ ($-1 < T_s - T_{dp} < 1$ K). Measurement accuracy of air temperature and controllability of surface temperature would need to be approximately $\pm 0.2K$ to achieve similar accuracy on $Q_o$ as that obtained by manipulating the liquid input rate (Section 2.3). This suggests it would be difficult to implement a control strategy eliminating evaporation by maintaining the liquid film at the dew point temperature.

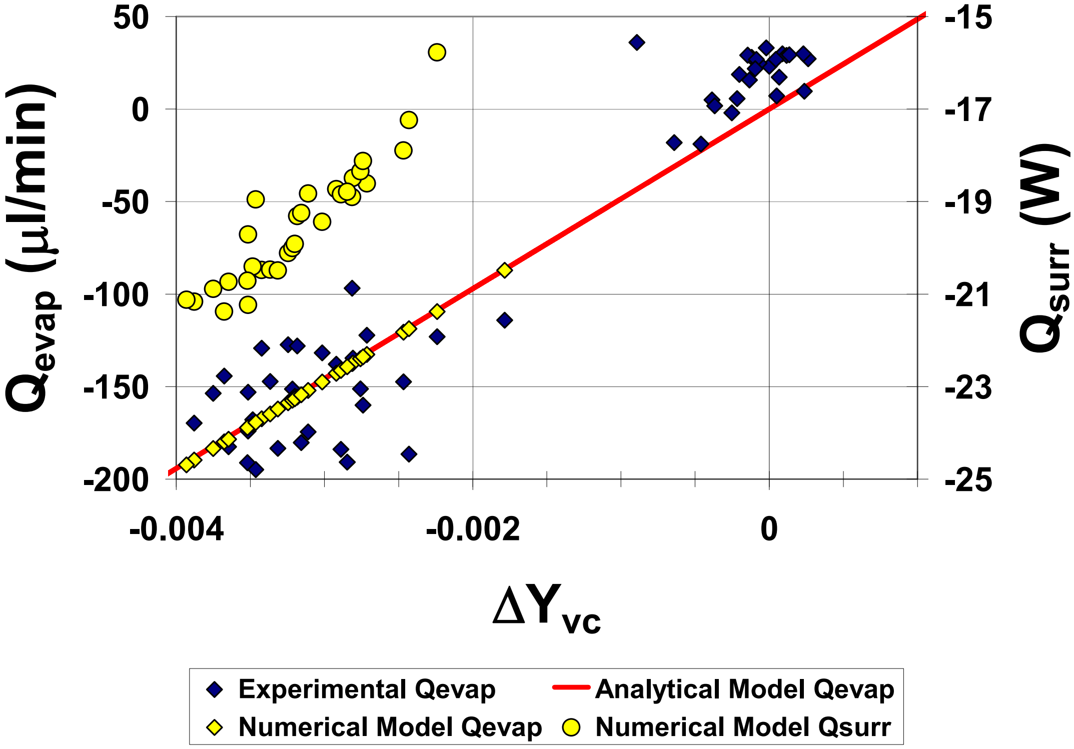

Figure 3.18: Experimental, analytical model, and numerical model mass transfer rates (µL/min), and numerical model external heat transfer rates versus characteristic vapor mass fraction difference from chilled WWC-100 experiments

Experiments for which the cyclone surface temperature was below the dew point temperature ($\Delta Y_{vc} < 0$) produced rates of condensation comparable to experimentally measured evaporation rates (~100 µL/min). Precision of ±25 µL/min was achieved in chilled cyclone condensation experiments. Chilling the cyclone surface is a potential strategy for eliminating the requirement to restock WWC systems with liquid consumables. Additional hardware and operating (electrical power) costs would be associated with thermal control of the cyclone. However, the tradeoffs of accuracy and cost may be justified when systems are placed in remote locations like HVAC ducts where operators cannot easily re-supply liquid supplies.

Heat transfer rates from the cyclone to the reservoir were calculated for chilled WWC-100 experimental air conditions. Rates of change of reservoir bath temperatures were measured with and without the cyclone operational. The rate of temperature change due solely to heat transfer through the cyclone to the water reservoir was calculated as the difference between the two measured rates of change. The non-operational temperature change was subtracted to account for heat transfer from the reservoir to the laboratory through the reservoir walls. A lumped capacitance model, with volume equal to the reservoir liquid volume, was then used to calculate the heat transfer rate, from the cyclone to the reservoir, required to cause the measured reservoir temperature changes with respect to time. Calculated values of the heat transferred to the reservoir, through the cyclone wall, ranged from 7 to 20 Watts.

#### 3.7.3.2. Approximate Analytical Model Predictions

The approximate analytical solution for net mass transfer rate (3.49) was used to model the experimentally measured condensation rates. The heat transfer coefficient resulting in the best fit of the data was $h_c = 295$ W/m$^2$K. No offset was required since no liquid was injected through the atomizer. The heat transfer coefficient is 60% larger than the value obtained whilst modeling the collecting threshold ($h_c = 180$ W/m$^2$K). The air flow rate was not measured for this set of experiments but this is not viewed as a likely cause of disagreement. The effects of surface area on heat and mass transfer are the most probable cause for the discrepancy in optimized model heat transfer coefficients.

Model predictions were based on a wetted surface area, $\mathrm{P}L$, equal to that of the inner cyclone bore. The entire cyclone was submerged in the chilled reservoir for experimental data shown in Figure 3.18. This represents a significant increase in the surface area over which condensation takes place. The WWC-100 inlet surface area was approximated by a truncated cone with base radius equal to the slot length and height equal to the distance from the inlet flange face to the centerline of the cyclone body. The approximate increase in wetted surface area is 85% with respect to the modeled surface area. Underestimating the model surface area resulted in an increased heat transfer coefficient required. The difference in modeled internal convection heat transfer coefficients from evaporation studies (180 W/m$^2$K) and condensation studies (295 W/m$^2$K) are resolved by noting for the difference in wetted area.

The approximate analytical model was used to predict evaporation and condensation rates over wide ranges of characteristic vapor mass fraction differences and surface/dew point temperature differences, $T_s - T_{dp}$. Random combinations of $T_\infty$, $RH_\infty$, and $T_s$ were chosen to represent all potential operational conditions. Figure 3.19 shows the net mass transfer rate is zero for $T_s - T_{dp} = 0$ and $\Delta Y_{vc} = 0$ with condensation and evaporation occurring for negative and positive values of the independent variables, respectively. Some scatter is observed when the data are plotted against the surface/dew point temperature difference. This is a physically familiar quantity but the characteristic vapor mass fraction difference is the variable of choice due to its appearance in the approximate solution to the governing equations. Air conditions for which the dew point was below freezing were not included because forming ice inside the cyclone is not preferred. Although the condensation rates appear large (~1000 μL/min), they represent only a small fraction (5-10%) of the total moisture content of the air-stream in the WWC-100.

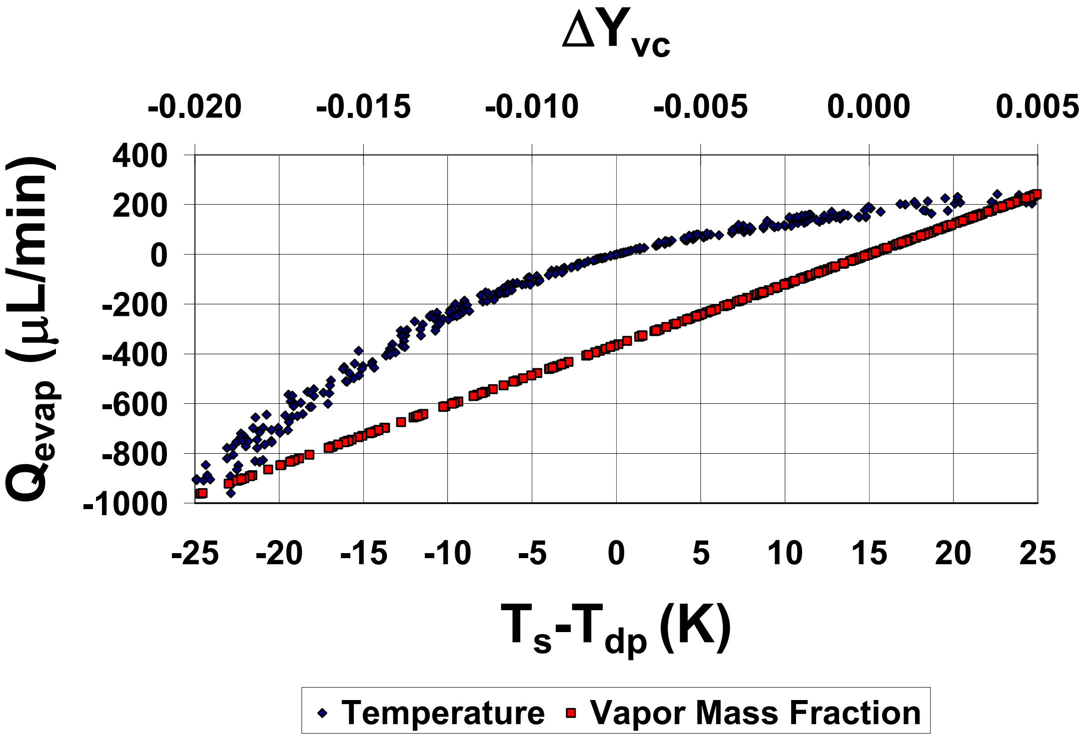

Figure 3.19: Approximate analytical model prediction of evaporation and condensation rates for the WWC-100 at various characteristic vapor mass fraction differences and surface/dew point temperature differences

### 3.7.3.3. Numerical Model Predictions

The numerical model was used to simulate condensation rates and required heat transfer rates associated with experimental data. Numerical model condensation rates are shown in Figure 3.18 and lie directly on the approximate analytical model predictions. This merely serves to show assumptions made in the analytical model are well justified for the constant liquid surface temperature case. Heat transfer rates to the surroundings cannot be calculated with the analytical model. Estimates would be required to size thermoelectric coolers needed to maintain the cyclone surface temperature below the dew point temperature. Experimental condensation rates measured here would require the extraction of approximately 15 to 21 Watts from the cyclone according to the numerical model. These predictions show good agreement with experimentally calculated heat transfer rates ($7 < Q_{surr} < 20W$).

### 3.7.4. CHILLED WWC-100 CLIMATE DESIGN FEASIBILITY

WWC-100 operation without liquid injection has been demonstrated. Cooling the cyclone walls to a point at which water vapor from the air-stream condenses inside the cyclone would allow the system to operate more autonomously by eliminating the need to refill liquid consumables. The feasibility of operating the cyclone in condensing mode was analyzed with respect to the environmental engineering considerations listed in MIL-STD-810G. This government standard is written to facilitate “realistic consideration of climatic conditions in the research, development, test, and evaluation of materiel used throughout their life cycles in various climatic regions throughout the world”. The climatic categories provided represent the most extreme climates in which a system may be required to function. Air temperature and relative humidity, and dew point temperature are given in Table 3.7 for 9 climate categories.

| **Climate Category** | **Daily Cycle** | **$T_\infty$ (°C)** | **$RH_\infty$ (dec)** | **$T_{dp}$ (°C)** | **$Q_{v\infty}$ for WWC-100 (μL/min)** |
|---|---|---|---|---|---|
| A1L | Hot Dry | 32 | 0.08 | -6 | 444 |
| A1H | | 49 | 0.03 | -7 | 412 |
| A2H | Basic Hot | 43 | 0.14 | 10 | 1418 |
| A2L | | 30 | 0.44 | 16 | 2194 |
| A3H | Intermediate | 39 | 0.43 | 24 | 3549 |
| A3L | | 28 | 0.78 | 24 | 3478 |
| B1H | Constant High Humidity | 24 | 1.00 | 24 | 3520 |
| B1L | | 24 | 0.95 | 23 | 3342 |
| B2H | Variable High Humidity | 35 | 0.74 | 30 | 4932 |
| B2L | | 26 | 1.00 | 26 | 3971 |
| B3H | Hot Humid | 41 | 0.59 | 31 | 5450 |
| B3L | | 31 | 0.88 | 29 | 4682 |
| C1H | Basic Cold | -21 | 1.00 | -21 | 134 |
| C1L | | -32 | 1.00 | -32 | 49 |
| C2H | Cold | -37 | 1.00 | -37 | 30 |
| C2L | | -46 | 1.00 | -46 | 12 |
| C3H | Severe Cold | -51 | 1.00 | -51 | 7 |
| C3L | | -51 | 1.00 | -51 | 7 |

Table 3.7: Natural climate design types and corresponding extreme air conditions taken from MIL-STD-810G, and free-stream vapor mass flow rate through WWC-100

A condensing WWC-100 could not be operated in Hot Dry, or any Cold categories because the dew point temperature is sub-freezing and could result in frost formation. However, a condensing system could be designed to function in all other climate categories.

Air conditions listed in Table 3.7 were used in the approximate model to determine the mass transfer rate for different values of the cyclone surface temperature. Mass transfer rates are shown in Figure 3.20 as a function of the cyclone surface temperature. Condensation rates of 250 µL/min should be achievable for categories A2 through B3. Corresponding heat extraction rates are shown in Figure 3.20 as calculated by the numerical model. Cooling loads ranging from 10 to 40 Watts should be sufficient to collect liquid at rates of approximately 250 µL/min.

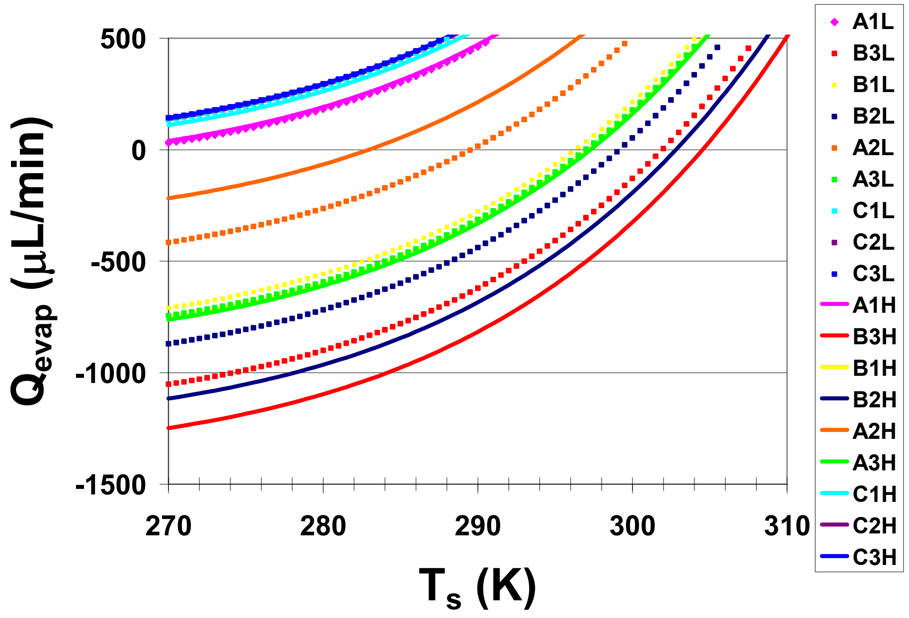

Figure 3.20: Net evaporation and condensation rates versus cyclone wall temperature for natural climate design types as specified by MIL-STD-810G

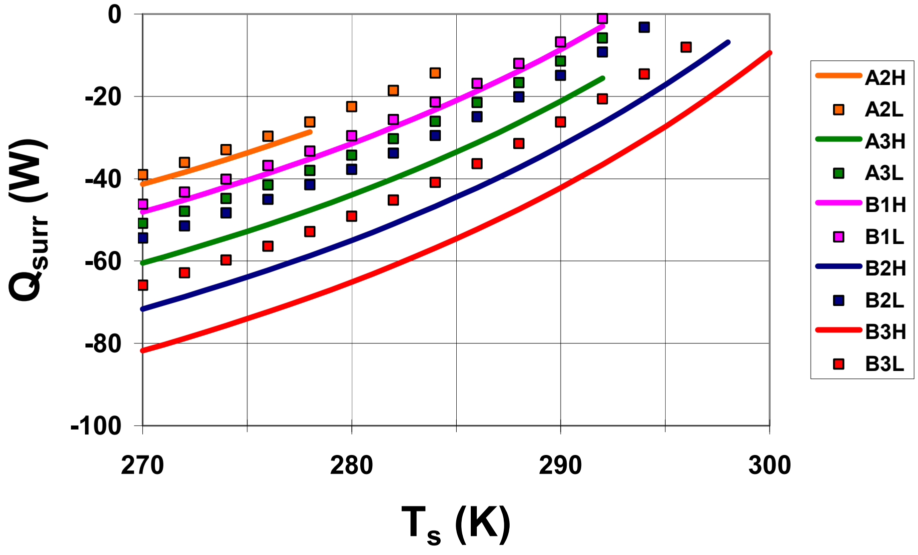

Figure 3.21: Cooling load required to maintain constant surface temperature for natural climate design types (MIL-STD-810G) calculated with the numerical model

## 3.8. Summary

Evaporative phenomena occurring within the cyclone were modeled numerically to gain improved control over the concentration factor. The following activities were completed to advance the WWC as an autonomous bioaerosol sampling for use with advanced detection technologies:

- formulated a one-dimensional, steady-state, heat and mass transfer model for co-annular air film flow
- wrote code to solve coupled set of conservation equations
- verified code was conservative in energy and mass, and displayed proper behavior under equilibrium conditions
- derived approximate analytical solutions under adiabatic and isothermal wall conditions providing fast, and accurate ($\pm 10\%$) approximations for the evaporation rate
- determined the set of physical parameters most relevant to overall system performance
- modeled dependence of WWC critical liquid input rate on air conditions and air flow rate
- developed semi-empirical performance correlations for improved system control algorithms
- devised a thermal management scheme to operate the cyclone in a condensing mode which eliminates the need to resupply the system with liquid consumables

# 4. IN-SITU HIGH SPEED IMAGING ANALYSIS OF WWC-100 MULTIPHASE FLOW

## 4.1. Background

Figure 4.1 shows an in-situ observation of multiphase flow patterns inside the WWC-100. Air and liquid flows are directed out of the plane.

Figure 4.1: In-situ borescope video observation of complex multiphase flow inside the WWC-100 with a liquid input rate of 1000 μL/min

Collection liquid is atomized upstream of the inlet slot and coalesces into a thin film on the particle impaction zone. The film breaks up into rivulets and droplets which are subsequently driven downstream by aerodynamic forces at the air-liquid interface. Adhesive forces oppose liquid motion at the solid-liquid interface. A force imbalance on the liquid causes it to move along the cyclone surface. Liquid flows underneath the skimmer and is siphoned off from the air flow. Chapter 4 is a qualitative description of the multiphase flow patterns and underlying physics. This characterization contributes to the overall understanding of system performance presented in Chapters 2 and 3 and is an ongoing effort.

## 4.2. Experiment

### 4.2.1. EXPERIMENTAL APPARATUS

A Kodak Ektapro High Speed Motion Analyzer and Imager (4540mx) were used to make in-situ observations of WWC-100 multiphase flow patterns. The system is capable of recording 24,576 frames at a maximum frame rate of 4500 frames per second (fps). Images are 256 x 256 pixels with 256 levels of gray. The camera was connected to a borescope (Hawkeye Slim, Gradient Lens) with a c-mount coupler (VC-75, Gradient Lens). The borescope was aligned with the axis of the cyclone as shown in Figure 4.2. To do so, the blower was removed from the axial flow path of the cyclone and re-routed through a 90 degree elbow.

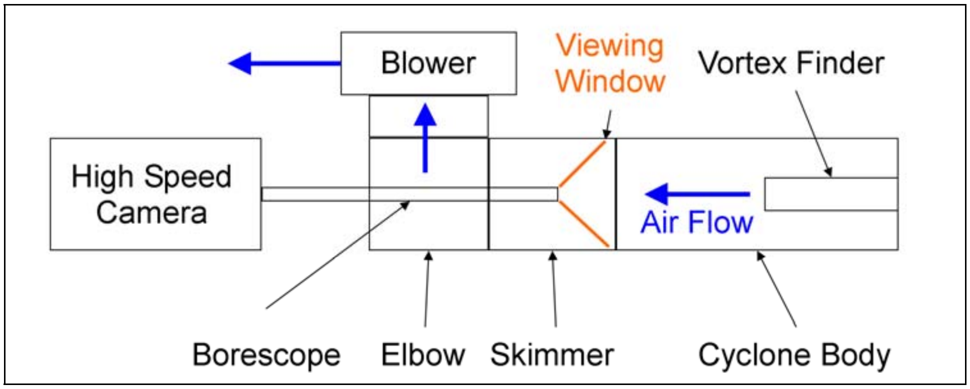

Figure 4.2: Experimental setup for WWC-100 in-situ high speed video analysis of multiphase flow

The tip of the borescope was located downstream of the skimmer nose. The skimmer nose can be seen in Figure 4.1 as the first dark ring inside the non-black region of the image. Vendor supplied software, Readcam.exe, was used to download images from camera memory. The inside of the WWC-100 was illuminated through both the borescope and vortex finder. A Luxxor 24 light source (Gradient Lens) was connected to the borescope. This projected light into the cyclone from the tip of the borescope. A special vortex finder was also constructed to provide lighting in the inlet slot region. Seo constructed a vortex finder to look inside the cyclone during operation (2007). He replaced the vortex finder shaft with a 10 mm glass culture tube adjusted to the same axial length as the actual vortex finder (Figure 4.3, left). For this study, the vortex finder base was machined from plexiglass and polished (Figure 4.3, right) to provide additional lighting from a gooseneck halogen lamp (Amscope, HL-150A) directed at the inlet slot through the vortex finder. The glass culture tube tip was darkened with silver paint to block light from shining directly into the camera lens.

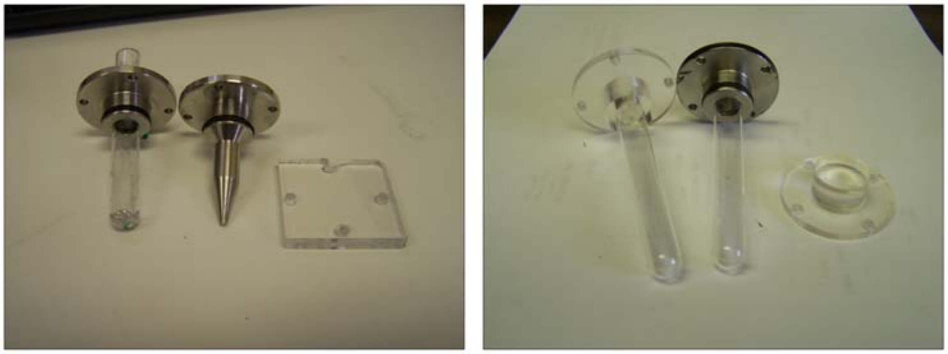

Figure 4.3: WWC-100 Plexiglass vortex finder assembly for backlighting high speed video

### 4.2.2. MATLAB IMAGE PROCESSING

Image processing was performed in Matlab. Different sequences of image operators were tested to determine which provided the best video quality. The adapthisteq() function was used to equalize the intensity histograms of both the background and target images. The equalized background image was then subtracted from the equalized target image with imsubtract() and inverted with the imcomplement()

function. Filtering functions were also tested although none improved the image quality to a greater degree than the sequence of operators given above.

### 4.2.3. HIGH SPEED VIDEO

Laboratory conditions for the following set of high speed videos were $26°C$ and $38\% RH$, corresponding to a critical liquid input rate of $Q_c = 138$ μL/min. Each video contains 1000 frames captured at a rate of 500 fps. The playback speed is 25 fps, or 1/20th of the actual speed. The real-time video duration was two seconds and began after the latency period had elapsed. Figure 4.4, Figure 4.5, and Figure 4.6 show multiphase flow patterns at liquid input rates of 760, 390, and 200 μL/min, or dimensionless liquid input rates, $Q_i^*$, of 4.5, 1.8, and 0.4, respectively.

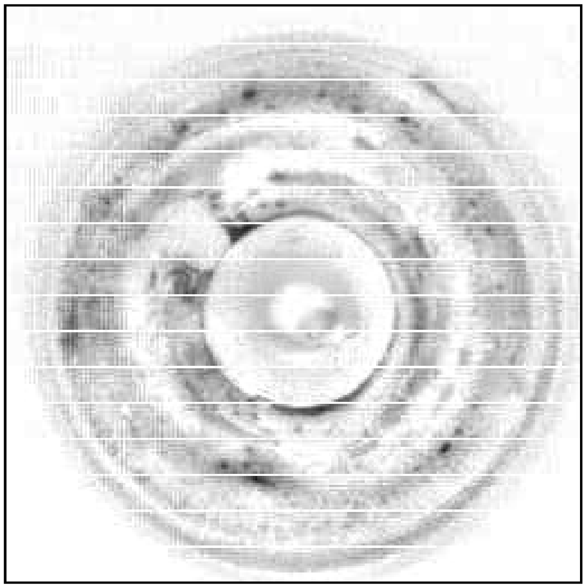

Figure 4.4: High speed borescope video observation of complex multi-phase flow inside the WWC-100 with a liquid input rate of 760 μL/min or a dimensionless liquid input rate of 4.5

The impaction zone is coated by a thin film. Film instabilities lead to the shedding of droplets that minimize total energy (Saber and El-Genk 2004). Droplet motion is then driven by aerodynamic forces at the air-liquid interface and opposed by adhesive forces at the solid-liquid interface. Adhesive forces are proportional to the area of contact and contact angle hysteresis. Contact angle hysteresis is the difference in advancing and receding contact angles and is determined by interactions between the liquid and solid surfaces. Droplets with large contact angle hysteresis will deform under increasing aerodynamic forces while the contact line remains pinned. The droplet will detach from the surface at some critical level of deformation (Schleizer and Bonnecaze 1999) which is often related to the Capillary and Weber numbers. Contact angles appear to be less than 90 degrees which suggests these wetting droplets slide along the surface (Basu et al. 1997) rather than roll.

A range of droplet sizes is observed with larger droplets having greater aerodynamic drag and consequently greater speed. A rough spatial mapping of the images suggests the largest droplets are approximately 1 mm in diameter. Stationary droplets are consumed by larger droplets as they travel along the surface. The largest droplets possess tails which often break up into a series of smaller droplets due to the concentration of aerodynamic forces at the droplet head (Schwartz et al. 2005). Occasional bursts of droplets also appear upstream of the skimmer and could be a consequence of liquid reaerosolization at the inlet slot.

Figure 4.5 and Figure 4.6 show changes in multiphase flow patterns as the liquid input rate decreases: film-droplet shedding becomes more clear, droplet speeds decrease, and tails are absent from the largest droplets. The droplet number density also decreases although the relative fraction of stationary droplets increases.

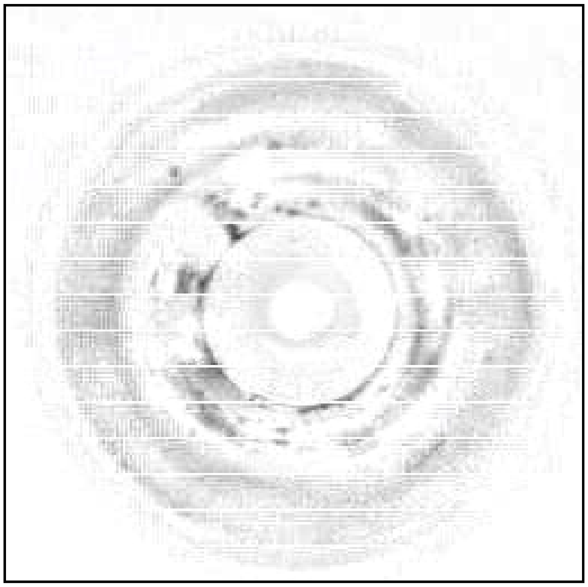

Figure 4.5: WWC-100 multiphase flow pattern at a liquid input rate of 387 μL/min or a dimensionless liquid input rate of 1.8

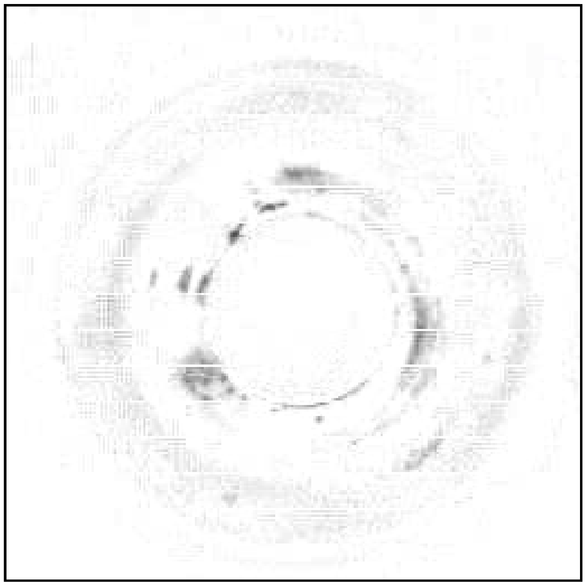

Figure 4.6: WWC-100 multiphase flow pattern at a liquid input rate of 196 μL/min or a dimensionless liquid input rate of 0.4

## 4.3. Analysis

### 4.3.1. FORCES

Scale analysis reveals which forces are dominant for this system. The Reynolds number is a ratio of inertial and viscous forces of the air stream,

$$Re = \frac{U \cdot H}{\nu} \tag{4.1}$$

where cyclone slot properties, $U \approx 10$ m/s, $H \approx 10^{-3}$ m, $\nu \approx 10^{-5}$ m$^2$/s, give $Re \approx 10^4$. This implies the air flow is turbulent. The Bond, Capillary, and Weber numbers compare gravitational, shear, and inertial forces, to droplet surface tension forces, respectively. The Bond number

$$Bo = \frac{(\rho_w - \rho_a) \cdot g \cdot D^2}{\sigma_w} \tag{4.2}$$

with $\rho_w - \rho_a \approx 10^3$ kg/m$^3$, $g \approx 10$ m/s$^2$, $D \approx 10^{-3}$ m, and $\sigma_w \approx 0.1$ N/m, gives $Bo \approx 10^{-1}$. Thus, in the absence of air flow, droplets have roughly hemispherical shape since surface tension forces limit deformation due to gravity.

Droplets will deform and detach from the wall if viscous or inertial forces exerted by the air stream are sufficiently large. The capillary number

$$Ca = \frac{\mu_a \cdot \gamma \cdot D}{\sigma_w} \tag{4.3}$$

where $\mu_a \approx 10^{-5}$ Ns/m$^2$ and $\gamma \approx 10^4$ s$^{-1}$ is $Ca \approx 10^{-3}$. This suggests droplet surface tension forces are large enough to resist deformation and detachment due to air stream shear forces. The Weber number

$$We = \frac{\rho_a \cdot U^2 \cdot D}{\sigma_w} \tag{4.4}$$

for this system is $10^1$. Therefore, droplet detachment and deformation is likely caused by inertial forces.

### 4.3.2. DROPLET SPEED ESTIMATE

Manual analysis of droplet trajectories was performed assuming droplets travel along helical paths with constant speed. Five droplets were tracked from the downstream edge of the inlet slot to the skimmer nose at liquid input rates of 920 and 470 μL/min. Droplet speeds ranged from 0.06 to 0.66 m/s, approximately one to two orders of magnitude less than the slot velocity. Axial velocities ranged from 0.03 to 0.2 m/s, also one to two orders of magnitude less than the bulk air velocity. The number of observations was insufficient to determine the general affects of liquid input rate on droplet speed.

### 4.3.3. EFFECTS ON WWC PERFORMANCE

A schematic of WWC internal multiphase flow structure is shown in Figure 4.7. This illustration presents the inner cyclone surface as unwrapped onto a plane. A thin film covers the impaction zone as the result of collection liquid being atomized in the cyclone inlet. At the critical liquid input rate, film evaporation and replenishment are equal and no droplets are shed from the film. For $Q_i - Q_c > 0$, droplets form and are driven downstream along paths parallel to the direction of air flow. Proportionality between the excess liquid input rate and rate of droplet shedding is proposed. System latency periods and evaporation rates are analyzed in light of this physical description.

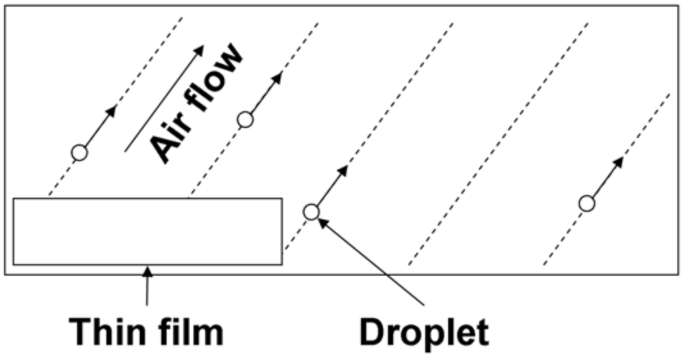

Figure 4.7: Schematic of internal WWC multiphase flow structure: film-droplet shedding and droplet motion

Film-droplet shedding is absent for $Q_i^* \leq 0$. The cyclone surface downstream of the film is assumed completely dry. The first droplet emerges once the liquid input rate is raised above the critical liquid input rate. The droplet formation rate is proportional to the excess liquid input rate, thus, the latency period decreases with increasing excess liquid input rate. Contact angle hysteresis causes the motion of a single droplet to be erratic and sluggish, explaining large scatter in latency period data as $Q_i^* \to 0$ (Figure 2.14). Increasing excess liquid input rate also decreases the fraction of time over which any section of surface remains dry. A simple physical model is proposed to explain why the latency period decreases when the surface is wet. A dry surface is characterized by some roughness, microscopic peaks and valleys, which increases contact angle hysteresis with respect to a smooth surface. Upon wetting, liquid smoothes the surface by filling the valleys and spanning the peaks. In this case, droplets would glide along a smooth surface. This notion is supported by experimental evidence. Steady-state system latency periods decrease significantly (Section 2.4.2) since the surface is pre-wetted.

Evaporative behavior in the WWC can also be examined in light of the multiphase flow patterns described above. The critical liquid input rate was modeled in

Chapter 3 as thin film evaporation. This formulation is supported by high speed video observations. The liquid exists exclusively as a film when the excess liquid input rate is zero. However, as the excess liquid input rate increases, the wetted-surface area increases due to the increase in droplet formation rate and droplet number density. In this regime, $Q_i^* > 0$, the rate of evaporation is proportionally related to the dimensionless liquid input rate through the fractional collection, $m$. Fractional collection data show some dependence on cyclone geometry and air flow rate, in addition to the critical liquid input rate. The existence of droplets and the influence of surface physics are plausible explanations for complicated behavior, dependence of $m$, which occur for $Q_i^* > 0$.

The effects of liquid chemical composition on evaporation were presented in Section 2.6. The addition of surfactant has been shown to increase droplet adhesion forces by increasing the wetted area (Mahe et al. 1988). Increased wetting would also decrease the height of a droplet, of equivalent volume, due to increased contact angle. The cumulative result is droplets with greater residence times within the cyclone and increased exposure to forced convection. This explains the increase in evaporation rates for liquids containing a small percentage of Triton X-100 surfactant. Increased adhesion is also likely to increase the latency period since restraining forces are greater.

## 4.4. Future Works

Multiphase flow characteristics like droplet size and speed distributions, droplet number density, and wetted surface area will be quantified through additional image analysis. The effects of air flow rate, chemical composition, and cyclone scaling on WWC performance will be studied once data processing algorithms are developed. Scanning electron microscopy will be used to characterize the roughness of the inner cyclone surface. Contact angle hysteresis will also be measured. Adhesive forces and droplet motion inception criteria will then be formulated from characterizations of solid-liquid interfacial interaction.

# Concluding Remarks

This work was a multi-scale effort to confront the rapidly evolving threat of biological weapons attacks through improved bioaerosol surveillance, detection, and response capabilities. Identifying the presence of airborne pathogens is critical to the rapid and effective implementation of emergency response protocols and mitigation procedures. A network of real-time biosensor systems is currently in place and the next generation of sensor systems should possess even higher sensitivity, specificity, and reliability. A family of wetted-wall bioaerosol sampling cyclones was characterized to optimize their use with advanced detection technologies. Because of this work the wetted-wall bioaerosol sampling cyclone is more able to meet the diverse requirements of real-time detection of airborne pathogens. Secondly, efficacious response to an atmospheric release of biological weapons relies on risk assessment tools and atmospheric dispersion models. A simple convection-diffusion-sedimentation model was formulated to analyze the effects of atmospheric transport on bioaerosol sampling. Contemporary sampling strategies and sampler designs were evaluated and recommendations were made based on simulated bioaerosol releases. In conclusion, the overall state of preparedness has been increased through this work.

# References

Abdul-Wahab, S.A., 2006. Impact of fugitive dust emissions from cement plants on nearby communities. Ecological Modeling 195, 338-348.

Arya, S.P., 1999. Air Pollution Meteorology and Dispersion. Oxford Press, New York.

Basu, S., Nandakumar, K., Masliyah, J.H., 1997. A model for detachment of a partially wetting drop from a solid surface by shear flow. Journal of Colloid and Interface Science 190, 253-257.

Boehm, M.T., Aylor, D.E., 2005. Lagrangian stochastic modeling of heavy particle transport in the convective boundary layer. Atmospheric Environment 39, 4841-4850.

Buser, M.D., Parnell, C.B., Shaw, B.W., Lacey, R.E., 2007. Particulate Matter Sampler Errors Due to the Interaction of Particle Size and Sampler Performance Characteristics: Background and Theory. Transactions of the American Society of Agricultural and Biological Engineers 50, 221-228.

Buser, M.D., Parnell, C.B., Shaw, B.W., Lacey, R.E., 2007. Particulate Matter Sampler Errors Due to the Interaction of Particle Size and Sampler Performance Characteristics: Ambient PM10 Samplers. Transactions of the American Society of Agricultural and Biological Engineers 50, 229-240.

Businger, J.A., Wyngaard, J.C., Izumi, Y., Bradley, E.F., 1971. Flux-Profile Relationships in the Atmospheric Surface Layer. Journal of the Atmospheric Sciences 28, 181-189.

Cengel, Y., Heat Transfer, Second Edition, Wiley & Sons, New York, 2003, pp. 759.

Chertoff, M., 2008. Confronting biological threats to the homeland. Joint Force Quarterly 51, 8-12.

Chun, J.H., Lee, W.J., Lee, U.C., 2006. Development of the film-splitting look-up table applicable to mechanistic annular film dryout model in annulus geometry, International Journal of Heat and Mass Transfer 49, 1350-1357.

Cimorelli, A.J., Perry, S.G., Venkatram, A., Weil, J.C., Paine, R.J., Wilson, R.B., Lee, R.F., Peters, W.D., Brode, R.W., 2005. AERMOD: A Dispersion model for industrial source applications. Part I: General Model formulation and boundary layer characterization. Journal of Applied Meteorology 44: 682-693.

Committee on Materials and Manufacturing Processes for Advanced Sensors, 2004. Sensor Systems for biological agent attacks: protecting buildings and military bases. National Research Council of the National Academies, Washington, D.C. pp 68.

Csanady, G.T., 1963. Turbulent diffusion of heavy particles in the atmosphere. Journal of the Atmospheric Sciences 20, 201-208.

de Mello, A.J., Beard, N., 2003. Dealing with 'real' samples: sample pre-treatment in microfluidic systems. Lab on a Chip 3, 11N-19N.

Dimitrakopoulos, P., Higdon, J.J.L., 1997. Displacement of fluid droplet from solid surfaces in low-Reynolds-number shear flows. Journal of Fluid Mechanics 336, 351-378.

Doran, J.C., Abbey, O.B., Buck, J.W., Glover, D.W., Horst, T.W, Lee, R.N., Lloyd, F.D., 1984. Field Validation of Exposure Assessment Models, Vol. 1: Data. EPA/600/3-84/0924, NTIS, Springfield.

Doran, J.C., Horst, T.W., 1985. An evaluation of Gaussian plume depletion models with dual-tracer field measurements. Atmospheric Environment 19, 939-951.

Etyemezian, V., Ahonen, S., Nikolic, D., Gillies, J., Kuhns, H., Gillete, D., Veranth, J., 2004. Deposition and Removal of Fugitive Dust in the Arid Southwestern United States: Measurements and Model Results. Journal of Air and Waste Management 54: 1099-1111.

Fair, R.B., Khlystov, A., Tailor, T.D., Ivanov, V., Evans, R.D., Srinivasan, V., Pamula, V.K., Pollack, M.G., Griffin, P.B., Zhou, J., 2007. Chemical and Biological Applications of Digital-Microfluidic Devices. IEEE Design and Test of Computers 24, 10-24.

Fredrickson, C.K. Fan, Z.K., 2004. Macro-to-micro interfaces for microfluidic devices. Lab on a Chip 4, 526-533.

Gifford, F.A., 1976. Turbulent Diffusion-Typing Schemes: A Review. Nuclear Safety 17, 68-86.

Graham, B, 2008. World at Risk: The Report of the Commission on the Prevention of Weapons of Mass Destruction Proliferation and Terrorism.

Hage, K.D., 1961. On the dispersion of large particles from a 15-m source in the atmosphere. Journal of Meteorology 18, 534-539.

Han, T., Mainelis, G., 2008. Design and development of an electrostatic sampler for bioaerosols with high concentration rate. Journal of Aerosol Science.

Hanna, S.R., 1981. Lagrangian and Eulerian Time-Scale Relations in the Daytime Boundary Layer. Journal of Applied Meteorology 20, 242-249.

Hashem, A., Parkin, C.S., 1991. A simplified heavy particle random-walk model for the prediction of drift from agricultural sprays. Atmospheric Environment 25A, 1609-1614.

Hazuku, T., Takamasa, T., Hibiki, T., Ishii, M., 2007. Interfacial area concentration in annular two-phase flow, International Journal of Heat and Mass Transfer 50, 2986-2995.

Hinds, Aerosol Technology, Second Edition, John Wiley & Sons, New York, 1999, pp. 111-127.

Hinds, W.C. 1999. Aerosol Technology. John Wiley & Sons, Inc., New York.

Hinze, J.O., 1955. Fundamentals of the hydrodynamic mechanisms of splitting in dispersion processes, AIChE Journal 1, 289-295.

Holmes, N.S., Morawska, L., 2006. A review of dispersion modeling and its application to the dispersion of particles: An overview of different dispersion models available. Atmospheric Environment 40: 5902-5928.

Hu, S., McFarland, A.R., 2007. Numerical Performance Simulation of a Wetted Wall Bioaerosol Sampling Cyclone, Aerosol Science and Technology 41, 160-168.

Huebner, A., Sharma, S., Srisa-Art, M., Hollfelder, F., Edel, J.B., deMello, A.J., 2008. Microdroplets: A sea of applications? Lab on a Chip 8, 1244-1254.

Incropera, F.P., Dewitt, D.P., 2002. Fundamentals of Heat and Mass Transfer, Fifth Edition, John Wiley & Sons.

Ishii, M., Grolmes, M.A., 1975. Inception Criteria for Droplet Entrainment in Two-Phase Concurrent Film Flow, AIChE Journal 21, 308-317.

Kataoka, Ishii, M., Nakayama, A., 2000. Entrainment and deposition rates of droplets in annular two-phase flow, International Journal of Heat and Mass Transfer 43, 1573-1589.

Kesavan, J., Doherty, R.W., Wise, R.G., McFarland, A.R., 2001. Factors that affect fluorescein analysis, ECBC-TR-208, 7-24.

Kim, B.H., Peterson, G.P., 1995. Analysis of the critical Weber number at the onset of liquid entrainment in capillary driven heat pipes, International Journal of Heat and Mass Transfer 38, 1427-1442.

Kim, E., Kalman, D., Larson, T., 2000. Dry deposition of large, airborne particles onto a surrogate surface. Atmospheric Environment 34, 2387-2397.

Kim, E., Larson, T., 2001. Simulation of large particle transport near the surface under stable conditions: comparison with the Hanford tracer experiments. Atmospheric Environment 35, 3509-3519.

Koeltzsch, K., 1999. On the relationship between the Lagrangian and Eulerian time scale. Atmospheric Environment 33, 117-128.

Lioumbas, J.S., Mouza, A.A., Paras, S.V., 2006. Effect of surfactant additives on co-current gas-liquid downflow. Chemical Engineering Science 61, 4605-4616.

Mahe, M., Vignes-Alder, M., Rousseau, A., Jacquin, C.G., Adler, P.M., 1988. Adhesion of droplets on a solid wall and detachment by a shear flow I. pure systems. Journal of Colloid and Interface Science 126, 315-328.

Mahe, M., Vignes-Alder, M., Adler, P.M., 1988. Adhesion of droplets on a solid wall and detachment by a shear flow II. rough substrates. Journal of Colloid and Interface Science 126, 329-336.

Mahe, M., Vignes-Alder, M., Adler, P.M., 1988. Adhesion of droplets on a solid wall and detachment by a shear flow III. contaminated systems. Journal of Colloid and Interface Science 126, 329-336.

Marchisio, D.L., Pikturna, J.T., Fox, R.O., Vigil, R.D., Barresi, A.A., 2003, Quadrature Method of Moments for Population-Balance Equations, AIChE Journal 49 (5) 1266-1276.

McAlister, G., Ettema, R., Marshall, J.S., 2005. Wind-driven rivulet breakoff and droplet flows in microgravity and terrestrial-gravity conditions. Journal of Fluids Engineering 127, 257-265.

McFarland, A.R., Haglund, J.S., King, M.D., Hu, S., Phull, M.S., Moncla, B.W., Seo, Y., 2009. Wetted Wall Cyclones for Bioaerosol Sampling. Journal of Aerosol Science and Technology.

Mills, A.F. Mass Transfer, First Edition, Prentice Hall, Upper Saddle River, New Jersey, 2001, pp. 33-68.

Moran, M.J., Shapiro, H.N., 2000. Fundamentals of Engineering Thermodynamics, Fourth Edition, John Wiley & Sons, New York.

Montgomery, D.C., Runger, G.C., 2003. Applied Statistics and Probability for Engineers. John Wiley & Sons, New York.

Niewstadt, F.T.M, van Ulden, A.P., 1978. A Numerical Study on the Vertical Dispersion of Passive Contaminants from a Continuous Source in the Atmospheric Surface Layer. Atmospheric Environment 12, 2119-2124.

Okawa, T., Kataoka, I., 2005. Correlations for the mass transfer rate of droplets in vertical upward annular flow, International Journal of Heat and Mass Transfer 48, 4766-4788.

Okawa, T., Kotani, A., Kataoka, I., 2005. Experiments for liquid phase mass transfer rate in annular regime for a small vertical tube, International Journal of Heat and Mass Transfer 48, 585-598.

Patankar, S.V, 1980. Numerical Heat Transfer and Fluid Flow. Hemisphere, New York.

Perry, S.G., Cimorelli, A.J., Paine, R.J., Brode, R.W., Weil, J.C., Venkatram, A., Wilson, R.B., Lee, R.F., Peters, W.D., 2005. AERMOD: A Dispersion Model for Industrial Source Applications. Part II: Model Performance against 17 field study databases. Journal of Applied Meteorology 44, 694-708.

Phan, H.N., McFarland, A.R., 2004. Aerosol-to-Hydrosol Transfer Stages for Use in Bioaerosol Sampling. Aerosol Science and Technology 38, 300-310.

Ragland, K.W., Dennis, R.L., 1975. Point Source Atmospheric Diffusion Model with Variable Wind and Diffusivity Profiles. Atmospheric Environment 9, 175-189.

Rizk, N.K., Lefebvre, A.H., 1984. Spray Characteristics of Plain-Jet Airblast Atomizers. Transactions of the ASME 106, 634-638.

Romay, F.J., Roberts, D.L, Marple, V.A., Liu, B.Y.H., Olson, B.A., 2002. A high performance aerosol concentrator for biological agent detection. Aerosol Science and Technology 36, 217-226.

Saber, H.H., El-Genk, M.S., 2004. On the breakup of a thin liquid film subject to interfacial shear. Journal of Fluid Mechanics 500, 113-133.

Sawant, P., Ishii, M., Mori, M., 2008, Droplet entrainment correlation in vertical upward co-current annular two-phase flow, Nuclear Engineering and Design 238, 1342-1352.

Sawford, B.L., Guest, F.M., 1991. Lagrangian statistical simulation of the turbulent motion of heavy particles. Boundary Layer Meteorology 54, 147-166.

Schadel, S.A., Leman, G.W., Binder, J.L., Hanratty, T.J., 1990. Rates of atomization and deposition in vertical annular flow, International Journal of Multiphase Flow 16, 363-374.

Schleizer, A.D., Bonnecaze, R.T., 1999. Displacement of a two-dimensional immiscible droplet adhering to a wall in shear and pressure driven flows. Journal of Fluid Mechanics 383, 29-54.

Schwartz, L.W., Roux, D., Cooper-White, J.J., 2005. On the shapes of droplets that are sliding on a vertical wall. Physica D 209, 236-244.

Scott, P.K., Proctor, D., 2008. Soil Suspension/Dispersion Modeling methods for estimating health-based soil cleanup levels of hexavalent chromium at chromite ore processing residue sites. Journal of Air and Waste Management 58: 384-403.

Seo, Y., 2007. Design of wetted-wall bioaerosol concentration cyclones. Texas A&M University. Ph.D. Dissertation.

Sigaev, G.I., Tolchinsky, A.D., Sigaev, V.I., Soloviev, K.G., Varfolomeev, A.N., Chen, B.T., 2006. Development of a cyclone-based aerosol sampler with recirculating liquid film: theory and experiment. Aerosol Science and Technology 40, 293-308.

Slater, J.W. 2007. NPARC Alliance CFD Verification and Validation Web Site. Tutorial on CFD Verification and Validation. http://www.grc.nasa.gov/WWW/wind/valid/tutorial/tutorial.html

Snyder, W.H., Lumley, J.L., 1971. Some measurements of particle velocity autocorrelation functions in a turbulent flow. Journal of Fluid Mechanics 48, 41-71.

Stock, D.E., 1996. Particle dispersion in flowing gases. Journal of Fluids Engineering 118, 4-17.

Stoecker, W.F., 1989. Design of Thermal Systems. McGraw-Hill, New York.

Thompson, D., Muriel, P., Russel, D., Osborne, P., Bromley, A., Rowland, M., Creigh-Tyte, S., and C. Brown, 2002. Economic costs of the foot and mouth disease outbreak in the United Kingdom in 2001. Revue Scientifique et Technique del Office International des Epizooties 21, 675-687.

Tsai, M.Y., Elgethun, K., Ramaprasad, J., Yost, M.G., Felsot, A.S., Hebert, V.R., Fenske, R.A., 2005. The Washington aerial spray drift study: modeling pesticide spray drift deposition from an aerial application. Atmospheric Environment 39, 6194-6203.

Tucker, D., 2009. Chilled WWC-100 condensation experimental data. Personal communication.

United States Department of Defense, 2008. Environmental Engineering Considerations and Laboratory Tests. MIL-STD-810G.

United States Department of Homeland Security, 2004. Biodefense for the 21st century.

United States Department of Homeland Security, 2007. Guide for the selection of biological agent detection equipment for first responders. Guide 101-06.

United States Environmental Protection Agency, 2005. Revision to the Guideline on Air Quality Models: Adoption of a Preferred General Purpose Dispersion Model. Federal Register, 40 CFR Part 51.

United States Environmental Protection Agency, 2009. Atmospheric Dispersion Modeling. http://www.epa.gov/scram001/dispersionindex.htm

Upadhyay, R.R., Ezekoye, O.A., 2006, Treatment of size-dependent aerosol transport processes using quadrature based moment methods, Journal of Aerosol Science 37, 799-819.

van Ulden, A.P., 1978. Simple Estimates for Vertical Diffusion from Sources Near the Ground. Atmospheric Environment 12, 2125-2129.

Vesovic, V., Auziere, A., Calvaic, G., Dauriat, A., 2001. Modeling of the dispersion and deposition of coarse particulate matter under neutral atmospheric conditions. Atmospheric Environment 35, S99-S105.

Wagner, W., and Pruss, A., 1993. International Equations for the Saturation Properties of Ordinary Water Substance. Addendum to Journal of Physical Chemistry Reference Data: 16, 783-787

Walker, E.R., 1965. A Particulate Diffusion Experiment. Journal of Applied Meteorology 4, 614-621.

Wang, L., Parnell, C.B., Buser, M.D., 2007. Theoretical Study of the Impact of Particulate Matter Gravitational Settling on Ambient Coarse Particulate Matter Monitoring for Agricultural Emissions. Journal of Air and Waste Management Association 57, 111-115.

Wang, Y., Miller, D.R., Anderson, D.E., McManus, M.L., 1995. A Lagrangian stochastic model for aerial spray transport above an oak forest. Agricultural and Forest Meteorology 76, 277-291.

Wells, M.R., Stock, D.E., 1983. The effects of crossing trajectories on the dispersion of particles in a turbulent flow. Journal of Fluid Mechanics 136, 31-62.

Wilson, J.D., 2000. Trajectory Models for Heavy Particles in Atmospheric Turbulence: Comparison with Observations. Journal of Applied Meteorology 39, 1894-1912.

Wyngaard, J.C., 1972. On Surface-Layer Turbulence in Workshop on Micrometeorology. Eds. Busch, N.E., and D.A. Haugen. pp 101-149.

Yu, T.S., Li, Y., Wong, T.W., Tam, W., Chan, A.T., Lee, J.H.W., Leung, D.Y.C., and T. Ho, 2004. Evidence of Airborne Transmission of the Severe Acute Respiratory Syndrome Virus. New England Journal of Medicine 350, 1731-9.

Yudine, M.I., 1959. Physical considerations on heavy-particle diffusion. Advances in Geophysics 6, 185-191.

Zhao, Y., Cho, S.K., 2006. Microparticle sampling by electrowetting-actuated droplet sweeping. Lab on a Chip 6, 137-144.

# Vita

Joshua Allen Hubbard was born in Wichita, Kansas on February 18, 1982 to Marilee Jane and Floyd Allen Hubbard. He graduated as the class valedictorian of Northeast Magnet High School, Wichita, Kansas, in May 2000. In May 2005 he was awarded a Bachelors Degree, summa cum laude, in Mechanical Engineering at Kansas State University. He then began his research career in aerosol physics at the Institute for Environmental Research, Manhattan, Kansas, and attained a Masters Degree in Mechanical Engineering under the mentorship of Distinguished Professor Chris Sorensen and Professor Steven Eckels in August 2006. Their work on small angle light scattering from dense random aggregates was featured in *Particle and Particle Systems Characterization* in 2008. After graduation he began studying bioaerosol risk assessment and sampler design at the Applied Research Labs at the University of Texas at Austin under the guidance of Professor Ofodike Ezekoye and Doctor John Haglund.

Permanent address: 9549 E. Lincoln Ct. Wichita, Kansas 67207

This dissertation was typed by Joshua Allen Hubbard